Irradiation Damage of Oxide Dispersion Strengthened Steels



Andrew James London

Wolfson College

University of Oxford

A thesis submitted for the degree of

Doctor of Philosophy

Trinity Term, 2015

To my Father,

whose PhD was never awarded.

1949–2014

Abstract

Irradiation Damage of Oxide Dispersion Strengthened Steels
Andrew James London
Wolfson College, Oxford
A thesis submitted for the degree of Doctor of Philosophy
Trinity Term, 2015

Advanced fission and fusion power offer long-term energy production from fundamentally carbon-free fuel sources, with high-energy densities and high reliability. However, for these power sources to be realised, many materials challenges need to be addressed. Oxide dispersion strengthened (ODS) ferritic alloys are recognized as potential fission fuel cladding and fusion structural materials because of their high-temperature stability and swelling-resistance imparted by the nano-scale oxide clusters they contain.

This work presents the study of a set of model ODS alloys with a systematic variation in alloy chemistry in order to investigate the influence of chemical additions on the oxide cluster nature and the irradiation resistance. To investigate these properties, the high-resolution characterisation techniques of atom probe tomography and transmission electron microscopy were applied in combination with nanoindentation to assess mechanical properties and X-ray diffraction to study the crystallinity.

The quantification of the character of the oxide particles in these ODS alloys by atom probe tomography presented a number of challenges and I extend the conventional analysis techniques in order to overcome these difficulties.

By comparison of the addition of Ti, and then Cr, to a Fe-Y_2O_3 alloy, the influence of alloy chemistry on the oxide particles was evaluated. The main aims were to investigate the microstructure, the oxide cluster composition and to set a baseline to which the irradiated samples were compared.

The irradiation damage of the oxide clusters was investigated using ion irradiation as an analogue for neutron damage. Irradiation experiments were performed at a range of temperatures and the stability of the clusters was assessed based on their size, number density and chemistry. Subtle changes in cluster chemistry at elevated temperatures and the dramatic changes which occurred after irradiation at low temperatures lead to conclusions about the competition of thermal diffusion and irradiation damage.

Preface

The work presented in this doctoral thesis has been carried out at the Department of Materials, University of Oxford from October 2011 to July 2015, under the supervision of Prof. Chris R.M. Grovenor and Prof. Sergio Lozano-Perez. All of the research carried out for this thesis is original, and where the work of others has been included it has been clearly referenced and acknowledged. All figures and tables reproduced from journal articles and books have been used with permission from the respective copyright owner. No part of this thesis has been submitted for a degree at this, or any other university. Some of the work has been published in peer reviewed journals and presented at conferences and seminars as detailed below:

Journal Articles:

London, A. J., Lozano-Perez, S., Santra, S., Amirthapandian, S., Panigrahi, B. K., Sundar, C. S., and Grovenor, C. R. M. (2014). *Comparison of atom probe tomography and transmission electron microscopy analysis of oxide dispersion strengthened steels.* Journal of Physics: Conference Series, 522(1), 012028. doi:10.1088/1742-6596/522/1/012028

Edmondson, P. D., **London, A.J.**, Xu, A., Armstrong, D. E. J., and Roberts, S. G. (2014). *Small-scale characterisation of irradiated nuclear materials: Part I–Microstructure.* Journal of Nuclear Materials. doi:10.1016/j.jnucmat.2014.11.067

London, A.J., Lozano-Perez, S., Moody, M., Amirthapandian, S., Panigrahi, B., Sundar, C., and Grovenor, C. (2015). *Quantification of oxide particle composition in model oxide dispersion strengthened steel alloys.* Ultramicroscopy. doi:10.1016/j.ultramic.2015.02.013

London, A. J., Santra, S., Amirthapandian, S., Panigrahi, B. K., Sarguna, R. M., Balaji, S., ... Grovenor, C. R. M. (2015). *Effect of Ti and Cr on dispersion, structure and composition of oxide nano-particles in model ODS alloys.* Acta Materialia, 97, 223–233. doi:10.1016/j.actamat.2015.06.032

London, A. J., Panigrahi, B. K., Tang, C. C., Murray, C., and Grovenor, C. R. M. (2015). *Glancing angle XRD analysis of particle stability under self-ion irradiation in oxide dispersion strengthened alloys.* Scripta Materialia. doi:10.1016/j.scriptamat.2015.07.037

Conferences:

London, A. J., Lozano-Perez, S., Santra, S., Amirthapandian, S., Panigrahi, B. K., Sundar, C. S., and Grovenor, C. R. M., *Atom probe tomography and transmission electron microscopy analysis of oxide dispersion strengthened steels*, Oral Presentation, National Student Conference in Metallic Materials (2013)

London, A. J., Lozano-Perez, S., Santra, S., Amirthapandian, S., Panigrahi, B. K., Sundar, C. S., and Grovenor, C. R. M., *Comparison of atom probe tomography and transmission electron microscopy analysis of oxide dispersion strengthened steels*, Oral Presentation, EMAG, York (2013)

London, A. J., Lozano-Perez, S., Panigrahi, B. K., Sundar, C. S., and Grovenor, C. R. M., *Atom Probe Tomography of Indian Model ODS alloys*, Oral Presentation, ODS workshop Dresden (2013)

A.J. London, Lozano-Perez, S., Moody, M.P., Amirthapandian, S., Panigrahi, B.K., Sundar, C.S., and Grovenor, C.R.M., *Quantification of oxide particle composition in model ODS steel alloys*, Oral Presentation - Shortlisted for the "Outstanding Young Scientist Award", APT&M, Stuttgart (2014)

Acknowledgments

This work was made possible by a generous donation from the Black Family Charity, and I am especially appreciative of the times I have spent with Dr Tom Black; I hope I have done justice to his research into irradiation damage conducted in 1984.

The work presented in this thesis was made possible through the support of many different people. First, I would like to thank my supervisors Prof. Chris R.M. Grovenor and Prof. Sergio Lozano-Perez for their continual support and guidance throughout my PhD; I would not developed into the researcher I am today without their encouragement. Their supervision has always been to the highest standard, always understanding and willing to go the extra mile for me.

My Indian collaborators have always inspired me with their optimistic attitude. I am very thankful for their very warm and generous hospitality and their acceptance of me as a colleague.

I am very grateful for the technical support from: all those in Electron Microscopy; Laurie Walton in the workshop; D. Armstrong for use of the nanoindenter; and C. Tang for the opportunity to use the Diamond Light Source. From EM, I would specifically like to thank J. Kim for her assistance and use of the OJ2200, and N. Young and G. Hughes for their time training me. I would like to thank two very knowledgeable men, M. Jenkins and G. Smith, for their helpful discussions, endless wisdom and encouragement.

I would like to thank all my colleagues at Oxford Materials who made my time there so joyful, especially the members of the Nanoanalysis, FIM/APT and MFFP groups, who have put up with my relentless questioning and have always been ready for lighthearted yet scientific discussion. Specifically, I would like to thank; C. Williams for her help getting me "up to speed" on all things APT and ODS; P. Bagot & T. Martin for training on the atom probe, 3DAP and sample prep.; D. Haley for his endless support with posgen and my frequent computer problems; and J. Zelenty for helping with the more mathematically demanding problems.

Special thanks go to my family, who never left me short-changed in terms of scientific explanations—even when I was too young to understand. And thanks go to my church family at Magdalen Road Church and all those who have stood by me throughout my time in Oxford.

Thank you to Hannah, my loving and dedicated wife. For all you've sacrificed, and all that you've done so that I could live out my dream, it won't be forgotten or taken for granted. It will always be remembered.

Dominus illuminatio mea

"The LORD is my light"

This work was conducted only by His ever-present grace, so that the truth of His world would be illuminated and His name glorified.

Acronyms

T_{irrd}	Irradiation Temperature
APT	Atom Probe Tomography
DBTT	Ductile-to-Brittle Transistion Temperature
DLD	Delay-Line Detector
dpa	Displacements Per Atom
EBSD	Electron Back-Scattered Diffraction
EFTEM	Energy Filtered Transmission Electron Microscopy
EMG	Exponentially Modified Gaussian function
FIB	Focused Ion Beam
FWHM	Full Width Half Maximum
GB	Grain Boundary
GIXRD	Glancing Incidence X-Ray Diffraction
HIP	Hot Isostaic Pressing
ICF	Image Compression Factor
IVAS	Imago Visualisation and Analysis Software
LEAP	Local Electrode Atom Probe
MA	Mechanical Alloying
MCP	Microchannelplate
MD	Molecular Dynamics
MSA	Multivariate Statistical Analysis
ODS	Oxide Dispersion Strengthened steel
PAS	Positron Annihilation Spectroscopy

PCA	Principal Component Analysis
PKA	Primary Knock-on Atom
RAFM	Reduced-Activation Ferritic/Martensitic steel
ROI	Region Of Interest
SANS	Small-Angle Neutron Diffraction
SIA	Self-Interstitial Atom
TEM	Transmission Electron Microscopy
TOF	Time-of-Flight
XRD	X-Ray Diffraction

Contents

1 Introduction **1**

2 Literature Review **5**

2.1 Introduction 5

2.2 Oxide Dispersion Strengthened Steels 6

2.2.1 Manufacture 8

2.2.2 Mechanical Properties 10

2.2.3 Microstructural Characterisation 11

2.2.3.1 Bulk Analysis 12

2.3 ODS Particle Characterisation 13

2.3.1 Stoichiometric Compositions 14

2.3.2 Non-Stoichiometric Compositions 16

2.3.3 Atom Probe Tomography 23

2.3.4 Discussion 25

2.3.5 Inhomogeneity 27

2.4 Irradiation Damage 28

2.4.1 Influence of Irradiation Damage 33

2.4.2 Irradiation Damage of ODS Particles 34

2.4.3 Discussion 38

2.5 Summary 41

3 Materials and Experimental Methods **43**

3.1 Materials 44

3.2 Ion Irradiation 45

3.3 Sample preparation 47

3.3.1 APT - Electropolishing 47

3.3.2 APT - Focused Ion Beam Milling 48

3.3.3 TEM - Focused Ion Beam Milling 49

3.4 Glancing X-Ray Diffraction 49

3.5 Nanoindentation . . . 51
3.6 TEM . . . 52
3.6.1 Imaging . . . 52
3.6.2 EFTEM - OJ2200 FEG TEM . . . 53
3.6.3 EFTEM & EELS - ARM200F . . . 53
3.6.4 Data Analysis . . . 53
3.6.5 Principal Component Analysis . . . 54
3.7 APT . . . 56
3.7.1 Data Acquisition . . . 58
3.7.2 Multiple Hits . . . 59
3.7.3 Reconstruction Methodology . . . 59
3.7.3.1 Calibration . . . 63
3.7.4 Reconstruction Artefacts . . . 65
3.7.5 Composition . . . 68
3.7.6 Visualisation . . . 71
3.7.6.1 Atom maps . . . 71
3.7.6.2 1D and 2D profiles . . . 72
3.7.6.3 Proximity histograms . . . 72
3.7.7 Clustering . . . 73
3.7.8 The Maximum Separation Method . . . 73
3.7.8.1 Parameter Selection . . . 76
3.7.9 Cluster Measurements . . . 80
3.7.9.1 Morphology . . . 80
3.7.9.2 Composition . . . 81

4 APT Analysis Techniques 84
4.1 Introduction . . . 84
4.2 Composition . . . 85
4.2.1 Systematic ranging . . . 85
4.2.2 Background correction . . . 87
4.2.3 Peak deconvolution . . . 87
4.2.3.1 Least-Squares versus Maximum Likelihood . . . 90
4.2.4 Quantification of Oxides . . . 91
4.3 Multiple Hit Analysis . . . 92
4.4 Trajectory Aberrations . . . 96
4.5 Extended Cluster Analysis . . . 98
4.5.1 Line profiles . . . 99
4.5.2 Cluster Composition . . . 100

4.5.2.1 Mass-peak overlaps . . . 100
4.5.2.2 Fe-Content . . . 100
4.5.3 Cluster Size . . . 103
4.5.3.1 Which measurement? . . . 103
4.5.3.2 Extent versus Range . . . 105
4.5.3.3 Comparison with TEM . . . 107
4.6 Inhomogeneity Measurement . . . 109
4.7 Summary . . . 112

5 The As-Received Model Alloys 113
5.1 Introduction . . . 113
5.2 Overview Data . . . 113
5.3 Particle Size . . . 117
5.3.1 Fe-Y; HIP versus Extruded . . . 117
5.3.2 Influence of Ti and Cr . . . 117
5.4 Cluster Composition . . . 120
5.4.1 Bulk Chemistry . . . 120
5.4.2 Individual Cluster Chemistry . . . 123
5.4.3 Local Cluster Chemistry . . . 131
5.5 Inhomogeneity . . . 138
5.5.1 Introduction . . . 138
5.5.2 Spatial Variation . . . 138
5.5.3 Measuring H . . . 139
5.6 Discussion . . . 140
5.6.1 FeY . . . 140
5.6.2 Processing Route . . . 141
5.6.3 Influence of Ti . . . 142
5.6.4 Influence of Cr . . . 143
5.6.5 Are Fe and Cr oxide components? . . . 145
5.6.6 Spatial Variation . . . 147
5.7 Summary and Conclusions . . . 147

6 Ion Irradiation Experiments 149
6.1 Introduction . . . 149
6.2 High-Temperature Irradiation . . . 150
6.2.1 FeY . . . 150
6.2.2 FeTiY . . . 156
6.2.3 FeCrTiY . . . 163

6.2.4 Comparison . . . 171
6.3 Low-Temperature Irradiation . . . 173
6.3.1 Introduction . . . 173
6.3.2 Crystal Structure . . . 173
6.3.3 Chemistry . . . 177
6.4 Subsequent Treatments . . . 182
6.5 Discussion . . . 188
6.5.1 FeY . . . 189
6.5.2 FeTiY . . . 191
6.5.3 FeCrTiY . . . 192
6.5.4 Displacement Mixing . . . 193
6.5.4.1 Mixing Model . . . 195
6.5.5 High-Temperature Irradiation . . . 198
6.5.6 Conclusions . . . 200
6.6 Summary . . . 201

7 Summary and Conclusions **203**
7.1 Introduction . . . 203
7.2 Summary . . . 203
7.3 Conclusions . . . 206
7.4 Suggestions for Future Work . . . 207

8 Bibliography **209**

A Appendices **228**
A.1 SRIM Calculation . . . 228
A.2 Principal Component Analysis Example . . . 228
A.3 File Formats . . . 230
A.3.1 .POS file . . . 230
A.3.2 .EPOS file . . . 230
A.3.3 .RRNG file . . . 230
A.4 Lorentzian Peak Fitting . . . 231
A.5 MATLAB Programs . . . 232
A.6 Cluster selection parameters . . . 233
A.7 knitr information . . . 236

List of Figures

2.2.1 A schematic of the processing sequence for ODS alloys. 10
2.2.2 Synchrotron X-ray powder diffraction analysis of mechanically milled ODS powder and annealed powders. 13
2.3.1 Phase of restored exit wave HRTEM image of a nano-scale $Y_2Ti_2O_7$ oxide in a MA957 alloy. 15
2.3.2 HRTEM image of a Ti-Y complex oxide particle of unknown structure. 18
2.3.3 Tensile yield strength measured as a function of temperature for 12YWT-like alloys. 19
2.3.4 EFTEM micrographs of a ODS particle with Ar bubbles. 20
2.3.5 Yttrium EELS spectra extracted from a large Y-rich particle in 12Cr-ODS. 21
2.3.6 EFTEM elemental maps for the Y–$N_{2,3}$ edge from raw data and after MSA "noise-free" reconstruction. 22
2.3.7 EELS composition measurement of a particle. 22
2.3.8 Atom maps of Y-Ti-O clusters in 12YWT crept at 800 °C for 14,500 h. 24
2.3.9 Atom maps of 14YWT showing a wide field-of-view. 24
2.3.10 Inhomogeneous distribution of titanium in a pre-alloyed Fe–14Cr–Ti powder particle. 27
2.3.11 The basis for publishing the "best looking" images. 28
2.4.1 Influence of neutron irradiation on the mechanical properties of ODS alloys. 34
2.4.2 Swelling versus displacement damage for the K3-ODS and JLF-1 (non-ODS) steels. 34
2.4.3 Halos of smaller particles around neutron irradiated DY ODS. 35
2.4.4 Refinement of particle size by ion irradiation to 150 dpa at 500 and 700 °C. 36
2.4.5 Influence of high-dosage ion-irradiation on particles as a function of irradiation temperature. 39
2.4.6 Adjustment of a particle size distribution by ion irradiation. 41

3.2.1 Dose as a function of depth as estimated by SRIM for 1.5×10^{17} 5 MeV Fe^{3+} ions and 9×10^{16} 1.76 MeV Fe^{+}ions in iron. 47
3.3.1 Comparison of Ga implantation by FIB at different energies. 49
3.4.1 $1/e$ attenuation depth as a function of glancing incidence angle, for GIXRD. 51
3.6.1 Example of eigen images and eigen vectors. 55
3.7.1 Schematic of the sample in a reflectron-fitted Local Electrode Atom Probe. 57
3.7.2 Electrical potential and electric field around an APT needle measured using electron holography. 60
3.7.3 Schematic showing the lengths used in the tip reconstruction. 61

3.7.4 Tip Profile reconstruction method. . . . 63
3.7.5 Reconstruction calibration routine. . . . 64
3.7.6 Simulations of a spherical precipitate of different evaporation properties observed using atom probe. . . . 66
3.7.7 Carbon and nitrogen segregation to the poles of the matrix material. . . . 67
3.7.8 Position artefacts relating to the time of evaporation. . . . 67
3.7.9 Example mass-to-charge spectrum. . . . 70
3.7.10 Important steps of the maximum separation algorithm. . . . 75
3.7.11 Clusters found after random relabelling. . . . 76
3.7.12 The results of different parameters when cluster searching using the maximum separation method. . . . 77
3.7.13 The variation of cluster measurements with cluster selection parameters. . . . 78
3.7.14 Output data from a cluster search. . . . 79
3.7.15 Variation of measured cluster composition as a function of D_{max}. . . . 83

4.2.1 Example peak fitting in the mass-to-charge spectrum. . . . 86
4.2.2 Example spatial dependence of peak overlaps. . . . 88
4.2.3 Fraction of O_2^+ in the 32 Da mass peak. . . . 89
4.3.1 Multiple hit distance 1D histogram comparing laser and voltage pulsing. . . . 93
4.3.2 Voltage mode: 2D multiple-hit location histograms 94
4.3.3 Multiple-hit ΔTOF histogram. . . . 95
4.3.4 2D multiple-hit correlation plot. . . . 95
4.4.1 Measured ionic density of the oxide clusters as a function of size. . . . 96
4.4.2 Cluster morphology as a function of size. . . . 97
4.4.3 2D Fe ionic density and Cr concentration plots. . . . 97
4.4.4 Combined TEM and APT of the same sample showing a large composite particle. . . . 98
4.4.5 Clustered solute ions showing a number of small flatter clusters and one larger cluster. 98
4.4.6 Atomistic simulation of the evaporation of a 0.5 nm radius low-field cluster. . . . 98
4.5.1 Example composition line profile volume of interest. . . . 100
4.5.2 Result of a per-cluster peak deconvolution: estimated ionic composition of a cluster. . 101
4.5.3 Mean ionic-density line profiles through clusters in the as-received Fe-Cr-Ti-Y alloy. 102
4.5.4 Fe fraction as a function of size, expressed in radius of gyration, l_g and reduced radius. 103
4.5.5 Comparison of cluster measurement methods. . . . 104
4.5.6 Comparison of different cluster size measurements on numerically simulated data. . . 106
4.5.7 The standard deviation of different measures of cluster radius derived from numerical simulation. . . . 107
4.5.8 Difference in mean measured radius and simulated radius for different cluster size measurements, including spatial noise. . . . 107
4.5.9 Correlative microscopy of ODS alloys (TEM+APT). . . . 108
4.5.10 Comparison of cluster radii measurements with the particle radius observed by TEM. 108
4.5.11 Comparison of particle size measured using Fresnel contrast on bright-field Fresnel images and EFTEM eigen images. . . . 109

4.6.1 Conversion from a real microstructure (a) to a population distribution chart. 110
4.6.2 Example of Garncarek's measure of spatial inhomogeneity. 110
4.6.3 Example measurements of spatial inhomogeneity using Garncarek's method in 3D . 111

5.2.1 Nanoindentation measure of hardness with depth of the three extruded alloys. 114
5.2.2 TEM images of needle samples before APT analysis and the resulting atom maps. . . 115
5.2.3 Carbon segregation to a GB in the as-received FeY alloy. 116
5.3.1 Composite yttrium (blue) and chromium (yellow) oxide particles as detected using EFTEM. 118
5.3.2 Composition line profiles along the z-axis through clusters in FeY and FeY-hi. 118
5.3.3 EFTEM images of the Y and Ti edges for the extruded as-received alloys. 119
5.3.4 Particle size distributions for FeY, FeTiY and FeCrTiY. 119
5.4.1 Comparison of GIX 2θ-scans of FeY and FeTiY. 121
5.4.2 Representative energy-loss eigen vectors from principal component analysis from EFTEM of FeY, FeTiY and FeCrTiY. 122
5.4.3 Matrix-corrected peak-deconvoluted cluster compositions averaged over all experiments. 123
5.4.4 Matrix-corrected cluster compositions grouped by cluster radius. 125
5.4.5 Oxygen fraction, not including Fe or Cr ions, of clusters in the 4 different as-received alloys grouped by cluster radius. 127
5.4.6 Median Y:Ti ratios of clusters in FeTiY and FeCrTiY grouped by cluster radius. . . . 128
5.4.7 Comparison of the spatial variation of oxide composition as measured by APT and EFTEM. 128
5.4.8 Y:Ti:O ratio of individual clusters as measured by APT. 129
5.4.9 Ternary diagram error analysis with estimated counting error for each component. . . 130
5.4.10 Y:(Ti+O) ratio of individual clusters as measured by APT. 131
5.4.11 X-ray diffraction of the $Y_2Ti_2O_7$ peaks in FeCrTiY and FeTiY. 132
5.4.12 Averaged composition line profiles parallel to the analysis direction in the as-received alloys. 133
5.4.13 Averaged ionic composition line profiles parallel to the analysis direction in FeY, FeTiY and FeCrTiY. 134
5.4.14 Averaged ionic line profile for clusters in FeY-hi. 135
5.4.15 Matrix-corrected Cr content of clusters in FeCrTiY and FeY-hi. 136
5.4.16 The matrix-corrected Cr composition line profiles scaled by the mean cluster radius in FeCrTiY. 137
5.4.17 Averaged ionic composition line profiles from FeTiY and FeY-hi excluding Fe. . . . 137
5.5.1 Varied spatial distribution of particles and particle sizes in FeCrTiY revealed by EFTEM. 138
5.5.2 The number density of clusters measured by APT for repeated experiments. 139
5.5.3 Measurement of spatial inhomogeneity of clusters in the as-received alloys. 140
5.6.1 Oxygen ions are observed to be spread laterally from the Y-Ti containing cluster. . . 146

6.2.1 Schematic showing the depth-damage dependence of APT samples taken perpendicular to the irradiated surface. . . . 150
6.2.2 EFTEM images from irradiated and unirradiated FeY. . . . 151
6.2.3 Large and small clusters in irradiated FeY. . . . 152
6.2.4 Small Y-rich clusters on a grain boundary in irradiated FeY. . . . 152
6.2.5 FeY: irradiated at 773 K, Y:O ratio as a function of irradiation damage. . . . 153
6.2.6 Y:O ratio for clusters in FeY before and after irradiation. . . . 154
6.2.7 Metal:Oxygen ratio of clusters in irradiated FeY and as-received FeY-hi. . . . 154
6.2.8 Mean ionic-density line profiles through clusters in as-received FeY-hi and irradiated FeY. . . . 155
6.2.9 FeY unirradiated and irradiated (773 K 150 dpa) examined by GIX. . . . 155
6.2.10 Hardness as a function of nanoindentation depth of irradiated and unirradiated FeTiY. 156
6.2.11 GIXRD diffractograms of FeTiY irradiated to a peak damage of 150 dpa. . . . 157
6.2.12 Diffractograms of the $Y_2Ti_2O_7$-(222) peak in irradiated FeTiY. . . . 158
6.2.13 The full-width at half maximum of the $Y_2Ti_2O_7$-(222) peak at 16.3 2θ in irradiated and unirradiated FeTiY. Error bars show 95% confidence intervals. . . . 159
6.2.14 The total integrated counts under the $Y_2Ti_2O_7$-(222) peak at 16.3° 2θ in irradiated and unirradiated FeTiY. . . . 159
6.2.15 Cluster size distribution of FeTiY irradiated to ~80 dpa at 773, 873 and 973 K. . . . 160
6.2.16 Individual cluster compositions in FeTiY after irradiation at high temperature. . . . 161
6.2.17 Distribution of cluster Y/Ti values in FeTiY after irradiation. . . . 162
6.2.18 Spatial location of clusters in irradiated FeTiY coloured by composition. . . . 162
6.2.19 Hardness as a function of nanoindentation depth of irradiated and unirradiated FeCrTiY. . . . 163
6.2.20 GIXRD diffractograms of FeCrTiY irradiated to a peak damage of 150 dpa. . . . 164
6.2.21 GIXRD: The $Y_2Ti_2O_7$ peak in irradiated FeCrTiY. . . . 165
6.2.22 The total integrated counts under the $Y_2Ti_2O_7$-(222) peak in irradiated and unirradiated FeCrTiY. . . . 166
6.2.23 Cluster size distributions for FeCrTiY after irradiation at high temperature. . . . 167
6.2.24 Individual cluster compositions in FeCrTiY after irradiation at high temperature. . . . 168
6.2.25 Distribution of cluster Y/Ti values in irradiated FeCrTiY. . . . 169
6.2.26 Grain boundary segregation in irradiated FeCrTiY. . . . 170
6.2.27 Average composition line profiles from clusters in irradiated FeCrTiY. . . . 170
6.2.28 Comparison of the FeY, FeTiY and FeCrTiY cluster sizes irradiated at different temperatures. . . . 172
6.2.29 Comparison of cluster compositions for FeCrTiY and FeTiY irradiated at high temperature. . . . 172
6.3.1 Nanoindentation of FeCrTiY irradiated at cryogenic temperatures. . . . 174
6.3.2 Nanoindentation of FeTiY irradiated at cryogenic temperatures. . . . 174
6.3.3 EFTEM of the Y and Ti edges in FeCrTiY irradiated at 120 K. . . . 175
6.3.4 EFTEM and HRTEM of FeCrTiY with T_{irrd} <150 K. . . . 176

6.3.5 Diffractograms from (a) as-received FeCrTiY (b) FeTiY irradiated to 100 dpa at <150 K. . . . 176
6.3.6 Integrated counts from the $Y_2Ti_2O_7$ peak in FeCrTiY after irradiation at cryogenic temperature. . . . 177
6.3.7 Atom map of FeCrTiY irradiated at 150 K. . . . 178
6.3.8 Atom map from FeTiY irradiated to 100 dpa. . . . 179
6.3.9 Solute content of the matrix after irradiation at < 150 K. . . . 179
6.3.10 Y:Ti:O ratio of individual clusters irradiated at $T_{irrd} < 150$ K, as measured by APT. . . . 180
6.3.11 Fe-fraction of clusters in FeCrTiY as a function of size, expressed in reduced radius, as-received and after irradiation at T_{irrd} < 150 K. . . . 180
6.3.12 Comparison of line profiles in as-received and FeTiY irradiated to 100 dpa at < 150 K. 181
6.3.13 Composition line profiles through clusters in FeTiY irradiated at cryogenic temperature ($T_{irrd} < 150$ K, max damage 100 dpa). . . . 181
6.3.14 Composition line profiles through clusters in FeTiY irradiated at cryogenic temperature ($T_{irrd} < 150$ K, max damage 100 dpa). . . . 182
6.3.15 Approximate Fe ionic density measured from averaged cluster line profiles in T_{irrd} < 150 K samples. . . . 182
6.4.1 Nanoindentation of FeTiY irradiated at cryogenic temperatures. . . . 183
6.4.2 Nanoindentation of FeCrTiY irradiated at cryogenic temperatures. . . . 184
6.4.3 Atom maps from FeTiY and FeCrTiY irradiated at cryogenic temperature and then subsequently irradiated or annealed. . . . 185
6.4.4 Cluster size distribution for irradiated clusters in FeTiY, T_{irrd}<150 K, followed by irradiation or annealing. . . . 186
6.4.5 Cluster size distribution for irradiated clusters in FeCrTiY, T_{irrd}<150 K, followed by irradiation or annealing. . . . 186
6.4.6 Y:Ti:O ratio of individual clusters irradiated at $T_{irrd} < 150$ K, and then irradiated again or annealed. . . . 187
6.4.7 Median Y, Ti, O ratios of clusters irradiated at <150 K, and then irradiated again or annealed. . . . 188
6.5.1 SRIM predicted solute concentration from an irradiated 5 nm layer of $Y_2Ti_2O_7$ and fitted diffusion profile. . . . 196
6.5.2 Fitted widths of low-temperature-irradiated cluster line profiles. . . . 197
6.5.3 The steady-state diffusion coefficient of Y during irradiation as a function of temperature. . . . 198
6.5.4 Comparison of the estimated diffusion coefficients of Ti and Y in iron during irradiation. . . . 201

7.2.1 Summary image showing the effects of different irradiation conditions. . . . 204

A.1.1 Screen shot of the TRIM calculation window. . . . 229

Chapter 1

Introduction

According to the BP statistical review, in 2011 global primary energy consumption rose by 2.5% despite the economic recession. Primary sources for this energy are oil and coal (33% and 30% respectively), neither of which can provide for the long-term population growth of the world [1]. Even if fossil fuels could meet the global demand for energy, the greenhouse gas emissions would cause dramatic climate change [2]. Conversely, advanced fission and fusion power are recognized to offer long-term energy production from fundamentally carbon-free fuel sources, with high-energy densities and high reliability [2, 3].

For these power sources to be realized, however, many materials challenges need to be addressed [4–8]. For example, generation-IV fission reactors will operate at higher temperatures (550–1000 °C) and to a higher fuel burn-up than previous reactors. The DEMO fusion reactor is expected to accumulate damage of 30 dpa per full-power year and 10 appm of helium per dpa in the structural materials [9]. A possible solution to these challenges is oxide dispersion strengthened (ODS) ferritic alloys, which have been recognized as potential fission fuel cladding and fusion structural materials [4, 6, 10–12].

Ferritic steels have a number of advantages over austenitic steels as structural materials subject to irradiation, with a better swelling resistance and lower activation potential [13]. However, the creep resistance and tensile strength at elevated temperatures (> 500° C) are not acceptable without some additional modification. Thermally stable oxide parti-

cles can be dispersed in the steel to make an Oxide Dispersion Strengthened (ODS) alloy. These oxide particles hinder dislocation motion, improving the high-temperature mechanical properties, and trap irradiation-induced defects and gases, increasing the irradiation tolerance. The oxide particles contribute significantly to the overall mechanical strength [14, 15], as well as refining the alloy grain size [16]. However, it is not yet understood how the processing and alloy chemistry influence the microstructure and mechanical properties of these new alloys. Though there have been many studies on specific aspects of processing and alloy chemistry [17], few have conducted systematic studies with well-controlled processing conditions and none have specifically investigated the effect of chromium on microstructure and oxide chemistry.

The evaluation of the radiation stability of ODS alloys is important for future use in fission and fusion environments. Many studies using neutron irradiation from thermal and fast fission reactors have been reported [18–20], but neutron irradiation is slow, expensive and produces radioactive samples. More importantly, there is no source of high-flux fusion-energy neutrons that can be used for simulating fusion-relevant damage mechanisms. Therefore, ion irradiation is commonly employed as an analogue for the neutron damage [21, 22]. Ion irradiation, which is quick and cheap and does not produce radioactive material, has been used to study the influence of irradiation damage on ODS alloys by several groups [23–25]. These studies have shown that the average residual nanocluster size depends on both the irradiation method, total dose, irradiation temperature and initial alloy microstructure. This thesis describes my work on ODS materials from an EPSRC funded Indo-UK collaboration with IGCAR, Kalpakkam and ARCI, Hyderabad, India. The contribution to this work from my collaborators is twofold; the alloys were produced by ARCI, followed by the preliminary sample preparation and ion-irradiation at IGCAR.

An introduction to ODS steels and the nature of the oxide particles they contain is given in Chapter 2. This chapter also contains a summary of the mechanism of irradiation damage relevant for the oxide particles in ODS steels and the reported influence of ion irradiation on the steel microstructure.

The starting materials are model ODS alloys produced at ARCI, with well-controlled processing parameters and a systematic variation in alloy composition, as detailed in Chapter 3. My work was to use this unique set of model alloys to explore the influence of alloy chemistry on the oxide particle dispersion using the high-resolution characterisation techniques of transmission electron microscopy (TEM) and atom probe tomography (APT), complemented by nanoindentation and synchrotron X-Ray diffraction. Chapter 3 also details the ion irradiation treatments performed on the different alloys and the characterisation methods used.

The quantification of the character of the oxide particles in these ODS alloys by atom probe tomography (APT) has presented a number of challenges. Chapter 4 details what I have contributed to extend the conventional analysis techniques, specifically measurements of the cluster composition, local chemistry and cluster size. This includes the improvement of the composition measurements by systematic analysis of the mass-spectrum, a spatially-specific peak-deconvolution method and a measure of the spatial inhomogeneity. APT relies on the evaporation of the atoms from the sample and so, the results must be understood in light of the different evaporation behaviour of different phases. I present new pragmatic ways forward to examine the cluster chemistry using line profiles and to measure the cluster size.

In Chapter 5, by comparing the addition of Ti, and then Cr, to a Fe-Y_2O_3 alloy, the influence of alloy chemistry on the oxide particles can be evaluated. The main aims of studying the as-received alloys were to investigate the microstructure, the oxide particle composition, the bias of different analysis techniques and to set a baseline to which the irradiated samples can be compared.

Samples of the alloys characterised in Chapter 5 were subject to Fe-ion implantation at a range of temperatures at IGCAR before I performed APT, TEM, nanoindentation and glancing incidence X-ray diffraction on them. The main aims were to characterise the particle stability, both structural and chemical, and explore the mechanism of the damage, and the relevant results are presented in Chapter 6. It was expected that oxide particle stability

would be a function of the irradiation temperature and this effect has been investigated by using a range of temperatures for the implantation.

Finally, the major findings of the work, a summary of the conclusions and suggestions for future work are given in Chapter 7.

Chapter 2

Literature Review

2.1 Introduction

Advanced fission and fusion power production present a number of challenges, specifically for their components, which will experience high-energy neutrons and high temperatures for prolonged periods [4–8]. ODS steels have improved high-temperature properties compared to ferritic steels because of the addition of nano-scale oxide particles which hinder dislocation motion. The oxide particles also act as sinks for the point defects produced by irradiation, thus improving the irradiation resistance of these alloys. To qualify these ODS materials for use in power plants, their safety needs to be guaranteed through a thorough exploration of the deleterious effects of radiation-induced damage on the microstructure and mechanical properties.

This review introduces ODS steels from a historical perspective before considering their properties in general. The characterisation of the oxide particles is given specific interest because the particle nature affects their growth and formation, irradiation resistance and the stability of the alloys themselves. Finally, an overview of irradiation damage in general is given, followed by a review of the in-depth characterisation of the irradiation damage of ODS steels.

2.2 Oxide Dispersion Strengthened Steels

Steel's abundance, low cost and high tensile strength make it an attractive structural material. Ferritic steels have historically been used in high-temperature environments such as boilers, but their potential use in fast fission [26] and fusion [27] reactors was recognised in the 1970s and was followed by extensive research [28, 29]. The ferritic steel matrix has many advantages; reasonable mechanical properties, low activation, acceptable corrosion resistance and swelling resistance [13]. However, most steels used in fission reactor fuel cladding contain nickel and have a very poor resistance to irradiation swelling [30]. This swelling resistance will be particularly important in the future as 10–15 appm He/dpa will be produced in the fusion reactor structure, about ten times higher than in fission reactors [31]. The activation of the ferritic matrix is also important for fusion applications as it is the only source of long-lived radioactive waste from fusion reactors. Reduced-activation ferritic/martensitic (RAFM) steels are a class of ferritic steels with some alloying additions replaced with similar chemical components but with reduced long-term neutron-induced radioactivity [32]. Example RAFM steels include the Japanese F82H and European Eurofer97 steels [33]. Comprehensive reviews of the development of ferritic steels and the associated irradiation-induced effects can be found in references [34–36]. What follows is a summary relevant for the investigation of the irradiation stability of oxide dispersion strengthened steels.

To maintain the strength of structural materials above 525 °C in new designs of high-temperature reactors, additional strengthening is required. Plastic flow in crystalline materials can be hindered by reducing the mobility of dislocations, and dispersion strengthening is one way of achieving this [37, 38]. Obstacles can be introduced by mechanical or thermal treatments, often termed dispersion strengthening and precipitation-age hardening respectively. The addition of very fine scale oxide particles to pin dislocations in steel creates a class of materials called Oxide Dispersion Strengthened steels (ODS). The presence of these oxide obstacles increases both the tensile strength and creep resistance [39]. A dispersion of yttrium-based oxides is preferable to a dispersion of carbide or nitride particles because

of the excellent thermal stability of oxides and the insolubility of yttrium in the bcc iron matrix (< 0.029 wt% at 800 °C [40]). Most of the literature reported uses a yttria or Y-Ti-O dispersion, though TiC precipitation also shows promise as conventional processing routes can be used [41]. Yttrium oxide, Y_2O_3, is often chosen as it has the largest free energy of formation [42], resulting in enhanced thermal stability.

The process of mechanical alloying was first developed by Benjamin [43]. Researchers used this process to add elements to ferritic steels including molybdenum, titanium and yttrium (Huet [44–46], Fischer [47]) in order to increase their mechanical strength. Fisher patented mechanical alloying of stainless-ferritic and yttria powders followed by hot consolidation to produce a fine-scale precipitation of yttrium oxides that gave both high tensile and high-temperature creep strength [47]. This research was furthered in the US in the breeder reactor program [48] and in Japan by Ukai and co-workers [17, 49–54]. Addition of titanium produces much finer Y-Ti-O particles [55] and improves the high temperature properties [56]. Hf and Zr have also been used to successfully refine the particle size [57]. In the literature a range of compositions are used, based on either low Cr ferritic/martensitic steels (9 wt%) or higher Cr ferritic steels (12–14 wt%), each with certain advantages for mechanical properties and ease of processing [58]. The nominal compositions of some commonly studied ODS alloys are presented in table 2.2.1. Many researchers also produce their own alloy grades especially to investigate the influence of minor alloying elements and different processing routes. This can often make comparison of the performance of different alloys difficult; in particular, contamination from ball milling and batch-to-batch variations of nominally the same composition can give different properties [59].

The lack of consistent naming of the oxide features in ODS steels reflects the controversy regarding their nature. In the literature, a wide variety of terms are used to describe the oxides—clusters, nanoclusters, nanofeatures, nanostructures, particles, precipitates etc. Current understanding is that the initial reinforcing oxide powder is intimately mixed and/or dissolved into the ferrite matrix [69, 70] and then precipitates out during high temperature consolidation [66]; see [71, 72] for details. Consequently the term *nanocluster-strengthened*

Name	Ref	Origin	Composition				
			Cr	W	Ti	Y_2O_3	Other
MA957	60	INCO	14	-	0.9	0.25	.3 Mo, traces of Al
PM2000	61, 62	Plansee	20	-	0.5	0.50	5.5 Al
F4	51	Japan	12	2	0.3	0.24	0.06 C
M11, M93	39	Japan	9	2	0.2	0.35	0.12 C
K1	63	Japan	19	0.3	0.3	0.30	
K3	64	Japan	16	1.8	0.3	0.35	4.6 Al
K4	63	Japan	19	2	0.3	0.30	4 Al
12Y1	65	Japan	12	-	-	0.25	
12YWT	65	Japan	12	3	0.4	0.25	
14YWT	66	USA	14	3	0.4	0.30	
ODS-Eurofer 97	67, 68	Europe	9	1.1	-	0.3 or 0.5	0.47 Mn, 0.2 V, 0.11 C & 0.14 Ta

Table 2.2.1 – Nominal compositions of commonly used ODS steels. All compositions in weight %, with the balance being Fe.

alloy or *nano-featured alloy* (NFA) is often preferred to distinguish these alloys from traditional dispersion-strengthened alloys where the reinforcement remains intact [36, 73]. Throughout this thesis I will maintain consistency by referring to oxide particles, or simply oxides, where some structure is implied, and to clusters where the structure is more ambiguous. For the alloys themselves, in keeping with the literature, I retain the term ODS steel.

2.2.1 Manufacture

Because yttrium is essentially immiscible in iron and yttria is much less dense than iron, traditional melt processing is not possible [70]. Yttrium must therefore be introduced to the ferritic matrix by a mechanical process or physical alloying—such as mechanical alloying (MA) [74]. This point was recognized by Benjamin [75] and was the motivation for developing the techniques further. For more detailed information, the reader is referred to the review of MA given in [76]. Recently, other novel techniques for introducing yttrium into iron have been researched, primarily to reduce production costs and increase yield,

including: spray forming and melt spinning [77]. Other manufacturing processes being investigated to increase the alloy yield also include reactive gas atomization [78, 79], selective laser melting [77] and spark plasma sintering [80].

Due to the commercial nature of ODS alloys produced by companies, the finer details of the processing route are obscured but some details are available [81]. The process can be described schematically as follows:

1. Production of a fine-scale base powder, either mixed elemental powders or a suitable base alloy that has subsequently been atomized.

2. Mixing of the alloy base and oxide reinforcement often 20–50 nm diameter yttria powder.

3. Mechanical alloying using a ball mill or attritor mill to intimately combine the components. This step can be done in vacuum or using some inert atmosphere.

4. Canning of the powder followed by degassing at 400–700 K and under moderate to high vacuum for an hour.

5. Hot consolidation > 1000 K. This is usually *hot isostatic pressing* (HIP) with a pressure between 100–200 MPa or *hot extrusion* through a die.

6. Additional heat treatments.

7. Cold and hot working to form the final shape.

This process is schematically represented in figure 2.2.1.

The processing parameters given can greatly alter the microstructure and performance of the resulting alloy [14]. For example, the gas used during milling can affect the creep properties [82] or form bubbles in the consolidated material even after degassing (presented later in figure 2.3.4 on page 20). Further processing parameters are not considered in detail in this review. The mechanical properties of ODS alloys are frequently compared to their non-ODS variants as a way of quantifying the effect of the oxide particles. But care must be

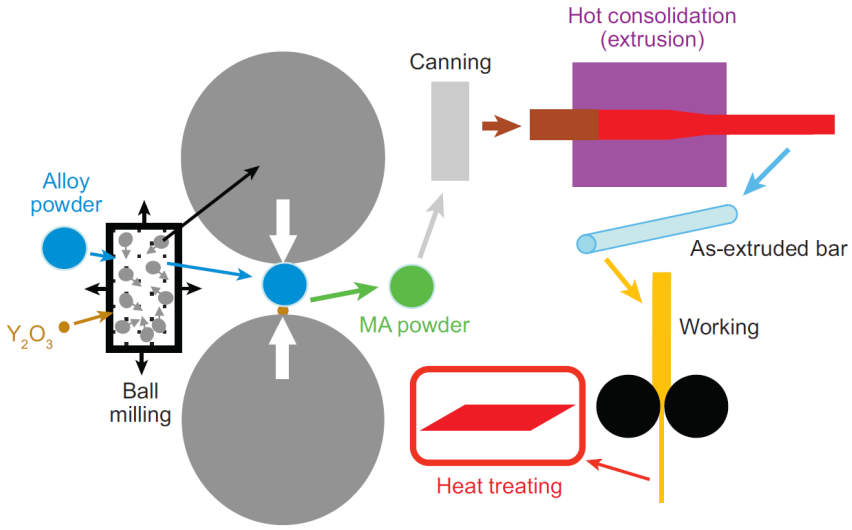

Figure 2.2.1 – A schematic of the processing sequence for ODS alloys: ball milling to mechanically alloy and combine the Y and O into metal powders, canning, hot consolidation, and post-consolidation thermal mechanical treatments. Reproduced with permission from [36]. Copyright © 2008, Annual Reviews.

taken to interpret these data in light of the other microstructural differences in ODS alloys compared to non-ODS alloys, such as the grain size, which is often refined in ODS alloys [14, 83].

2.2.2 Mechanical Properties

Microstructure of ODS alloys affects the mechanical properties, for which there are many different characterization techniques. Most mechanical properties are strongly affected by the temperature, rate of deformation and even sample size, so usually should be compared with identical experiments. Though the mechanical stability of these alloys is important, this is not the main focus of this work and in some part the mechanical behaviour is determined by the microstructure [84].

As the particles are the primary source of high-temperature strength, their stability and resistance to irradiation during reactor service is of most importance. To safely predict the in-service mechanical properties as a function of time, temperature and fluence, the

irradiation stability of the oxides must be investigated. To quantitatively describe a change, both as-received and irradiated states must be characterized in sufficient detail. Quantities and parameters describing the particle dispersion can be gained indirectly by observations of the before and after states. Alternatively, particle stability can be assessed directly during irradiation using *in-situ* studies. Thus, the characterization and observation of the response of the oxide particles to irradiation damage is the main focus of the remainder of this review.

2.2.3 Microstructural Characterisation

Understanding the nature, formation and thermal stability of the oxide particles is key to quantitatively describing the irradiation response of these alloys, and so this section reviews the microstructural characterization of unirradiated ODS steels by various means. There exists a great disparity in scales between the functional structures and the nano-scale oxides which determine their mechanical properties. Such a disparity of scale cannot be bridged by a single characterization technique; several characterization techniques must be be combined to fully describe the steels. This section introduces common techniques applied to ODS steels, before considering the fine-scale characterization required to adequately describe the oxide particles. These techniques include:

- Electron microscopy (SEM, TEM, STEM) and micro-analysis (EFTEM, EELS, EDX and Auger spectroscopy). TEM is the primary tool for investigating grain structures [85] and identifying particles. SEM, with micron to nanometer resolution, is a technique that is applied mainly to topology (e.g. fracture surfaces), but electron backscattered diffraction (EBSD) is often used to measure grain orientation and structures [86].

- Neutron Diffraction (SANS) [87, 88]. This is useful for bulk samples but sensitive to nanometre features. It is used to describe the particle size distributions of particles in bulk ODS samples. Assumptions are required that limit the applicability of the results*.

*Unknown feature coherent scattering length is assumed to be 0 and a log-normal distribution of spherical

- X-Ray powder diffraction (XRD, SAXS) measures the distribution of crystalline lattice spacings in bulk samples.

- Positron annihilation spectroscopy (PAS) [90, 91]. This is used for bulk samples but sensitive to small vacancy clusters and similar features. Positrons are trapped by open volumes and embedded phases, giving information about vacancy clusters and particles in ODS alloys.

- Atom probe tomography (APT). The sampling volume is limited but it provides picometre resolution [92] and atomic chemical identification.

Due to the practicalities of most techniques, they can only be performed *ex-situ*—after the sample has been irradiated. To quantify the microstructural damage, both the initial and irradiated states must be compared by some metric, for example tensile strength [93] or the oxide particle size distribution [23]. There are a few techniques that can follow the irradiation damage *in-situ* during the irradiation; for example, using TEM, the response of a single oxide particle or grain can be observed as a function of electron [94, 95] or ion [96] dose [94–96].

2.2.3.1 Bulk Analysis

XRD reflections for Y_2O_3, $Y_2Ti_2O_7$ and Y_2TiO_5 are frequently detected (figure 2.2.2) in consolidated alloys and annealed MA powders [97–100] but this is biased towards the larger particles, which give sharper and stronger reflections. In most alloys, the yttria content is only a few tenths of a weight percent and so the signal is not easily detected using lab-based XRD analysis [97]. The use of bright synchrotron X-Ray analysis is required to track subtle changes in the oxide particle distribution, which has a small volume fraction and nano-crystalline phases [101].

SANS is spatially sensitive to length scales from microns down to nanometers, but involves many assumptions about the particle nature, morphology and chemical composition,

particles is often assumed [89].

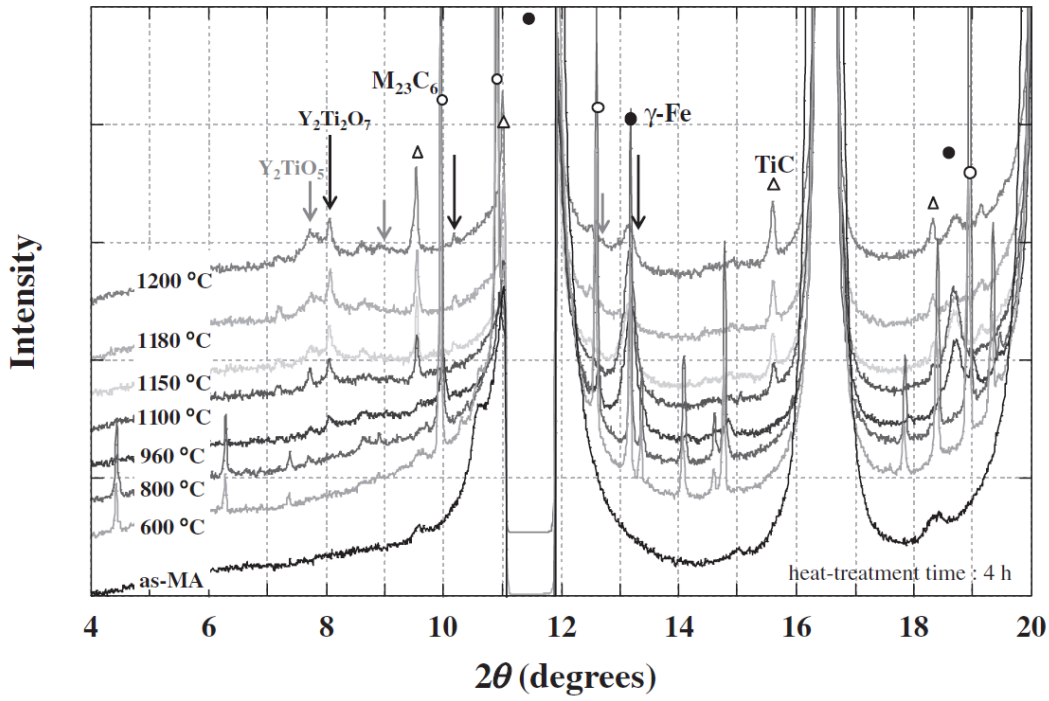

Figure 2.2.2 – Results of synchrotron X-ray powder diffraction analysis on mechanically milled ODS powder and the result of annealing at temperatures from 600 °C to 1200 °C for 4 h. Reproduced with permission from [101]. Copyright © 2009 The Japan Institute of Metal and Materials.

as well as a practical neutron source [89]. It can be very useful in studying the whole material, e.g. for the total particle size distribution [36, 102], but does not account well for multiple types of particle or composition. However, by combining small-angle X-ray scattering with SANS, the alloy contrast variation method can be applied. Using this method, the $Y_2Ti_2O_7$ phase been reported in a 9Cr-ODS alloy [103] and the evolution of the oxide particle phases as a function of temperature can be tracked [101].

2.3 ODS Particle Characterisation

TEM is routinely employed to measure the local crystallography using diffraction techniques. The measured diffraction patterns containing symmetry information, angles and plane spacings are frequently compared with the known values for the bulk Y-Ti oxides (see table 2.3.1 [104–106]).

In titanium-free ODS alloys, cubic and monoclinic Y_2O_3 phases are frequently iden-

	Formula	Crystal system	a (Å)	b (Å)	c (Å)	Atomic Fraction	Y/Ti
1	Y_2TiO_5	Orthorhombic	10.35	3.7	11.25	$Y_{.25}Ti_{.13}O_{.63}$	2
2	Y_2TiO_5	Hexagonal	3.61	3.61	11.84	$Y_{.25}Ti_{.13}O_{.63}$	2
3	$Y_2Ti_2O_7$	Cubic	10.09	10.09	10.09	$Y_{.18}Ti_{.18}O_{.64}$	1
4	$YTiO_{2.085}$	Cubic	10.18	10.18	10.18	$Y_{.24}Ti_{.24}O_{.51}$	1
5	$YTiO_3$	Orthorhombic	5.33	5.62	7.6	$Y_{.20}Ti_{.20}O_{.60}$	1
6	YTi_2O_6	Orthorhombic	7.41	10.81	5.13	$Y_{.11}Ti_{.22}O_{.67}$	½

Table 2.3.1 – Known bulk Y–Ti complex oxides, adapted from [106].

tified in larger 10–40 nm particles [14, 98, 107, 108] and smaller Y-Cr oxides have also been observed in higher chromium content alloys [109]. Particles can be extracted by dissolving the matrix (extraction process) or capturing the particles in a carbon replica; Y_2O_3 and Y_2SiO_5 phases have been identified in this way [98]. The precipitates in titanium-containing ODS alloys often fall into three groups: large, medium and small particles of diameters 300–50 nm, 50–10 nm and < 5 nm respectively [110]. The large particles have a low number density and varying composition depending on alloy chemistry, but are commonly Cr-Ti oxides [110], nitrides [109] and carbides [98].

2.3.1 Stoichiometric Compositions

The main focus of results reported in the literature is the nature of the smaller particles (sub-10 nm diameter) as they provide the high-temperature creep resistance and represent a huge surface area for irradiation-induced point defect and helium trapping [36, 111]. The structural determination of the oxide phases, either through HRTEM or diffraction, when compared with the bulk oxide parameters defined in table 2.3.1, often yields the conclusion that the oxide phases are stoichiometric; these stoichiometric oxide structures are given in table 2.3.2. This collection of previous data shows that many authors report observing the stoichiometric oxide compositions of $Y_2Ti_2O_7$ or Y_2TiO_5. However, these studies conclude the oxide *composition* from an assessment of the oxide *structure*, and these two properties may not be as well correlated for the nano-particles as the bulk oxides. In XRD diffraction, peaks from both species are often present [97, 101], but indexing the reflections is often complicated by overlaps. In TEM there are specific difficulties in distinguishing $Y_2Ti_2O_7$

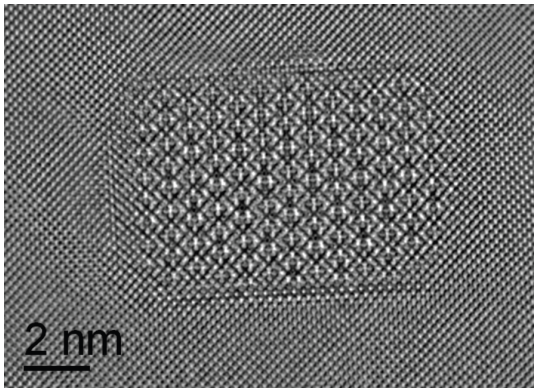

Figure 2.3.1 – Phase of restored exit wave HRTEM image of a nano-scale $Y_2Ti_2O_7$ oxide in a MA957 alloy showing direction-dependent interfacial coherence. Reproduced with permission from [119]. Copyright © 2012 Microscopy Society of America.

from Y_2TiO_5 due to the similarity of their plane spacings [112].

In the work of Klimianko and Yamashita [104, 105, 112, 113], the predominant oxide particles in 9Cr-ODS alloys were identified as the cubic pyrochlore $Y_2Ti_2O_7$ phase. 1–10 nm polyhedral Y-Ti oxides have also been reported in MA957 [106, 108] and similar ODS alloys [114]. Recent advances in TEM techniques, such as spherical aberration correction and processing techniques like exit wave restoration [115, 116], show quite convincingly that $Y_2Ti_2O_7$ can form in MA957—figure 2.3.1. Al is a known contaminant of MA957 and, as measured by APT, strongly segregates to the particles [117]. Kasada et al. [63] demonstrate how Al alters the chemistry and structure of the oxide particles. This point was noted by Sakasegawa et al. [118] who asserted that the influence of Al would affect the formation of $Y_2Ti_2O_7$, and with the evidence given here it appears that Al promotes the formation of polyhedrally shaped $Y_2Ti_2O_7$.

Where stoichiometric compositions have been reported by APT, it has been only through the underlying assumption that the clusters are the $Y_2Ti_2O_7$ type [120] or after annealing where Y_2O_3 clusters and YO clusters were observed simultaneously [121]. Williams et al. [121] performed a calibration experiment on bulk cubic-Y_2O_3 for laser pulsed APT and observed a Y:O ratio of 0.58, c.f. the expected 0.66. This Y-deficiency was explained by evidence of Y loss due to multiple hits and detector dead time [122]. Despite this result, in a 14Cr ODS alloy, both Y_2O_3 and YO clusters were observed in the same analysis volume.

Year	T* °C	ODS alloy	Technique	Stoichiometric	Ref
1990	-	12Cr-ODS	-	$Y_2Ti_2O_7$ and/or Y_2TiO_5	[123]
1995	1000	13Cr-ODS (High Ti and Y2O3)	XRD, SAXS	$Y_2Ti_2O_7$ and Y_2TiO_5	[97]
2000	1150	12YWT	TEM, APFIM, XRD	$Y_2Ti_2O_7$ and Y_2TiO_5	[98]
2002	1200	12Cr-ODS	EDS	$Y_2Ti_2O_7$ and/or Y_2TiO_5	[124]
2002	1150	1DS, 1DK	EDS	Not possible to tell.	[125]
2004	1050	9Cr-RAFM-ODS	HRTEM	$Y_2Ti_2O_7$	[104]
2005	1050	9Cr-RAFM-ODS	HRTEM	$Y_2Ti_2O_7$	[113]
2007	1175	12Cr-ODS	TEM, EFTEM, APT	$Y_2Ti_2O_7$	[14]
2009	1200	9Cr-ODS	SANS	$Y_2Ti_2O_7$	[103]
2009	NS	MA957	XRD, STEM, EDS	$Y_2Ti_2O_7{}^{L}$	[99]
2009	NS	MA957	HRTEM, EDS, SANS, APT	$Y_2TiO_5{}^{L}$	[102]
2011	NS	MA957	HRTEM, EDS	$Y_2Ti_2O_7{}^{L}$	[118]
2012	1060	MA957	EDS, HRTEM	$Y_2Ti_2O_7$ (generally)	[106]
2012	1100	14Cr-ODS	HRTEM, EFTEM	$Y_2Ti_2O_7$ (and Y_2O_3)	[114]
2012	1060	MA957	APT	$Y_2Ti_2O_7$	[120]
2012	1100	14Cr-ODS	HRTEM, SANS	$Y_2Ti_2O_7$	[126]
2012	1100	Sol-gel 14Cr	HRTEM	$Y_2Ti_2O_7$	[127]
2012	1150**	EPFL-E-Fe2Y		Y_2O_3	[128]
2012	1150	18Cr ODS	EDS	Y_2TiO_5 & $Y_2Ti_2O_7$	[129]
2014	1150	ODM 401	HRTEM, EDS	$Y_2Ti_2O_7$	[130]
2014	1200	14YWT	HRTEM/APT	$Y_2Ti_2O_7{}^{L}$	[131]

Table 2.3.2 – ODS particle nature with a reported ***stoichiometric*** composition, listed by *consolidation temperature, alloy and measurement technique. ^{L} denotes larger (>15 nm diameter) particles. ** Annealed for 100 h at 1200 °C.

This shows that laser-pulsed APT can measure the expected composition of particles in ODS alloys but this experiment also serves to illustrate some of the difficulties of using APT to study these compounds.

2.3.2 Non-Stoichiometric Compositions

As demonstrated in table 2.3.3, there is still a degree of uncertainty about the composition of the Y-Ti oxide particles, which is reflected in the number of non-stoichiometric compositions reported. Using HRTEM alone to distinguish between the two crystal structures

Year	T* °C	ODS alloy	Technique	Non-stoichiometric	Ref
2000	1150	12YWT	TEM, APFIM, XRD	Y-Ti-O (Y/Ti=0.28)	[98]
2002	1150	1DS, 1DK	EDS	1< Y/Ti < 2	[125]
2003	1150	12YWT	APT	Y-Ti-O (Y/Ti=0.46)	[132]
2004	NS	MA957	APT	Y-Ti-O (Y/Ti=0.47)	[60]
2004	1200	9Cr-ODS 12Cr-ODS	HRTEM, EDS	$Y_2Ti_2O_7$ (Y/Ti>1)	[105]
2004	1200	12Cr-ODS	HRTEM, EDS	$Y_{0.6}Ti_{0.4}O_?$ (Y/Ti>1)	[112]
2004	1150	9Cr-ODS	EDS	~ $Y_2Ti_2O_7$ or Y_2TiO_5	[133]
2005	1150	12YWT	APT	Y-Ti-O (Y/Ti=0.19)	[134]
2005	1150	MA957	APT	Y-Ti-O (Y/Ti=0.48)	[134]
2006	850	14YWT	APT	Y-Ti-O (Y/Ti=0.18)	[66]
2007	850	12Cr-ODS	TEM, EFTEM, APT	Y-Ti-O (Y/Ti=0.16–0.33)	[14]
2008	1150	MA957	APT	$Y_{15}Ti_{38}O_{43}$	[117]
2009	NS	MA957	XRD, STEM, EDS	Y-Ti-O (Y/Ti=0.5)	[99]
2009	NS	MA957	HRTEM, EDS, SANS, APT	1<Y/Ti<2	[102]
2010	1150	9Cr-ODS	EFTEM, APT	Y/Ti ~1 EFTEM, ~0.5 APT	[135]
2011	1200	Fe–0.2Ti –0.3Y_2O_3	HRTEM, EDS, XRD	Y-Ti-O clusters and Y_2O_3	[136]
2011	850	14YWT	STEM	Y/Ti < 1 NaCl defective structure	[137]
2011	800	14Cr-ODS	APT	$Y_{33}Ti_{27}O_{40}$	[138]
2011	NS	MA957	HRTEM, EDS	Y-Ti-O	[118]
2012	1150	14YWT	EDS, HRTEM	1<Y/Ti<2 (10–50 nm), < 5 nm unknown	[110]
2012	1060	MA957	EDS, HRTEM	0.8<Y/Ti<2 particles	[106]
2012	850	14YWT	STEM, EELS, APT	Y/Ti << 1	[108]
2012	850	14YWT	STEM	NaCl structure	[139]
2012	1150	18Cr ODS	EDS	Y/Ti=2.5	[129]
2013	1150	EPFL-E-Y2O3	APT	$Y_7Ti_{12}O_{24}Cr_{49}$	[140]
2013	1150	EPFL-E-Fe2Y	APT	YO	[121]
2014	850	14YWT	APT	Y/Ti=0.43	[141]
2014	1100	14YWT	APT	Y–Ti–Si–O	[142]
2014	1100	Numerous	APT	$YTiO_2$	[143]
2014	850	14YWT	APT	Y/Ti = 0.43	[141]
2014	1200	14YWT	HRTEM	37% Y/Ti 0.1–0.6	[131]
2015	1100	14YWT	EELS	$Y_2Ti_2O_{7-x}$	[144]

Table 2.3.3 – ODS particle nature with a reported ***non-stoichiometric*** composition, listed by *consolidation temperature, alloy and measurement technique.

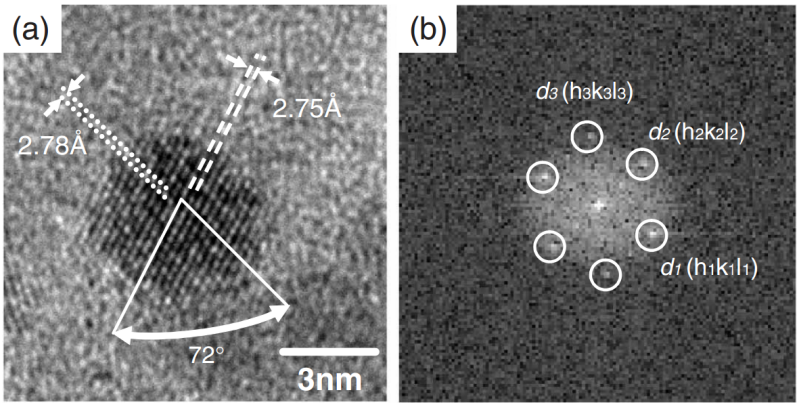

Figure 2.3.2 – HRTEM image (a) and accompanying FFT image (b) of a Ti-Y complex oxide particle of unknown structure, produced by the extraction replica technique. Reproduced with permission from [112]. Copyright © 2004 Taylor & Francis

is difficult in the presence of a ferromagnetic matrix that degrades the microscope performance. To reduced this effect, FIB sample preparation [145] can be used to isolate a small volume of material or extraction replica [106] can be made to examine only the particles, as shown in figure 2.3.2. But even in this case the particle in figure 2.3.2 could not be identified. The larger particles are more easily identified using diffraction techniques as they produce a strong signal compared to the sub-10 nm particles. But smaller particles will always be difficult to analyse. For example, Kim et al. [98] were unable to obtain diffracted spots or amorphous rings from the 3–5 nm particles in the titanium containing 12YWT ODS alloy, and De Castro et al. [109] had difficulty indexing the diffraction spots of some particles, noting complications arising from the surface-grown oxide [146] and the influence of strain [147].

Using nano-diffraction on 2–4 nm particles, Brandes et al. [108] observed no crystallographic structure and therefore proposed that the particles contained a relatively large vacancy concentration. This is in contrast to those reported by Wu et al. [106], who identified the smallest particles as the cubic pyrochlore $Y_2Ti_2O_7$. Differing consolidation temperatures (850 °C for Brandes and 1060 °C for Wu) could explain why the smallest particles observed by Brandes et al. [108] lacked crystallographic structure. Hoelzer et al. [14] examined 4 alloys of various compositions and extruded at two temperatures (850 and 1175 °C). For the high temperature extrusion, larger (19.8 ± 7.6 nm) $Y_2Ti_2O_7$ particles were

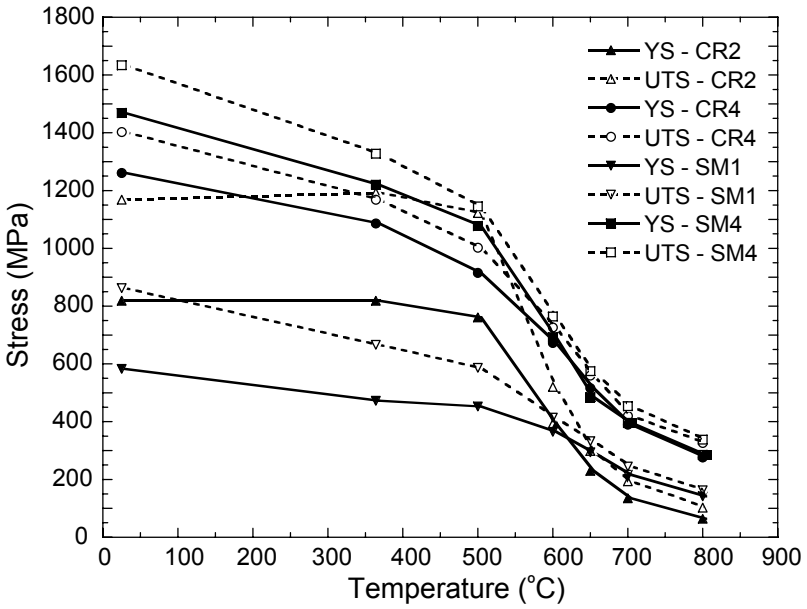

Figure 2.3.3 – Plot comparing the tensile yield strengths measured as a function of temperature up to 800 °C for the 12YWT-like alloys: CR2, CR4, SM1, and SM4. SM1 contained no yttria and had room temperature low strength, but still had reasonable high-temperature strength due to < 5 nm TiO_2 particles. SM4 had 0.3 wt% yttria and exhibited higher strength compared to the 0.25 wt% yttria CR4 alloy that had generally lower strength but similar high-temperature strength. SM1, SM4 and CR4 were extruded at 850 °C. CR2 (0.25 wt% yttria) was extruded at 1175 °C and demonstrated low high-temperature strength due to the relatively large 20 nm $Y_2Ti_2O_7$ particles. Reproduced with permission from [14]. Copyright © 2007 Published by Elsevier B.V.

found and the lower temperature extruded alloys contained a high density of ~5 nm Y-Ti-O clusters (analyzed using APT). Hoelzer nicely illustrated the influence of these differences in particle distribution on the yield strength of the alloys, as illustrated in figure 2.3.3.

To improve the high-resolution characterization of ODS alloys, STEM is now commonly used to image and investigate the particles [108, 137, 144, 148]. STEM has been combined with computer simulation and image analysis to explain the particle structure at the atomic level [137]. Hirata et al. [137] used compositional data from APT to build structural models, simulated their STEM images and matched them to an experimental image of a 2 nm oxide particle in an alloy extruded at 850 °C. The result was a vacancy-rich NaCl rock salt structure that had full coherency with the bcc iron matrix. The vacancy-rich structure agrees with some other work [73] but the NaCl structure has not been observed in any other experiment. Furthermore, this work was criticized by Wu et al. [106] as Hirata did not consider the effect of a surface oxide, ignored the effect of defocus on the image contrast

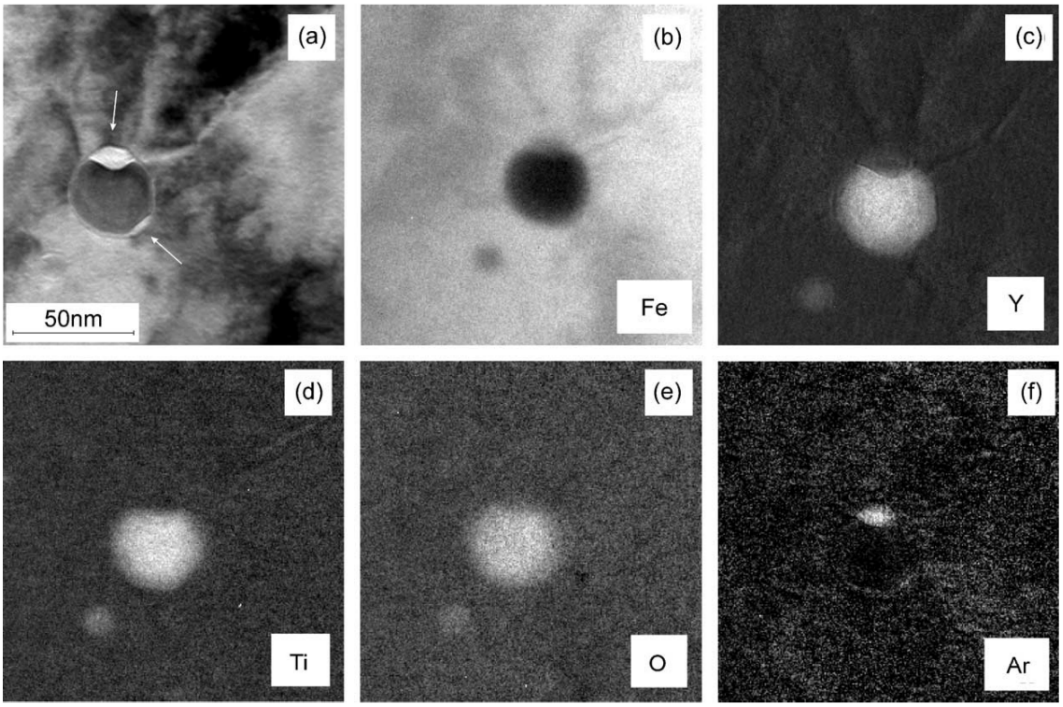

Figure 2.3.4 – EFTEM micrographs taken of one ODS particle using the a two-window background selection and a third window to acquire the signal. (a) Shows the bright field image, whereas the images using the Fe $L_{3,2}$, Y $M_{5,4}$, Ti $L_{3,2}$ O K, and Ar $L_{3,2}$ edges are presented in (b)–(f), respectively. Image taken from [113]. Reproduced with permission, Copyright © 2004 Elsevier Ltd. All rights reserved.

and gave no account of the thickness of the particle interface or surface effects.

Where a chemically sensitive technique such as Energy Dispersion X-Ray analysis (EDS) in the TEM [99, 105, 124, 125, 133] or APT is applied, then frequently non-stoichiometric compositions are reported, as summarised in table 2.3.3. The smaller particles produce a weaker signal, but yttrium-rich regions as small as 2.5 nm have been measured using EDS line scans [149]. The quantification of the EDS signal is not trivial, with quantification accuracy limited by the calibration measurements and the sample geometry [146, 150]. To complicate interpretation of the literature further, details of the quantification, or even the software used, are often missing from published papers. Taking the reported results at face value, the ability to distinguish between the two structurally similar Y_2TiO_5 and $Y_2Ti_2O_7$ oxides by measuring the Y:Ti ratio is attractive [14, 102] but the reliability of this approach is difficult to judge [108, 125, 137].

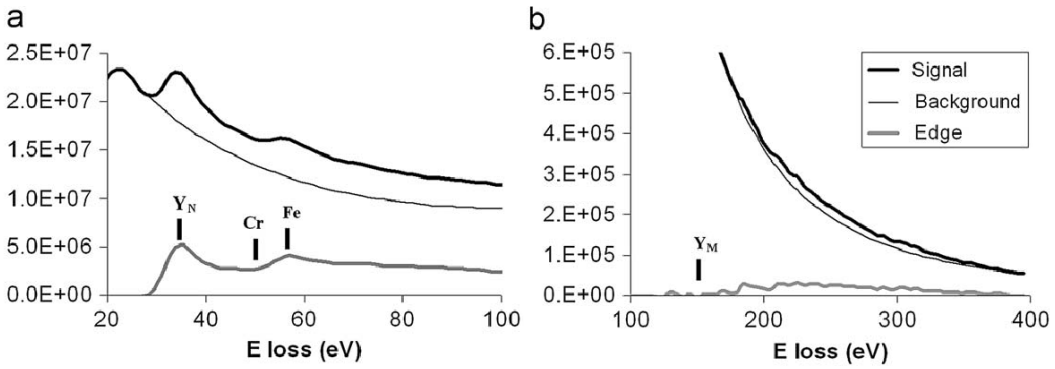

Figure 2.3.5 – Yttrium EELS spectra extracted from a large Y-rich particle in 12Cr-ODS. (a) Y–$N_{2,3}$ edge and (b) Y–$M_{4,5}$ edge. Reproduced with permission from [153]. Copyright © 2009 Elsevier B.V. All rights reserved.

Energy-filtered imaging (energy-filtered TEM, EFTEM) or electron energy loss spectrometry (EELS) are used for reliably imaging lighter elements [96, 100, 108, 113]. Kliminkou et al. [113] used EFTEM to demonstrate the presence of argon bubbles trapped on the surface of oxide particles in a 9Cr-ODS alloy, as shown in figure 2.3.4. Klimenkov et al. [151] also used EELS with EDS to study the chemical structure of an oxide particle, showing it had a 2 nm shell rich in Cr and V around a Y, O, Mn core [151]. The strongest sample signal is obtained from the matrix, and iron jump ratio maps have successfully been used to measure large numbers of particles for investigating irradiation stability [135]. The signals produced by yttrium, shown in figure 2.3.5, are difficult to quantify. The $M_{4,5}$ edge (~157 eV) has a delayed maximum, the L_3 edge (>2 keV) provides only a weak signal, and the $N_{2,3}$ edge (~26 eV) is very close to the bright plasmon peak between 20 and 25 eV [135], but quantification may be possible through the use of model-based parameter estimation [152].

Lozano-Perez et al. [153] applied principal component analysis [154] to EFTEM micrographs obtained using a double spherical aberration-corrected microscope from a 12Cr-ODS alloy. With the added statistical information available in the EFTEM images, lower noise elemental maps could be produced, showing yttrium particles of sub-nanometer diameter [153] (figure 2.3.6). Similar attempts to quantify the oxide composition using EELS have shown a non-stoichiometric composition, with a Ti/O ratio of 3.14 ± 0.2, c.f. 3.5 for

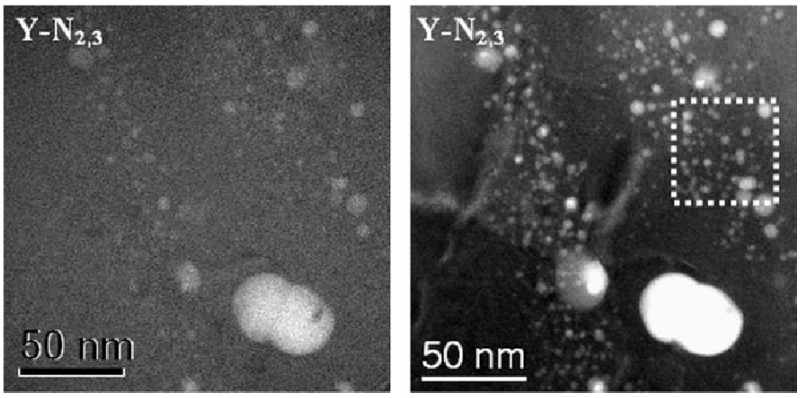

Figure 2.3.6 – EFTEM elemental maps for the Y–$N_{2,3}$ edge from raw data (left) and after MSA "noise-free" reconstruction (right) from the low-loss energy data set. Reproduced with permission from [153]. Copyright © 2009 Elsevier B.V. All rights reserved.

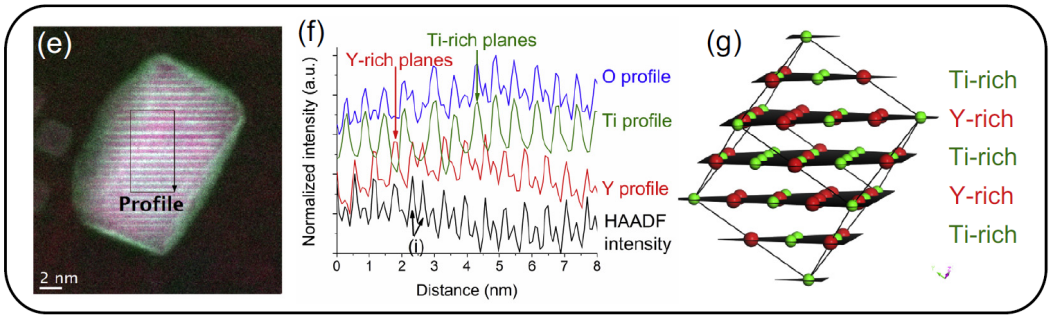

Figure 2.3.7 – EELS measurement of a particle. (e) RGB elemental map (red = Y, green = TI, blue = O) with (f) the intensity profiles of the HAADF image, Y, O and Ti (g) corresponding pyrochlore $Y_2Ti_2O_7$ (222) planes observed represented without the O atoms. Reproduced with permission from [144]. Copyright © 2014 Elsevier B.V. All rights reserved.

$Y_2Ti_2O_7$ [144]. Badjeck et al. [144] also identified structural defects (twins or stacking faults) in the particles, shown in figure 2.3.7, which could explain some of the difficulty in identifying the particle structure, and therefore inferred composition, noted above. As well as defects inside the particles, variations in surface chemistry have been identified, including; Cr-rich shells [117, 144, 151, 155], a Y-rich shell around TiO_2 [118] and a variation in Ti oxidation state at the particle-matrix interface [144]. These results are not surprising in light of *ab initio* modelling, which also predicts a Cr-shell [156] and the possibility of a chemical gradients towards the particle centre [157]. Additionally, the segregation of Ti to the metal-oxide interface [158, 159] may affect the oxide growth and stability.

2.3.3 Atom Probe Tomography

APT can provide chemical information and spatial data accurate to 0.1 nm and has regularly been applied to the study of the oxides in ODS alloys [65, 98, 128, 132, 160]. Where reported, the measured Y/Ti ratios are given in summary in tables 2.3.2 and 2.3.3. APT is suited to studying fine-scale clustering [161] and (radiation-induced) segregation, for example in austenitic steel [162] and Eurofer [163].

Initial APT experiments used a time-of-flight mass spectrometer in conjunction with a 2D detector (3-DAP) to produce chemical maps as a function of sample depth [65, 98]. Larson et al. [65] were limited to examine small volumes of material (6400 nm^3) at pulse rates of only 1.5 kHz, but still observed small 2–5 nm clusters of Y-Ti-O atoms with a Y:Ti ratio of 0.28. Contrary to the TEM results presented above, the clusters apparently contained almost 80 at% iron, and only 0.9 % Y, 3 % Ti and 2.9 % O (Y/Ti/O = 13/45/43). Miller et al. [132] observed ~4 nm darkly imaging particles using FIM but noted that the "imaging behaviour and the small size of the particles prevented a reliable determination of the amorphous or crystalline nature of the particles" [132]. Using APT, Miller measured the particle radii and number density, selecting clusters from the data using the maximum separation of solute ions method, shown in figure 2.3.8. The composition was reported as the average composition of all the clusters and the average composition of all cluster ions measured, which was similar to the composition according to Larson et al. [65]: 7.6 % Y, 21.4 % Ti and 23.8 % O (Y/Ti/O=14/41/45).

Advancements in APT technology resulted in the energy-compensated optical position-sensitive atom probe (ECOPoSAP) and then local electrode atom probe (LEAP), with energy-compensation offering enhanced mass resolution and the 1st generation LEAP allowing much higher data acquisition rates of 100 kHz and larger field-of-view [134]. With these tools, Miller et al. [134] investigated the thermal stability of the oxide particles. Further technical advances of the local electrode method increased acquisition rates to 200 kHz and increased the field-of-view, as shown in the atom maps in figure 2.3.9.

Marquis [117] examined 3 different ODS alloys using a 3rd generation LEAP-3000HR

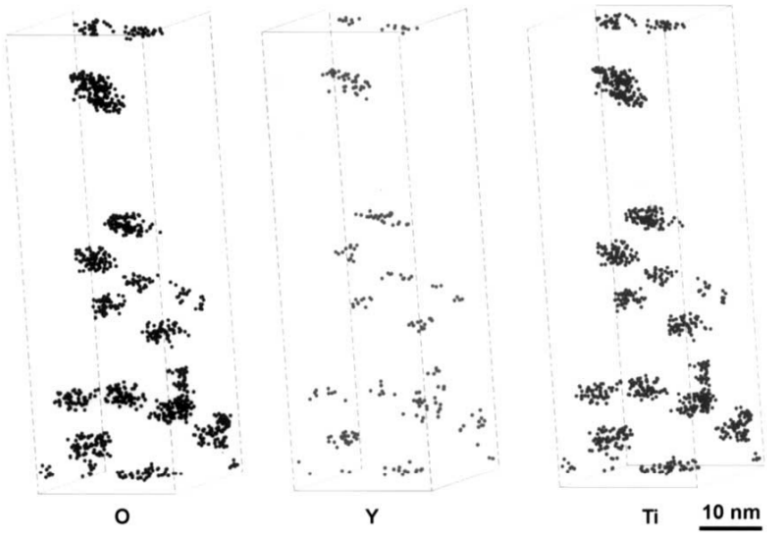

Figure 2.3.8 – Atom maps of Y-Ti-O clusters in 12YWT crept at 800 °C for 14,500 h at a stress of 138 MPa. Only the solute atoms are shown as the matrix atoms were eliminated by the maximum separation method. Reproduced with permission from [132]. Copyright © 2002 Elsevier Science B.V. All rights reserved.

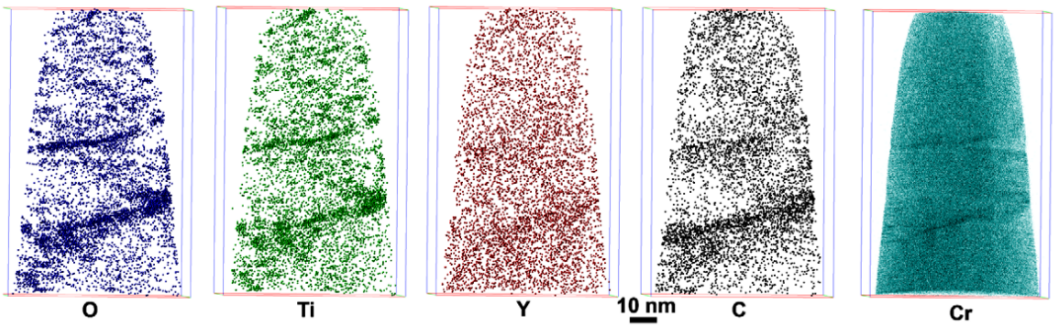

Figure 2.3.9 – Atom maps of 14YWT milled for 40 h and then extruded at 850 °C showing a much wider field of view than the atom maps in figure 2.3.8. Reproduced with permission from [66]. Copyright © 2006 Elsevier Science B.V. All rights reserved.

(200 kHz acquisition rate) system using voltage- and laser-pulsed modes [117]. In addition to the core-shell structure consistent with Klimenkov's findings, the average particle compositions are summarized in table 2.3.4. Marquis [117] noted the influence of trajectory aberrations that increased the atomic density at the particles up to four times higher than in the surrounding matrix, c.f. the imaging behaviour noted by Miller et al. [132] using FIM. This is consistent with the focusing-in of the matrix resulting from flattening of the surface due to preferential evaporation of the oxide particles. The lateral spreading of oxygen ions perpendicular to the analysis direction was confirmed, as noted by Miller in previous work,

Alloy	O	Ti	Y	Cr	V	M:O
MA957	42.8 ± 3.6	37.9 ± 3.0	14.6 ± 1.2	4.6 ± 1.0	-	1.3
ODS Fe12Cr	36.9 ± 3.5	-	24.8 ± 5.8	37.1 ± 4.8	-	1.7
ODS Eurofer	35.9 ± 4.2	-	24.7 ± 3	4.4 ± 6.2	33.9 ± 2.3	1.8

Table 2.3.4 – Concentrations in oxide core/shell oxide clusters with sizes less than 5 nm, including the metal:oxygen ratio, measured by APT. All measurements in at % and subject to a matrix-correction to remove ions present due to trajectory aberrations. Reproduced with permission from [117]. Rights managed by AIP Publishing LLC.

and partially attributed to chromatic aberrations [160]. Such aberrations caused distortions to the smaller particles over a distance of 2 nm, as large as the particles themselves. Some quantity of Al was measured in the core of the MA957 oxides and is probably responsible for their precipitation behaviour noted previously [106, 112].

Wells et al. [120] describe some artefacts that could be present in the APT analysis of the oxide particles. In their experimental work, a Y:Ti ratio of approximately 1 is measured in the centre of oxide clusters in MA957, which agrees with their TEM results presented in figure 2.3.1. Wells highlighted the need to understand some of the experimental concerns raised by Marquis and Hyde [164] when interpreting APT data. This will be a major focus of the work presented in this thesis.

2.3.4 Discussion

There is considerable evidence from XRD studies that multiple oxide phases are present in ODS alloys (figure 2.2.2), and HRTEM has shown that on a particle-by-particle basis specific stoichiometric compositions (inferred from the crystallographic structure) are present. However, analytical TEM using EDS and EELS has shown non-stoichiometric and even defective structures [137, 144] to be present. Kinetic Monte Carlo (KMC) modelling has shown that, in small clusters, different phases can form in a mixed fashion [157]. APT should, in principal, be the best technique for achieving accurate compositional measurements, even at the smallest cluster size range. Looking at a relatively early paper by Miller et al. [132], a distinction is made between measuring the cluster composition based on either the total cluster ions or the average compositions of the individual particles, with these

two methods being sensitive to the larger and smaller clusters respectively [132]. Without knowing the number of ions detected, it is not possible to estimate the statistical counting error of these measurements, but looking at the standard deviation of the average individual cluster compositions, the relative compositional error is 85%, 44% and 45% for Y, Ti and O. Assuming the counting error due to the small number of ions is 45%, then there is a greater variation in the measured Y-content than expected. Williams et al. [155] also noted a variation in individual cluster composition greater than the statistical error, suggesting size as a possible factor in cluster composition as well as the difference between intra-granular clusters and grain boundary clusters.

Sakasegawa et al. [118], using EDS, observed an increase in Y/Ti ratio with particle size; from 0.5 to 1.4 for >20 nm diameter particles, suggesting that particle composition is a function of size. Using APT, Williams et al. [155] also noted a change in particle composition with size, with a metal:oxygen ratio of 1:2 for smaller clusters and 1:1 for larger ones. Contrary to this, Lescoat et al. [25] measured a Y/Ti of 0.6 independent of cluster size (from 1–10 nm diameter) in a 18Cr-0.6Y_2O_3 ODS alloy. These differences can probably primarily be explained by alloy composition, as Williams had no Ti, Sakasegawa had Al and Lescoat had a high Cr-content and Ti, but this is an area for further study. Ribis et al. [114] explained the change in morphology of the particles based on elastic strain, but did not comment on the variation of composition with size.

In an XRD study of sintered Y_2O_3, Ti and Fe_2O_3 powders, Okuda [16] found that when mixed in the ratio 1:1:1 and heated to 1133 K for 1 h both $Y_2Ti_2O_7$ and Y_2TiO_5 formed, but when the Ti content was doubled, only $Y_2Ti_2O_7$ was formed [16]. This shows that the composition of oxide formed depends on the elements available, and therefore chemical inhomogeneity in the mechanically alloyed powder might translate into an inhomogeneous distribution of oxide compositions.

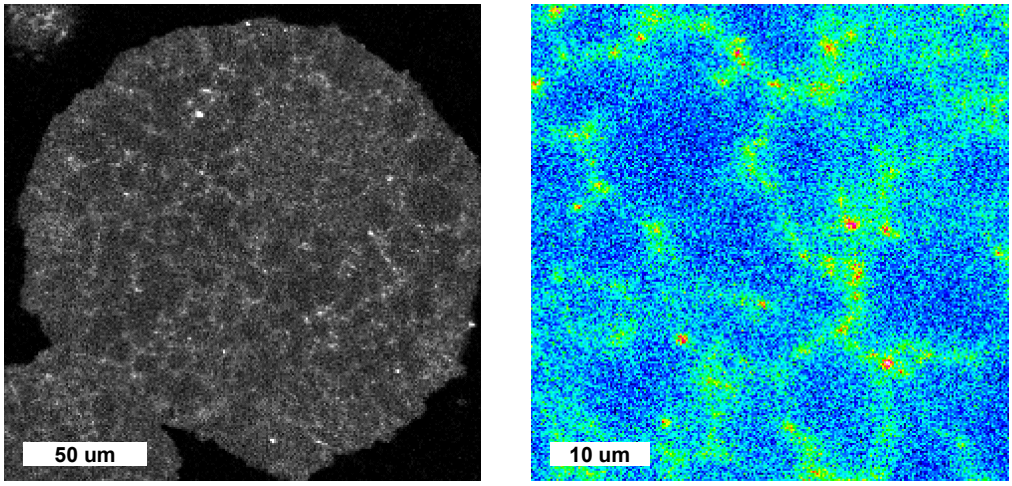

Figure 2.3.10 – Inhomogeneous distribution of titanium in a pre-alloyed Fe–14Cr–Ti powder particle, qualitative scale. Unpublished images courtesy of Z. Hong, Oxford Materials.

2.3.5 Inhomogeneity

Oxide dispersion strengthened alloys are inhomogeneous by their nature, containing at least two phases, one of ferrite and one of oxide. The powder processing of these alloys also often produces an inhomogeneous spatial distribution of oxide particles within the steel matrix. As figure 2.3.10 shows, the starting materials may be heterogeneous; in this case the distribution of titanium has a web-like structure. In the consolidated material, the oxides may have a distribution of sizes, shapes, and potentially a variation in local chemistry. Particle size distributions are frequently reported, and although spatial heterogeneity is often commented on [109, 155, 165, 166], it is never quantified. Bulk techniques like XRD and SANS are insensitive to spatial inhomogeneity, and in TEM and APT authors naturally report the "best looking", or most homogeneous, micrographs when trying to find the most representative images. For example, figure 2.3.11 compares the atom maps from figures 4 and 7 in [25] with the atom map at the lower-right of figure 12; clearly (a) and (b) show a dispersion of smaller more numerous clusters than shown in (c).

There have been several attempts in other fields to quantify inhomogeneity in various systems, such as in computer science [167] and microstructural analysis [168, 169] . For a

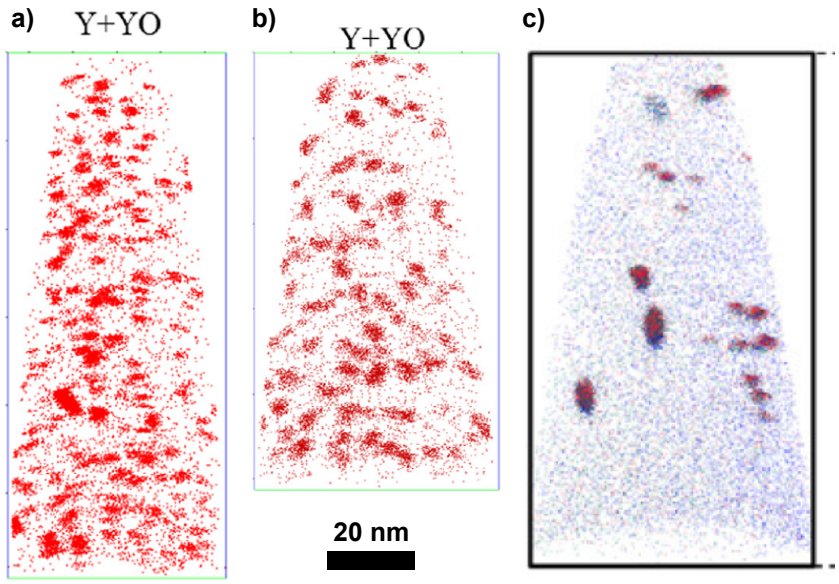

Figure 2.3.11 – 3D APT ion maps showing the distribution of oxide clusters in an Fe18Cr ODS alloy (a) as-received, (b) after irradiation and (c) an unirradiated specimen, taken from figures 4,7 and 12 respectively from reference [25]. (a–c) Compare nominally the same sample but (c) shows a very different cluster distribution, highlighting the bias in published figures. All figures are at the same scale showing at least Y and YO ions. Reproduced with permission from [25]. Copyright © 2014 Acta Materialia Inc. Published by Elsevier Ltd. All rights reserved.

general review of the correlation between heterogeneous structures and their properties see [170]. For example, it has been shown that an inhomogeneous carbide distribution can influence the movement of dislocations and so affect the mechanical properties of steels [171]. In the field of composite materials there has been research into the distribution of fibres [172] and particles [173] in two-component composites, and perhaps a similar methodology could be adopted for investigating the effect of the dispersed oxide particles on the mechanical properties of ODS alloys.

2.4 Irradiation Damage

Gaining electricity from atomic energy involves releasing the binding energy of atomic nuclei in nuclear reactions, capturing the energy of the products and converting that heat into electricity. In the case of fission (splitting) and fusion (combining) reactions, neutrons are produced carrying some proportion of the released energy. Equation 2.4.1 shows the

energetic neutrons and ions produced by the fusion of deuterium and tritium.

$$\mathrm{D}^{+} + \mathrm{T}^{+} \rightarrow {}^{4}\mathrm{He}^{2+}(3.56\,\mathrm{MeV}) + n(14.03\,\mathrm{MeV}) \tag{2.4.1}$$

Because of the Columbic repulsion between the deuterium and tritium ions, a combination of high temperature, confinement time and pressure is required—such as that produced in a tokamak fusion reactor.

Equation 2.4.2 shows an example of the fission of uranium-235 into lighter elements via the transient uranium-236 isotope.

$$^{235}U + n \rightarrow ^{236}U \rightarrow ^{92}Kr + ^{141}Ba + 3n \sim (200\,\mathrm{MeV\,total}) \tag{2.4.2}$$

The fission neutrons produced are used to propagate the reaction, interact with the moderator and give energy to the coolant via inelastic collisions. In a similar way, in a fusion reactor, the energetic neutrons are captured by the reactor vessel and blanket, producing heat, which can be extracted to generate electricity.

A neutron fluence (neutrons per unit area) incident on a material can result in several events; elastic scattering of the neutrons, absorption of neutrons leading to transmutation and inelastic scattering where energy is transferred to the material. This concentrated energy transfer can lead to *knock-on* or irradiation damage.

As described in a extensive review of irradiation damage by Kinchin et al. [174] in 1955, the effect of irradiation of various forms was identified towards the end of the 19th century. Research accelerated with the discovery of high-energy sources and the development of fission reactors, leading to a basic understanding of the mechanistic details involved [175, 176]. With the invention of the Transmission Electron Microscope (TEM), irradiation-induced defects could be studied directly [177] (for a more detailed description see [178]). Computer simulation, including molecular dynamics, allowed the atomistic detail of irradiation damage to be investigated. Simulating volumes large enough to capture the full nature of irradiation damage is computationally expensive, so it was not until the development of

more efficient models and faster computers in the 1980s that larger-scale models became possible [179, 180].

A damage event occurs when an energetic particle[†] collides with a nucleus. If the ballistic collision provides enough energy to displace the atom from its equilibrium site, then a primary knock-on atom (PKA) is produced and a vacant site is left behind. Where the knock-on atom comes to rest, a self-interstitial atom (SIA) defect is produced; together the vacancy and interstitial form a Frenkel pair. A sufficiently high-energy PKA can displace many atoms, generating a displacement cascade. The total number of these displacements is frequently approximated as the displacements per atom (dpa) calculated by the modified Kinchin-Pease formulation [174], usually referred to as the Norgett, Robinson, and Torrens (NRT) model [181]:

$$N_d = \frac{\kappa(E - \hat{Q})}{2E_d} = \frac{\kappa \hat{E}}{2E_d}, \qquad \hat{E} > \frac{2E_d}{\kappa} \tag{2.4.3}$$

From the total energy transferred in the collision E, some energy $\hat{Q}$ is lost to electronic excitation, resulting in $\hat{E}$ energy available to generate atomic displacements. E_d is the threshold energy for displacement and a value of $\kappa = 0.8$ is used to account for realistic non-hard sphere scattering and gives better agreement with experiments [182, 183]. Once there is an estimate of the number of subsequent displacements produced from a single energetic collision, the total dpa can be calculated. The incident particle flux, the possible PKA energies and the probability (cross-section) of collision in a time interval are integrated to estimate the total dpa. Assuming the number of displacements is proportional to the number of defects, this integration gives an idea of the number of defects produced purely on the basis of the material-dependent damage parameter, E_d, and the properties of the incident particle flux. This simplicity makes dpa an attractive measure of irradiation dose, allowing the comparison of similar materials exposed to different particle fluxes—for example when comparing the effect of neutron irradiation on similar materials from reactors which have different neutron energy spectra. But as numerous experiments and molecular dynamics

[†]Not necessarily a neutron, but an ion, electron or high-energy photon.

simulations have shown, the dpa value does not accurately report the number of remaining defects produced, due to the recombination of the SIA with vacancies or annealing just after the displacement cascade.

As the irradiation-produced defects are not simply Frenkel pairs, a more representative description is required to understand the number of defects that are produced, cluster and survive long enough to cause microstructural evolution. The concept of a displacement cascade captures the highly localized nature of the energy dissipation by a relatively low energy PKA (<50 keV), and molecular dynamics modelling (MD) is commonly used to approximate the number and nature of surviving defects. For example, for a 50 keV iron ion into iron, 500 displacements are predicted by the NRT model (equation 2.4.3) but only 168 defects are shown to remain in 9 averaged molecular dynamics simulations after 15 ps at 100 K [184]. Although MD can capture timescales long enough to observe the evolution of an individual cascade, the microstructural evolution due to irradiation damage takes place over days and years. KMC modelling is capable of simulating this length of timescale and is therefore used to understand the long-term migration of these defects [185].

When estimating the range and extent of damage, simple simulations such as that implemented in the program Stopping and Range in Matter (SRIM) [186] are commonly cited in literature. SRIM uses the displacement energies of atomic species and the binary collision approximation to estimate the displacement damage, stopping force and projectile range in materials, but uses a simple probabilistic simulation and ignores crystallography. To gain a more accurate picture of defect production and displacement damage, models such as MD are used [187]. Other computer codes are available, including SUSPRE produced by the University of Surrey [188] and UT-MARLOWE by the University of Texas [189]. These simulation tools are primarily for dopant implantation into semi-conductors; using them for metals and fast-heavy ions requires great care [190].

The measured dpa value also fails to represent any influence of transmutation or the atomic replacements, where one atom is moved onto the site of another, which can be described as *ion-beam* or *displacement mixing* [191]. The concept of a locally disordered

region produced by the dissipation of the projectile's energy in a small volume was familiar to Siegel, who proposed that disordered regions were formed in an ordered $AuCu_3$ alloy by irradiation [192]. TEM of ordered Au-Cu alloys confirmed Seitz's hypothesis [193], that the disordered region is formed by a displacement cascade, where a number of atomic replacements and collisions take place in quick succession, resulting in atomic mixing and disordering of the alloy. The atomic mixing that takes place may be important for the response of oxide particles in ODS alloys to irradiation [190], especially at low temperature [24]. This process is often referred to as a ballistic mechanism, because it only depends on the atomic density and mass [18]. However, Wang et al. [194] irradiated 300 keV Xe^{3+} Cu–Au and Cu–W bi-layers and found that the miscible Cu-Au bi-layer mixed 10 times more readily than the immiscible Cu-W system, showing that, as the energy of the displacement cascade dissipates, thermodynamically driven un-mixing can occur [195]. Enhanced mixing of species has also been reported [196]. Thus, in general, it is necessary to use modelling, such as MD, to properly account for the displacement mixing [197].

Therefore, when considering the irradiation damage of ODS steels, it is necessary to consider the effect all of the possible mechanisms involved:

- Ballistic damage - dominant in irradiation experiments using electrons.
- Displacement mixing - especially important for the modification of existing phases in the material.
- Irradiation induced defects - these defects are mobile, causing enhanced diffusion and non-equilibrium segregation and can coalesce in clusters, forming dislocation loops and voids [198].
- Transmutation - which can produce gases that enhance irradiation-induced swelling and degrade mechanical properties.

Experiments showing the damaged caused by various incident particles are summarised in the next section, followed by a survey specifically of the irradiation damage of the oxide

particles in ODS steel. Understanding the influence of irradiation in ODS steels is vital if they are to be used safely and reliably in advanced fission and fusion power plants.

2.4.1 Influence of Irradiation Damage

Irradiation is well known to cause hardening, with increasing hardness at higher fluence. Figure 2.4.1a compares the effect of irradiation to 9 dpa on ODS MA957 and two other steels. Although the ODS alloy starts with a higher yield stress, it has a greater resistance to irradiation hardening than the non-ODS alloys [199]. McClintock et al. [200] compared the yield stress of ODS variants of Eurofer and 14WT (Eurofer ODS and 14YWT) after irradiation in HFIR to 1.5 dpa (2.1×10^{21} n/cm^2 E>0.1 MeV) and found about a 230 MPa increase in the yield stress of Eurofer, Eurofer ODS and 14WT, but only 100 MPa in 14YWT [200], as well as an increase in yield strength and accompanying loss in ductility and fracture toughness. Oh et al. [201] irradiated the K2 (14Cr–4Al) ODS alloy in the Japan Materials Testing Reactor to a dose of 5.56×10^{20} n/cm^2 (>1 MeV) and measured the fracture toughness by Charpy impact testing, as shown in figure 2.4.1b. Oh measured an increasing DBTT, with a decreasing upper shelf energy, as the irradiation temperature was decreased.

As well as reducing the irradiation hardening, the oxide particles, and the grain refinement they produce, help reduce irradiation swelling. Yutani et al. [64] used dual-ion irradiation of 6.4 MeV Fe^{3+} and 1.0 MeV He^{+} ions to investigate the swelling behaviour of a 16Cr–2W–4.6Al–0.3Ti–0.37Y_2O_3 ODS alloy (K3) and a 9Cr–2W-0.5Mn reduced-activation ferritic steel (JLF). TEM revealed a difference in the cavity population of the two alloys. The ODS alloy had a high number density and small mean size whereas the non-ODS alloy had a lower number density of larger cavities and a significant proportion of large voids, diameter > 10 nm; the swelling calculated from these TEM observations is shown in figure 2.4.2.

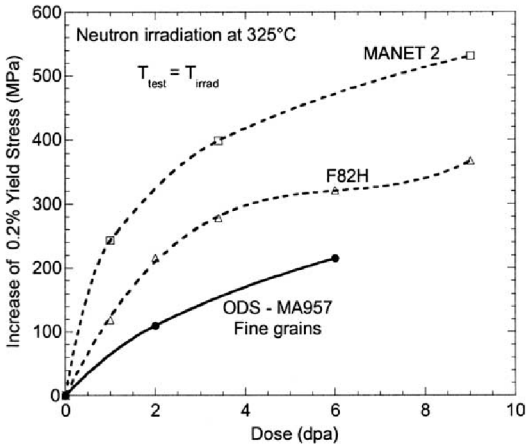

(a) Increase of yield stress as a function of neutron dose (dpa) of ODS MA957, a reduced activation F82H (7.5Cr2WTaV) steel and a conventional MANET2 (10Cr0.6MoVNb) martensitic steel. Reproduced with permission from [199]. Copyright © 2004 Published by Elsevier B.V.

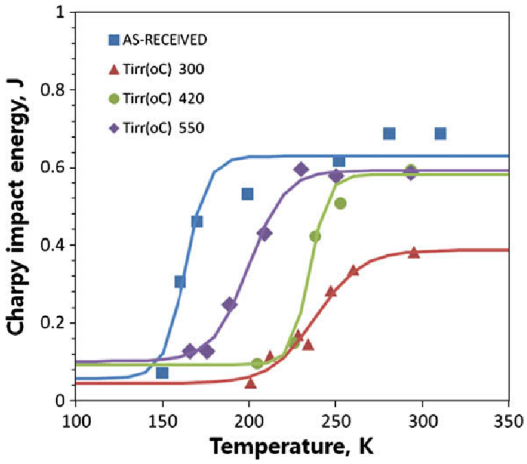

(b) Effect of the irradiation temperature on the Charpy impact energy of 14Cr-4Al (K2) ODS steel as a function of the test temperature. The DBTT is increased and the upper shelf energy is reduced with decreasing temperature. Fast neutron fluence of 5.56×10^{20} n/cm^2 (>1 MeV). Reproduced with permission from [201]. Copyright © 2008 Elsevier B.V. All rights reserved.

Figure 2.4.1 – Influence of neutron irradiation on the mechanical properties of ODS alloys.

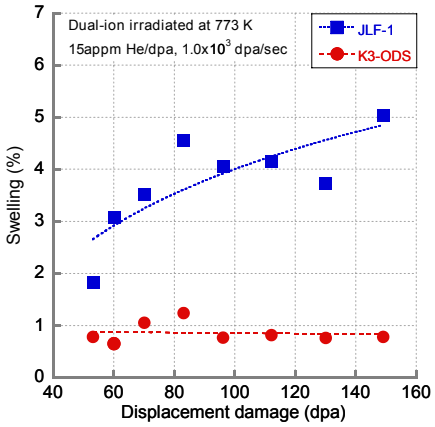

Figure 2.4.2 – Swelling percentage as a function of displacement damage caused by 6.4 MeV Fe^{3+} ions with simultaneous 1 MeV He^+ irradiation at a rate of 15 atomic parts per million of He per dpa in the ODS K3 alloy and the non-ODS JLF-1 alloy (T_{irrd} = 773 K). Reproduced with permission from [64]. Copyright © 2007 Elsevier B.V. All rights reserved.

2.4.2 Irradiation Damage of ODS Particles

Historically the emphasis has been on measuring the swelling resistance of ferritic ODS alloys under irradiation. Although particles were identified as being still being present up to a high dose of 150 dpa, their chemical composition remained uncertain [202].

Some studies only focused on swelling and ignored the particle stability [98, 203–205]. In other cases, despite the exposure to a high dose, no change to the oxide particles was

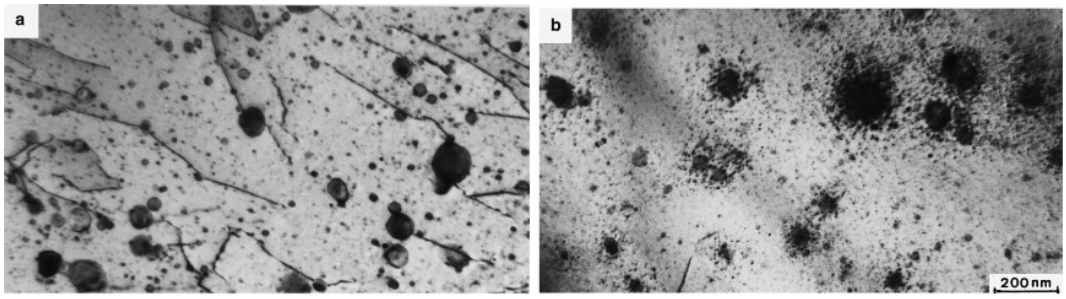

Figure 2.4.3 – The oxide dispersion in the DY ODS steel following 600 hour neutron irradiation, showing halos of smaller particles around larger particles: (a) before irradiation, (b) after irradiation at 532 ℃ to 78.8 dpa. BF-TEM micrographs. Reproduced with permission from [18]. Copyright © 2004 Elsevier B.V. All rights reserved.

observed, but these conclusions were not backed up by quantitative measurements [82, 94, 206, 207]. Loss of the smaller particles, partial large particle dissolution and reprecipitation were reported by Dubuisson and Schill [208], and a micrograph is shown in figure 2.4.3. The dissolution of the oxides could be reproduced by electron and ion irradiation but the halo formation is likely due to the long irradiation time of the neutron experiment, 600 hours at over 400 °C, with an increasing halo radius at longer times [18]. Monnet et al. [18] used a STEM/EDX electron probe of 7 nm to examine the particle compositions and noted a loss of aluminium. This demonstrates that chemical modification of the particles was possible but its importance may not yet be fully recognized.

Similarly, the loss of small (< 3 nm) particles was reported by Yamashita [105, 125] along with a decrease in measured number density, but although he used neutron irradiation under similar conditions to [208] and [18], halos of smaller particles were not observed and the larger particles grew. In 2007 Yamashita et al. [209] also observed growth of the large particles, 75 to 85 nm, after neutron irradiation in the JOYO experimental fast reactor to 100 dpa, as well as an increased minimum particle size (5.2 to 9.5 nm) [209]. But in a later study of JOYO neutron-irradiated 9Cr and 12Cr ODS, Yamashita et al. [210] showed, using particle size distributions, that there was no observable change in particle size even after irradiation to 30 dpa at 1100 K (4660 h approximate duration).

The studies above used material from fast fission reactors, requiring long duration experiments and producing radioactive samples. Ion-irradiation has commonly been used as

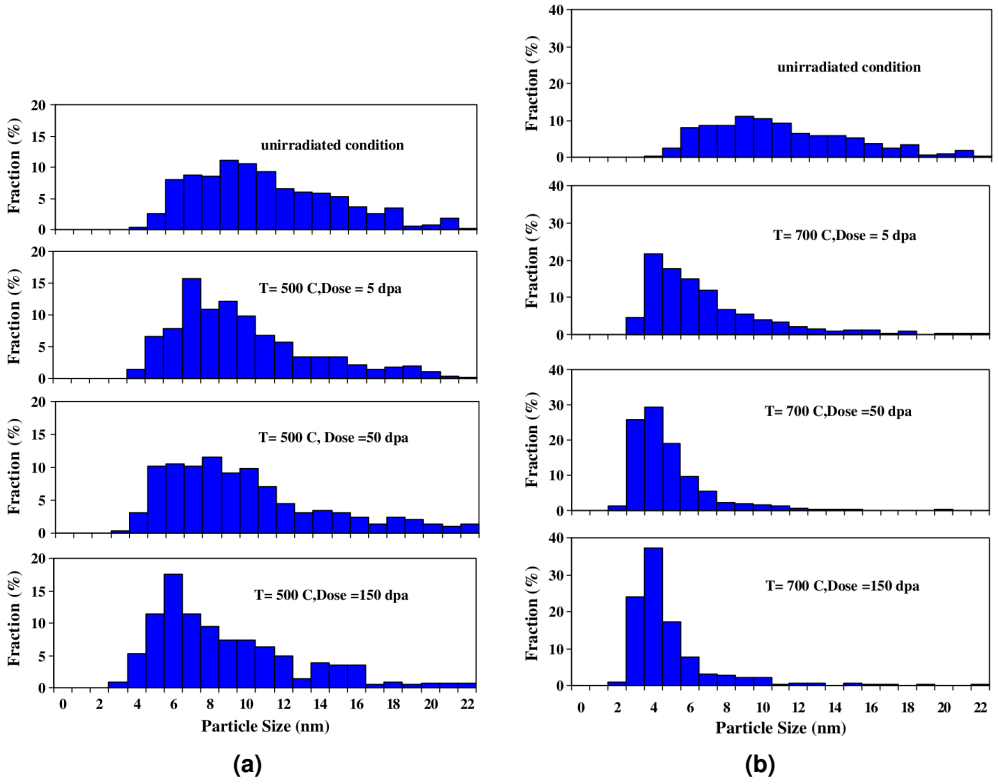

Figure 2.4.4 – 5 MeV Ni ion irradiations by Allen et al. [23] of a 9Cr-ODS alloy showing a refinement of the particle size distribution, measured from BF-TEM micrographs, at two different temperatures (a) 500 °C and (b) 700 °C. Reproduced with permission from [23]. Copyright © 2007 Elsevier B.V. All rights reserved.

an analogue of neutron damage to produce displacement damage in materials with great flexibility in the temperature, dose and dose rate of the ion-irradiation without the complication of activation [21]. Ion irradiation has also been used to study the irradiation damage of the oxide particles in ODS alloys. Allen et al. [211] first identified a square-root dependence for the decrease of the oxide particle radius with ion irradiation dose, consistent with purely ballistic mixing [211]. But later work [23] brought this mechanism into question by showing the irradiation response depends on the irradiation temperature [23]. The refinement of the particle size distributions as a function of temperature is shown in figure 2.4.4. Despite the advancement of TEM technology and the use of BF STEM imaging, the smallest (2 nm) particles remained elusive [23, 212], making accurate quantification of the full particle size range difficult even at high (>100 dpa) ion doses [212].

From 2008, an increasing number of ion irradiation studies have been made and atom probe analysis [20, 163, 213–216] has been applied to the irradiated materials [135]. With better microscopy, the particle sizes could be reliably reported after irradiation at low doses [217, 218]. Although there were hints that the particle distribution was modified [212], the stability of the particles was argued from their persisting presence after high dose irradiation.

Turning to the smaller particles, the use of EFTEM in an *in-situ* ion irradiation experiment can track changes in individual particles as a function of dose [96]. Lescoat et al. [96] found that the sub-10 nm particles were stable when irradiated to 45 dpa at 500 °C, but also observed modification of the larger particles. High-voltage TEM was the method of choice for investigating irradiation damage *in-situ* before *in-situ* ion irradiation was possible [82, 94, 95]. Monnet et al. [18] compared three possible dissolution mechanisms; electronic interactions, displacement-cascade damage and Frenkel pair dissolution using light ions, heavy ions and electrons respectively. This paper highlighted the instability of the oxide particles as well as trying to validate a simple ballistic dissolution mechanism for electron irradiation. Electron irradiation dissolved the oxides only when the energy exceeded the displacement threshold for the metallic component of the oxide (by comparing magnesium and yttrium oxide reinforced ODS alloys), but the simple model of ballistic dissolution does not account for any temperature-dependent behaviour, such as thermal diffusion of solute. Monnet et al. [18] suggested that further modelling work should include the effect of diffusion and point defects. Using *ab initio* modelling, Brodrick et al. [219] investigated the stability of the Fe-Y_2O_3 interface and reported that the particles are unaffected by a flow of defects and that incoming vacancies did not trigger outward diffusion of Y or O atoms. Lazauskas et al. [220] demonstrated the stability of a 2 nm Y_2O_3 particle in response to a 5 keV PKA iron atom using molecular dynamics. Even with a displacement cascade approximately the size of the particle, the Y and O atoms remained as part of the particle and were not mixed into the iron matrix. This agrees with the findings of Wang et al. [194] that the immiscibility of the Fe-Y_2O_3 system inhibits the displacement mixing.

Rarely, the displacement of an oxygen atom was caused by the direct collision of a PKA with an oxygen atom [220] consistent with the results of the electron irradiation carried out by Monnet et al. [18].

In order to study the influence of only the ballistic processes of irradiation damage, several authors have performed ion irradiation with T < 300 K to "freeze out" thermal and irradiation-enhanced diffusion [24, 25, 190, 221]. Analytical STEM, with EDX and EELS used simultaneously, was applied to study the chemical mixing of larger Ti-C-O particles in 14YWT [190] showing that at a high dose, relatively high dose rate and cryogenic temperature (173 K), displacement mixing dominates. The extent of ballistic and cascade mixing was measured as ~20 nm (for 180 dpa with Pt ions). Parish et al. [190] noted that in the high-dose regions no small particles were observed. Irradiation at -75 °C showed firstly a reduction in cluster radius (as measured by APT) and an increase in particle radius (as measured by EFTEM) but a decrease in number density as measured by both techniques at a dose of 50 dpa. At 100 dpa the APT showed no "statistically significant evidence of clustering" although some >20 nm Ti-O particles were observed by EFTEM. Particle dissolution at low temperatures was also reported by Parish et al. [221] (160 dpa 173 K) and Lescoat et al. [25] (150 dpa 300 K) using STEM EDS and APT respectively. These results show the naivety of early studies, which concluded the particles were totally stable or unaffected by irradiation; they also underline the importance of back-diffusion as a "self-healing" mechanism of repair of the oxide particles.

2.4.3 Discussion

Clearly the simple question *Are the particles stable?* is a complex one, drawing on many factors that are still poorly understood, especially solute mixing and diffusion under irradiation. Firstly, a summary of particle size evolution at 100–150 dpa as a function of temperature is shown in figure 2.4.5. No obvious trend is apparent, but both the starting conditions and alloy compositions vary between the different researchers. Some observations show growth of the particles and others refinement relative to their starting materials.

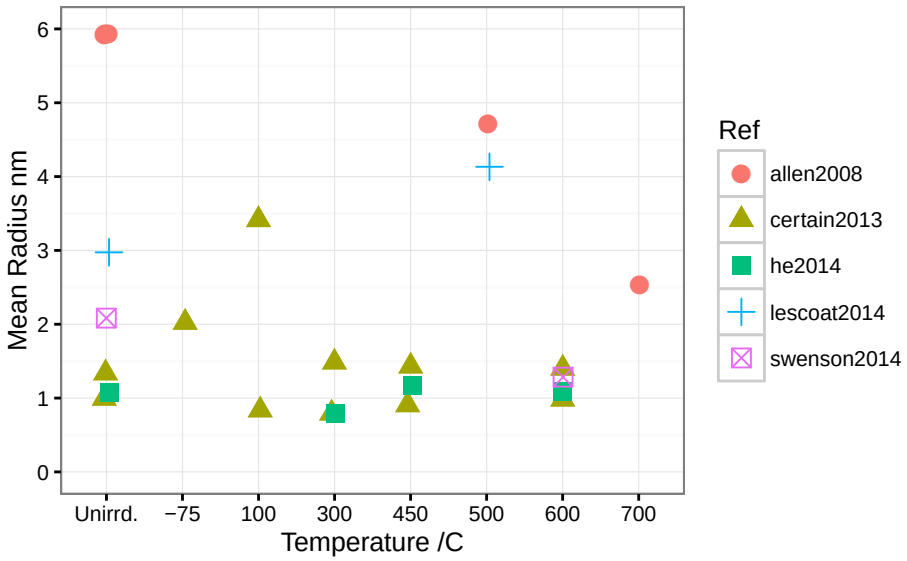

Figure 2.4.5 – Influence of high-dosage ion-irradiation (100–150 dpa) on oxide particles in several ODS alloys as a function of irradiation temperature. Data from [23–25, 141, 224].

These contrary effects of irradiation are analogous to observations of irradiation hardening or softening [222], as well as irradiation-induced ordering or disordering [223] which are dependent on the initial material conditions. Lescoat et al. [25] and Allen et al. [23] started out with alloys of different particle radii (3 and 6 nm), but after irradiation to 150 dpa at 500 °C both observed particles with a radius of ~4.5 nm.

Ion-irradiated samples are an example of a driven system where there is a constant input of external energy, in this case from the ion beam. In these systems, a non-equilibrium steady-state is eventually reached [225]. Bellon et al. [225] identified three regimes defined by temperature for a particular irradiation condition called the low, intermediate and high temperature regimes, where thermal diffusion dominates at high temperatures and irradiation effects dominate at low temperatures. Heinig et al. [226] show using experimental results and Monte Carlo modelling that a particle distribution can grow or be refined by irradiation depending on the irradiation temperature T and the characteristic/critical temperature T^* as shown in figure 2.4.6. Heinig et al. [226] define the high-temperature regime described by [225] as $T > T^*$ where the particles coarsen by Ostwald ripening when thermal diffusion dominates. This Ostwald ripening may be accelerated by the presence of the

irradiation defects, called irradiation-enhanced Ostwald ripening.

Ribis et al. [227] observed irradiation-enhanced Ostwald ripening at 500 °C from 1.1 to 4.5 nm with ion irradiation 75 dpa (Fe-14Cr-1W-0.3Ti-0.3Y_2O_3), but not with neutron irradiation of MA957 (Fe-14Cr-0.3Mo-1Ti-0.25Y_2O_3 irradiated to 75 dpa; radius change 2.0 to 2.5 nm). Ignoring the difference of the alloys investigated, which have an order of magnitude difference in particle number density 2.9×10^{23} and 5.4×10^{22} as well as a difference in composition, these results are in agreement with the theory of irradiation-enhanced Ostwald ripening. Lescoat et al. [25] (starting with 2 nm particles) noted the similarity between particle growth by ion-irradiation at 500 °C to 150 dpa (4.1 nm particle size) with thermal annealing at 1300 °C (4.5 nm), as well as the morphological transformation from spheres to polyhedral shapes as predicted by [114], showing the similarity between the radiation-enhanced effects and thermal annealing. Subject to irradiation an alloy can reach a steady state equivalent to equilibrium conditions with a different effective temperature (after [191]), the T_{eff} for the experiment in [25] is 1000 K, not 1300 K as they found experimentally. However, the coarsening behaviour of the oxide particles may not be linear [89], or the parameters in their diffusion model may be incorrect.

At lower temperatures, when $T < T^*$, the combination of displacive damage and thermal diffusion causes a reduction in particle size, called inverse Ostwald ripening (IOR), but when $T \ll T^*$, then IOR and precipitation can occur. This IOR behaviour presumably explains the results of Allen et al. [23], who observed a reduction in particle size from 6 nm to 2.5 nm after irradiation to 150 dpa at 700 °C. Although this theory helps to explain some of the contradictory results presented, it still leaves a number of unanswered questions, including: What is critical stability temperature of the oxide particles? How does it depend on irradiation conditions other than temperature? What are the kinetics involved in irradiation-enhanced precipitation and growth? Is a universal T^* is appropriate, or does it depend on the alloy chemistry and particle character?

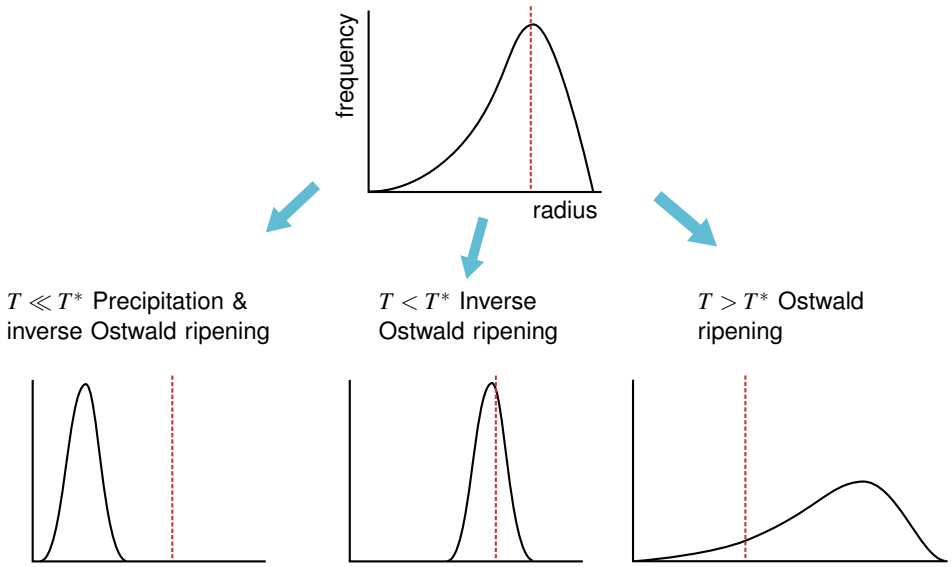

Figure 2.4.6 – Summary of the work presented in [226]—an existing particle size distribution can grow or be refined by irradiation. The red-dashed line shows the modal particle size in each case.

2.5 Summary

Presented above is an overview of the development and characterisation of oxide dispersion strengthened ferritic alloys, which are potential future fission fuel cladding and fusion structural materials. The addition of nano-sized oxide particles increases the strength and creep resistance of the ferritic base material. These oxides have shown good thermal stability up to 1200 °C and irradiation resistance to over 150 dpa at elevated temperatures. As the oxide particles impart the high-temperature stability, swelling resistance, grain refinement and transmutation gas-trapping abilities to these alloys, they are the focus of most research. The varied manufacturing routes and alloy compositions used have made a unilateral determination of their nature difficult. As the particles often have diameters less than 5 nm and are embedded in a magnetic matrix, detailed characterisation by TEM has been limited, but with the advancement of imaging and analytical techniques, the identification of the cubic $Y_2Ti_2O_7$ pyrochlore structure has become more convincing. This is not the only structure observed and with the use of APT, computer modelling and advanced TEM, the case for the particles having a non-stoichiometric composition is becoming more convincing, and

increasing emphasis has been placed on structural defects. There is also evidence of a range of oxide compositions, specifically looking at the Y:Ti ratio, which could be a function not only of spatial location but of particle size as well. One point to emphasize is the sensitivity of the oxide particle chemistry to minor alloying additions and impurities; just 0.3 wt% of Ti has a drastic refining effect on the particles, and in MA957 Al is frequently detected in the oxides.

As described in section 2.4, the effects of radiation damage in simple elemental metals are far from simple, and the analysis is complicated by the many methods used to induce radiation damage, while for ODS alloys, the addition of the oxide particles introduces another complication. Some headway has been made into understanding the fundamental damage mechanisms through experimentation, particularly through using a wide range of irradiation temperatures [24, 25], and through computer simulation [220]. However, there is still a wide range of irradiation parameters to explore, and many models make over-simplifications which restrict their applicability. Additionally, there is little systematic understanding of how the alloy composition and particle character play a part in determining the materials' response to irradiation damage. Some of these limitations will be the focus of the work reported below.

Chapter 3

Materials and Experimental Methods

This chapter gives technical detail regarding the materials and experimental methods used. Specific details of the processing of the ODS alloys is given first as this will be important for later sections. The parameters of the ion irradiation experiments are given, including the methodology for estimating the irradiation damage as a function of depth. The preparation methodology of samples for each of the characterisation techniques are described and the operational details of the experimental equipment are reported. These include the use of the I11 beam line at The Diamond Light Source X-Ray facility, nanoindentation, transmission electron microscopy and atom probe tomography. The conventional data analysis techniques for TEM and APT are presented, but the new analysis methodology for interpretation and treatment of the APT data is given in Chapter 4. This document has been compiled using Knitr [228] for LaTeX, as a Rnw file, meaning that, where possible, graphs and their accompanying source code are included in the source of this document itself. The source files are available in the Oxford Research Archive `https://ora.ox.ac.uk/`.

3.1 Materials

The three model ODS alloys were prepared by mechanical alloying and hot extrusion in India. High purity elemental powders of Fe, Ti, Cr, and Y_2O_3 were weighed and mixed to give alloy precursors with the desired compositions of Fe-0.3Y_2O_3, Fe-0.2Ti-0.3Y_2O_3 and Fe-14Cr 0.2Ti-0.3Y_2O_3 in weight percent. The Y_2O_3 powder (Alfa Aesar) had an average particle diameter of ~ 22 nm and the bcc crystal structure. The powders were mechanically alloyed by ball milling (Simolayer CM-08) in an argon atmosphere for four hours at 1000 RPM with a ball to powder ratio of 10:1. A study using the same high-energy Simolayer mill found steady-state conditions for the crystallite sizes after 3 hours of milling [229]. The vial and ball were hardened steel. The Fe-0.3Y_2O_3 and Fe-0.2Ti-0.3Y_2O_3 mechanically alloyed powders were extruded at 1323 K followed by annealing at 1223 K for two hours and then air cooling, similar to the conditions given in [230]. The mechanically alloyed Fe-14Cr-0.2Ti-0.3Y_2O_3 powder was extruded at 1423 K and then quenched and tempered at 1023 K for two hours and air cooled, similar to the method described in [231]. Finally, consolidated model ODS rods of 12 mm diameter were prepared from all three alloy compositions. The carbon content was measured independently for the three alloys, Fe-0.3Y_2O_3, Fe-0.2Ti-0.3Y_2O_3 and Fe-14Cr 0.2Ti-0.3Y_2O_3, and was found to be 0.03, 0.02 and 0.02 wt% respectively. Additionally, one Fe-0.3Y_2O_3 alloy was produced by blending (100 RPM in argon), ball milling for 20h in argon and consolidated by hot isostatic pressing (HIP) at 1423 K for 2 h at a pressure of 195 MPa. The carbon content of this alloy was not measured. From here on, the extruded alloys above will be referred to by the codes given in table 3.1.1 and the HIP alloy will be called FeY-hi.

Preparation of disks (12 mm diameter, 0.5 mm thick) cut from the extruded rods was performed in India prior to subsequent analysis. The disks were polished to a mirror finish using successively finer grit grades down to 4000 grit, followed by 5 μm diamond paste, 2 μm diamond paste and then an electropolishing treatment to remove the mechanically damaged surface layer.

	Target Elemental Composition in at%					
Code	Fe	Cr	Ti	Y	O	C
FeCrTiY	84.46	14.85	0.23	0.15	0.22	0.09
FeTiY	99.48	-	0.23	0.15	0.22	0.09
FeY	99.70	-	-	0.15	0.22	0.14
FeY-hi	99.63	-	-	0.15	0.22	-

Table 3.1.1 – Target alloy compositions in atomic percent (at%) including the (independently) measured carbon content.

3.2 Ion Irradiation

Ion irradiation is a fast and convenient method to introduce displacement damage, similar to neutron damage, into a material. Though there are differences in the type of damage created and the duration of the experiment, compared to neutron irradiation, ion irradiation can give high levels of damage in less than a day without the complications of sample radioactivity. In this project, I studied the influence of ion irradiation as an analogue for neutron damage, with ion-irradiation temperatures from 120 to 970 K.

Ion irradiation was performed at IGCAR, India using a 1.7 MV Tandetron accelerator equipped with a SNICS ion source for metallic ions. Two ion energies were used in this work, 5 MeV Fe^{3+} for high temperature irradiation experiments and 1.76 MeV Fe^{+} for the mixed-temperature irradiation experiments. The *average* dose rate at the peak damage depth was maintained between 2.8–3.1 $\times 10^{-3}$ dpa/s during all irradiation conditions; however, the beam was rastered over a 10 mm square area at a frequency of 1 kHz in x and y. This means the instantaneous damage rate is zero or much greater than 3×10^{-3} dpa/s. For the per-sample details of the high-temperature irradiation experiments see table 3.2.1 and for the cryogenic irradiation conditions, see tables 3.2.2 and 3.2.3.

High-temperature ion irradiation was performed at 773, 873 and 973 ± 5 K. Temperature was measured using a thermocouple attached to sample and by infrared Pyrometer with a spot size of 2 mm. It took 3 hours to heat the sample from room temperature to 973 K. Once the irradiation was over and heating was stopped, from 973 K the sample reached ~423 K within ~25 minutes, followed by slow cooling to 343 K over the next 30–45 minutes. A

	773 K	773 K	873 K	973 K
Samples	FeY	FeTiY/FeCrTiY	FeTiY/FeCrTiY	FeTiY/FeCrTiY
Fe^{3+}ion current /μA	3.3	3.8–4	3.16–3.4	2.8–3.1
Current density /μA cm^{-2}	2.91	3.36–3.53	2.79–3.00	2.47–3.27
Peak damage rate /10^{-3} dpa s^{-1}	2.9	3.7	2.9	2.8

Table 3.2.1 – Details of the high-temperature ion irradiation experiments using a Fe^{3+} ion energy of 5 MeV. Total dose: 1.5×10^{17} ions/cm^2. Irradiation time 14 h for each sample.

FeCrTiY	Sample	C05	C05H	C0510	C010	C010H	C01010
1st Irradiation	Peak dpa	50	50	50	100	100	100
	T /K	143	118	118	150	118	118
	Time /h	4.75	4.75	4.75	9.5	9.5	9.5
2nd Irradiation	Peak dpa	-	0	100	-	0	100
	T /K	-	973	973	-	973	973
	Time /h	-	9.5	9.5	-	9.5	9.5

Table 3.2.2 – A peak damage of 50 dpa and 100 dpa corresponds to an average dose of 4.51×10^{16} ions/cm^2 and 9.03×10^{16} ions/cm^2 respectively. 1.76 MeV Fe^+ ions.

FeTiY	Sample	B05	B05H	B0510	B010	B010H	B01010
1st Irradiation	Peak dpa	50	50	50	100	100	100
	T /K	119	121	121	130	117	117
	Time /h	4.75	4.75	4.75	9.5	9.5	9.5
2nd Irradiation	Peak dpa	-	0	100	-	0	100
	T /K	-	973	973	-	973	973
	Time /h	-	9.5	9.5	-	9.5	9.5

Table 3.2.3 – Details of the irradiation of the FeTiY alloy at cryogenic temperatures using 1.76 MeV Fe^+ ions.

vacuum of 1×10^{-5} Pa was maintained during the temperature ramp and throughout the irradiation. For ion irradiation at cryogenic temperatures, the sample was held at 117–150 K using a liquid nitrogen cooled stage. Selected samples were subsequently irradiated at 973 K with half the surface masked so that it experienced the same heat treatment but without irradiation.

Stopping Range In Matter (SRIM) calculations were performed using the “simple”

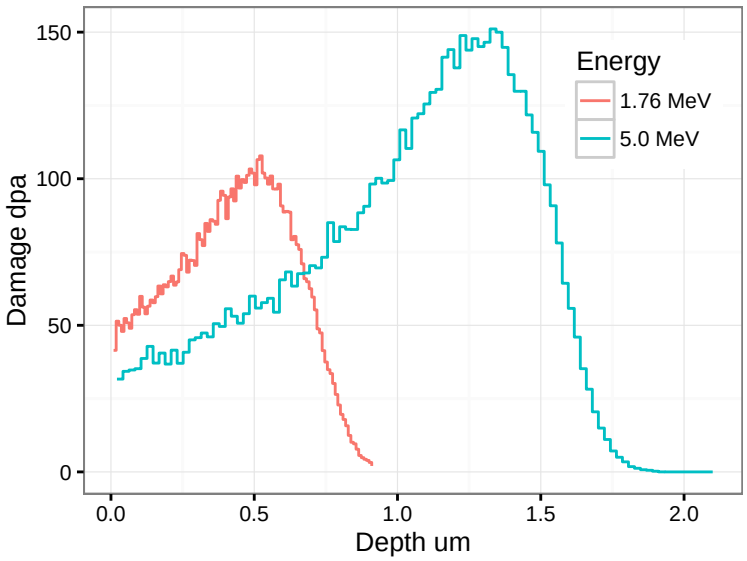

Figure 3.2.1 – Dose as a function of depth as estimated by SRIM for 1.5×10^{17} 5 MeV Fe^{3+} ions and 9×10^{16} 1.76 MeV Fe^{+}ions in iron.

Kichin-Pease mode with 40 eV displacement energy and 0 eV lattice binding energy as per the guidelines given in [184]; 10,000 ions were simulated in the SRIM 2013 version with the 2008 stopping power version. Details of the calculation and operation can be found in [186] and an image of the TRIM calculation window is included in Appendix A.1. The damage in dpa was calculated from the VACANCY.txt output by summing the vacancies due to ions and recoils, multiplying by the ion dose (ions cm^{-2}) and dividing by the number of atoms in a 1 cm^2 area by 1 Å thick layer, 8.48×10^{14} for Fe. The SRIM predicted damage-depth dependence is shown in figure 3.2.1.

For the 5 MeV irradiation, the peak damage region receives 150 dpa of damage at a depth of 1.2 µm, and for the 1.76 MeV irradiation, 100 or 50 dpa at a depth of 525 nm.

3.3 Sample preparation

3.3.1 APT - Electropolishing

From the as-received samples, matchstick bars ($12\times0.5\times0.5$ mm) were cut using a slow-speed diamond saw. These bars were then electropolished by standard methods using 20%

perchloric acid in acetic acid (5–14 V) and then 2% perchloric acid in 2-butoxy ethanol (3–6 V), both at room temperature, to give sharp APT needle specimens with a tip radius of 50–100 nm [232].

3.3.2 APT - Focused Ion Beam Milling

Samples were prepared from the bulk irradiated samples using well established focused ion beam methods (FIB) [233]; only a summary is given here. In a FIB, a focused ion beam of Ga^+ ions is scanned across the sample surface in a similar manner to a scanning electron microscope. The Ga^+ ions are accelerated to 30 kV into the ion column where they are focused and directed onto the sample using electrostatic lenses. On impact, secondary electrons are produced and atoms are sputtered from the surface. The secondary electrons are used to form an image (imaging) and the sputtering removes the material (milling). This technique is site-specific and was used to make cantilevers of material approximately 20 μm long, 1 μm thick and 5 μm deep from the surface. The original surface is protected from the Ga^+ beam initially by a layer of e-beam-deposited tungsten, followed by a layer of FIB-deposited tungsten. The double W layer is important at a subsequent stage because it is used as a reference to estimate the depth of the tip of the final sample from the surface. From the cantilever of material, rectangular section blanks of material are fixed onto a silicon micro-post array, with each cantilever yielding 5–8 stumps. Each of these blanks are then sharpened using the FIB to form sharp needles with an approximate tip radius of 80 nm, with each tip starting at a known depth from the original surface. This depth is used to estimate the ion dose experienced during the ion irradiation as predicted by the SRIM calculations (figure 3.2.1). During this final sharping step, a 2 kV accelerating voltage and 240 pA current were used to limit Ga^+ penetration into the sample. Figure 3.3.1 shows the difference in Ga concentration in APT samples prepared with 2 kV and 30 kV accelerating voltages.

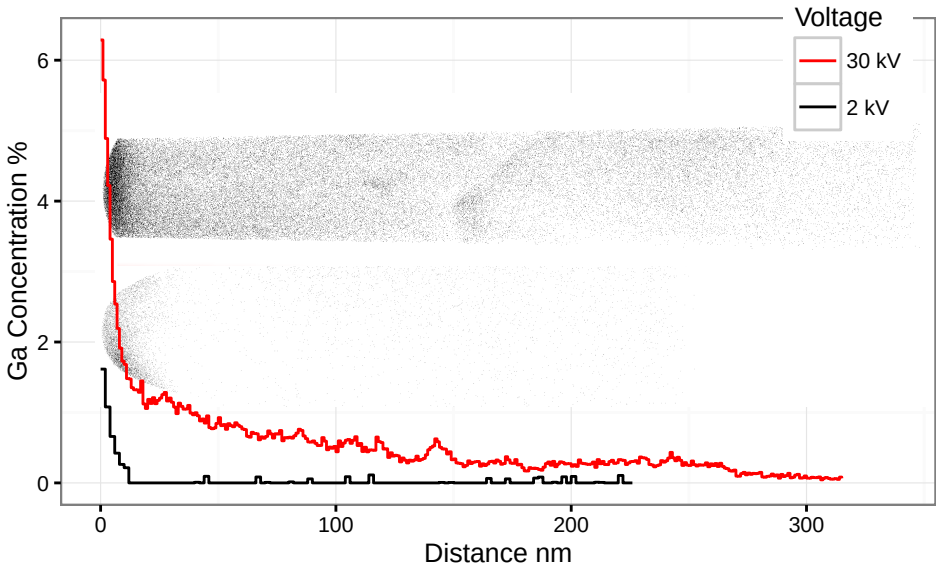

Figure 3.3.1 – Comparison of atom probe samples prepared with 30 kV and 2 kV accelerating voltages for the FIB Ga^+ beam. The 30 kV beam implants to a much greater depth and causes more damage than the 2 kV beam.

3.3.3 TEM - Focused Ion Beam Milling

TEM samples were produced in a similar fashion to the APT samples, by the "liftout" method. Large trenches about 20×15 µm were milled using a 30 kV 3.5 nA ion beam and the foil was thinned to 500 nm thickness using a 700 pA beam before lifting out. Once attached to the 3 mm copper half-grid (Omniprobe) using ion-beam deposited tungsten, the foil was thinned with a 300 pA beam until transparent to 10 kV secondary electrons. To compensate for the effect of the ion beam tails, the sample was tilted to $\pm 1.5^\circ$ relative to the ion-beam on each side. Electron transparency at 5 kV was achieved by milling with a 2kV 240 pA ion beam at an angle of 15° relative to the ion beam. A 2 kV accelerating voltage was used to minimise the Ga damage to the sample, but the remaining damage still prevented detailed analysis of defects created by the irradiation experiments.

3.4 Glancing X-Ray Diffraction

Synchrotron X-ray diffraction measurements were performed on the I11 beam line at the DIAMOND Synchrotron Light Source [234]. This high brightness beamline is designed to

perform high-resolution powder diffraction experiments such as the detection of weak features in crystalline structures or low-concentration components in complex phase mixtures. The diffractometer consists of five identical nine-crystal multi-analyzing crystal (MAC) arms deploying 45 crystals and detectors mounted on the 2θ-circle at 30° intervals, thus producing a high peak-to-background signal [234]. Recently, a new alignment stage has been added to the I11 beamline for glancing incidence X-ray diffraction (GIXRD) [235]. With precise control of the angle between the incident X-ray beam and sample surface, and hence the penetration depth, this addition can further improve the signal/background contrast which is particularly beneficial to study changes in phase distributions just below the sample surface (~ nm–μm) caused by a specific treatment or processing. Due to the shallow damage range of self-ion irradiation, the new apparatus was used to probe the stability of oxide particles in the ODS materials described above.

GIXRD experiments were carried out using a X-ray beam of λ=0.8256501 Å (March 2014) or λ=0.825815 Å (Jan 2015) with a beam energy of 15 keV. The wavelength was calibrated using a high-quality silicon powder (SRM640c). Incident angles between 0.25, 1, 2 and 4 degrees were used, resulting in the calculated attenuation depths of of 45, 400, 800 and 1610 nm respectively—shown graphically in figure 3.4.1. These x-ray $1/e$ attenuation depths were calculated as a function of glancing incidence angle for a $Fe_{88}Cr_{12}$ mixture using a 15 keV beam energy and the method detailed in [236].

Using a beam size of 0.15 (vertical) x 2.5 mm (horizontal) [234], an illuminated footprint of a few mm^2 was achieved for each measurement. At incident angles of 2 and 4°, the approximate illuminated area is 4.3×2.5 and 2.15×2.5 mm^2 respectively. While the samples had an irradiated area greater than this, there may still be influence of the position of the beam footprint on the measured diffraction intensity.

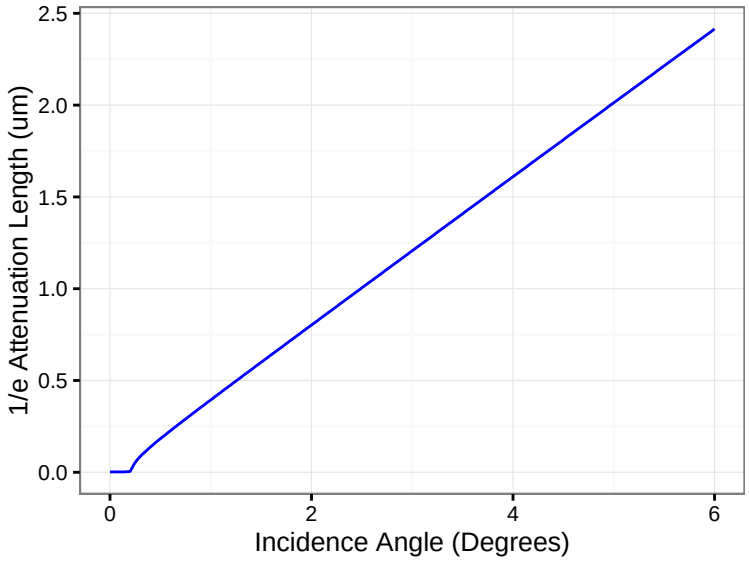

Figure 3.4.1 – $1/e$ attenuation depth as a function of glancing incidence angle for a $Fe_{88}Cr_{12}$ mixture using a 15 keV X-ray beam energy and the method detailed in [236].

3.5 Nanoindentation

The self-ion irradiation produces hardening of the material but only to a depth similar to the range of the ions into the surface, ~2 µm. Nanoindentation has been used to investigate thin layers and shallow ion-irradiated layers [237, 238], and I investigated the irradiation-induced hardening as a function of depth up to 2 µm. A MTS Nanoindenter XP, was used to create arrays of nine, or 16, two µm deep indents with a spacing/pitch of 50 µm. A Berkovich diamond indenter was used and calibrated against fused silica to find the area as a function of indent depth. By using the continuous stiffness measurement mode, the modulus and hardness could be recorded continuously as a function of depth into the sample surface [239]. A frequency of 45 Hz and displacement amplitude of 1 nm was used for the continuous stiffness measurement. For more information on the use of nanoindentation and its limitations to probe thin films, see [237].

Due to the poor surface finish, especially of the samples ion irradiated at high temperature, some anomalous load-displacement curves were ignored. The remaining curves binned into 100 evenly spaced displacement increments to give the mean and standard deviation values for hardness as a function of depth. Curves further than 3σ from the mean were discarded as outliers.

3.6 TEM

FIB methods were also used to produce cross-sectional samples for TEM. The advantage of FIB preparation over standard 3 mm diameter disks is two-fold: first, it is possible to select a specific region of interest and have fine control over the thickness and finish of the final sample. Second, the volume of material in a FIB-TEM sample is approximately $0.5\times15\times10$ μm^3, which is 10^7 times smaller than a 3 mm x 50 μm thick disk; thus the influence of the ferrite sample's magnetism on the TEM experiment is greatly reduced. Unfortunately, the FIB damage of the surface, even when using the 2 kV final cleaning step, complicates the analysis of the bulk ion-irradiation damage [240]. Therefore, only observation of the particles and grain boundaries was possible using diffraction imaging. HRTEM images were take of the particle structures and chemical analysis was performed with EFTEM and EELS.

3.6.1 Imaging

200 keV TEM observations were made using a Philips CM20 (CM20), a LaB_6 JEOL JEM-2100 (JEM-2100), a JEOL 2200MCO FEG TEM (OJ2200) and a JEOL ARM200F (ARM200). Additionally TEM and STEM imaging was performed at 300 keV using a JEOL JEM-3000F FEGTEM (JEM-3000). The JEOL 2200 was fitted with a monochromator, two spherical aberration (Cs) correctors and an Ω-filter to perform energy-loss imaging. The ARM200 was fitted with a spherical aberration STEM probe corrector and a Centurion EDX detector and Gatan GIF Quantum 965 ER featuring Dual EELS and EFTEM capabilities. TEM observations were made using a double-tilting beryllium 3 mm TEM grid holder. TEM of the atom probe needles was made using a Fischione 2050 on-axis 360° rotation tomography holder.

3.6.2 EFTEM - OJ2200 FEG TEM

The largest (120 µm) condenser aperture was used and the beam was focused to give an an image with a diameter slightly bigger than the CCD to maximise intensity. The convergence and objective aperture half-angles were 6 mrad and 20 mrad, respectively. Low-loss energy-filtered series collected from the 20–80 eV energy-loss range included the $Y_{N2,3}$ (26 eV), $Ti_{M2,3}$ (35 eV), $Cr_{M2,3}$ (42 eV) and $Fe_{M2,3}$ (54 eV) edges. Steps of 1 eV, using a 2 eV slit and 6–8 s acquisition time per image were used, and images were hardware binned by 4 to 1024×1024 pixels. The brightness of the field-emission source, even without the monochromator applied, was too low to allow core-loss images to be acquired.

3.6.3 EFTEM & EELS - ARM200F

Low-loss EFTEM spectrum images were acquired from 20–80 eV using a 1 eV slit width and a 1 eV step and exposed for 1 s per energy-loss. Core-loss spectrum images were acquired from 450 to 750 eV to capture the Ti_L (456 eV), O_K(532 eV), Cr_L (575 eV) and Fe_L (708 eV) edges. A slit width and step of 5 eV were used with a 10 s exposure.

3.6.4 Data Analysis

Before any quantification or analysis of the EFTEM data, a number of treatments were necessary. These are detailed below:

1. Anomalous pixels caused by X-Rays striking the phosphor scintillator or “spikes” were removed using a median filter on pixels with an intensity greater than six standard deviations from the mean.

2. Sub-pixel accuracy drift correction using the Statistically Determined Spatial Drift program plug-in [241] for DigitalMicrograph. A window 32-128 pixels square was chosen which contained a feature with sufficient contrast for the cross-correlation to give reliable matching between images. In the low-loss EFTEM series image filtering was not often necessary, but the Heavy Low Pass noise-reduction filter and the

Sobel edge-detection filter were the most appropriate combination when filtering was applied.

3. Areas of vacuum (holes) were removed by thresholding the image of the sum of all energy loss images using the MATLAB script: *EFTEM_removeVacuum.m* or by deleting rectangular sections in DigitalMicrograph.

3.6.5 Principal Component Analysis

Principal component analysis (PCA) was performed on the EFTEM data using the singular value decomposition (SVD) method described in [153, 242, 243] and implemented in HyperSpy [243]. A minimal example is given in section §A.2; for more information regarding PCA, see [244]. PCA identifies non-noise components in the data and returns eigen images and eigen values each containing some amount of the "variance" of the original data. A selection of eigen images (with the most variance or that are least noise-like) are used to reconstruct a new "noise-free" data set. Either the identified eigen images or the reconstructed data is used for further analysis. PCA assumes that the noise is Gaussian, but this is rarely the case for electron spectroscopy data, which has Poissonian noise. Therefore, the decomposition (on data loaded into the variable "s") was performed after scaling the data so that the Poissonian noise is more Gaussian, using the command below in HyperSpy.

```
s.decomposition(normalize_poissonian_noise = True)
```

The decomposition of EFTEM spectrum images gives 2D eigen images and 1D energy loss spectra. These results often highlight the Y and Ti signals from the oxide particles in the low-loss spectra, or small variations in the particle chemistry highlighted by variations in the Ti/Cr overlap at ~40 eV energy loss, without having to reconstruct the decomposed data. Figure 3.6.1 shows two eigen images and their eigen vectors. Factor 3 obviously shows a positive contribution from the Y and Ti peaks and a negative contribution from Fe at 60 eV, which shows the position of two larger particles and several smaller ones (in the right

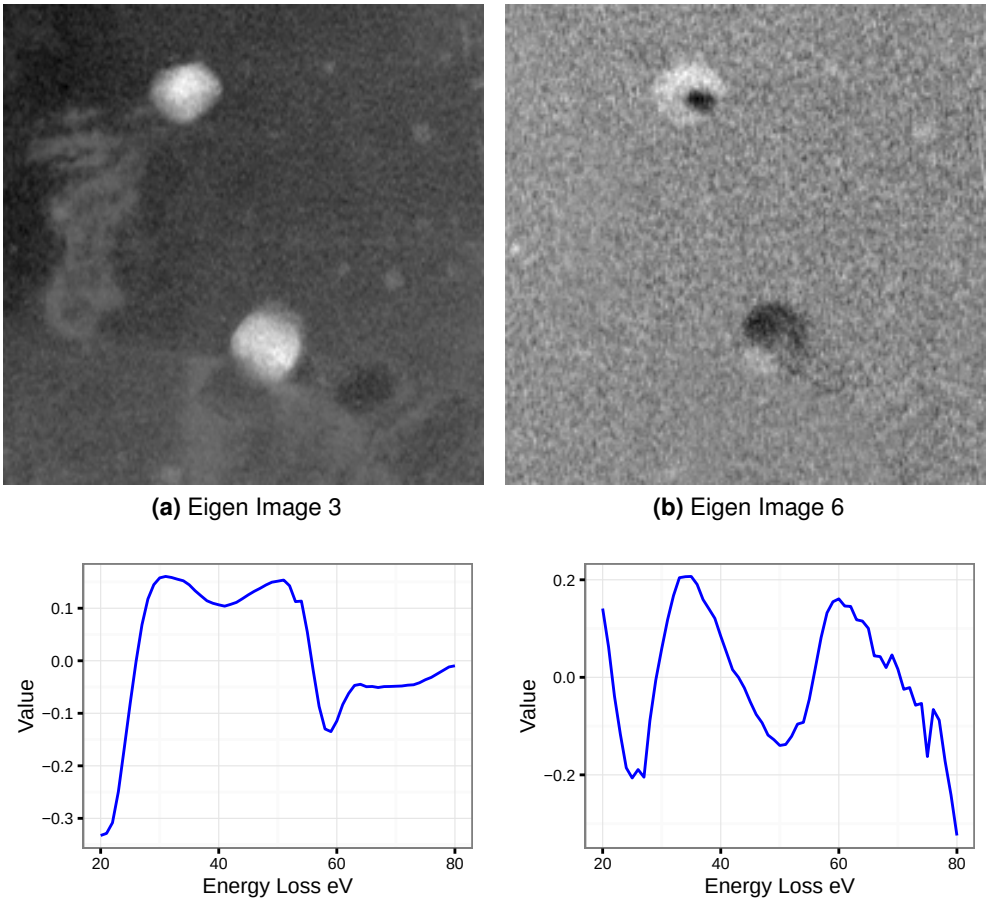

(a) Eigen Image 3 **(b)** Eigen Image 6

(c) Eigen Vector 3 **(d)** Eigen Vector 6

Figure 3.6.1 – Example of eigen images (a; b) and vectors (c; d) following factorization using SVD in HyperSpy of oxide particles in an ODS steel. The images in (a; b) are 430 nm across.

of the image). Factor 6 shows that the two large particles are actually composite particles, although it is not clear from the energy loss spectrum which elements are present.

The orthogonality requirement of the factorization means the resulting factors are not necessarily physically representative of the original signals that made up the starting data. Blind Source Separation (BSS) aims to resolve the decomposed components into a more physical representation of the original signal using independent component analysis. BSS is performed in HyperSpy using the FastICA algorithm [242].

3.7 APT

Atom Probe Tomography (APT) is a destructive technique that yields 3D chemical information with sub-nanometer resolution. Figure 3.7.1 shows the important components of the Local Electrode Atom Probe (LEAP). A standing voltage (2–10 kV) is applied to the sample using the local electrode, which, with a <100 nm sample radius, gives an electric field high enough to cause field evaporation of ions from the tip. In the LEAP-3000X HR, a curved reflectron is used to focus ions with differing kinetic energies, but the same mass-to-charge, onto the spatial detector so they arrive at the same time. As shown by the red and blue tracks in figure 3.7.1, higher energy ions will travel deeper into the reflectron, traveling a longer path than those ions with a lower kinetic energy. The total flight path, used to convert from time-of-flight to mass-to-charge, is 382 mm, but the equivalent tip-detector distance in a straight flight-path atom probe is shown by the position of the "virtual detector", which is an image plane conjugate with the detector after the reflectron.

Pulsed evaporation is required to provide the time-of-flight (TOF) mass spectrum to identify the identity of the ions, and pulsed voltage or a pico-second laser pulse are used. Laser pulsing, or *laser mode,* APT means a wide range of materials can be investigated with a high yield of successful experiments. The details of the atom probe experiment and the reconstruction of the data affect the interpretation of the observations and so the most important points are given in summary here. For more information, see [232, 245–247].

By the application of a large positive voltage V, an electric field F is concentrated at the tip of a sharp needle, radius R, to a value of:

$$F = \frac{V}{k_f R} \tag{3.7.1}$$

k_f is the field factor, ~2–4, a geometric factor which accounts for the tip shape and local electrostatic environment. Field penetration is negligible for metallic materials but not for insulating materials; thus the field penetration may account for the production of molecular ions and reduced resolution of the oxide clusters [248]. The evaporation process

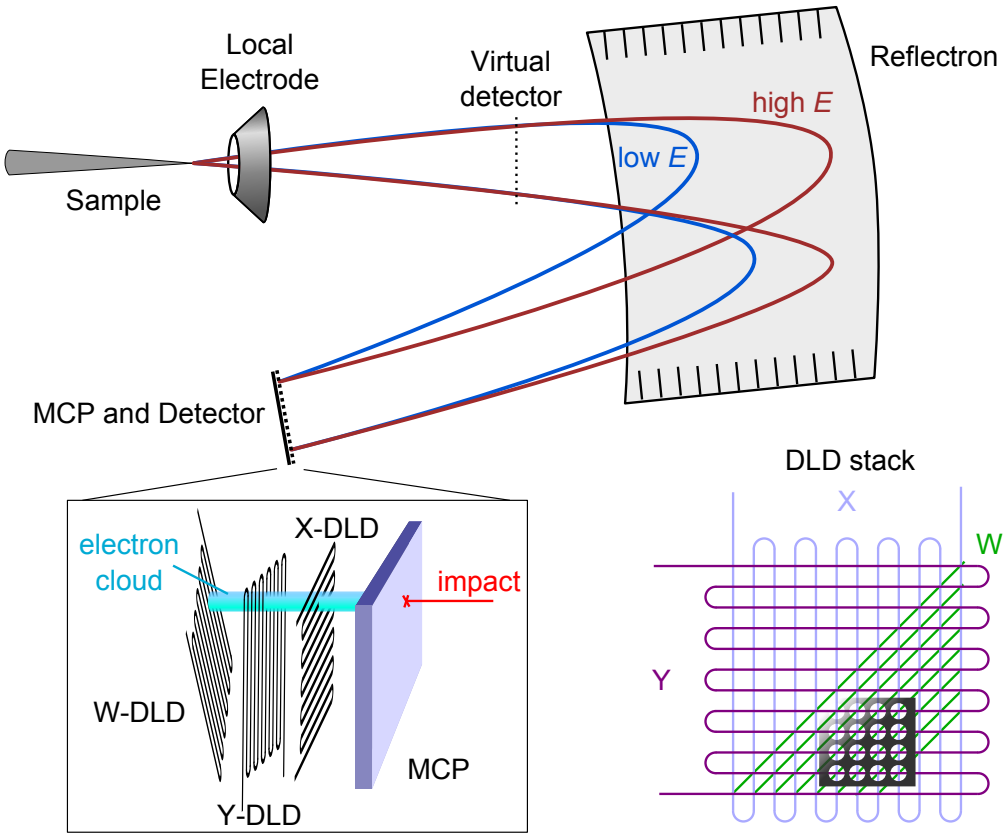

Figure 3.7.1 – Diagram of the reflectron-fitted Local Electrode Atom Probe showing the position of the sample relative to the local electrode, the flight path of low (blue) and high (red) kinetic energy ions through the curved reflectron and the delay-line detector (DLD) stack. The detector stack has a multichannelplate front face and three DLD behind it to detect the resulting electron cloud produced from an ion impact. Geometry not to scale.

using voltage pulsing is reasonably well understood, with the origin of multiply charged ions explained by the post-ionisation model [249]. In laser mode, the laser-tip interaction and the mechanisms involved are less well understood, but the evaporation is dominated by thermal processes; hence thermal transport in the sample is important. If the tip remains hot, then ions evaporate over a relatively long period of time (delayed evaporation), which gives a long tail to the peaks in the time-of-flight spectrum. The second deleterious influence of this high temperature is that enhanced surface diffusion can lead to artefacts and reduced spatial resolution [250].

Ions are detected by a delay-line detector (DLD) stack (inset bottom left figure 3.7.1) behind a microchannelplate (MCP) [251] which amplifies the single ion impacts. Two DLDs

give the X_D and Y_D positions and a third DLD helps resolve mutliple hits and reduces the detector dead time [252].

The raw data (RRAW and RHIT files) contain the detector timings and experimental conditions for each detected hit. The detector coordinates, ion TOF and hit multiplicity are calculated from the detector timings using the commercial IVAS 3.6.6 software from Cameca. 3D positions with chemical identities are reconstructed from the detector coordinates and ion identity, as detailed in section 3.7.3. The output point cloud data was visualized using the IVAS 3.6.6 software from Cameca, but I also used the MATLAB environment by MathWorks and the open source statistics package R [253] for much of the data analysis, processing and plotting [254]. The details of the novel data analysis I performed is detailed in chapter 4.

3.7.1 Data Acquisition

Atom probe analyses were performed using a LEAP-3000X HR microscope. During analysis, samples were maintained at 50 K and a 532 nm wavelength laser with a pulse width of 10 ps, repetition rate of 200 kHz, pulse energy of 0.3–0.4 nJ and spot size of less than 10 μm were used to promote field evaporation. The analysis chamber vacuum was maintained $<4 \times 10^{-9}$ Pa. These parameters were chosen based on previous work to give a good compromise between data quality and data yield .

In the LEAP-3000 there are three delay-line detectors, arranged at 0, 45 and 90 degrees, behind a multichannelplate (MCP). Each delay-line, known as X, W and Y, produces a pair of timing measurements for each single impact, therefore giving six measurements in total. As the length of the delay-line and speed of electron propagation are known, using the signals from the three delay-lines the detector hit positions (X_D and Y_D) can be measured. The W delay-line is used to help deconvolute hits of ions arriving from the same pulse. The timing between pulses is greater than 5000 ns, and with a standing voltage greater than 2 kV, in the iron-ODS system, there are no heavy ions that evaporate on the $n-1^{th}$ pulse and arrive at the nth pulse (spectrum over-run). Some ions do evaporate on the same pulse,

$\Delta P = 0$, and may have a difference in time-of-flight, ΔTOF. When detected, these impacts are called *multiple hits*.

3.7.2 Multiple Hits

When ions evaporated on the same pulse arrive at the detector within the "dead-time" of the detector, they are lost to ion *pile-up*. This pile-up may give a systematic bias to composition, as the first (lighter) ion will be detected preferentially, and so should be avoided. Using laser pulsing reduces the field at the tip required to cause field evaporation and therefore results in fewer multiple hits [121]. Using voltage pulsing with 20% pulse fraction 7.5% of hits from the ODS samples were multiples; 16% in the clusters and 5% in the matrix. As noted by Williams et al. [121], the spatial correlation of multiple hits involving solute ions will be enhanced due to the concentration of the solute to the clusters.

For a list of ion pairs, the ΔX_D and ΔY_D detector positions can be calculated from the data provided in the *epos* data file. The pair-wise distance between multiple hits is calculated using the Pythagorean distance $\sqrt{\Delta X_D^2 + \Delta Y_D^2}$. For single hits, the "pair distance" was counted as the distance between consecutive non-multiple hits. To normalise the pair-distance histogram, it is divided by the histogram formed by random ion pairs. This normalisation therefore accounts for the greater number of pairs observed at larger separations ($2\pi rdr$, increasing counts with increasing separation) but also the limited spatial extent of the observations because ions can only be detected in circle of radius ~15 mm (reduces counts of larger separations). Additionally, the ΔX_D and ΔY_D detector positions were observed using a 2D histogram to investigate if the relationship between multiple hit positions is symmetrical. The analysis of the multiple hits is presented in section 4.3.

3.7.3 Reconstruction Methodology

In metallic samples the penetration depth of the electric field into the surface of the needle is sufficiently shallow that it can be considered that only the atoms on the surface may evaporate. The standard reconstruction protocols use a point-projection model to translate from

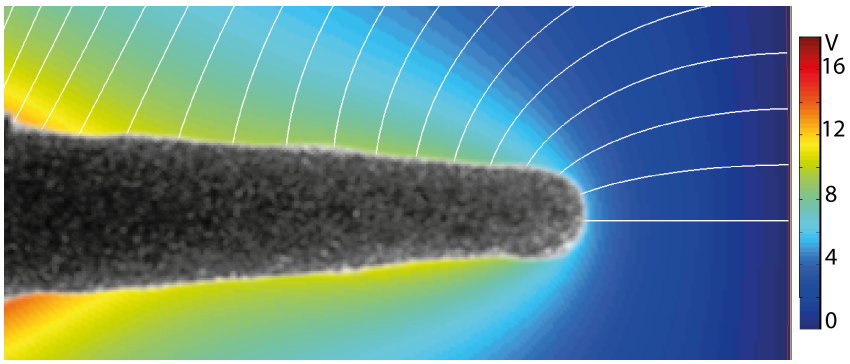

Figure 3.7.2 – Electrical potential (colour scale) and electric field (white lines) around an APT needle measured using electron holography. Figure produced in collaboration with V. Migunov, reproduced with permission.

detector coordinates back to an x,y position on the tip's surface. It is assumed that the ions leave the tip with a radial trajectory but that their actual trajectories are compressed (relative to the emission from a sphere) due to the shank of the needle behind the tip. Figure 3.7.2 shows the experimentally measured electric field around a bias atom probe tip examined in situ using electron holography in a TEM.

Figure 3.7.3 defines the lengths used to define the point projection model. The macroscopic measurements define the flight length L_{Det} and the detector position R_{Det}. The ion initially leaves at θ_{Launch} but is detected at an angle of θ_{Det}, which is m times the tip radius r. m is related to the *image compression factor* (ICF) by $\xi = m+1$. By trigonometry it can be shown that [247]:

$$s = r.\left(m\cos(\theta_{Det}) + \sqrt{1 - m^2\sin^2(\theta_{Det})}\right) = r\gamma$$

Therefore the relation between the launch angle and the detection angle is:

$$\tan(\theta_{Launch}) = \frac{\gamma\sin(\theta_{Det})}{\gamma\cos(\theta_{Det}) - m}$$

which simplifies in the case of small θ_{Det} to:

$$\theta_{Launch} = \xi\,\theta_{Det}$$

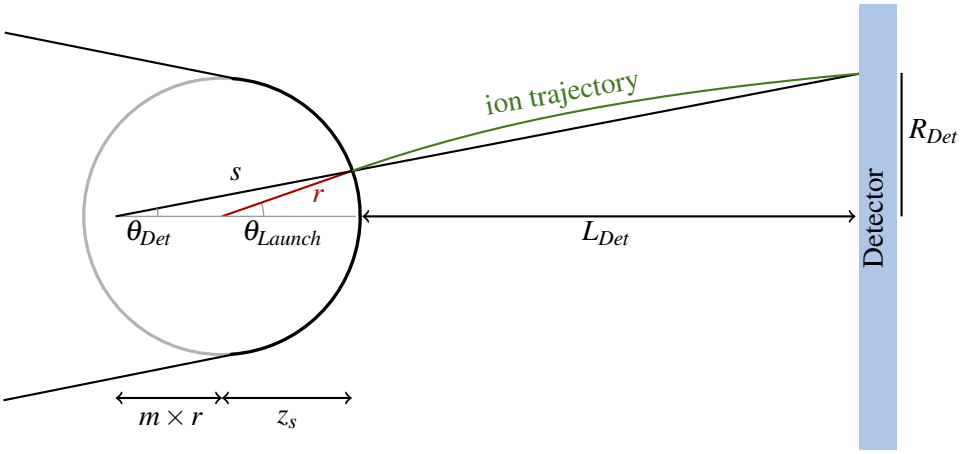

Figure 3.7.3 – Schematic showing the lengths used in the tip reconstruction.

This relationship means that the ICF can be determined experimentally from the distance between features observed on the detector and known crystallographic angles in the sample. Note that to calculate θ_{Det}, the value of L_{Det} is required. L_{Det} is not equal to the total flight path (shown in figure 3.7.1) but is the distance from the tip to the virtual detector position, an image plane conjugate with the actual detector before the ions enter the reflectron. The flight path length in the LEAP-3000X HR is 382 mm but L_{Det} was measured as approximately 42–44 mm. ICF is discussed further in section 3.7.3.1.

For each ion impact, an additional volume, equal to that of the ion, is spread over the observed sample area to give an increment of depth dz, the increase in z for each detected ion:

$$\mathrm{d}z = \frac{\Omega}{\varepsilon w_V(z)}$$

where Ω is the ionic volume, ε is the detection efficiency (37% for the LEAP-3000X HR [247]) and $w_V(z)$ the function which describes how reconstructed volume evolves with depth z. The ionic volumes are defined in the IVAS database, in the ROOT file for each reconstruction and in the RRNG range file. If peaks in the mass spectrum are misidentified, then the ionic volumes used will not be correct. For most reconstructions, the samples contain 85-99% Fe and up to 14% Cr, which have well known ionic volumes and so the

reconstructed volume is insensitive to misidentification of minor components. Reconstruction protocols differ on the form of $w_V(z)$ which is also related to how the tip radius evolves with the depth analysed. If the tip has a tapering shank (a shank angle > 0), then as atomic layers are removed the tip shape will evolve and the tip radius will increase. Therefore, a function is required that describes the evolution of the radius with depth:

$$\frac{\mathrm{d}r}{\mathrm{d}z} = w_R(z)$$

The tip radius is often estimated using the voltage[255]:

$$r = \frac{V}{k_f F_e} \tag{3.7.2}$$

using the standing voltage V, field enhancement factor k_f and the electric field required to cause field evaporation F_e. $\frac{\mathrm{d}r}{\mathrm{d}z}$ can also be described by a fixed shank angle, which is either measured from the voltage curve of the experiment or measured from an image of tip the before the experiment. The most flexible description of $\frac{\mathrm{d}r}{\mathrm{d}z}$ is available using the Tip Profile reconstruction method in IVAS, shown in figure 3.7.4. Where possible in this work, images of samples before APT were taken and used to aid the reconstruction process. Further calibration of the reconstruction is possible using features identified in both TEM and APT as detailed in section 3.7.3.1.

In most cases, experiments were reconstructed using the modified Geiser Protocol [247, 255], using 3.7.2 with $k_f = 3.3$ and $F_e = F_{Iron} = 33$ V/nm, so that the reconstructed radius evolves with the standing voltage recorded during the experiment. So, for example, in the small angle approximation and with a shank angle of zero, the depth increment for a specific ion impact at R_{Det} with ionic volume Ω:

$$\mathrm{d}z = \frac{\Omega L_{Det}^2}{r^2 \varepsilon \pi R_{Det}^2 \xi^2}$$

The next section explains how the reconstruction parameters (specifically r and ξ) were calibrated for each APT experiment.

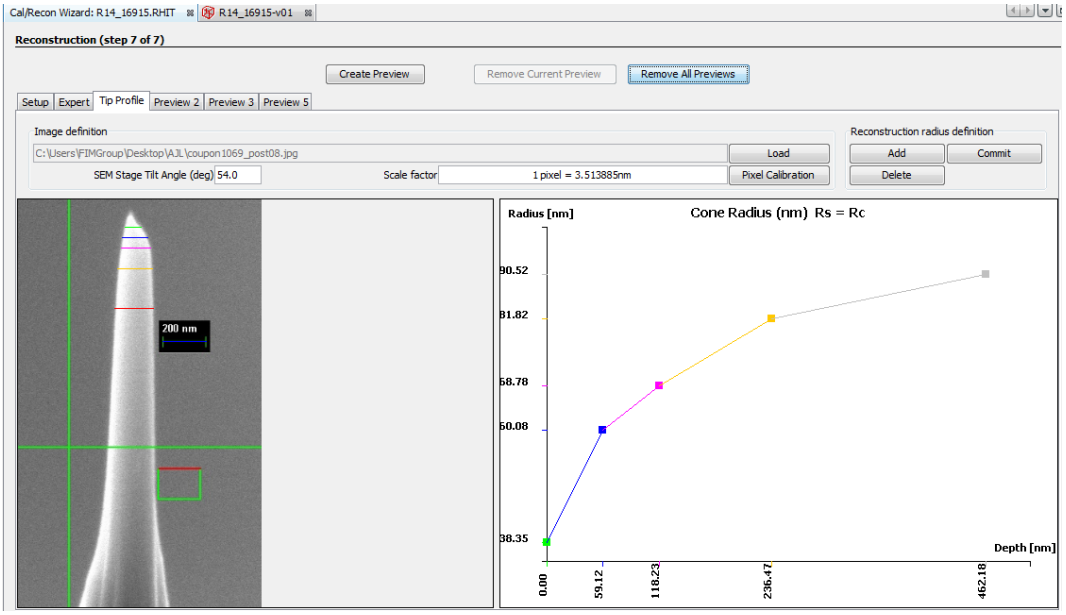

Figure 3.7.4 – The Tip Profile reconstruction method available in IVAS 3.6+. The user profiles a calibrated image of the tip before APT analysis (left) and then defines an initial radius ($z = 0$) and subsequent radii with increasing depth to describe the $\frac{dR}{dz}$ function (right) which is used in the tip reconstruction.

3.7.3.1 Calibration

For most experiments, a low-order crystallographic pole is in the field of view, such as the 200, 110 or 222 poles. When using laser-pulsed evaporation, the zone lines are less clear compared to voltage-pulsed evaporation experiments, and the reflectron reduces the lateral resolution of the atom probe. When poles were observed and could be reliably indexed, the depth resolution was sufficient to resolve the plane spacing perpendicular to the evaporation surface. The plane spacing was measured using the spatial distribution maps in the *Reconstruction Explorer* tool in IVAS. A sub-volume was selected from the detector coordinates (X_D, Y_D) and radius 2–3 mm around this point on the detector was reconstructed with the projection centre so that the planes were aligned in the X-Y plane. Once planes were aligned, a spatial distribution map was made in the X-Z or Y-Z plane to measure the plane spacing. When multiple poles are present, it is possible to adjust the ICF and the initial tip radius so that both the plane spacings and angles between poles match the expected crystallographic spacings and angles, as shown in figure 3.7.5.

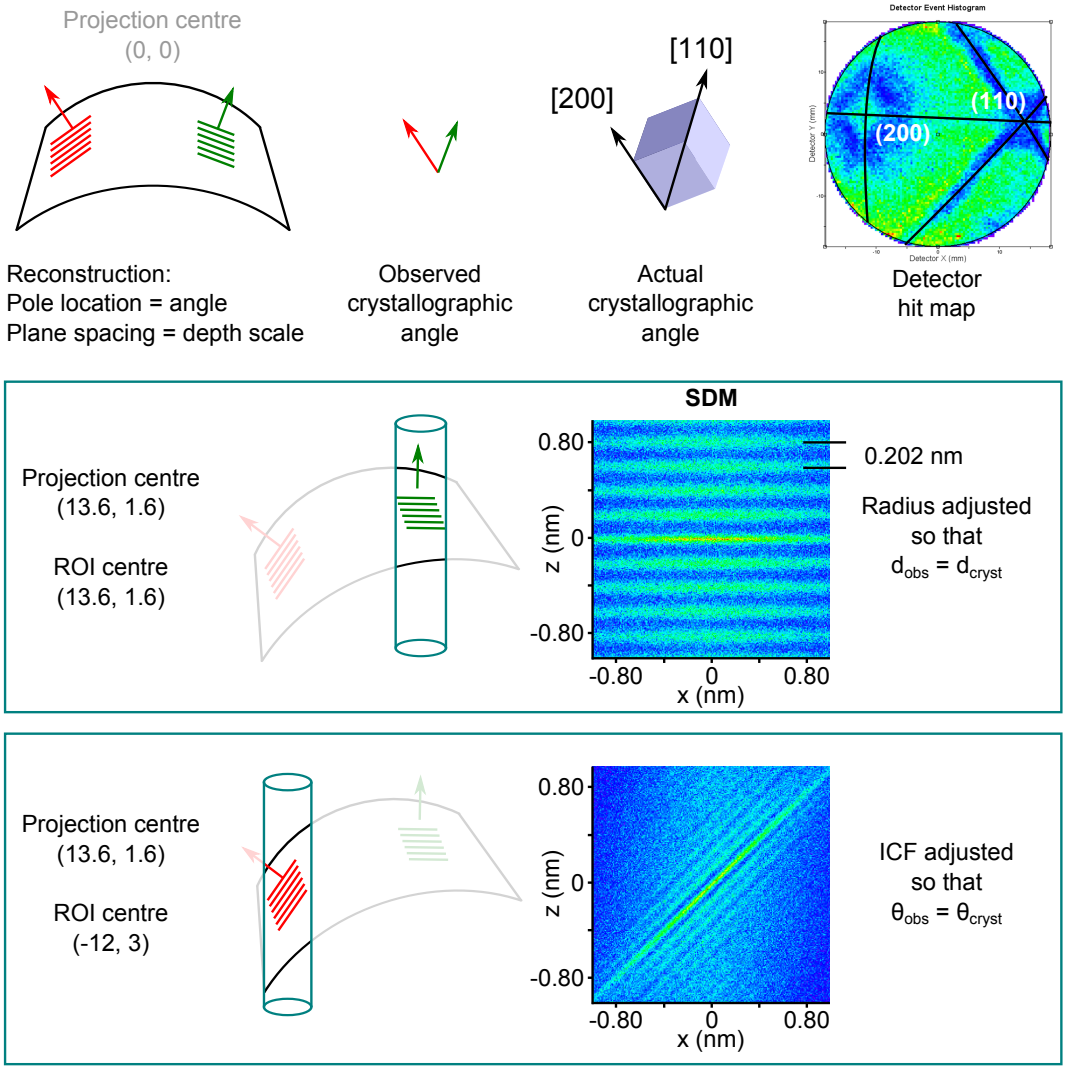

Figure 3.7.5 – Poles are indexed using the zone lines observed in the detector hit map (top right); these poles have specific crystallographic angles and plane spacings. The reconstruction parameters can be adjusted so that the observed angles and spacings match the expected values. Here (200) and (110) are aligned roughly in the X-Z plane, allowing a direct measurement of the angle between the planes using the spatial distribution map (SDM). A sub-volume around the (110) pole is aligned with planes perpendicular to X-Y using a projection centre of (13.6, 1.6). Moving to the (200) pole position, the angle of the planes can be adjusted to 45° using the image compression factor.

3.7.4 Reconstruction Artefacts

Our current reconstruction model has a very limited geometry, meaning that any deviations away from a simple tip shape, or even a change in tip shape during the experiment will result in an inaccurate reconstruction. The magnification of the tip in an atom probe experiment depends on the tip radius; thus it is common to think of the tip as the lens in an optical system. Using the terminology of this system, distortions from the ideal are called aberrations, which result in the blurring of the reconstructed ion positions due to the uncertain trajectory of the ions from the tip. Because the geometry depends on the tip material and sample shape, these aberrations are not consistent but can vary throughout an experiment. Aberrations fall into two broad categories: atomistic and microscopic.

Atomistic aberrations occur over very short distances and are due to differences in evaporation field or immediate environment. Depending on the acquisition parameters, different evaporation fields of atoms in a compound may cause preferential evaporation of one species. Differences in evaporation field can result in the z-coordinate being reconstructed out of order [256]. The local environment, either geometric or chemical, can cause trajectory aberrations. Geometric variations and the atomic roughness resulting from step-edges and facets in the crystal structure give rise to zone lines, areas of enhanced and reduced intensity relating to the crystallography of the sample [257]. The chemical environment can also cause ionic positions to be reconstructed incorrectly, causing chemical shift, with the position of particles displaced towards low-order crystallographic poles [160].

Microscopic aberrations are due to larger changes in tip shape, which occur due to grain boundaries, different phases and voids. Oberdorfer et al. [258] have established a methodology for simulating atom probe relevant volumes, and have demonstrated the result of evaporating a particle that has a lower evaporation field relative to its surroundings or a particle that has a finite dielectric constant [259]–see figure 3.7.6. These are the possible situations for oxide particles in ODS alloys. For a particle with a low evaporation field and with a dielectric particle, the reconstructed shape is laterally contracted perpendicular to the evaporation surface. Note that in the case with relatively large particles, the size of the

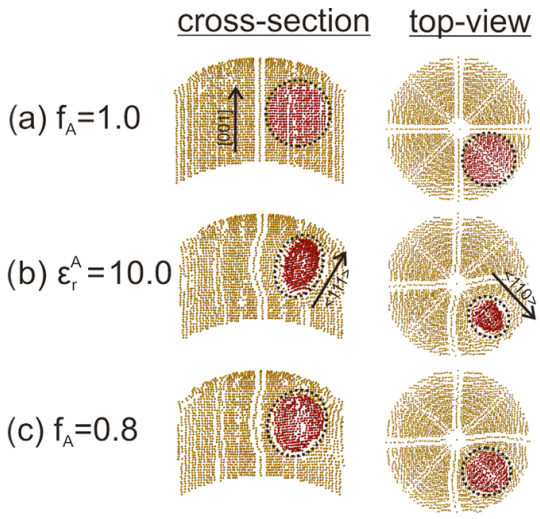

Figure 3.7.6 – Reconstructed shapes of an initially spherical precipitate (red) dependent on different evaporation properties: (a) homogeneous evaporation, (b) dielectric case, (c) metallic case with favored evaporation relative to the matrix (yellow). Reproduced with permission from [259]. Copyright © Microscopy Society of America 2011.

particles parallel to the evaporation direction remains unchanged. These artefacts arise from the tip shape during the evaporation. For figure 3.7.6(b), the preferential evaporation of the particle reduces the local tip radius, giving a local demagnification. This demagnification results in lateral contraction of the particle and increased ionic density (see section 4.4 for details).

In addition to the artefacts listed above, thermally activated surface migration of species enhanced by the electric field may cause repartitioning of solute ions (especially C, N, Si and P) [250]. It was frequently observed in my experiments that C and N would segregate to low-order poles in the matrix prior to evaporation, shown in figure 3.7.7, and as such these linear features (parallel to z) in the analysed volumes were ignored.

Figure 3.7.8 shows some subtle artefacts relating to the measured evaporation timing and position of $^{56}Fe^{2+}$ ions. Figure 3.7.8b shows how the colours relate to the timing of the evaporation. The earliest evaporating ions originate from one side, this may be because it is the side illuminated by the laser or because of a failed bowl correction. The majority of ions, $m/z = 27.97$, evaporate around the low-order 200 pole and the later evaporating ions are observed further from the pole. $^{56}Fe^{+}$ ions originate from the 200 pole, suggesting it

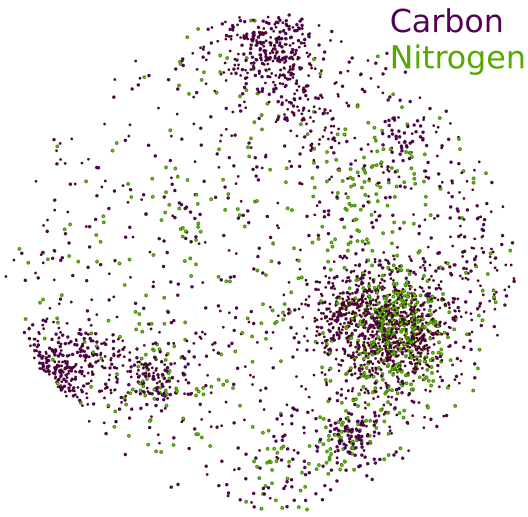

Figure 3.7.7 – X-Y slice showing apparent carbon and nitrogen segregation to the low-order poles of the matrix material. The 200 pole is in the lower right of the image, showing considerable N segregation. Experiment ID R14_16559.

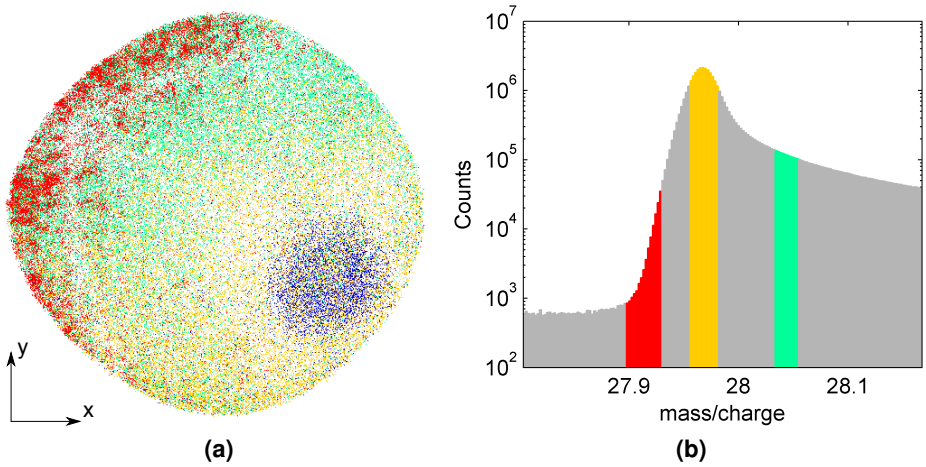

Figure 3.7.8 – (a) shows an X-Y slice atom map with $^{56}Fe^{2+}$ ions ranged as shown in (b) with $^{56}Fe^{+}$ ions shown in blue. The earliest ions to evaporate (red) originate from the edge which the laser impinges on (top-left). The majority of ions, $m/z = 27.97$, evaporate around the low-order 200 pole (lower-right). The later evaporating ions (cyan) are observed further from the pole. $^{56}Fe^{+}$ ions (blue) originate from the 200 pole suggesting it is a lower field region. ID: R14_16559.

is a lower field region. Comparatively, there are few ions evaporating early and the ions in the peak tail are generally evenly distributed spatially. Therefore, this should not have a significant influence on the analysis, but it does demonstrate the complex evaporation behaviour of the tip.

3.7.5 Composition

From the mass-to-charge spectrum, peaks must be identified as particular ions before chemical analysis or reconstruction. These ions can be atomic or molecular and take integer charge states. They are identified by their m/z and their isotopic abundance, or finger print. Currently there are no robust tools for peak identification, but the *weights tool*[*] was used to check for simple errors. A complete list of all possible ions, and their m/z value in Da, considered in this work is given in table 3.7.1. Note that some ions have very similar m/z values (<0.045 ΔDa), these ions are considered to be overlapped and are dealt with later in section 4.2.3. Identification of m/z peaks is not consistent between data sets because the evaporating ions are variable: Cr-containing alloys have Cr-containing ion species, but, for example, the Fe-$Y_{extruded}$ alloy contains some Cr-oxide impurities but not in every data set. Therefore, the ranging process is dependent on the microstructure and analysis volume.

An example mass spectrum is shown in figure 3.7.9 which shows the major peaks identified in a Fe-14Cr-Ti-Y ODS alloy. The peaks at 1, 2, 17 and 18 Da were identified as H or OH species present from the chamber and therefore are not counted in the composition for any dataset. The 16 Da peak has a low concentration in the matrix, and so may come from the chamber or the sample, but is strongly generated by the oxide particles and therefore is identified as $^{16}O^{+}$ (see discussion in section 4.2.4).

The ions which evaporate from the tip have well known masses and integer charge states, theoretically giving sharp lines in the m/z spectrum. Timing error in the detector electronics, evaporation uncertainty and delayed evaporation cause broadening of the time-of-flight (TOF) spectrum and the resulting m/z spectrum. This reduces the mass resolution, leading to overlaps, but also gives peak tails for sufficiency-intense peaks. As well as peak tails, there is also a constant noise level in the TOF spectrum which can be removed using a time-independent background subtraction. The whole area under each peak represents the total signal, but it is not often possible to range the whole peak because of the background or because of collisions with other peaks. Therefore, to quantify the composition, a repre-

[*]http://sourceforge.net/projects/apttools/files/extras/ see also [260]

m/z	Ion	m/z	Ion	m/z	Ion	m/z	Ion
6.0	$^{12}C^{2+}$	34.0	$^{56}Fe^{12}C^{2+}$	54.0	$^{54}Cr^{+}$	71.0	$^{71}Ga^{+}$
12.0	$^{12}C^{+}$	34.0	$^{54}Fe^{14}N^{2+}$	54.0	$^{54}Fe^{+}$	72.0	$^{56}Fe^{16}O^{+}$
14.0	$^{14}N^{+}$	34.5	$^{53}Cr^{16}O^{2+}$	55.0	$^{54}Fe^{1}H^{+}$	73.0	$^{57}Fe^{16}O^{+}$
14.0	$^{28}Si^{2+}$	34.5	$^{57}Fe^{12}C^{2+}$	55.0	$^{55}Mn^{+}$	78.0	$^{46}Ti^{16}O_2^{+}$
14.5	$^{29}Si^{2+}$	34.5	$^{69}Ga^{2+}$	56.0	$^{56}Fe^{+}$	79.0	$^{47}Ti^{16}O_2^{+}$
15.0	$^{30}Si^{2+}$	35.0	$^{54}Cr^{16}O^{2+}$	57.0	$^{57}Fe^{+}$	80.0	$^{48}Ti^{16}O_2^{+}$
16.0	$^{16}O^{+}$	35.0	$^{56}Fe^{14}N^{2+}$	57.0	$^{56}Fe^{1}H^{+}$	81.0	$^{49}Ti^{16}O_2^{+}$
20.0	$^{40}Ar^{2+}$	35.0	$^{54}Fe^{16}O^{2+}$	58.0	$^{57}Fe^{1}H^{+}$	82.0	$^{50}Cr^{16}O_2^{+}$
23.0	$^{46}Ti^{2+}$	35.0	$^{89}Y^{16}O^{3+}$	59.0	$^{50}Cr^{52}Cr^{16}O^{2+}$	82.0	$^{50}Ti^{16}O_2^{+}$
23.5	$^{47}Ti^{2+}$	35.5	$^{57}Fe^{14}N^{2+}$	60.0	$^{52}Cr^{52}Cr^{16}O^{2+}$	84.0	$^{52}Cr^{16}O_2^{+}$
24.0	$^{12}C_2^{+}$	35.5	$^{71}Ga^{2+}$	60.5	$^{52}Cr^{53}Cr^{16}O^{2+}$	85.0	$^{53}Cr^{16}O_2^{+}$
24.0	$^{48}Ti^{2+}$	36.0	$^{12}C_3^{+}$	60.5	$^{89}Y^{16}O_2^{2+}$	86.0	$^{54}Cr^{16}O_2^{+}$
24.5	$^{49}Ti^{2+}$	36.0	$^{56}Fe^{16}O^{2+}$	60.7	$^{182}W^{3+}$	86.0	$^{54}Fe^{16}O_2^{+}$
25.0	$^{50}Cr^{2+}$	36.5	$^{57}Fe^{16}O^{2+}$	61.0	$^{183}W^{3+}$	88.0	$^{56}Fe^{16}O_2^{+}$
25.0	$^{50}Ti^{2+}$	39.0	$^{54}Fe^{12}C_2^{2+}$	61.3	$^{184}W^{3+}$	89.0	$^{57}Fe^{16}O_2^{+}$
26.0	$^{12}C^{14}N^{+}$	39.0	$^{46}Ti^{16}O_2^{2+}$	62.0	$^{46}Ti^{16}O^{+}$	91.0	$^{182}W^{2+}$
26.0	$^{52}Cr^{2+}$	39.5	$^{47}Ti^{16}O_2^{2+}$	62.0	$^{186}W^{3+}$	91.5	$^{183}W^{2+}$
26.5	$^{53}Cr^{2+}$	40.0	$^{40}Ar^{+}$	63.0	$^{54}Fe^{56}Fe^{16}O^{2+}$	92.0	$^{184}W^{2+}$
27.0	$^{54}Cr^{2+}$	40.0	$^{56}Fe^{12}C_2^{2+}$	63.0	$^{47}Ti^{16}O^{+}$	93.0	$^{186}W^{2+}$
27.0	$^{54}Fe^{2+}$	40.0	$^{48}Ti^{16}O_2^{2+}$	64.0	$^{50}Cr^{14}N^{+}$	98.0	$^{50}Cr^{16}O_3^{+}$
27.5	$^{55}Mn^{2+}$	40.5	$^{57}Fe^{12}C_2^{2+}$	64.0	$^{56}Fe^{56}Fe^{16}O^{2+}$	98.0	$^{182}W^{14}N^{2+}$
28.0	$^{56}Fe^{2+}$	40.5	$^{49}Ti^{16}O_2^{2+}$	64.0	$^{48}Ti^{16}O^{+}$	98.5	$^{183}W^{14}N^{2+}$
28.0	$^{28}Si^{+}$	41.0	$^{50}Cr^{16}O_2^{2+}$	64.5	$^{56}Fe^{57}Fe^{16}O^{2+}$	99.0	$^{184}W^{14}N^{2+}$
28.5	$^{57}Fe^{2+}$	41.0	$^{50}Ti^{16}O_2^{2+}$	65.0	$^{49}Ti^{16}O^{+}$	100.0	$^{52}Cr^{16}O_3^{+}$
29.0	$^{29}Si^{+}$	42.0	$^{52}Cr^{16}O_2^{2+}$	66.0	$^{52}Cr^{14}N^{+}$	100.0	$^{186}W^{14}N^{2+}$
29.7	$^{89}Y^{3+}$	42.5	$^{53}Cr^{16}O_2^{2+}$	66.0	$^{50}Cr^{16}O^{+}$	101.0	$^{53}Cr^{16}O_3^{+}$
30.0	$^{30}Si^{+}$	43.0	$^{54}Cr^{16}O_2^{2+}$	66.0	$^{54}Fe^{12}C^{+}$	102.0	$^{54}Cr^{16}O_3^{+}$
31.0	$^{46}Ti^{16}O^{2+}$	43.0	$^{54}Fe^{16}O_2^{2+}$	66.0	$^{50}Ti^{16}O^{+}$	105.0	$^{89}Y^{16}O^{+}$
31.5	$^{47}Ti^{16}O^{2+}$	44.0	$^{56}Fe^{16}O_2^{2+}$	67.0	$^{53}Cr^{14}N^{+}$	107.0	$^{182}W^{16}O_2^{2+}$
32.0	$^{50}Cr^{14}N^{2+}$	44.5	$^{57}Fe^{16}O_2^{2+}$	68.0	$^{54}Cr^{14}N^{+}$	107.5	$^{183}W^{16}O_2^{2+}$
32.0	$^{16}O_2^{+}$	44.5	$^{89}Y^{2+}$	68.0	$^{52}Cr^{16}O^{+}$	108.0	$^{184}W^{16}O_2^{2+}$
32.0	$^{48}Ti^{16}O^{2+}$	45.5	$^{182}W^{4+}$	68.0	$^{56}Fe^{12}C^{+}$	109.0	$^{186}W^{16}O_2^{2+}$
32.5	$^{49}Ti^{16}O^{2+}$	45.8	$^{183}W^{4+}$	68.0	$^{54}Fe^{14}N^{+}$	121.0	$^{89}Y^{16}O_2^{+}$
33.0	$^{52}Cr^{14}N^{2+}$	46.0	$^{184}W^{4+}$	69.0	$^{53}Cr^{16}O^{+}$	214.0	$^{182}W^{16}O_2^{+}$
33.0	$^{50}Cr^{16}O^{2+}$	46.5	$^{186}W^{4+}$	69.0	$^{57}Fe^{12}C^{+}$	215.0	$^{183}W^{16}O_2^{+}$
33.0	$^{54}Fe^{12}C^{2+}$	48.0	$^{12}C_4^{+}$	69.0	$^{69}Ga^{+}$	216.0	$^{184}W^{16}O_2^{+}$
33.0	$^{50}Ti^{16}O^{2+}$	50.0	$^{50}Cr^{+}$	70.0	$^{54}Cr^{16}O^{+}$	218.0	$^{186}W^{16}O_2^{+}$
33.5	$^{53}Cr^{14}N^{2+}$	52.0	$^{52}Cr^{+}$	70.0	$^{56}Fe^{14}N^{+}$	230.0	$^{182}W^{16}O_3^{+}$
34.0	$^{54}Cr^{14}N^{2+}$	52.5	$^{89}Y^{16}O^{2+}$	70.0	$^{54}Fe^{16}O^{+}$	231.0	$^{183}W^{16}O_3^{+}$
34.0	$^{52}Cr^{16}O^{2+}$	53.0	$^{53}Cr^{+}$	71.0	$^{57}Fe^{14}N^{+}$	232.0	$^{184}W^{16}O_3^{+}$
						234.0	$^{186}W^{16}O_3^{+}$

Table 3.7.1 – Potential ions from APT analysis of an Fe-Cr-Ti-Y_2O_3 alloy, showing mass number and charge state, with their mass-to-charge (m/z) ratios in Da. This table was produced using the *isotopeList.m* script.

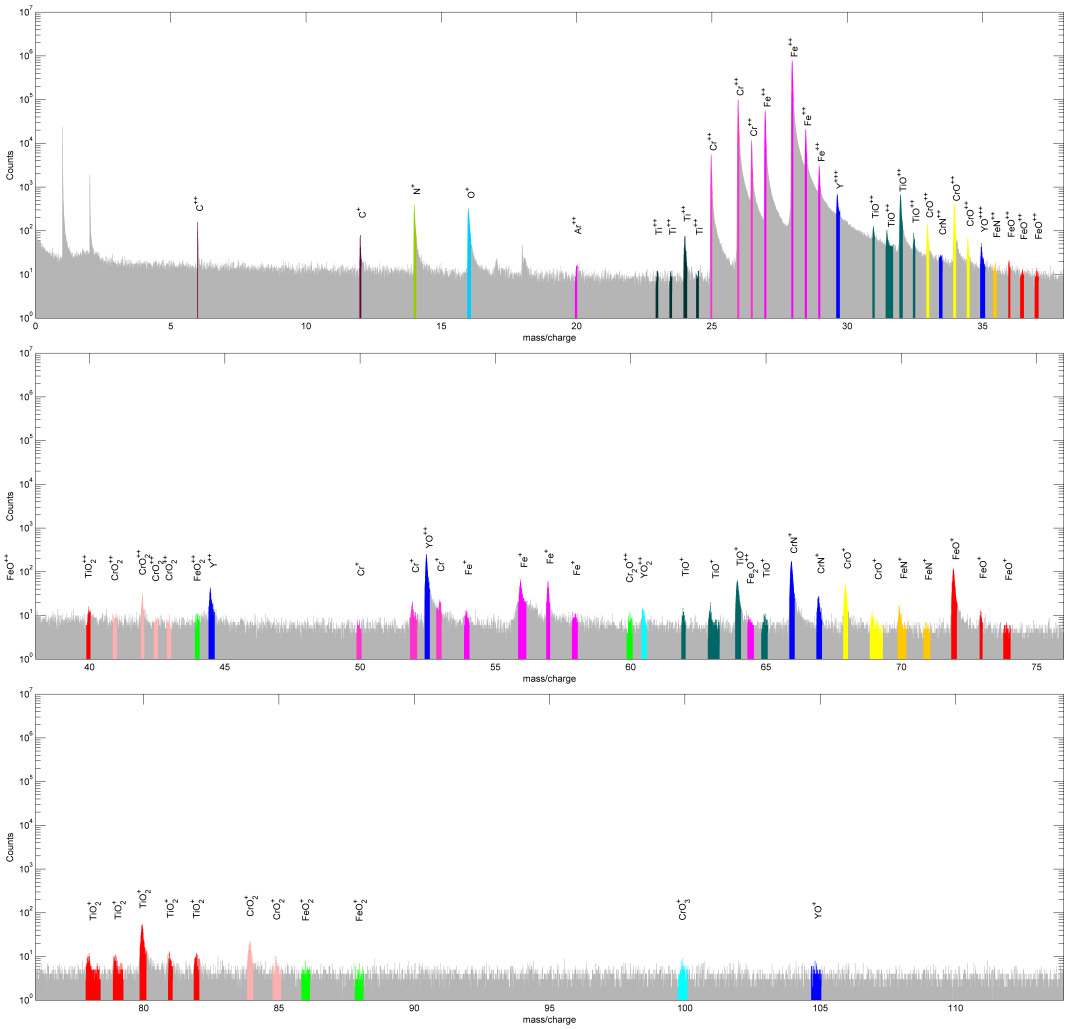

Figure 3.7.9 – Example mass-to-charge spectrum from reconstruction ID R14_15868. Ions are labelled above the coloured ranges. The counts are shown with a logarithmic scale which emphasises the peak broadening. Ranges shown are approximately full-width one-tenth maximum. All possible ranges are shown, even if no peak is present in this data set.

sentative proportion of each peak's area must be selected. This means the range width is a function of peak shape and peak intensity. Wider ranges must be used for broader peaks and narrower ranges for less intense peaks so to capture the same fraction of peak area. This systematic approach to mass-peak ranging is detailed in section 4.2.1.

The mass resolution of the main $^{56}Fe^{2+}$ peak at 28 Da has a $\frac{m}{\Delta m}$ of 500-1000 at full-width half maximum and signal:noise ratio of better than 10^3. Even so, with this mass resolution, it is not possible to resolve some overlapping species. Composition error is greatest when

peaks are misidentified [260]; thus where overlapping peaks are encountered the overlaps must be resolved. Major overlaps existed at 24 Da, $C_2^+/^{48}Ti^{2+}$, 32 Da, $O_2^+/^{48}TiO^{2+}$ and 64 Da $^{56}Fe_2O^{2+}/^{48}Ti^{16}O^+$. To some extent, these overlaps are spatially segregated and, using the expected isotopic abundances, they can be deconvoluted. The current implementation in IVAS only allows for a single range file for each pos file; therefore the ranging and composition analysis of the oxide clusters has been extended to include variation of overlaps between *different* clusters, as detailed in section 4.2.3.

3.7.6 Visualisation

The result of an APT experiment, after reconstruction, is a list of 3D positions and a list of mass-to-charge ratios; four pieces of information per ion, which are stored in a *pos* file (see Chapter A for specification). This data can be extended with the additional information available in the extended-*pos* (*epos*) file, defined in Chapter A, including the raw time-of-flight value in ns, the detector hit coordinates and the pulse number. Fundamentally, APT data is *point-cloud* data; visualisation and analysis are made of this point cloud using its positions and properties. The implication is that primarily analysis is made based on either the density (positions) or the concentration (ionic identities). For example, atom maps and the maximum separation clustering algorithm are density-based analyses and line profiles and concentration maps are concentration-based analyses. Therefore, one must be aware of the difference between these different techniques and note that a high density *does not* equal high concentration (a common problem at phase boundaries) and vice versa.

3.7.6.1 Atom maps

Atom maps, or more correctly, ion maps (as molecular ionic species may be detected), show point cloud data using the 3D position of detected ions with their ionic identity distinguished by different colours. This data is often rendered with points or spheres as a 2D projection to highlight specific microstructural features. Throughout this thesis, a consistent colour scheme is used and a colour key will accompany relevant figures.

3.7.6.2 1D and 2D profiles

1D line profiles or 2D maps are used to show the spatial dependence of concentration or ionic density. Most of the line profiles and concentration maps have been generated using the IVAS software, with the major exception of the average concentration line profiles detailed in section 4.5.1. IVAS uses voxelisation (binning the data into cuboid regions of space) of the point-cloud data to calculate the 2D analyses, see [261] for details. 3x3x3 nm voxels with a uniform 1.5 nm delocalisation were used for producing 3D concentration iso-surfaces, unless otherwise specified.

1D concentration profiles were produced using cylindrical or square cross-section regions of interest (ROIs) in IVAS. 2D concentration and density profiles were produced using IVAS on cuboid ROIs, so they show a distribution of ions as a slice through clusters—useful for showing the influence of trajectory aberrations. The size and shape of the ROIs varies with the feature being investigated and is given where necessary.

3.7.6.3 Proximity histograms

The proximity histogram, or "proxygram", is the geometric generalisation of a line profile taken perpendicular to a surface [262], such that the concentration profile is plotted verses its *proximity* to an interface. These plots are useful for investigating larger compositional features which can be easily described by an iso-concentration surface, and show the chemistry of both sides and the interface region. As the proximity histogram is averaged over the whole surface, the implicit assumption is that the composition change is the same over the whole surface (isotropic). In the case of smaller oxide clusters, this is not valid due to the trajectory aberrations caused by the varied tip shape as the clusters evaporate (for details, see section 3.7.4), making the application of proximity histograms to these features difficult. All proxygrams have been created using IVAS 3.6.6 and details of the iso-concentration surface that produced them are given with each proxygram.

3.7.7 Clustering

Visual inspection of the data confirmed that there were clustered ion species. In these alloys, the clusters are concentrated in solute and there is a low solute content in the matrix. The following terminology is used: cluster and matrix to distinguish between clustered ions and the surrounding non-clustered ions; clustering species are called solute. The point-cloud data can be split into solute and matrix ions of interest, with the solute further separated into clustered and non-clustered ions. Different cluster detection methodologies differ on the definition of the clustered ions using either the relative position of solute ions [263], their concentration [246, 264] or nearest neighbour distance [265]. Rather than a parameterised selection, it is also possible to use entropy, information theory or maximum likelihood estimation to define the clusters with little parameterisation [266], but these methods have only been recently applied to APT data. Therefore, in this work, the method of Maximum Separation of core ions is used to define the clusters. This method has a well established history and application to ODS alloys [132, 263, 267, 268], as well as automated tools for calculating the cluster statistics (size, shape, composition etc.). The maximum separation method was applied to the data sets using both the IVAS and posgen implementations. IVAS is slower to use but the calculations are faster, but a number of features are missing; therefore, the command-line driven posgen program was used for more complicated analysis coupled with MATLAB. For a specific list of programs and scripts I wrote and used, see section §A.5.

3.7.8 The Maximum Separation Method

The Maximum Separation method for cluster finding works on the assumption that solute ions that are clustered are closer together than solute ions that are not clustered. Strictly the algorithm defined below is core-linkage, but I retain the term maximum separation (core-linkage when $k = 1$) to be congruent with the IVAS nomenclature. It uses a number of parameters to define the clusters and filter the results:

- D_{max} the maximum separation of ions that defines which solute ions are *core ions*. This defines how sensitive the method is; a larger D_{max} will return a greater number of clusters with a larger measured size. Because D_{max} depends on the solute concentration of the data set, a D_{max} was selected separately for each analysis volume, with a range 0.5–1.5 nm; a full list is given in appendix A.6.

- *Order* parameter k, the minimum number of ions within D_{max} of this ion for it to count as clustered [269]. This parameter was used to select only the very centre of the clusters, as ions near the edge have fewer solute neighbours.

- The standard algorithm only selects solute ions, but the *includes* or *envelope* distance L includes non-solute ions, within a distance L of core ions, into that cluster. Only the ions that strongly partition to the clusters and have a low background concentration (Y,YO and TiO ions) are used to define the clusters. To include other ions (CrO, Fe_2O, O etc.) and because Fe and Cr are excluded from most of the composition analysis of the clusters, L is set to D_{max} to include as many additional ions as possible.

- E_r the erosion distance from around the periphery of defined clusters, to exclude matrix ions being included around the edge. Again, because Fe and Cr are normally excluded from the cluster composition, $E = 0$ so that no erosion occurs.

- N_{min} the minimum number of core ions to constituent a cluster. Even in a random solution, statistically some solute ions may be close enough to be considered clustered, but these clusters can be excluded by setting an N_{min} value.

The most important steps in defining the clusters,D_{max}, N_{min} and L are illustrated in figures 3.7.10 a, b and c respectively. Figure 3.7.12 shows the selection of a cluster from real data (a) and the result of various cluster selection parameters, (c) includes distance L, (e) erosion distance E_r and (g) order k.

During the application of this method, it is common to compare the clusters found in the data set after randomly relabelling the ion identities, these are called *background* or *random*

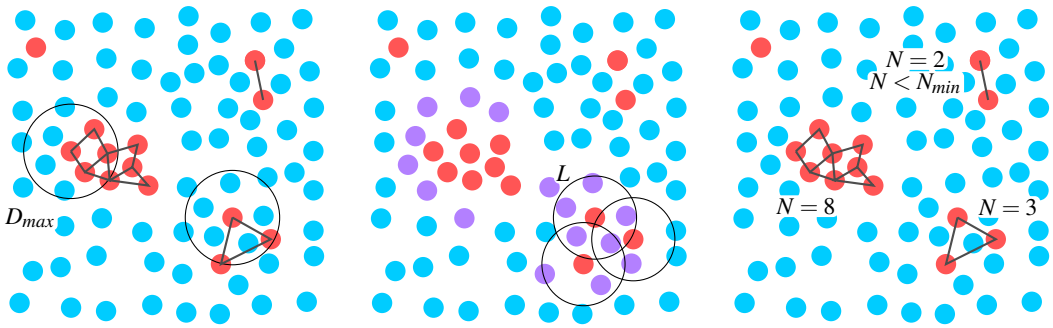

(a) Cores linked using D_{max} **(b)** Non-core ions included by L distance **(c)** Clusters filtered by N_{min}

Figure 3.7.10 – Important steps of the maximum separation algorithm.

clusters. Even in a random solution, a suitably sensitive D_{max} search will identify apparent clusters due to statistical variations. Figure 3.7.11 shows a histogram of cluster sizes with several different D_{max} values in a randomised data set (whole) and the same data set with the most obvious clusters removed and then randomised (matrix). The randomisation step is re-run 20 times because the number of large detected clusters is low (poor counting statistics); this is only possible using posgen and not with IVAS at the current time. The whole data has a much higher solute concentration, meaning that more random clusters are identified than in the matrix data. With increasing D_{max}, more numerous and larger random clusters are detected, as expected. Therefore, for each data set, this random relabelling was performed to determine the N_{min} required to exclude random clusters so that the data contained at most 1% random clusters; see [268] for details. One improvement I would recommend to the method given in [268] would be to perform multiple random trials (c.f. figure 3.7.11) to improve the reliability, but this is computationally expensive and has not been used here. In addition to the variables defined above, a minimum solute fraction c_{min} can be used to filter the cluster results and help exclude random clusters [270].

The order parameter limits the clustering to only those ions with at least k nearest neighbours. This effect is shown in figure 3.7.12(g) with $k = 25$. Unlike erosion, which does not remove solute ions, k will remove solute ions on the periphery of the cluster and reduce the measured cluster radius.

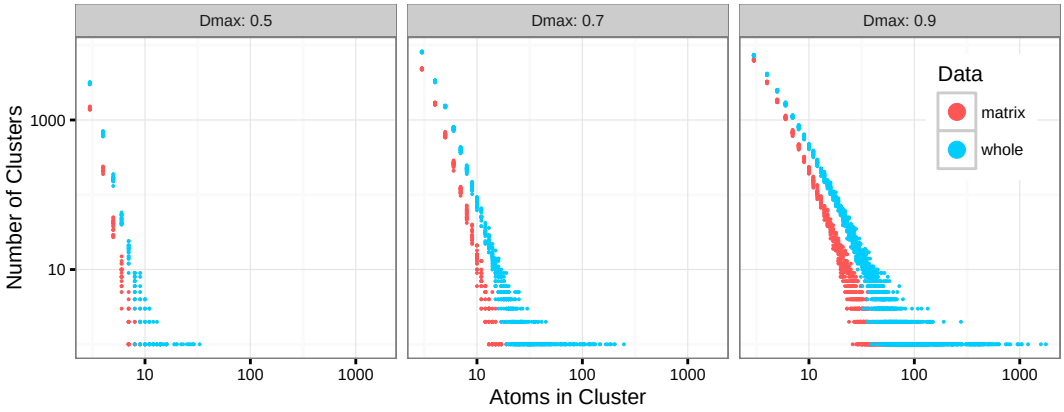

Figure 3.7.11 – Clusters found, using three increasingly sensitive values of D_{max}, in two data sets: randomised data set (whole) and same data set with the most obvious clusters removed and then randomised (matrix). The randomisation was repeated 20 times in each.

3.7.8.1 Parameter Selection

The maximum separation algorithm is a parameter-based method and the selection of these parameters strongly affects the results. This sub-section outlines the parameter selection process and its effects on the cluster measurements. The clusters are defined iteratively, first with a cluster count distribution and then N_{min} is adjusted; these steps are followed by visual inspection of the resulting indexed cluster pos file.

A cluster count distribution is shown in figure 3.7.13a, which is the result of many individual maximum separation searches to give the number of detected clusters as a function of D_{max}. In the ODS data sets in this work, the cluster count distribution contains three stages:

1. Rapid increase in the number of detected clusters, as high-density regions of solute are split into many smaller clusters.

2. Steady number of clusters as D_{max} increases. Either the detected clusters are invariant of D_{max} or as many new clusters are detected as old ones are joined together.

3. A second increase of the number of clusters as solute in the matrix is detected as clusters.

Ideally, D_{max} is chosen in the range of stage two, where the number of clusters is not strongly

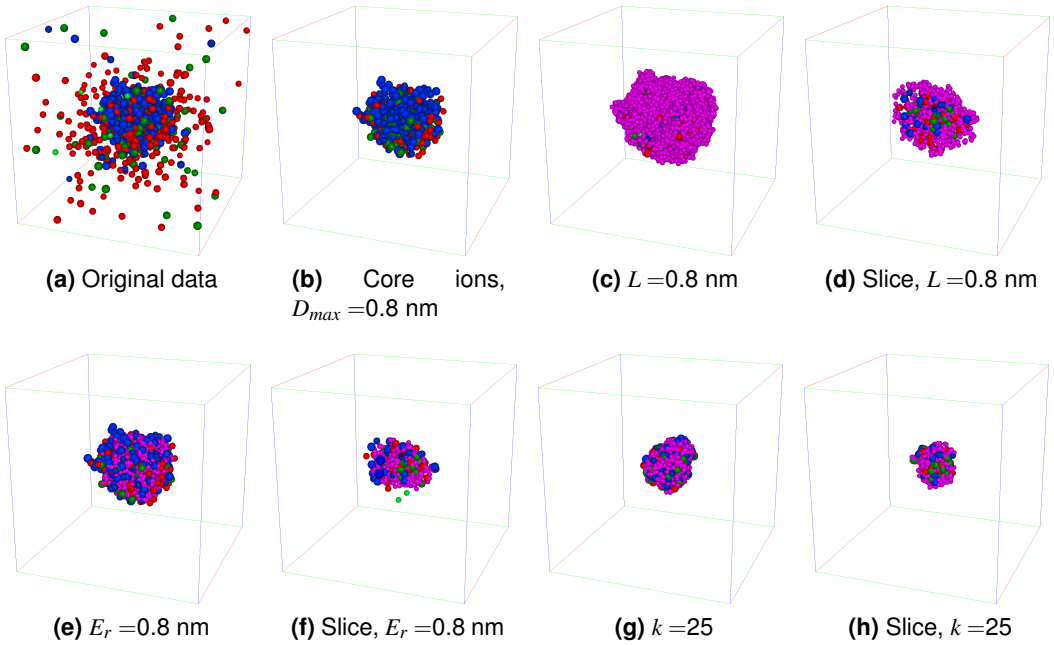

(a) Original data **(b)** Core ions, D_{max} =0.8 nm **(c)** L =0.8 nm **(d)** Slice, L =0.8 nm

(e) E_r =0.8 nm **(f)** Slice, E_r =0.8 nm **(g)** k =25 **(h)** Slice, k =25

Figure 3.7.12 – The results of different parameters when cluster searching using the maximum separation method. All figures: Yttrium, Titanium, Oxygen and Iron containing ions are blue, green, red and magenta respectively; D_{max} = 0.8 nm. (c-h) includes distance set to 0.8 nm. (d, f, h) show a 0.5 nm thick slice through the middle of the cluster to show its core. The volume is 15x15x15 nm^3 in each image.

dependent on D_{max}. In figure 3.7.13a this corresponds to D_{max} =0.65–0.75 nm for this data set. The actual D_{max} depends on the solute concentration and the mass spectrum quality. Long thermal tails may necessitate less sensitive parameters, and in the worst case certain ions can be excluded from the cluster selection; for example, O^+ is rarely used to define the clusters as it has a relatively high matrix concentration and it spreads laterally from the clusters.

Next, the value of N_{min} is optimized using a cluster size-distribution analysis (such as those shown in figure 3.7.11) with D_{max} equal to the "plateau" region identified previously. The size-distribution analysis is compared between the real data and the randomly relabelled data set to find the value of N_{min} that minimises the number of random clusters detected. Relabelling the whole data set, rather than removing obvious clusters first, provides a conservative value N_{min}. The first two steps can be repeated to converge on acceptable trial values of D_{max} and N_{min}.

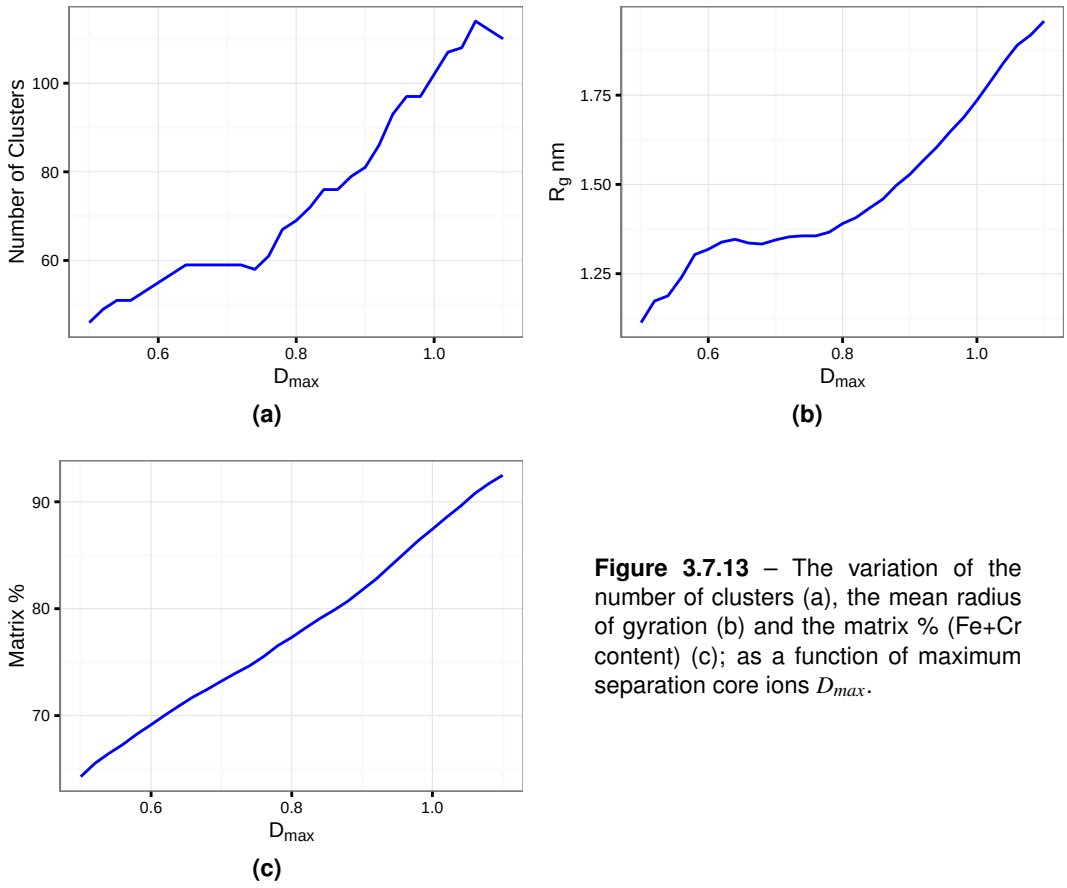

Figure 3.7.13 – The variation of the number of clusters (a), the mean radius of gyration (b) and the matrix % (Fe+Cr content) (c); as a function of maximum separation core ions D_{max}.

The includes distance L is set equal to D_{max} to include the greatest number of ions into the clusters whilst avoiding different clusters claiming the same ion (if $L > D_{max}$). In this work, the erosion distance was set to zero and order to one. Because most of the analysis of the cluster composition ignores ions with the same composition as the matrix, there is no effect on the Y, Ti and O measurements by including additional matrix in the periphery of the clusters. For one cluster, the Y, Ti and O content each had a standard deviation of <0.2% over the D_{max} range 0.5–1.1. On the other hand, figure 3.7.13c confirms that the mean matrix content (Fe+Cr ions) of the clusters increases monotonically with D_{max}. Figure 3.7.13b shows that the mean radius of the clusters, as a function of D_{max}, is also stable in stage 2. For an individual cluster, the radius increases monotonically with D_{max} until stage 3, when additional solute ions far from the cluster start to be included into the cluster (stage 3).

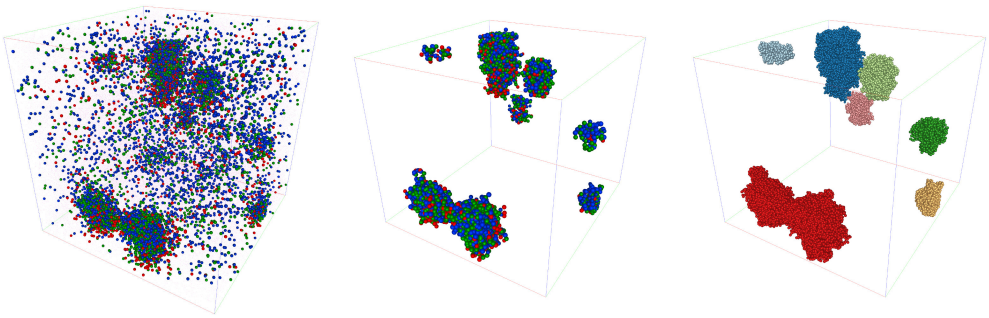

(a) Original data **(b)** Cluster data **(c)** Indexed cluster data

Figure 3.7.14 – The output files resulting from a cluster search. The solute ions are shown as spheres in (a,b) and all the cluster ions are shown in (c). Each image has a dimension of 30x30x30 nm.

The result of a cluster analysis in IVAS is a cluster statistics spreadsheet containing the position information, size descriptors and composition of each cluster; and optionally a family of pos files can be exported:

cluster.solute.pos Contains only solute ions which have been identified as being clustered.

cluster.pos All the ions which have been identified as being clustered. If $L > 0$, then this will include solvent as well as solute ions.

matrix.pos The complement to cluster.pos, containing all the remaining ions from the original data.

cluster.indexed.pos Contains the same ions as the cluster.pos file but with ionic masses assigned to the cluster ID number instead of their mass-to-charge ratio. Accompanying this file is a cluster.indexed.rrng file which has a range and colour for each cluster ID.

The cluster statistics and exported files are the start of the MATLAB work flow, detailed in the next chapter, through which the results are processed. Example original data, cluster data and indexed cluster data are shown in figure 3.7.14.

The cluster.indexed.pos file is viewed side by side with the original data so that the result of the cluster search can be evaluated by eye. Without the use of an objective metric, such as that used in principal component analysis or maximising the information content, adjusting

the maximum separation parameters until the cluster search returns a "good looking" result is the best compromise.

3.7.9 Cluster Measurements

3.7.9.1 Morphology

Cluster measurements can be made using different ions: solute ions, all ranged ions or all ions including un-identified ions. In this work, the solute bias is used to make the cluster position and morphology measurements. The spatial basis can also be changed so that it matches the principal axes of the cluster being measured.

The centre of a cluster is defined by the centre of mass:

$$\mathbf{p_{COM}} = \frac{\sum_{i=1}^{N} m_i \mathbf{p_i}(x_i, y_i, z_i)}{\sum_{i=1}^{N} m_i}$$

where m_i and $\mathbf{p_i}$ are the mass and coordinates of the ions in a cluster which contains N ions. The radius of gyration is frequently used to report the cluster size and it can be calculated for each of the coordinate axes [271]:

$$l_x = \sqrt{\frac{\sum_{i=1}^{N} m_i (x_{COM} - x_i)^2}{\sum_{i=1}^{N} m_i}}$$

The radius of gyration of the cluster is then given by:

$$l_g = \sqrt{l_x^2 + l_y^2 + l_z^2}$$

for a sphere of a uniform density of points with a maximum radius of r; then the radius of gyration is:

$$l_g = \sqrt{\frac{3}{5}} r$$

Therefore l_g underestimates the hard-sphere radius by 23%, and l_x underestimates the radius by 55%.

A more direct measurement of the cluster radius is given by the extent measurement E (subscript for the specific axis of interest), which in IVAS is defined as:

$$E_x = \text{larger of} \begin{cases} \bar{x} - \min(x) \\ \max(x) - \bar{x} \end{cases} \tag{3.7.3}$$

A more intuitive definition would be to use the range:

$$Range_x = \frac{\max(x) - \min(x)}{2}$$

The average extent measurement of cluster size is:

$$E = \frac{E_x + E_y + E_z}{3}$$

A discussion of suitability of each of these size measurements is given in section 4.5.3 on page 103.

3.7.9.2 Composition

Identification of ion species from the mass-to-charge spectrum and ranging are covered in detail in section 3.7.5 and issues relating to systematic ranging and resolving peak overlaps are dealt with in section 4.2 on page 85. This section covers the composition calculation and accompanying statistical analysis of the identified ions.

Standard definition of composition of a component A is given by the number of A atoms n_A divided by the total number of atoms analysed N:

$$C_A = \frac{n_A}{N}$$

The standard error of this composition measurement, from counting statistics alone, is given by the square root of the variation of a binomial distribution:

$$\sigma_A = \pm\sqrt{\frac{C_A(1-C_A)}{n_A}}$$

The Fe content of the clusters needs to be considered carefully as it results from the evaporation behaviour of the clusters and the limitations of the reconstruction protocol (trajectory aberrations), as well as from the cluster selection. The evaporation behaviour is discussed in detail in section 4.5.2.2 on page 100, but the influence of the cluster selection is considered briefly here. The variation of composition with D_{max} is shown in figure 3.7.15. As D_{max} increases, the amount of Fe included in the clusters increases; no erosion was applied to this data. This is as expected when considering a single solute ion surrounded by matrix; as D_{max} increases, the total volume of the cluster increases but the solute count remains constant. Making the assumption that the Fe is erroneously included in the cluster (by the cluster selection and the evaporation artefacts) and removing it is called a *matrix correction* [155]. In the chromium-containing materials, for every Fe ion detected in the particle, it is equally likely that a proportional amount of chromium (e.g. 13 at% of the matrix ions) would also be incorporated to the particle erroneously. Cr may be present both in the original cluster and by trajectory aberrations; therefore the number of Fe atoms detected in the cluster Fe_c is used to find the *matrix-corrected* Cr composition [155]:

$$Cr_c^* = Cr_c - \frac{Cr_m}{Fe_m}.Fe_c \tag{3.7.4}$$

where Cr_c^* is the corrected Cr cluster counts, Cr_c are the original Cr cluster counts and Cr_m and Fe_m are the matrix Cr and Fe counts respectively. Ignoring the Fe counts, the corrected cluster composition is calculated using the Cr_c^* counts with the counts of yttrium, titanium and oxygen. The concentration of elements other than Cr in the matrix is assumed to be zero.

The identification of the mass peaks in the mass-to-charge ratio spectrum is not unique and contains overlapping peaks; this behaviour is dealt with in the following chapter (4.2.3).

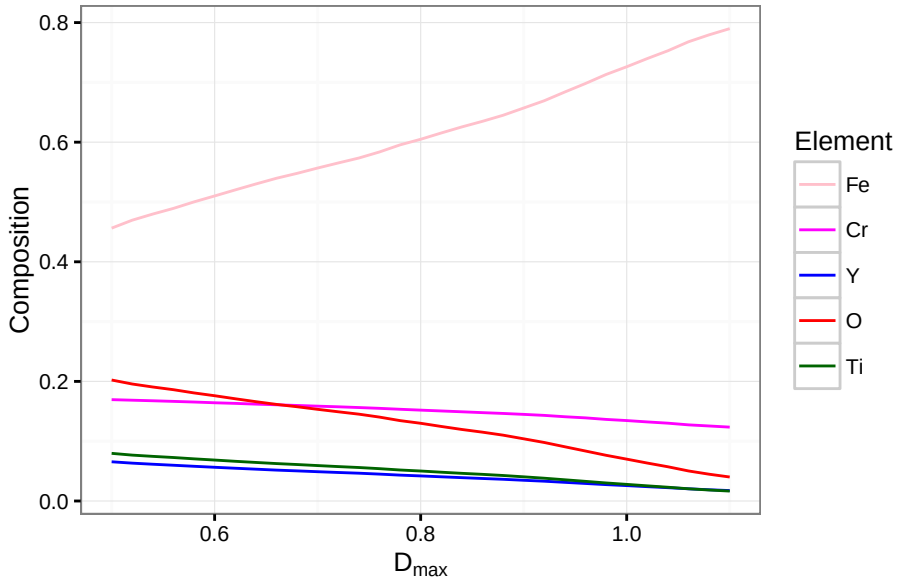

(a) Cluster composition

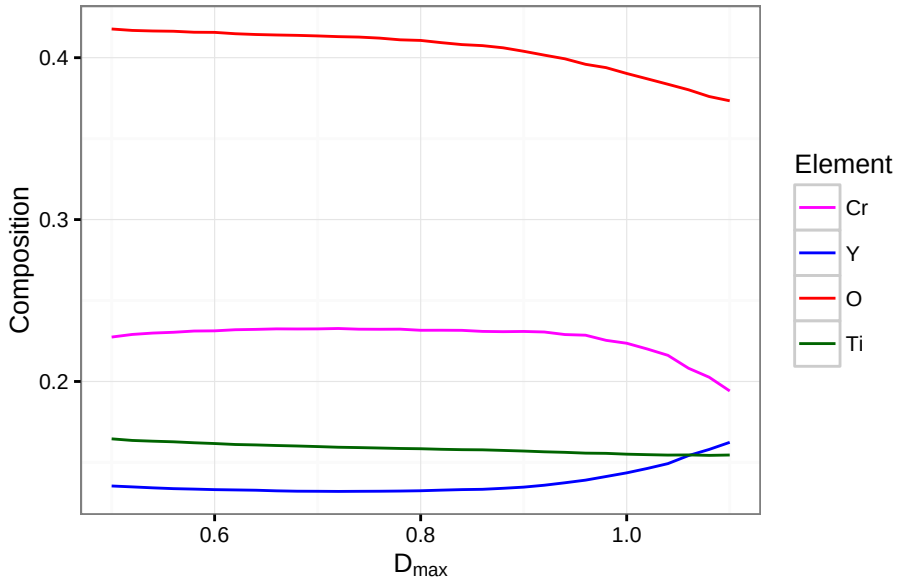

(b) Matrix corrected

Figure 3.7.15 – Comparison of the variation of the mean cluster composition as a function of D_{max} with (a) all ions and (b) with Fe ions removed with a proportional amount of Cr. In the matrix-corrected composition (b) A value of Cr > 0 means an enhanced concentration compared to the Cr concentration in the bulk.

Chapter 4

APT Analysis Techniques

4.1 Introduction

The quantification of the character of the oxide particles in the oxide dispersion strengthened alloys described in Chapter 3 by atom probe tomography (APT) has presented a number of challenges. This chapter details what I have done to extend the conventional analysis described in sections 3.7.5 and 3.7.9, specifically regarding measurements of the cluster composition, local chemistry and cluster size.

First, the composition measurement protocol was improved by systematic analysis of the mass spectrum. By fitting the peaks in the mass spectrum, a specific and consistent fraction of the peak area can be captured. Where mass peaks of different ions overlap, a deconvolution has been applied. The composition of the oxide clusters can vary significantly, but existing software can only apply the deconvolution globally. Therefore I have applied this peak deconvolution to each individual cluster. For deconvoluting the peak overlaps, the maximum likelihood method was slower but yielded smaller errors than the least-squares approach.

APT relies on the evaporation of the atoms from the sample and so the results must be understood in light of the different evaporation behaviour of different phases. The trajectory aberrations resulting from the different evaporation behaviour of the oxides is discussed and

I present a pragmatic way forward to examine the cluster chemistry using line profiles and to measure the cluster size.

Last, I introduce a method to measure spatial inhomogeneity and discuss how this can be applied to APT data. The heterogeneity of the material could be as equally important as the particle size, number density and chemistry in determining the materials' properties.

4.2 Composition

As described in section 3.7.5, there are two key areas which need addressing: ranging methodology and resolving peak overlaps. As well as describing my solutions to these issues, this section also details the processing of the mass spectrum and includes a discussion of the quantification of oxide compositions by atom probe tomography.

4.2.1 Systematic ranging

Ionic identities are determined by ranges of m/z values and these ranges are initially defined by hand per experiment. It is not always possible to consistently range the whole peak; therefore a representative and proportional area from each peak should be ranged. Initially full-width at half maximum height is used because peak shape, width and height vary from peak to peak and between experiments. The initial ranging and identification of ions is described in section 3.7.5.

Hudson et al. showed that the FWf(x)M systematic approach to ranging resulted in a reduction in the variation of composition measurements between data sets [272]. To follow this approach here, a systematic ranging approach has been implemented using a custom MATLAB program to refine the range definitions (*rangeCorrector.m*). Mass peaks are fitted to an exponentially modified Gaussian function (EMG) [273], shown in equation 4.2.1, to give a smooth peak shape and the full width at 20% maximum peak height (FW0.2M) was defined following the initial ranging. This value of FW0.2M was chosen to maximise the peak area measured but avoid range overlap due to the narrow separation of some peaks.

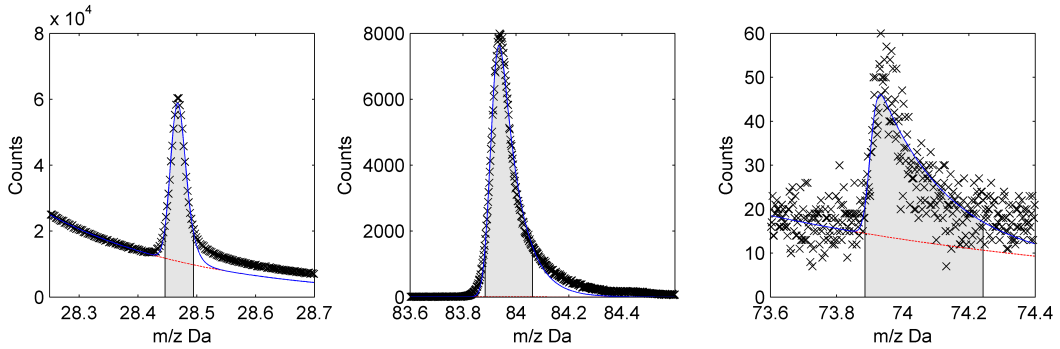

Figure 4.2.1 – Example peak fitting in the mass-to-charge spectrum of large, medium and small peaks (left to right respectively). The experimental data is shown by black x, fitted background with a red-dashed line, the fitted peak with a solid blue line and the full-width 20% maximum range is shaded in grey.

This new MATLAB program is highly customisable with respect to the level of FWf(x)M required, definition of peaks and fitting parameters.

Outline of the *rangeCorrector.m* program:

1. Approximate the peak centre, assuming a local maximum.

2. The region before the peak, "pre-noise", has a background fitted using an exponential decay in the square root of m/z space (TOF-like), see *noiseFit.m*. This fitting function was a good compromise between complexity and robustness. If the fitting function returns an error, then a simple mean of the pre-noise region is used.

3. Fit the peak using the exponentially modified Gaussian (EMG) function:

$$y = A.\frac{|\lambda|}{2}\left[1-\text{erf}\left(\frac{(x_g-x)\lambda}{\sigma_g|\lambda|\sqrt{2}}+\frac{\sigma_g}{|\lambda|\sqrt{2}}\right)\right].\exp\left(\frac{x_g-x}{\lambda}+\frac{\sigma_g^2}{2\lambda^2}\right) \qquad (4.2.1)$$

   where A is the amplitude, λ is the asymmetry value, x_g is the Gaussian centre, σ_g is the Gaussian width and erf denotes the error function.

4. The FWf(x)M points are found using the *fwhm.m* function.

5. The results written to a new rrng style range file.

The fitting results of three peaks of various sizes and with varied backgrounds are shown in figure 4.2.1. The peak-tails in this data set are not very well described by the EMG

function. In these materials, in general, the full-width 20% maximum (FW0.2M) lies above the long tail of the peak. For one example data set, FW0.2M ranges captured $88 \pm 3\%$ of the fitted peak area. Without prior knowledge of the exact peak shape, which varies between different ions and experimental conditions, it is not possible to measure how much FW0.2M truly captures of the peak area. The value above shows the upper bound of the peak area captured because the EMG function does not fit broad tails well.

4.2.2 Background correction

If the evaporation is thermally activated by a laser pulse, then the peak tail can be described by the heat transfer from the tip. Therefore, Vella et al. [274] modelled the background using a 1D heat diffusion equation:

$$T(t) = T_0 + \frac{T_{rise}}{\sqrt{1 + \frac{t}{\tau}}}$$

Though this fitting function could be used, it was not robust—meaning that many backgrounds were poorly fitted or the fitting failed. Therefore an exponential decay fitted in "time-of-flight space", i.e. with the m/z coordinate squared, was used:

$$background = a.\exp\left(b.\left[\frac{m}{z}\right]^2\right)$$

where a and b are fitting parameters. An exponential decay in TOF-space robustly approximates the heat transfer out of the tip following the short laser pulse. An example of this fitting is shown in figure 4.2.1 as the red-dashed line. When there is insufficient signal to fit the background using the exponential, or the fitting fails, a simple mean of the noise before the range is used.

4.2.3 Peak deconvolution

Where peaks overlap in the m/z spectrum, the natural abundances of different isotopes can be used to separate the contribution of each isobaric ion to a particular peak, called peak

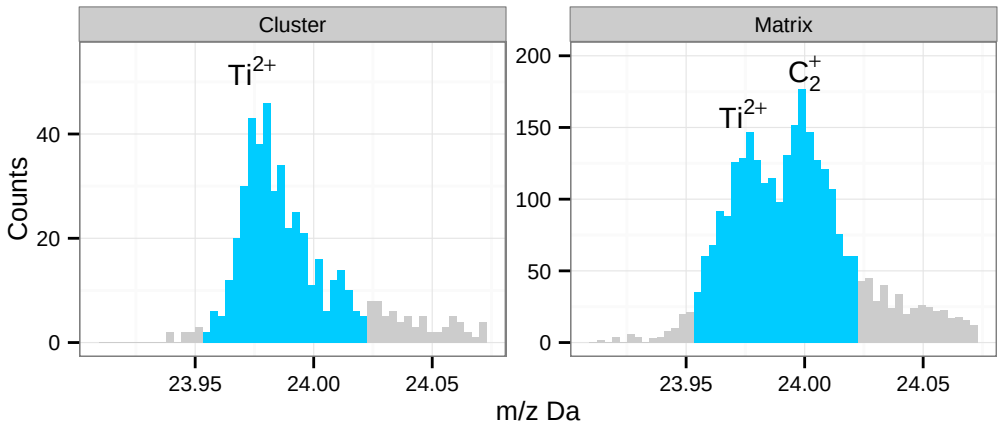

Figure 4.2.2 – Mass spectrum appropriately ranged for Ti^{2+} in the clusters (left), but inappropriately ranged for the matrix (right) showing contributions from both Ti^{2+} and C_2^+ ions.

deconvolution or decomposition [245]. The IVAS software inconsistently refers to "decomposition" as the process of peak deconvolution or calculation of an elemental composition from an ionic one; the convention used in this work is to *deconvolute* overlapping peaks and to *decompose* ionic counts into elemental ones. Conventionally, peak deconvolution is applied globally across the entire reconstructed volume, but the nature of these overlaps differs between the matrix and clusters (and indeed between different types of clusters). Given this, there are significant benefits in using a local deconvolution approach to carry out accurate chemical characterisation.

For example, in the model ODS alloys an overlap exists between $C_2^+/^{48}Ti^{2+}$ at 24 Da, which is avoided by separating the Y-Ti oxide clusters from the matrix because the $^{48}Ti^{2+}$ ion is generally only contained in the clusters. Figure 4.2.2 shows the peak at 24 Da, with the matrix data showing two peaks which are almost resolvable as titanium at 23.97 Da and carbon at 24.0 Da. In the data isolated from the clusters, only a single peak is visible.

Beyond separating the clusters from the matrix, different oxide clusters may evaporate with different ionic compositions, meaning ion overlaps must be considered on a cluster-by-cluster basis. One example is the 32 Da peak, which is important because it contributes roughly 20 % to the total ionic cluster composition (not including Fe or Cr). A variety of complex molecular oxide ions are routinely generated by the oxide clusters, including

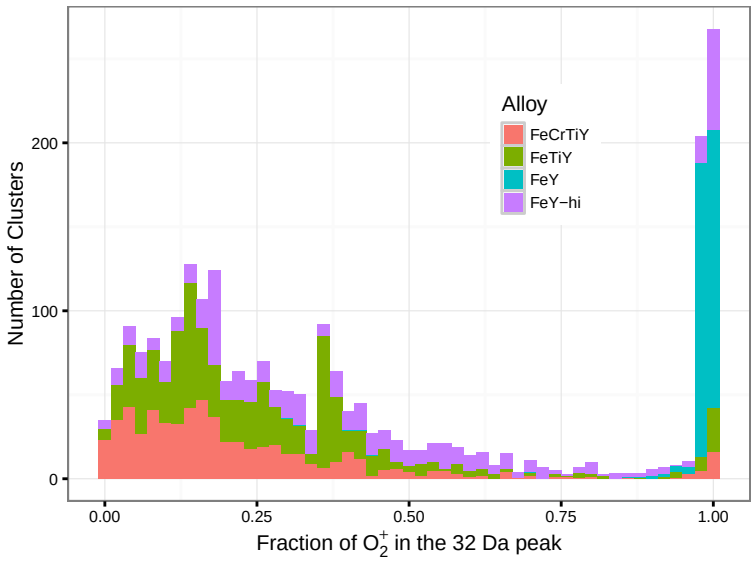

Figure 4.2.3 – Measure of O_2^+ in the 32 Da mass peak (reminder is TiO^{2+}) using the deconvolution method given in section 4.2.3. 75% of the clusters contained no O_2^+ but are not included for clarity. Analysis of 9400 clusters from all samples.

O_2^+ and TiO^{2+}ions, both with a m/z of approximately 32 Da. Depending on the alloy, experimental conditions and original particle chemistry, either O_2^+ or TiO^{2+} species will predominate in this peak. Figure 4.2.3 shows the number of clusters which contained a specific O_2^+ content, calculated using the methodology described below (excluding 75% of clusters which contained only TiO^{2+}). The FeY alloy, which has no Ti, contained only O_2^+ in the 32 peak, but the FeY-hi alloy which contains Ti as a contaminant, has a wide range of O_2^+ contents in the 32 peak. After removing Fe and Cr ions from the clusters, ions with a m/z of 32 are the majority component, 24% in one analysis, followed by 20% Y, 16% YO, 14% FeO and additionally there are 8% with a m/z =64 Da (another overlap). Thus, to correctly measure the composition of the clusters, these overlaps must be deconvoluted, and as figure 4.2.3 shows, this cannot be done on a global basis.

Therefore, a method has been developed to deconvolute the peaks of each cluster individually. Clusters of Y-, Ti- and O-containing ions were identified in reconstructed atom maps using the method of maximum separation detailed in section 3.7.8. Cluster position and size data were exported to MATLAB along with the original atom maps for further analysis. A custom MATLAB script (*clusterIndex.m*) isolated each cluster from the original data to generate a mass spectrum per cluster. *clusterDecompTablesIonic.m* uses this data to produce a new set of ionic ranges for this cluster; the ionic ranges can contain non-integer

components, e.g. the peak at 32 could contain 0.72 TiO and 0.28 O_2. This new ionic range table can be used to calculate the composition of the cluster as well as to correct ionic line profiles (see section 4.5.1). The ionic ranges are produced by least-squares estimation from the range counts and isotopic abundance data.

4.2.3.1 Least-Squares versus Maximum Likelihood

Ionic abundance per mass range M, multiplied by n counts of N ions, gives the observed counts per range b:

$$M \times n = b$$

For example, if range 1 contains only A ions, range 2 B ions and range 4 C ions, but range 3 has an overlap, then using the isotopic abundances of A, B and C the formulated problem would look like:

$$\begin{bmatrix} 1 & 0 & 0 \\ 0 & 0.5 & 0 \\ 0 & 0.5 & 0.9 \\ 0 & 0 & 0.1 \end{bmatrix} \times \begin{bmatrix} n_A \\ n_B \\ n_C \end{bmatrix} = \begin{bmatrix} range_1 \\ range_2 \\ range_3 \\ range_4 \end{bmatrix}$$

Here, C has 90% abundance in range 3 and 10% abundance in range 4, b is the vector of observed counts and n are the number of ions.

M is known from elemental data and b is found from the noise-corrected cluster mass spectrum. n can be estimated using a least-squares (LS) approach which minimises the sum of squared errors:

$$sum\,of\,squared\,errors = (b - M \times n)^T \times (b - A \times n)$$

The least-squares solution is unbounded, and so the *lsqcovnonneg* function, which only returns positive values for n, was used in MATLAB to estimate n. After retrieving n, an

	$\frac{n_B}{n_C}$	σ_B %	σ_C %
LS	2	2.5	5.5
MLE	2	2.5	4.9
LS	20	2.3	49.7
MLE	20	1.4	27.8

Table 4.2.1 – Comparing different methods of resolving peak overlap; least squares (LS) and maximum likelihood estimation (MLE) with high and low concentrations of C, $\frac{n_B}{n_C}$ equal to 2 and 20 respectively. The standard deviation is measured from 100 random samples of $n_B + n_C \simeq 3000$ atoms. Results produced by the MATLAB script *peakDecompExample_miller1996.m*

ionic range table is produced specifying which mass ranges contain which ions.

There are alternative methods to solve this problem, such as considering the problem as a multinomial distribution where each ion has a probability of arriving in each range p and then maximising the likelihood estimator (MLE) formulated using p and the counts per range [232]. This has the advantage of giving smaller errors when estimating compositions that are small, but is more difficult to use than least-squares, which has standard implementations. Comparing *lsqcovnonneg* to my MLE implementation, *mle_solver2.m*, the LS approach is ~500 times faster, with an execution time of 0.4 ms. In the example above, with $n_B = 2n_C$, both LS and MLE gave similar standard errors of 100 random samples from ~3000 atoms, but MLE gave reduced variation when there was a smaller fraction of C, $n_B = 20n_C$, as shown in table 4.2.1. MLE has not been used in this work generally because of the time cost, but it could be used in future work, especially when an overlap exists with a major and minority components.

4.2.4 Quantification of Oxides

Bachhav et al. [275] made a detailed study of the influence of the APT analysis conditions on the measured composition of würsite, $Fe_{1-x}O$. The peak at 16 Da was assigned to O_2^{2+}, in agreement with others who studied ZnO and SiO_2 [276, 277], but note that others have reported accurate stoichiometries in simple oxides by assigning the 16 Da peak as O^+ [278–280]. Although the measured oxygen content can be increased by assigning 16 Da as O_2^{2+}, Bachhav et al. [281] later went on to show that in α-Fe_2O_3 doped with ^{18}O, the 16 Da peak

contained O^+ ions only. This gives a similar result, as reported by others [282], that the measured composition is oxygen deficient (42.5 at% versus the expected 60% in alumina [282]).

The two most probable mechanisms of oxygen loss are due to off-pulse evaporation [283] or the dissociation of oxygen containing ions into neutrals during flight [284]. These mechanisms are influenced by the acquisition parameters and will be material dependent [275, 281, 283].

Generally sub-stoichiometric (oxygen-deficient) compositions are reported for the oxide clusters in ODS alloys (Section 2.3 on page 13) but the improvements in mass-peak identification given above may give a more reliable measure of the oxygen content. For example, in my results from the FeTiY alloy, the 64 Da peak was deconvoluted to contain predominantly Fe_2O, rather than TiO as expected, and this greatly influences the measured Ti/O ratio.

Another artefact that may affect the measurement of the composition measured by APT is the loss of ions in multiple-hit events. These were studied briefly and the results are summarised in the next section.

4.3 Multiple Hit Analysis

To investigate the spatial correlation between multiple hits (ions generated by and detected during same pulse), the distance between the first impact and the second were measured. These measured-pair distances are compared, in figure 4.3.1, between laser and voltage pulsing modes. There was significant spatial correlation of both the multiple and and single hits, consistent with the theory from De Geuser et al. [285]. De Geuser suggested that once an atom has evaporated, the surrounding atoms experience a higher field and are therefore more likely to evaporate [285]. The multiple hits show fewer ion pairs with small separations compared to the single hits, which is shown in detail in figure 4.3.1. This may be because ions are less likely to originate from exactly the same position on the same pulse,

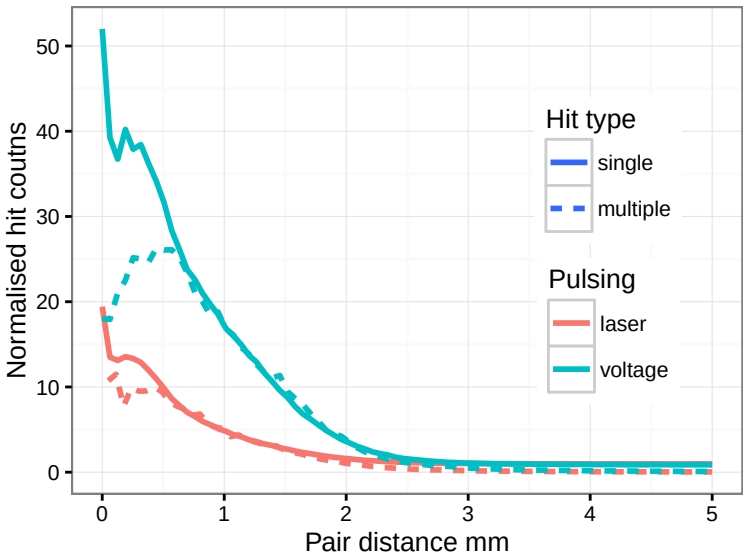

Figure 4.3.1 – Histogram of the distance between multiple-hit pairs and consecutive single pairs observed using either laser or voltage pulsing modes. Calculated using detector coordinates. Histograms are averaged for two different experiments for each of laser and voltage pulsing. The counts from multiples are scaled by 15% and 60% for the laser and voltage pulsed results respectively.

or it may be due to the dead-zone on the detector.

To visualise the dead-zone on the detector, 2D histograms of the ΔX_D and ΔY_D distances were plotted for multiple-hit pairs and consecutive single hits from a voltage-pulsed and a laser-pulsed experiment; these are shown in figures 4.3.2a and 4.3.2c respectively. In these plots, the distribution of hits is mostly symmetrical except for a slight variation in ΔX_D, towards the positive for the multiples and towards the negative for singles.

It is expected that the dead-zone on the detector would be a function of the time between the first impact and the second. The number of multiples arriving as a function of ΔTOF is shown in figure 4.3.3. Most of the multiples (~60%) arrive within 50 ns of the first impact; the percentage numbers on the graph indicate the approximate distribution of timing events. The different sections or slices through ΔTOF are marked by the blue vertical lines at 3, 5, 15, 25 and 50 ns; these correspond to the 2D ΔX_D, ΔY_D hit maps shown in figure 4.3.4. The 5–15 ns ΔTOF slice shows an off-centre elliptical dead-zone about 1 mm wide. Surprisingly, however, between 3–5 and 15–25 ns, different detector algorithms seem to be in operation, which actually give a large number of hits within 0.5 mm of each other.

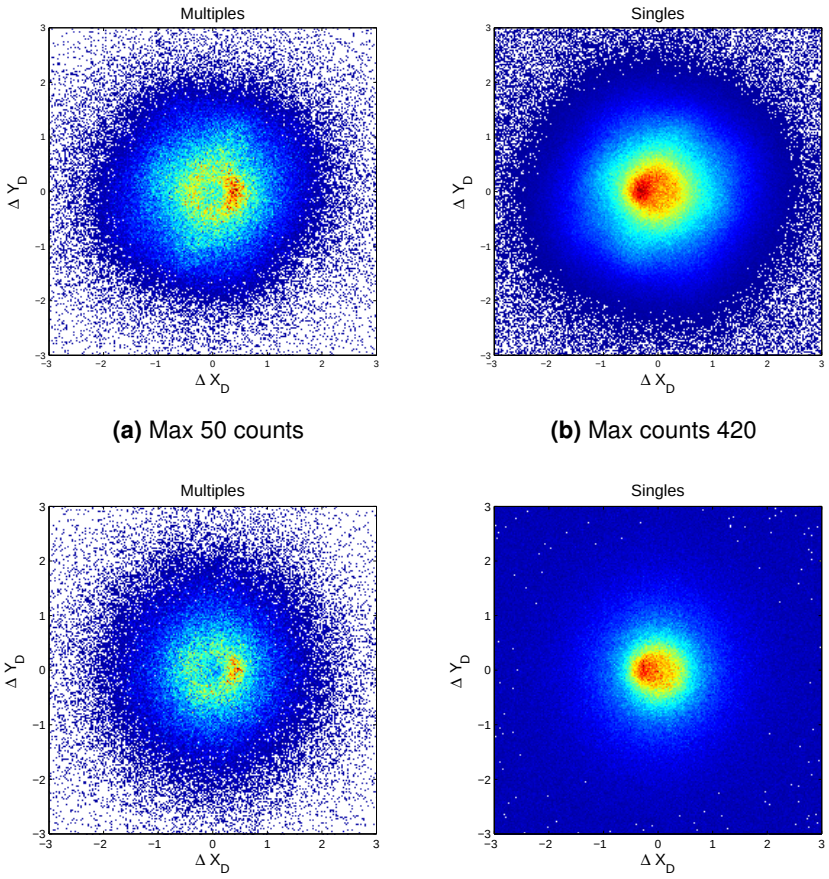

(a) Max 50 counts **(b)** Max counts 420

(c) Max 40 counts **(d)** Max counts 240

Figure 4.3.2 – (a) and (b) Voltage mode: 2D hit histograms showing the distance between the first and second hit as ΔX_D and ΔY_D. For single hits, "pairs" consist of ions detected consecutively. 7.5% multiple hits. (c) and (d) similarly for laser mode, 2.4% multiple hits.

As the detector and its electronics are commercial products and the processing algorithms are unknown, this is an area which is difficult to investigate without further knowledge. Composition bias from the signal loss due to multiple hits has been investigated in other ODS alloys, and it was found that the effect was minimised by using moderate laser power in laser mode APT; it is estimated to make only a -5% difference to the measurement of the yttrium composition of the clusters [121].

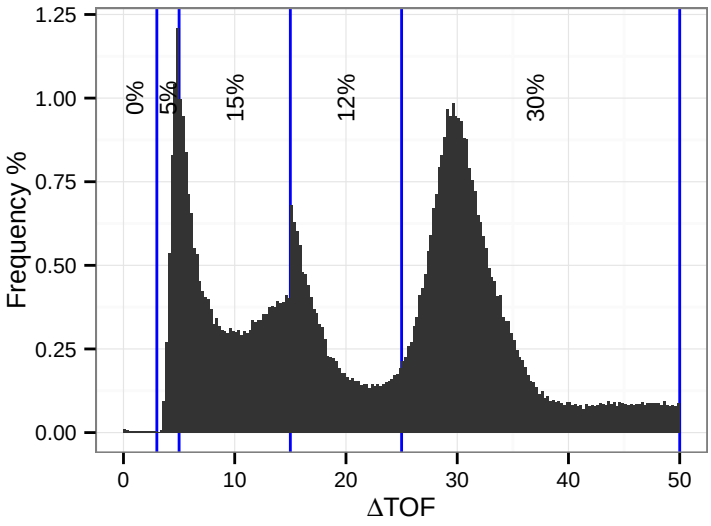

Figure 4.3.3 – Histogram of the difference in time-of-flight from the first impact to the second impact of a multiple-hit event. The percentage values show the proportion of the total multiple hits that have that range of ΔTOF.

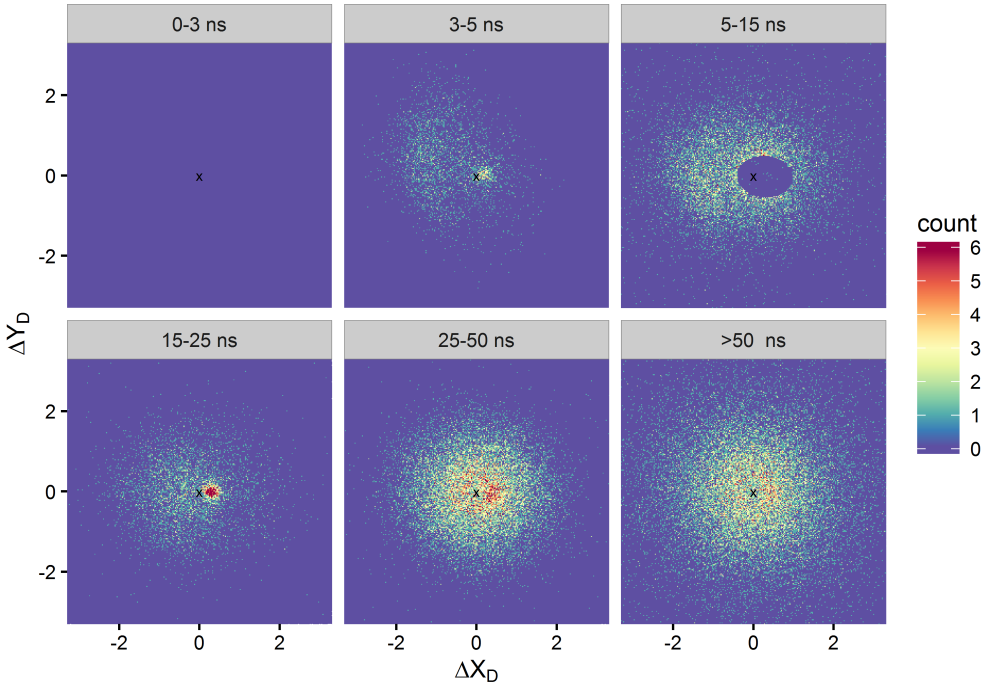

Figure 4.3.4 – 2D multiple-hit correlation plot as a function of ΔTOF.

4.4 Trajectory Aberrations

The difference in evaporation field of the oxide particles and the matrix causes macroscopic trajectory aberrations. Two pieces of evidence for the demagnification of the clusters are their high ionic density and the shape change as a function of size. Figure 4.4.1 shows the density (ions nm^{-3}) of 2500 clusters as a function of their size. For clusters with a radius < 5 nm, the density increases to over 100 ions nm^{-3}, more than three times the expected ionic density of the matrix (31 ions nm^{-3}). Such a high density is unphysical and is an artefact of the reconstruction methodology, coupled with the anomalous evaporation of the clusters. The lateral (x-y) size of the larger clusters is demagnified, so that they appear contracted in the x-y direction. This behaviour is shown in figure 4.4.2; the average line shows that below $\sqrt[3]{Solute} = 10$ the clusters appear flattened and when $\sqrt[3]{Solute} > 10$ the clusters have shape elongated along the z-axis.

The influence of these trajectory aberrations on a particular cluster is shown in figure 4.4.3. The cluster has a very high ionic density as the evaporation surface reaches the cluster (at the top) and there is evidence of a partial Cr-shell at the top and bottom of the cluster—shown in the Cr concentration map. Oberdorfer and Schmitz [259] noted that the size of low-field particles remained unchanged if they were measured along the analysis direction. This is consistent with the data presented above for the larger clusters, and an

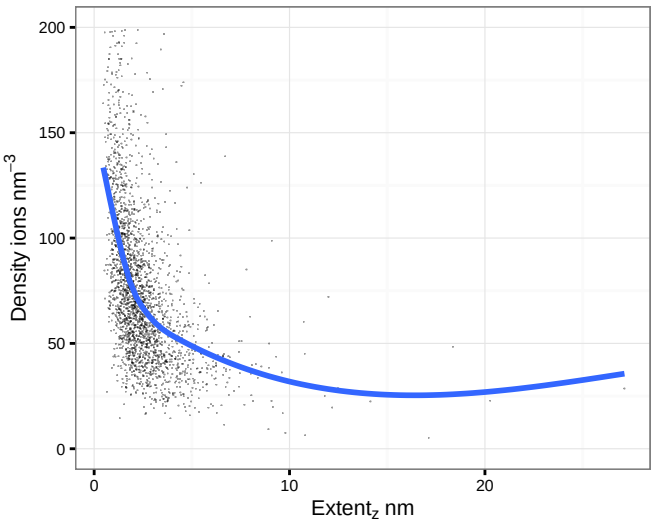

Figure 4.4.1 – Measured ionic density of the oxide clusters as a function of size (extent along Z). The ionic density in the metal matrix is 31 ions nm^{-3}. 2480 clusters in various alloys. The blue smoothed line shows the best fit (generalised additive model).

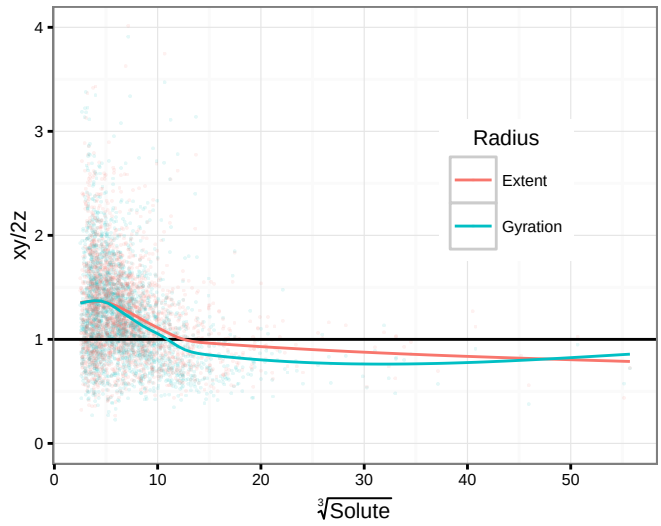

Figure 4.4.2 – Morphology of the clusters ($\frac{x+y}{2z}$) as a function of cube root solute ion count. 1 is spherical, <1 is elongated along z, >1 is flat relative to a sphere. $\sqrt[3]{Solute}$ is proportional to the cluster radius. Measured using either extent or radii of gyration.

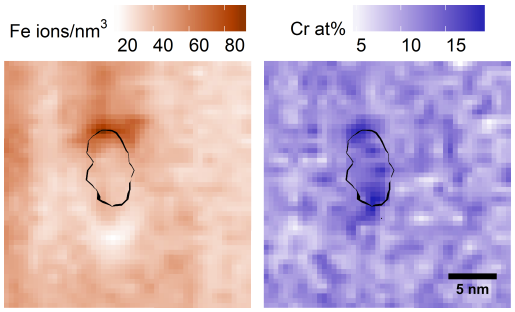

Figure 4.4.3 – (left) The Fe ionic density in a 5 nm thick X-Z slice containing a 8 nm oxide cluster (black outline) in the as-received Fe-Cr-Ti-Y alloy. (right) The associated Cr concentration. The maximum Fe density is unphysically high, 93 ions/nm^3, at the top of the cluster due to reconstruction protocol limitations. A partial Cr-shell, 20 at% Cr, is observed at the top and bottom of the cluster. Below the cluster a very low Fe density is observed. The analysis direction is aligned vertically.

example is shown in figure 4.4.4, which shows TEM of the same particle before APT and the extracted cluster data from APT; the size along the analysis direction remains unchanged but the x-y dimension has been compressed.

For the smaller clusters, the z-coordinate may also be incorrectly reconstructed. If the clusters are relatively easy to evaporate compared to their surroundings, and they contain very few atoms, the whole cluster may evaporate in a short number of pulses and be reconstructed with a very flat appearance. This is the case in figure 4.4.5, which shows 4 small flat clusters and one larger cluster. This out-of-order evaporation is similar to that noted by Boll et al. [256], and figure 4.4.6 taken from [286] shows that incorrect reconstruction of z-coordinates may occur leading to foreshortening in z in very small clusters.

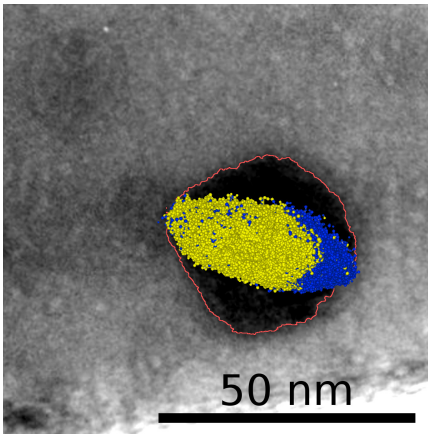

Figure 4.4.4 – Combined TEM and APT of the same sample showing a large composite particle, outlined in red in the TEM image, overlaid with the extracted cluster from the reconstructed APT data (blue and yellow points are Y and Cr containing ions respectively). The z-axis is aligned right to left; thus the APT data shows that the cluster is compressed perpendicular to the analysis direction. ID R14_15645.

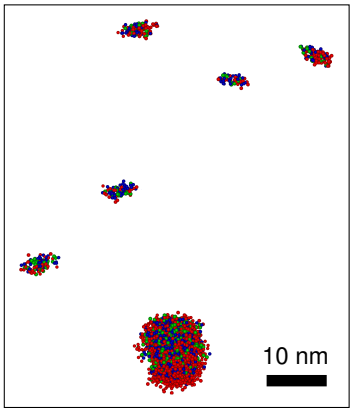

Figure 4.4.5 – Clustered solute ions from experiment R14_18002 showing a number of small flatter clusters and one larger cluster. The z-axis is aligned vertically. Colours: Y, Ti and O are blue, green and red respectively.

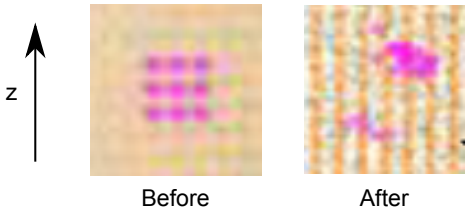

Figure 4.4.6 – Atomistic simulation of a 0.5 nm radius cluster evaporating from a ~22 nm radius tip with a evaporation field 70% of that of the matrix. (left) The cluster before the simulation and (right) reconstructed data after simulated evaporation. Image adapted from [286].

4.5 Extended Cluster Analysis

As detailed in section 3.7.8, clusters are selected by the maximum separation of solute ions. The output files are the inputs for the next stage of data analysis. The following sections detail my work to overcome the challenges of measuring cluster size, composition and local chemistry in light of the effects of trajectory aberrations, which distort the reconstructed data.

4.5.1 Line profiles

As shown in section 4.4 and especially figure 4.4.3, line profiles taken parallel to the analysis direction avoid the majority of the influence of the trajectory aberrations. Though the lateral compression still includes matrix ions into the centre of the clusters, z-axis composition line profiles (now referred to simply as line profiles) give the best resolution of the local chemistry of the clusters, including investigating any core/shell structure [117, 155]. Using line profiles dates back to the original 1D atom probes, which could only analyse a very small area of the tip in depth profile [287]. The current analysis software (IVAS) creates line profiles from individually placed regions of interest (ROIs). This has been used to measure many single clusters, but it is difficult and time consuming to accurately place many ROIs. IVAS can average many proximity histograms together at once, but this analysis assumes a spherical concentration profile, which is not appropriate due to the trajectory aberrations. Therefore, a new tool was written in MATLAB to perform many line profiles automatically.

To compare line profiles from different-sized clusters, the length of the line profile is normalised to that of the cluster. The line profiles are set to have a length equal to 5 times the cluster extent along z (E_z*) and a square cross-section, width equal to the radius of gyration l_g of the cluster. An example is shown in figure 4.5.1. This synthetic cluster has a hard-sphere radius of 2 nm and l_g = 1.57 nm; the blue box shows the total length and width of volume that the line profile is taken from. The length is split into 100 sub-volumes of equal height, each with $volume = l_g \times l_g \times \frac{5E_z}{100}$. The composition of each sub-volume is decomposed using the ionic range table calculated above (section 4.2.3) to give a number of ions for this "profile point". Therefore, for each cluster, there are 100 profile points where the composition is measured and profile points of the same number can be compared between clusters of different sizes.

*Defined in section 3.7.9, equation 3.7.3

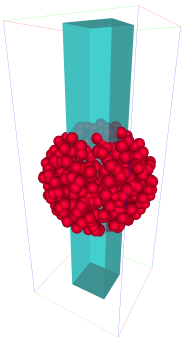

Figure 4.5.1 – Example line profile for a synthetic cluster of hard sphere radius 2 nm. The blue box shows the volume of line profile analysis, 1.57x1.57x10 nm. The length is $5 \times 2 = 10$ nm because the cluster has a 2 nm z-extent.

4.5.2 Cluster Composition

4.5.2.1 Mass-peak overlaps

As described in section 4.2.3, there are a number of peak overlaps in the m/z spectrum which are specific to species which evaporate from the clusters. The ionic composition varies between clusters and therefore so do the magnitude of the peak overlaps. Using the methodology in section 4.2.3, peak overlaps were deconvoluted on a per-cluster basis. When a cluster contained too few counts for the least-squares to give a reliable estimate of the ionic composition, or the deconvolution failed, this cluster was added to a *small cluster* list and at the end of the analysis all the clusters in this small cluster list were added together. This loses the specificity of knowing the extent of peaks overlaps for each small cluster, but instead assumes they all have the same peak overlaps. This could be extended so that small clusters are grouped by their composition estimated from non-overlapping m/z peaks. Figure 4.5.2 shows the ionic composition of the ranges for a single cluster, with the bars coloured to show the estimated percentage of each ion they contain.

4.5.2.2 Fe-Content

The origin of trajectory aberrations is given in section 4.4, and the result causes the surrounding matrix ions (predominantly Fe, but also Cr in the Fe-Cr ODS alloy) to be detected in the clusters. Fe and Cr are not expected in the oxide core of clusters based on thermodynamic considerations [156] and Fe has not been found in extracted particles [106]. In the sub-2 nm clusters, some Fe may remain from the mechanical alloying process, but the

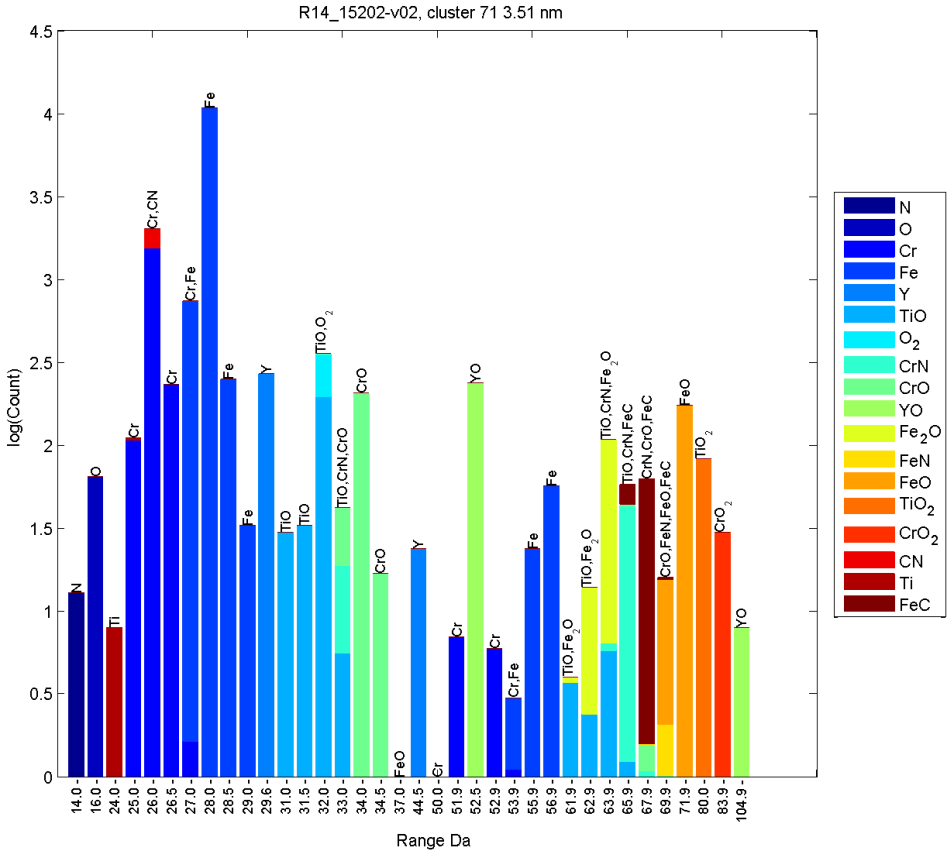

Figure 4.5.2 – Result of a per-cluster peak deconvolution: estimated ionic composition of a cluster, expressed as the portion of the coloured bar, and the height of the bar shows the logarithm of range counts. Produced by *zprofileCacheOverlaps.m* after loading *clusterDecomp-Data2015e.mat*

reduced spatial resolution of the atom probe in the vicinity of these very small low-field clusters prevents adequate quantification.

Using the line profile methodology detailed in section 4.5.1, the average behaviour of the clusters can be shown as well as the dependence on cluster size. Figure 4.5.3 shows the mean ionic-density line profiles of more than 1000 clusters in the as-received Fe-Cr-Ti-Y alloy as a function of cluster radius (E_z).

Taking the detector efficiency into account the expected Fe ion density is 31 ions nm^{-3}, but around the clusters the Fe-density changes significantly. The oxide clusters have an Fe density *greater* than that the surrounding metal. The Fe-density increases slightly at the start of the clusters (at profile point ~25), then sharply increases at the cluster interface

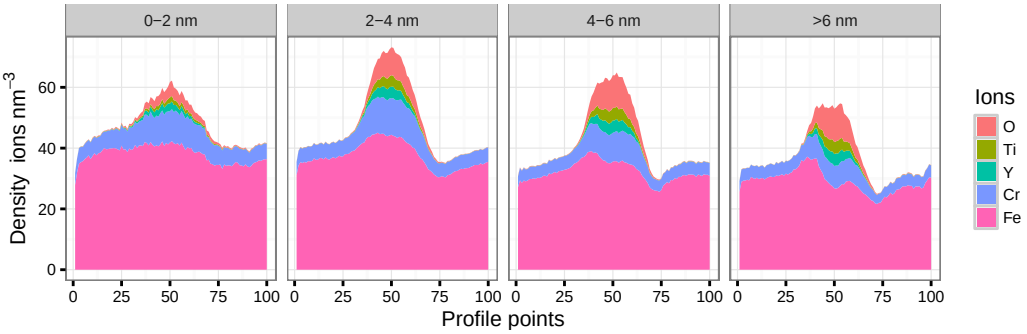

Figure 4.5.3 – Mean ionic-density line profiles through clusters in the as-received Fe-Cr-Ti-Y alloy. The clusters are grouped by size (shown at the top of the figure) and the 4 plots contain data from 511, 412, 105 and 29 clusters for 0–2, 2–4, 4–6 and >6 nm E_z respectively. Profile points from 30–70 represent the total extent of the cluster, $2.E_z$ nm.

(30), dropping slightly in the centre of the larger clusters. The Fe-density peaks again at the bottom interface (60) before dropping to a minimum below the cluster (profile point ~75). This is consistent with the behaviour shown in figure 4.4.3, but figure 4.5.3 shows how the Fe density varies in general as a function of cluster size. The drop in Fe density after the cluster shows that the evaporation after the cluster is reduced as the tip returns to an equilibrium shape.

The extent of any local magnification will be a function of both cluster size and the instantaneous tip radius. Indeed, it was observed that the apparent Fe content increased with increasing tip radius, and therefore with acquisition voltage. As the electrostatics governing the evaporation process have no inherent scale, the cluster radii can be expressed helpfully as the dimensionless reduced radius r' =cluster radius over the instantaneous tip radius, given by the Geiser et al. method [255]:

$$r' = \frac{r.k_F.F_e}{V}$$

where r is the cluster radius, k_f the field factor, F_e the theoretical evaporation field of the matrix and V the evaporation voltage.

The apparent Fe content of the clusters was seen to increase with increasing voltage, so using reduced radius removes this complication and allows us to show simply the dependence of included Fe ions as a function of cluster size. Figure 4.5.4 shows how the Fe

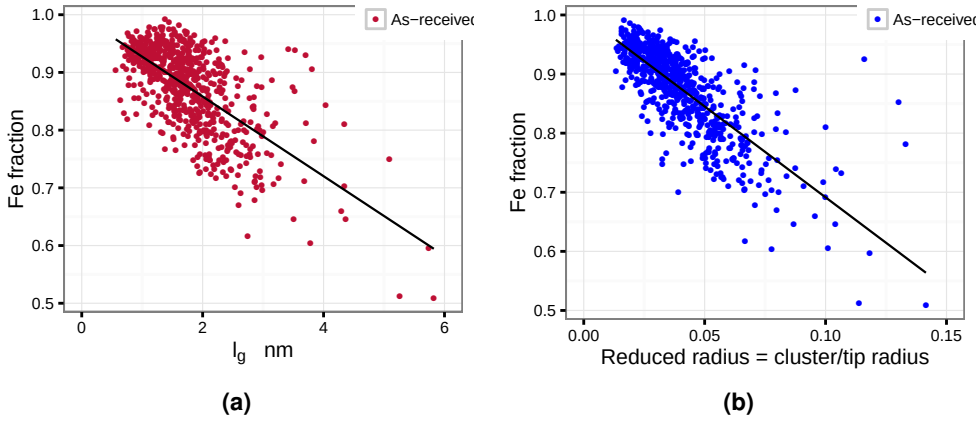

Figure 4.5.4 – Fe fraction as a function of size, expressed in (a) radius of gyration l_g and (b) reduced radius, for 700 clusters measured in the as-received alloys. Black line a linear fit.

fraction varies as a function of cluster size for over 700 oxide clusters in both the as-received Fe-Cr-Ti-Y and Fe-Ti-Y alloys, with the cluster size measured by l_g and r'. Using r', instead of simply l_g, gives a more linear dependence of Fe-content on cluster size (4.5.4b).

Part of the size–Fe-content dependence comes from the cluster-selection method, which includes a region of matrix ions surrounding each cluster in the composition because no erosion was applied to remove this region. Small statistically random clusters may also be present which have low solute concentrations [270]. But the overall trend is for smaller clusters to apparently contain more Fe.

4.5.3 Cluster Size

4.5.3.1 Which measurement?

Clusters of solute ions are identified using the method of maximum separation and the radius of gyration l_g is a convenient way of measuring cluster size [232]. As explained in section 3.7.9.1 and in [271], l_g does not directly measure the extent of a cluster, but the hard-sphere radius of a cluster of homogeneous density is given by $\sqrt{\frac{5}{3}}l_g$. I propose that measurement of the clusters should be performed parallel to the analysis direction, the direction least affected by trajectory aberrations [259] (see section 4.4 for details). Therefore the z-component of l_g, l_{gz}, was used. This makes the assumption that the evaporation surface

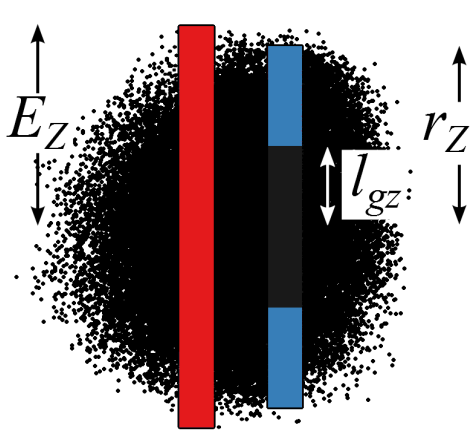

(a) Left: $Extent_Z$ (red); Right: l_{gz} and r_Z (blue)

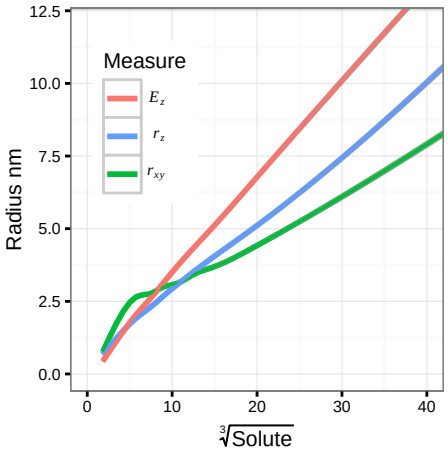

(b) Comparison of radii measurements of observed clusters in the as-received alloys against the cube root of atomic count, which is proportional to cluster radius.

Figure 4.5.5 – Comparison of different cluster size measurement methods.

is perpendicular to the z-axis, which is more appropriate for smaller launch angles (aligned with the z-axis). In some simulations (with larger fields of view), the clusters appear more tilted off-axis and distorted along the normal to the evaporation surface, as in figures 4.4.6 on page 98 and 3.7.6 on page 66.

The extent or range along the z-axis (E_z) and the atomic count are also considered as measurements of cluster size. Atomic count is assumed to be proportional to atomic volume and therefore the cube root of atomic count is proportional to cluster radius. Only solute ions (Y, Ti and O) are considered to avoid matrix-effects. Figure 4.5.5a compares the measurements of E_z, l_z and r_z (r_z =corrected l_z, that is, $l_z\sqrt{5}$) of cluster size along the Z direction of a real cluster. l_g is multiplied by $\sqrt{5}$ to give the approximate hard-sphere radius [232]. The corrected radius of gyration r_z gives an intuitive estimate of the cluster length and E_z gives a slight overestimate due to the spatial blurring of the cluster ions. These measurements are consistent for other clusters, and the cluster radii for all detected clusters (~9300 total) are plotted against atomic count in figure 4.5.5b.

The measurement of extent is consistently greater than that of r_z by 20% for the larger clusters. This is thought to be because of the reduced spatial resolution (figure 4.5.5a) in

the vicinity of the clusters as a result of trajectory aberrations. The X-Y component of the Guinier radius is shown in figure 4.5.5b with comparison to r_z showing the aspect ratio of the clusters as a function of size. This expresses the behaviour shown in figure 4.4.2, that larger clusters were long and thin and smaller clusters tended to a flatter appearance. These findings are consistent with the evaporation behaviour of relatively low-field clusters with the accompanying aberrations and incorrect z reconstruction. Following these findings, I used the corrected z-component of the radius of gyration r_z as a measure of cluster radius in our APT data.

4.5.3.2 Extent versus Range

In IVAS, the cluster extent is defined for each Cartesian axis:

$$E_x = \text{larger of} \begin{cases} \bar{x} - \min(x) \\ \max(x) - \bar{x} \end{cases} \tag{4.5.1}$$

A more intuitive definition would be to use the range:

$$Range_x = \frac{\max(x) - \min(x)}{2}$$

In one experiment, the mean and standard deviations of the extent and range were 3.2 ± 3.0 and 2.9 ± 2.6 nm, so the range measurement is smaller and has slightly less variation 87% versus 92% (*extentComparison.m*, experiment R14_18138). The range measurement is smaller because the IVAS extent measurement always picks the larger of two values (equation 4.5.1). Most of the variation in the experimental measurement comes from the actual variation in cluster sizes. In a numerical simulation, the measurement can be repeated many times for different spatial coordinates of ions with the same cluster radius. The bias imposed by the limited detector efficiency can also be simulated numerically in this way.

Simulated clusters were made using a fixed total number of atoms, from 8 to 27,000, and 63% of these atoms were removed at random to simulate the 37% detection efficiency

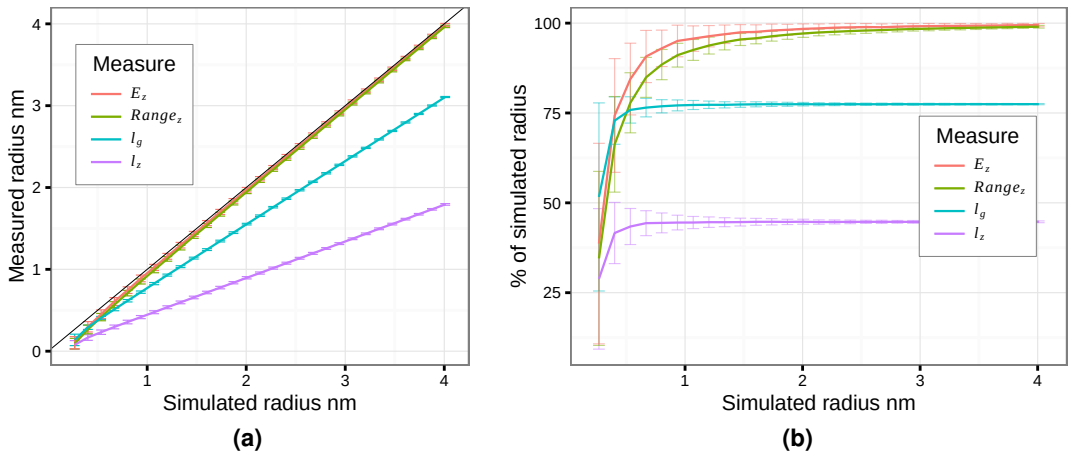

Figure 4.5.6 – Comparison of different cluster size measurements on numerically simulated data, including a detector efficiency of 37%.

of the LEAP-3000. Measurements of the range and extent were repeated 500 times for each cluster size with random spatial coordinates and with random atoms removed. The comparison of the different measurements of cluster radius, radius of gyration l_g, the z-component of l_g, extent and range, is shown in figure 4.5.6a. Figure 4.5.6b compares the relative difference of the cluster size measurements, showing that l_g and l_z may be corrected by constant factors of $\sqrt{\frac{5}{3}}$ and $\sqrt{5}$ respectively to give r_g and r_z.

The standard deviation is shown separately for the *corrected radii* (r_g and r_z) in figure 4.5.7, which shows that the error in the measurement of range is smaller than that of extent $\sigma(r_z) > \sigma(r_g)$, because r_g depends on r_x, r_y and r_z, whereas r_z is a single measurement. The compression of the x-y radii is the reason for using r_z instead of r_g despite the increased error. If a small amount of Gaussian spatial noise is introduced, $\sigma_{x,y} = 0.2$ and $\sigma_z = 0.1$ nm, then as shown in figure 4.5.8, the r_z measurement gives the best approximation of the simulated radius. This is also in agreement with the conclusion presented earlier that analysis should be made parallel to the analysis direction to avoid the influence of trajectory aberrations.

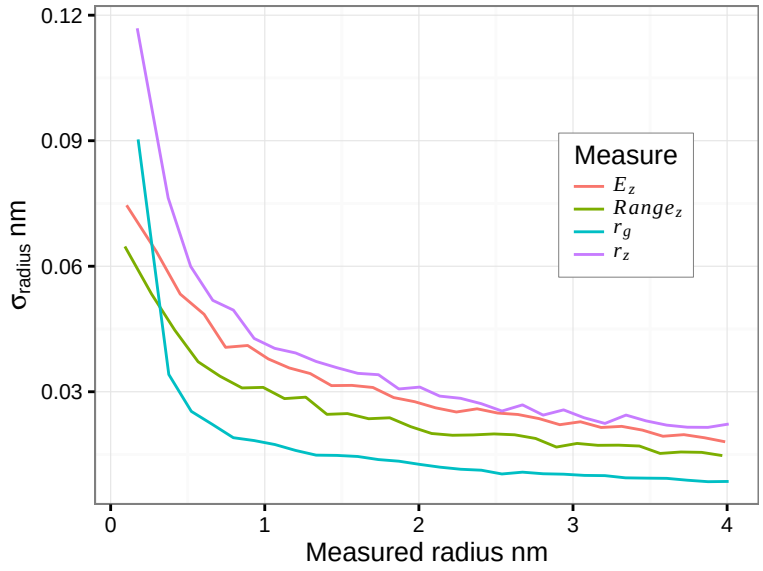

Figure 4.5.7 – The standard deviation of different measures of cluster radius derived from numerical simulation. Original cluster sizes 8–27,000, 37% detector efficiency, 500 samples for each cluster size.

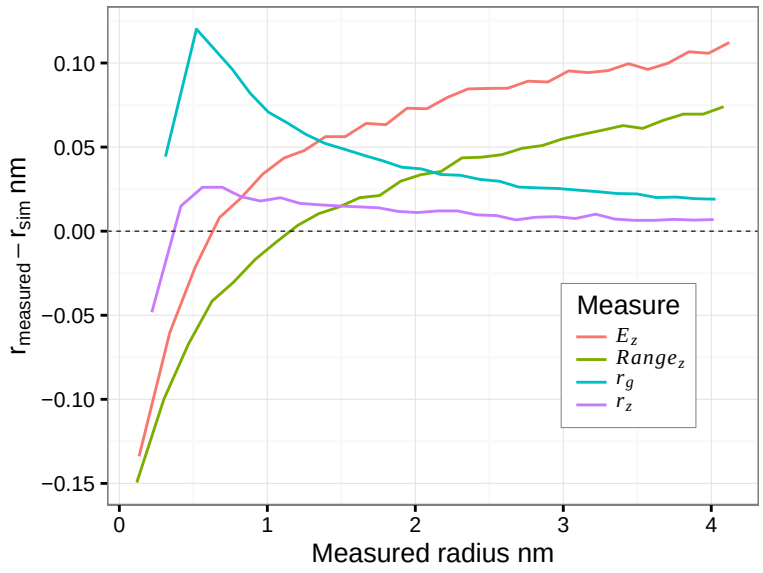

Figure 4.5.8 – Difference in mean measured radius and simulated radius for different cluster size measurements, including spatial noise of $\sigma_{x,y} = 0.2$ and $\sigma_z = 0.1$ nm.

4.5.3.3 Comparison with TEM

There are many methods for measuring particle sizes in alloys, but using TEM has the advantage of being able to examine atom probe samples prior to APT analysis—correlative microscopy [288]. Particle sizes measured by TEM are regarded as being directly interpretable, although the image size and contrast mechanisms must be taken into account [289]. Figure 4.5.9 gives two examples of Fe-Y (a) and Fe-Ti-Y (b) TEM images before APT analysis and the accompanying atom maps. Both images contain composite particles: in (a), the

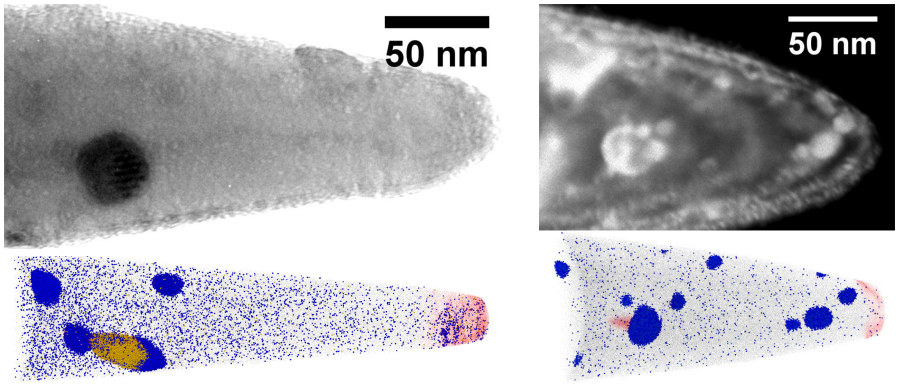

(a) Fe-Y **(b)** Fe-Ti-Y

Figure 4.5.9 – Correlative microscopy of ODS alloys. In the APT reconstructions (a) and (b), oxide clusters are highlighted by Y-containing ions (blue). FeO ions (red) indicate the surface oxide on the tips. This APT data was reconstructed using the tip profile image to ensure the global scale is correct.

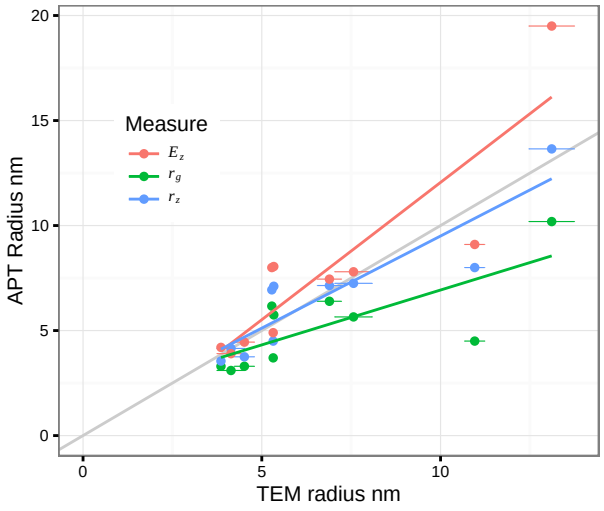

Figure 4.5.10 – Comparison of cluster radii measurements with the particle radius observed by TEM. Linear lines of best fit and $y = x$ are shown to guide the eye. Extent E_z and correct radius of gyration r_z are measured parallel to the analysis direction. r_g includes the compression of the clusters due to trajectory aberrations in the x-y plane. The TEM radius is adjusted to correct for the increased image size in bright-field imaging.

larger particle shows moiré fringes in TEM and is composed of a Cr oxide attached to a Y oxide; in (b) the larger particle is revealed by APT to be half Y oxide and half Fe oxide. Reconstructions were performed using the tip-profile method in IVAS [247] and inconsistencies in tip shape due to the clusters were accounted for by modifying the tip radius profile [290].

Figure 4.5.10 compares the different cluster size measurements from APT with the radius measured from the TEM images shown in figures 4.5.9a and 4.5.9b. The measurements from APT are smaller compared to the radius measurement of the same particles in TEM.

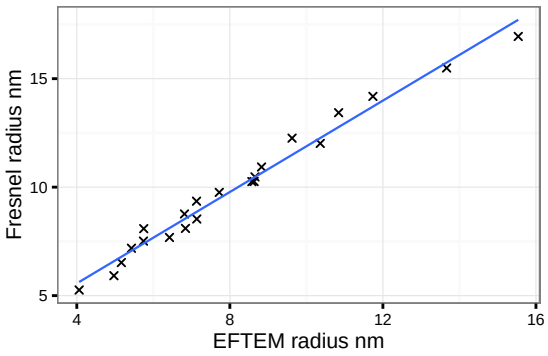

Figure 4.5.11 – Comparison of particle size measured using Fresnel contrast on bright-field Fresnel images (+9 um defocus) and EFTEM eigen images. Good agreement between the imaging techniques, but the Fresnel image size is $25 \pm 7\%$ greater than the radius measured by EFTEM.

There is some disparity between the radius measurements, which may be due to the imaging condition, especially in dark-field imaging, where the particles appear larger. The TEM particle image size was compared from a single region of interest using Fresnel contrast [104] (+9 um defocus) and an eigen image obtained from EFTEM analysis (figure 4.5.11). The large defocus used was to highlight the smaller particles in the image but adds to the uncertainty of the measurement and it increases the measured size by $25 \pm 7\%$ compared to the EFTEM.

In conclusion, the size measurements made by either TEM or APT need careful consideration. I use r_z because of its intuitive measurement of the cluster size and the limited influence of trajectory aberrations. r_z gives a smaller measurement of the same features observed by TEM (in diffraction imaging conditions), but this could be due to the exaggerated image size from the choice of imaging condition.

4.6 Inhomogeneity Measurement

Section 2.3.5 on page 27 gave an introduction to the inhomogeneous nature of ODS alloys and how this microstructure may affect the materials' properties. In order to measure the spatial inhomogeneity, I have implemented Garncarek's method [168, 169, 291].

From a real spatial distribution, such as that shown schematically in figure 4.6.1a, a population distribution chart (PDC) can be calculated for different grid sizes; figures 4.6.1b & 4.6.1c show PDCs for grids of small and large sizes respectively. Thus at one particular

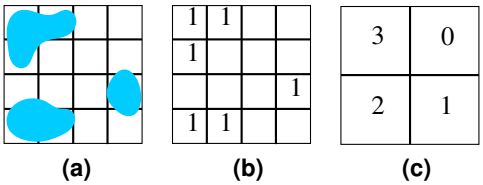

Figure 4.6.1 – Conversion from a real microstructure (a) to a population distribution chart of a small scale (b) and a larger scale (c).

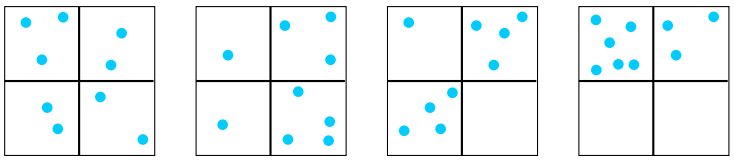

Figure 4.6.2 – Garncarek's measure of spatial inhomogeneity for 9 items in 4 sub-volumes with different distributions (a)–(d) ranging from (a) stronger than random, (b) random, (c) inhomogeneous and (d) very inhomogeneous.

grid scale, there are n points in κ cells, so the measure h of the degree of inhomogeneity can be written as [168]:

$$h = -\frac{n}{\kappa - 1} + \frac{\kappa}{n(\kappa - 1)} \sum_{i=1}^{\kappa} n_i^2$$

For a homogeneous PDC, h is zero because each cell has $n_i = n/\kappa$ and the maximum h is observed when all n items are in a single cell; so $h \to n$. Garncarek et al. [168] note that this h measure can be compared to the expected value for a random distribution and therefore compute a new measure, H:

$$H = \sqrt{\frac{n(\kappa - 1)}{2(n - 1)}} \left(\frac{1 - n - \kappa}{\kappa - 1} + \frac{\kappa}{n(\kappa - 1)} \sum_{i=1}^{\kappa} n_i^2 \right)$$

With this new measure, negative values correspond to a distribution which is stronger than random (ordered), $H = 0$ for random distributions and large positive values are obtained from inhomogeneous distributions. This allows families of PDCs to be compared even if they contain differing numbers of total items. PDCs corresponding to these H values are shown in figures 4.6.2(a)–(d).

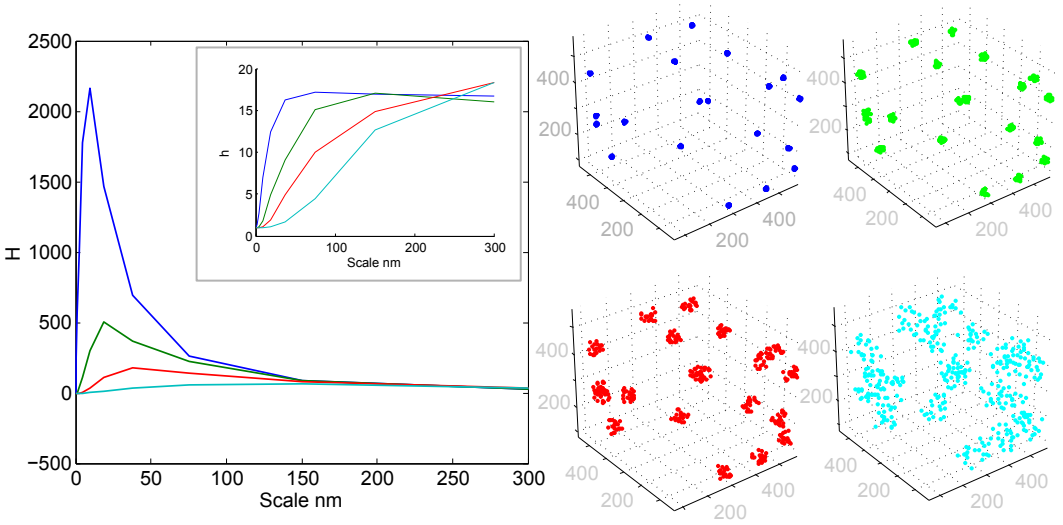

Figure 4.6.3 – Example measurements of spatial inhomogeneity using Garncarek's method in 3D. (left) Normalised inhomogeneity H versus the same number of randomly distributed points, (inset) raw inhomogeneity measure h, both compared to the measurement scale in nm. Total volume = (600 nm)^3. Inhomogeneity in the microstructure was simulated by clustering 20 points around each centre with a specific radius. The radii are: 5, 15, 30 and 60 nm for the blue, green, red and cyan points respectively.

The calculation of h and H is straight forward, but segmentation of the data to produce the finest scale PDC is the most challenging step, especially as the 3D data from APT does not have a regular shape following the reconstruction. First, a cuboid is found which will fit inside the constraints of the data and then the cluster centres within this volume are used to calculate the inhomogeneity measures. To find the approximate bounds of the data, a convex hull [292] of a sample of 8000 ions is made (*maxBox.m*). 10,000 random boxes are placed within the convex hull and the one of the greatest volume is accepted as the sample volume. Because this step is random, and depends weakly on the sample ions used to make the convex hull, there is some variation in the exact volume chosen. H is calculated using the cluster centres only by the *inK.m* function with a minimum scale of 2^{-8} times the smallest sub-volume dimension; therefore the minimum scale is about 0.5 nm for most experiments.

For interpretation of the values of H observed for example microstructures, see figure 4.6.3. In figure 4.6.3, inhomogeneous distributions were obtained by randomly placing clusters of 20 points with varied cluster radii. For a very small cluster radius, H is very large at small scales because some cells contain a large number of points and others zero, but at

larger scales $H \to 0$ because the clusters of points themselves are randomly distributed.

4.7 Summary

Due to the challenges posed by the atom probe analysis of the oxide particles in ODS steels, a number of new analysis techniques have been developed. An automated-systematic approach to defining ranges of ions in the m/z spectrum gives better reliability in measuring the composition of many experiments, allowing them to be compared with more confidence. By examining the nature and spatial location of the peak overlaps in the m/z spectrum, a more accurate measurement of the cluster composition can be made without disregarding the spatial information. Using composition line profiles parallel to the analysis direction, it is possible to gain the best resolution measurements of the local chemistry of the clusters, and by normalising the profile length many clusters can be compared with ease. These line profiles also allowed the errors in the reconstruction protocol to be studied by looking at the average Fe-density through hundreds of clusters as a function of size. Serious consideration has been given to the best measurement of cluster radius by comparison with numerical simulations and direct comparison with transmission electron microscopy. Finally, the application of the Garncarek's measure of spatial inhomogeneity allows a less well studied aspect of the microstructure to be explored quantitatively.

As I have implemented these new analysis techniques, I have developed a growing collection of programs for the MathWorks MATLAB environment. The most important of these scripts and functions are given in the Appendix. All of the programs used are available as supplementary materials to this thesis in digital format.

Chapter 5

The As-Received Model Alloys

5.1 Introduction

This chapter presents the characterisation of all the materials in their "as-received" state without modification. The data analysis results presented here are will be used as a comparison for the influence of irradiation at low and high temperature in Chapter 6. This chapter outlines the baseline properties of each of the alloys given in 3.1 so they can be used as a comparison, but also includes a detailed discussion about the influence of alloy composition and processing on the final character of the oxide particles. As stated in Chapter 2, I refer to oxide *particles* where some structure is implied, and to *clusters* where the structure is more ambiguous—specifically with measurements made by APT.

First of all, the hardness, microstructural observations and bulk compositions are given below as an overview of the alloys, before considering the issues raised in more detail.

5.2 Overview Data

The hardness of the as-received FeY, FeTiY and FeCrTiY alloys was measured by nanoindentation so that they can be compared with the hardening caused by ion-irradiation. Figure 5.2.1 shows the averaged nanoindentation hardness as a function of depth from the surface. Adequate control experiments could not be performed for FeY and FeTiY due to

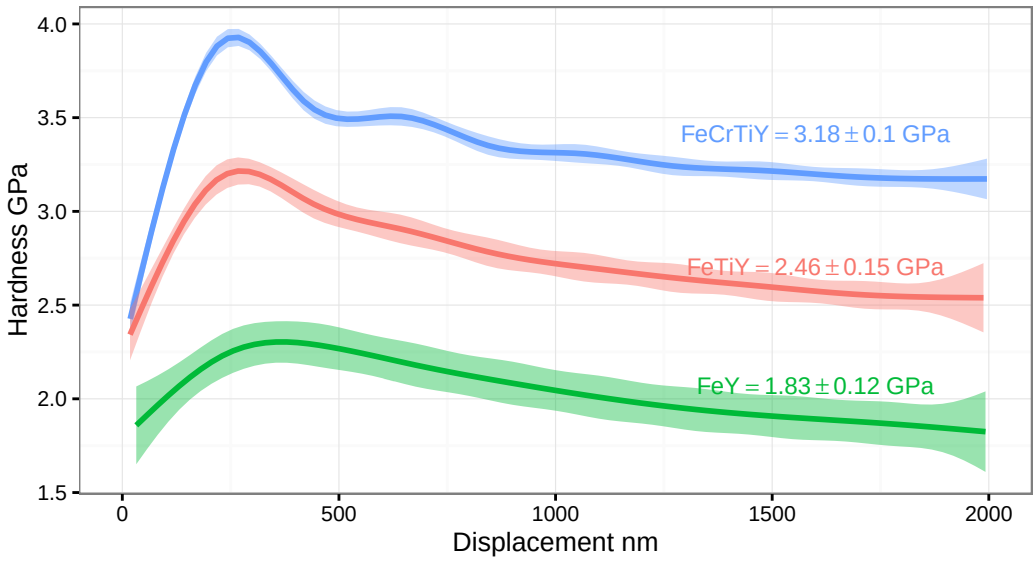

Figure 5.2.1 – Nanoindentation measure of hardness with depth of the three extruded alloys. Results are averaged over all experiments, including ion-irradiated samples, therefore the mean hardness is taken after a depth of 1.5 µm to 2 µm to avoid any surface effects.

sample mounting and poor surface finish. Therefore, all of the nanoindentation results (including ion-irradiated samples) were averaged together and the "bulk" hardness was taken from a depth > 1.5 um, beyond the influence of the irradiation. The hardness increased from 1.8 to 2.5 GPa when Ti was added to FeY alloy composition and the hardness further increased from 2.5 to 3.2 GPa when Cr was also added.

The composition of the as-received alloys was measured by atom probe tomography and is listed in table 5.2.1. Atom maps with accompanying TEM images are shown in figure 5.2.2. These "bulk" compositions include the whole experimental dataset for each alloy and so the variation in measured oxygen content is high due to the infrequent inclusion of surface oxide in the analysis; similarly for carbon, which was found primarily at grain boundaries and in carbides.

Figure 5.2.3a shows a grain boundary with segregation, which increases the overall measured carbon content in this experiment. The carbon concentration well ahead of the boundary is 0.028 at% and the boundary has approximately 2.8 carbon atoms per nm^2 segregated to it (0.15 monolayers or $0.23/a^2$). This is consistent with the findings by Suzuki et al. [293], who measured a grain boundary carbon concentration of $0.5/a^2$ in a low-alloy steel

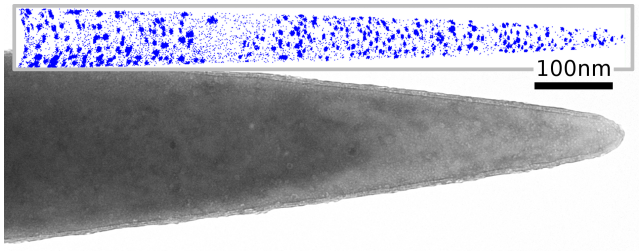

(a) FeY-hi

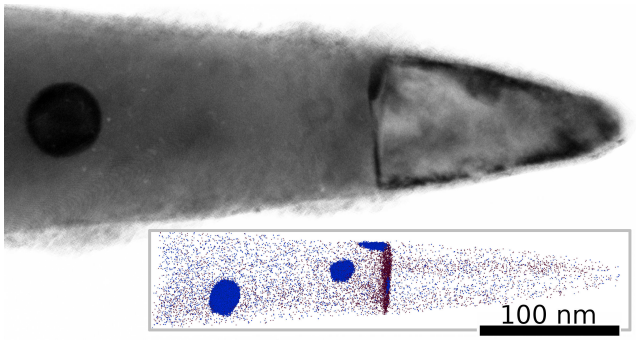

(b) FeY

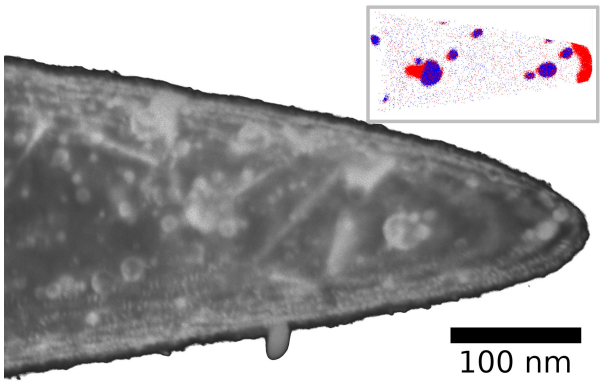

(c) FeTiY

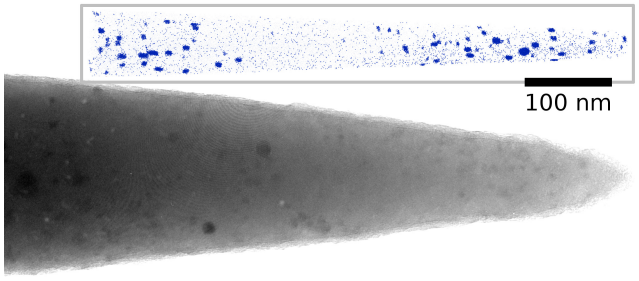

(d) FeCrTiY

Figure 5.2.2 – Example TEM images of needle samples from the 4 different alloys before APT analysis and the resulting atom maps. Y and YO ions are blue, carbon brown and FeO red.

	FeCrTiY		FeTiY		FeY		FeY-hi	
	Comp.	*Err.*	Comp.	*Err.*	Comp.	*Err.*	Comp.	*Err.*
Ar	0.00	*0.01*	0.01	*0.01*	0.04	*0.05*	0.01	*0.01*
C	0.01	*0.01*	0.07	*0.07*	0.17	*0.15*	0.03	*0.01*
Cr	11.78	*0.31*	0.01	*0.02*	0.22	*0.30*	0.05	*0.02*
N	0.07	*0.03*	0.02	*0.02*	0.06	*0.03*	0.04	*0.03*
O	0.60	*0.36*	0.75	*0.33*	0.86	*0.95*	1.48	*1.95*
Si	0.02	*0.04*	-	-	0.01	*0.02*	0.01	*0.02*
Ti	0.21	*0.11*	0.26	*0.08*	-	-	0.06	*0.03*
Y	0.16	*0.05*	0.20	*0.07*	0.17	*0.15*	0.19	*0.04*

Table 5.2.1 – Compositions as measured by atom probe tomography in atomic % with Fe as the balance. The error is the standard deviation of the measurements over at least three datasets for each alloy. Total ions: FeCrTiY 2.45, FeTiY 1.12, FeY 0.77 and FeY-hi 0.99 $\times 10^8$.

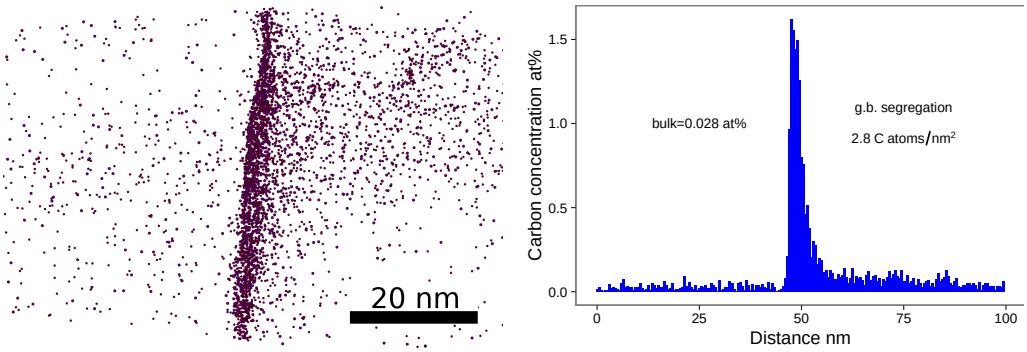

(a) Side-view of carbon ions segregated to a grain boundary in FeY. Analysis direction left to right.

(b) Quantitative composition line profile across the g.b. shown in (a). The line profile had a length of 100 and a radius of 17.5 nm.

Figure 5.2.3 – Carbon segregation to a GB in the as-received FeY alloy. Experiment ID 15576

[293]. The concentration profile along the analysis direction is very asymmetrical, with some carbon being retained after the grain boundary has evaporated (figure 5.2.3b). The small sample volume of atom probe measurement gives a large variation in the measurement of trace elements, which are not spatially homogeneous. However, in the nominally Cr- and Ti-free FeY-hi alloy, trace amounts of Cr and Ti were detected dispersed throughout and segregated to the oxide clusters. Their influence is discussed in the next section.

5.3 Particle Size

5.3.1 Fe-Y; HIP versus Extruded

By comparing the APT measurements of the HIP and extruded alloys, it is possible to infer how these different processing methods affect the microstructure. As the example images in figures 5.2.2a and 5.2.2b show, there is a great difference in the particle density and size between the alloys consolidated by hot-isostatic pressing (HIP, FeY-hi) and by extrusion (FeY). The mean and standard deviation of the cluster radius r_z (measured by atom probe) were 6.6 ± 3.6 nm for the extruded alloy and 2.1 ± 0.9 nm for FeY-hi. This also corresponds to a great reduction in the cluster number density in the extruded alloy; only 12 clusters were detected in FeY and 1046 in FeY-hi. The cluster number density was estimated as $8 \pm 4 \times 10^{21}$ m^{-3} in the extruded material, which is much lower compared to $4.7 \pm 0.9 \times 10^{23}$ m^{-3} in the FeY-hi alloy; here the error is expressed as the standard deviation of all the measured sample volumes.

Another major difference between these two alloys are the levels of contamination. The FeY alloy contains some Cr-containing oxides, which are highlighted in figure 5.3.1. Some of these are attached to Y-oxides (A) or in isolation (B). In one APT experiment, a Cr-oxide particle was detected (figure 4.4.4 on page 98), giving an overall Cr content of 0.6 at%, but none of the other experiments contained Cr; therefore the measured composition in table 5.2.1 is 0.22 ± 0.30 %. The FeY-hi sample consistently contained Cr, 0.053 ± 0.021 % total, with most of that segregated to the clusters, which contained 0.36 ± 0.05 % Cr. Figure 5.3.2 shows averaged composition line profiles through the clusters (methodology: section 4.5.1) and demonstrates the Cr and Ti partitioning to the clusters in the FeY-hi sample.

5.3.2 Influence of Ti and Cr

Looking now only at the extruded alloys, by comparing FeY to FeTiY, and then FeTiY to FeCrTiY, the influence of Ti and Cr can be observed. Figure 5.3.3 shows EFTEM images of

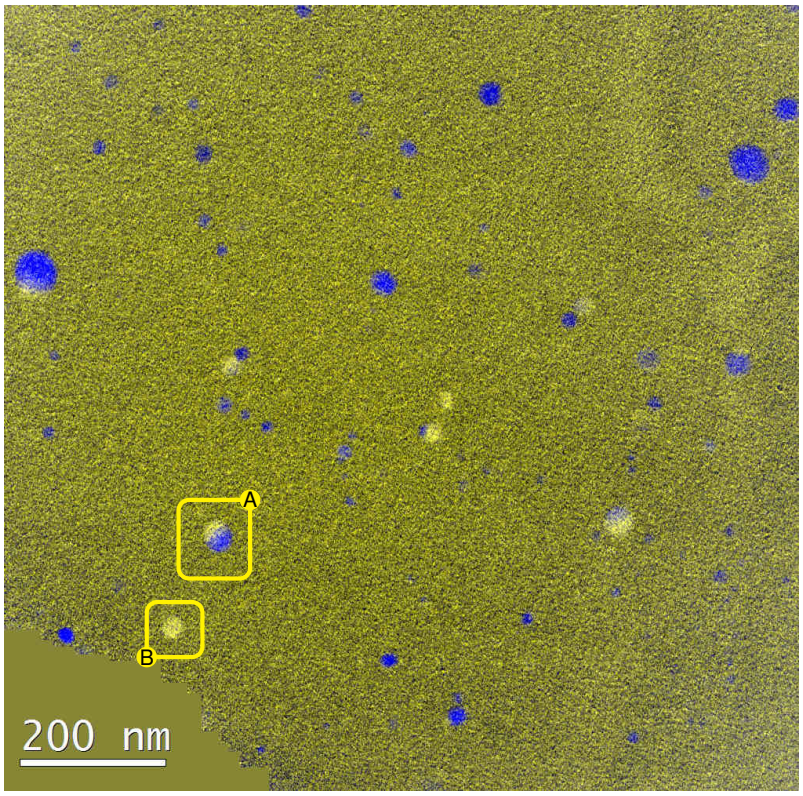

Figure 5.3.1 – Composite EFTEM image showing two eigen images overlaid in different colours (blue and yellow). The blue eigen image shows the Y-$N_{2,3}$ edge and the yellow eigen image shows the location of Cr. The background Cr is due to overlap with the Fe energy loss; there is very little Cr in the matrix as measured by atom probe. (A) shows a composite yttria particle attached to a Cr-oxide. (B) shows a Cr-only oxide.

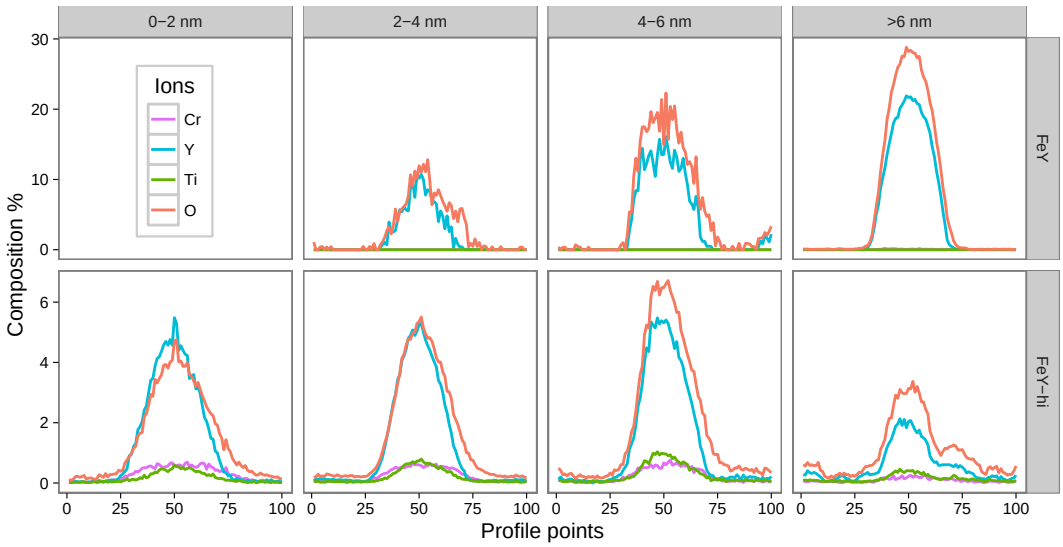

Figure 5.3.2 – Composition line profiles along the z-axis through clusters (APT data) in FeY (top) and FeY-hi (bottom). FeY-hi contains both Ti and Cr contaminants, which are strongly partitioned into the clusters.

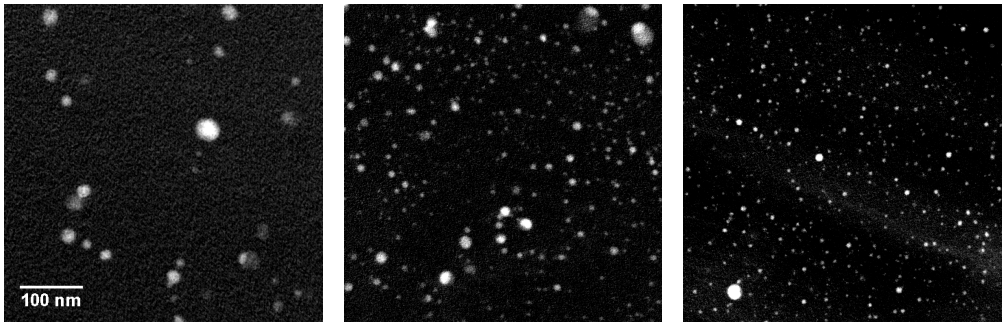

(a) FeY **(b)** FeTiY **(c)** FeCrTiY

Figure 5.3.3 – Low-loss EFTEM images of the Y and Ti edges (25-40 eV energy loss) for the extruded as-received alloys. The scale is consistent for all images. Fourier-log thicknesses measured as $\log(l/l_0)$, (a) 0.4, (b) 0.8 and (c) 1.2.

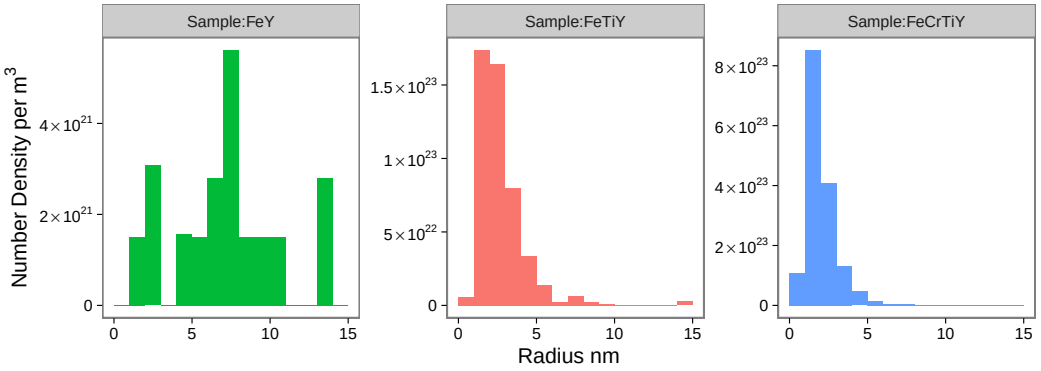

Figure 5.3.4 – Particle size distributions measured by APT for FeY, FeTiY and FeCrTiY, scaled by volume to give particle number density.

the particles in the three as-received alloys. This data shows that the particle size is reduced and the particle number density is increased when Ti is added to the FeY composition, and the particles are further refined by the addition of Cr. These data agree with the cluster size distribution as measured only by APT, which is shown in figure 5.3.4. Table 5.3.1 summarises the number density change and size difference between the different alloys. The APT data confirms the effect of Ti and Cr on the cluster sizes and density, and this is consistent with similar cluster volume fractions in each alloy, which were 3.4 ± 3.0 % for FeY, 3.6 ± 1.7 % for FeTiY and 4.0 ± 2.4 % for FeCrTiY. Clearly the modification of the alloy chemistry directly affects the number and size of the resulting oxide particles. The chemical changes of the oxides are investigated next.

Sample	APT		TEM	
	Num. Dens. $\times 10^{23}$ m^{-3}	Radius nm	Num. Dens. $\times 10^{23}$ m^{-3}	*Radius nm*
FeY	0.08 ± 0.04	6.6 ± 3.6	0.009	9.3 ± 3.8
FeTiY	1.0 ± 0.8	3.0 ± 1.7	0.13	5.4 ± 2.9
FeCrTiY	3.1 ± 1.6	2.1 ± 1.2	0.48	3.0 ± 1.0

Table 5.3.1 – Mean particle number densities and mean radii in FeY and FeTiY as measured by APT and TEM. The standard deviation, from repeated experiments, is listed next to each number, and does not represent the error of the measurement. The standard deviation of the corrected radius of gyration r_z is given next to the mean, again this is not representative of the error of the measurement.

5.4 Cluster Composition

5.4.1 Bulk Chemistry

The crystalline structure was assessed using synchrotron X-ray powder diffraction data (see figure 5.4.1), which showed a weak reflexion from cubic-Y_2O_3 in the FeY alloy (c.f. [294]) but no Y_2O_3 reflexions in the FeTiY alloy. However, FeTiY did show a relatively strong (222) reflexion from $Y_2Ti_2O_7$ at 16.3 $^\circ 2\theta$. The average chemistry of the particles was measured qualitatively using low-loss EFTEM. The processed energy-loss spectra (for images similar to those in figure 5.3.3) are shown in figure 5.4.2, showing that the oxide particles contain Y, Ti and Cr. Therefore, XRD and TEM agree that Ti not only modifies the particle size and number density but also their composition and structure. The cluster compositions were studied in detail using APT.

The oxide cluster compositions (measured by APT and averaged by experiment) are given in table 5.4.1, and the three main features are: the apparent Fe-content increases with decreasing average cluster size; the measurements are sensitive to the local microstructure; and there can be a large variation between experiments on the same alloy. Additionally, trace amounts of Ar were frequently detected at the cluster interface, and bubbles attached to particles were observed by TEM. As the powders were milled in an Ar atmosphere, it is likely that these bubbles contain Ar trapped during the consolidation process [113]. The variation of Fe-content is covered in detail in section 4.5.2.2 and it is removed from

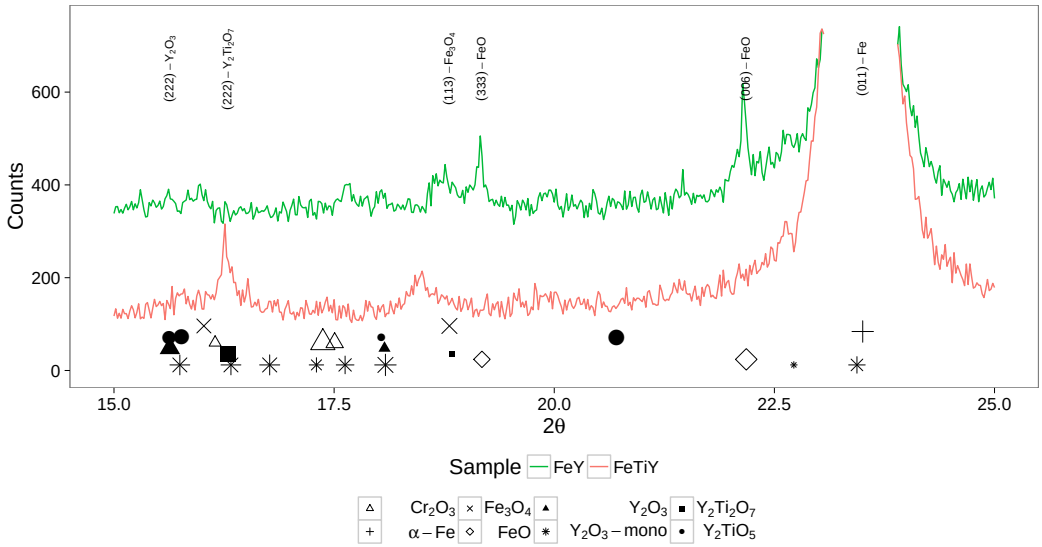

(a)

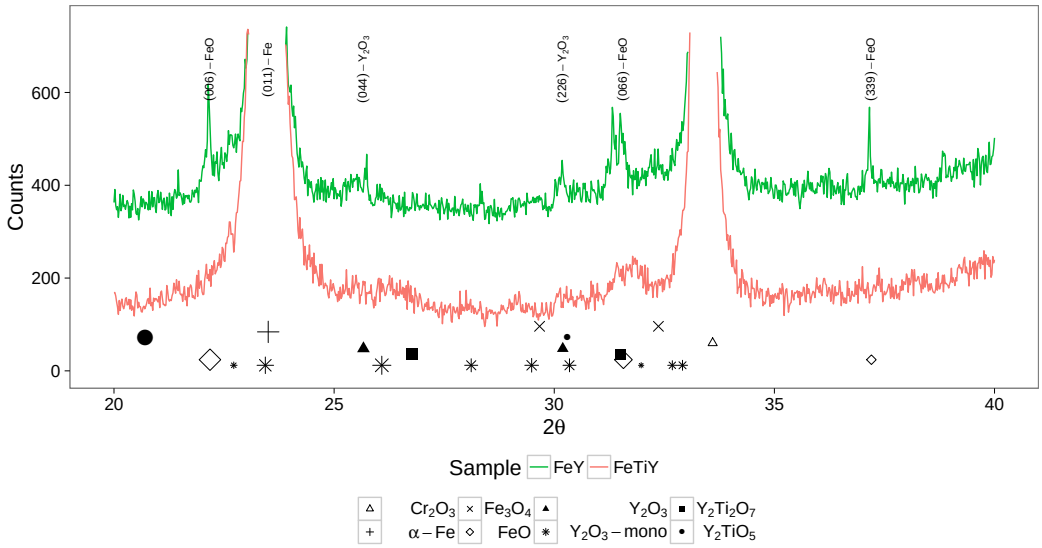

(b)

Figure 5.4.1 – Comparison of synchrotron glancing-incidence X-ray powder diffraction 2θ-scans of FeY and FeTiY. Specific reflexions are identified with the planes and phases responsible shown. The symbols at the bottom of the graph show all possible phase reflexions. X-ray wavelength $\lambda = 0.8258\,\text{Å}$

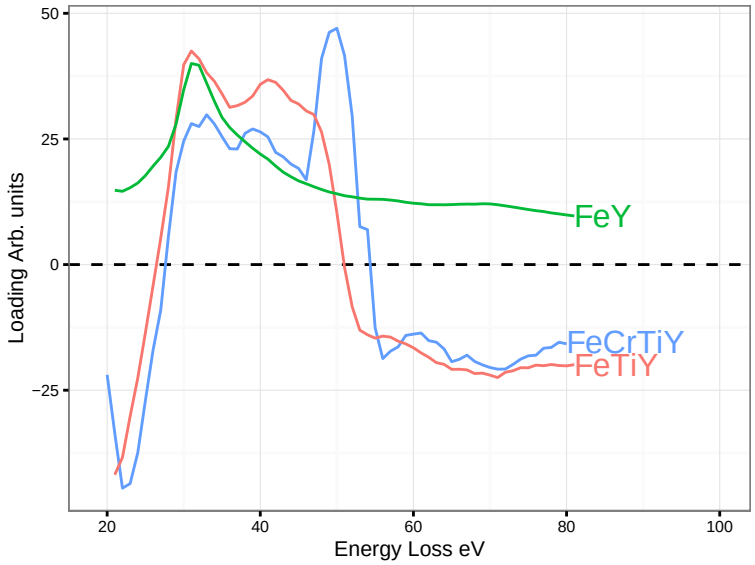

Figure 5.4.2 – Representative energy-loss eigen vectors from principal component analysis using EFTEM data. Each eigen vector corresponds to an eigen image showing bright particles on a dark background. FeY shows an energy-loss at 31 eV, FeTiY at 31 and 40 eV and FeCrTiY at 31, 40 and 50 eV; these values correspond to the energy losses of $Y_{N2,3}$ (26 eV), $Ti_{M2,3}$ (35 eV), $Cr_{M2,3}$ (42 eV) respectively with an energy shift of ~5 eV.

Element	FeY	FeTiY	FeCrTiY	FeY-hi
Ar	0.07 ± 0.09	0.03 ± 0.01	0.01 ± 0.03	0.03 ± 0.02
C	0.48 ± 0.33	0.14 ± 0.05	0.06 ± 0.13	0.10 ± 0.02
Cr	2.6 ± 3.8	0.11 ± 0.17	14.8 ± 1.1	0.36 ± 0.05
N	0.2 ± 0.1	0.07 ± 0.02	0.35 ± 0.09	0.10 ± 0.04
O	14.9 ± 8.1	13.3 ± 5.4	9.44 ± 3.89	3.3 ± 1.62
Ti	<0.01	4.7 ± 2	3.4 ± 1.4	0.28 ± 0.12
Y	6.0 ± 3.7	4.3 ± 1.1	2.40 ± 0.58	2.11 ± 0.53

Table 5.4.1 – Mean cluster compositions isolated from the matrix, all in at% where the balance is Fe. Compositions are averaged over several experiments for each material and the error given is the standard deviation. O has a high variance due to the occasional inclusion of surface oxidation. C has a high variability as it is segregated to grain boundaries and so the measurement depends on the microstructure in the analysed volume. Similarly, Cr contamination was found in some experiments (c.f. figure 5.3.1), but no or very little Cr was detected in the Fe-matrix of either FeY or FeTiY.

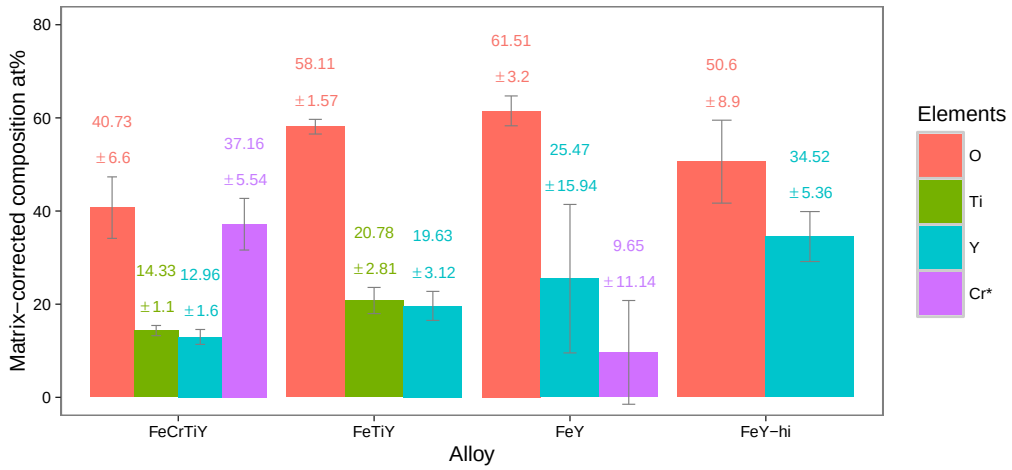

Figure 5.4.3 – Matrix-corrected peak-deconvoluted cluster compositions averaged over all experiments with error bars showing the standard deviation. * The Cr content in FeCrTiY is the Cr remaining after removing $0.13 \times Counts(\mathrm{Fe})$ from the cluster composition.

subsequent analyses.

The matrix-corrected cluster compositions (averaged over different experiments) using equation 3.7.4 on page 82 with a bulk Cr-content of Cr_m =0.13 are shown in figure 5.4.3. In FeY and FeY-hi, the cluster composition is consistent with Y_2O_3, though the O-fraction in FeY-hi is lower than expected. The Cr in FeY is included from a Cr-oxide attached to a Y-oxide in one experiment. The average cluster composition in FeTiY is consistent with the $Y_2Ti_2O_7$ bulk oxide with some oxygen deficiency. In FeCrTiY, even after removing the Cr associated with the matrix, the clusters still contain a significant proportion of Cr. This lowers the M:O ratio to 60:40, which would not be a charge-neutral stoichiometry without an unrealistic concentration of vacancies. These measurements neglect the variation of the cluster composition as a function of size or any change in interfacial chemistry, which are covered in the following sections.

5.4.2 Individual Cluster Chemistry

There are two methods for measuring the average cluster composition. Let C_k equal the average cluster composition of species k, with a total of J clusters and if a specific cluster j has n_{ij} counts of species i:

1. Sum the ions from all clusters and then calculate the average composition

$$C_k = \frac{\sum_j n_{kj}}{\sum_i \sum_j n_{ij}} \tag{5.4.1}$$

2. Calculate the composition for each cluster and then average

$$C_k' = \frac{1}{J} \sum_{j=1}^{J} \left(\frac{n_{kj}}{\sum_i n_{ij}} \right) \tag{5.4.2}$$

Method (5.4.1) is biased toward the composition of the larger clusters, which contain the majority of the ions analysed, whereas method (5.4.2) is biased towards the composition of the smaller clusters, which are more numerous. The results using method (5.4.1) averaged over all experiments were summarised in figure 5.4.3, and figure 5.4.4 shows the results using the second method (5.4.2).

The variation of the composition measurement is greater using (5.4.2), but this may be due to statistical counting error, which dominates in small cluster compositions. The plots in figure 5.4.4 are separated by cluster radius to investigate this effect. Though the variation is higher for the 0–3 nm radii clusters (e.g. 2.7 at% for Y in FeCrTiY) than for the >6 nm clusters (1.8 at%), the variation of the composition in the large clusters is still greater than the counting error (0.9 at% for FeCrTiY >6 nm clusters containing a mean of 11500 ions).

The variation in the measurement of cluster composition can be explained in two ways:

- If all the clusters have identical composition, then the variation comes from random error in the measurement. As shown above, this may be due to statistical counting error for the smallest clusters, but must come from some unidentified source for the larger clusters.

- The clusters have a range of compositions.

Due to the complexity of the evaporation process and data analysis of the atom probe technique, a thorough estimation of the random error in the composition measurement has

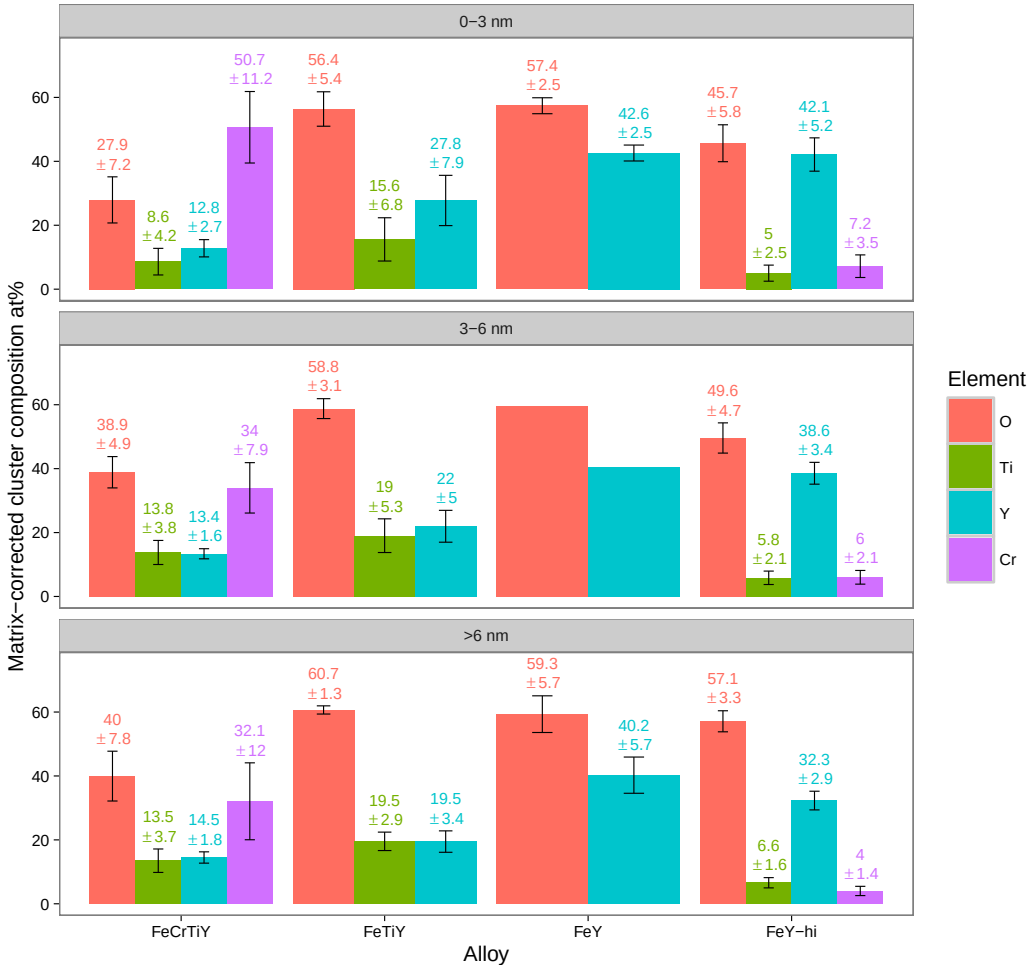

Figure 5.4.4 – Matrix-corrected cluster compositions grouped by cluster radius. Results are averaged and exclude clusters with a Y:O of < 0.2, which are commonly surface oxides.

not been made. Throughout this work the best effort has been made to ensure consistency between analyses, especially concerning the mass-spectrum analysis and the cluster selection. However, the ambiguity of the evaporation process and the use of commercial closed-source detection systems and reconstruction software hinders a quantitative estimate of the random and systematic errors. For an overview of the contributions to random error in m/z, see the appendix in [247].

Assuming that the greatest source of compositional error comes from the misidentification of ion peaks [260], and given that my deconvolution protocol helps limit this, an estimate of the random error can be made using the measured Fe:Cr ratio in all samples from the FeCrTiY alloy. The Fe:Cr ratio is a good candidate because there is minimal over-

lap of the mass-peaks, the Cr distribution in the matrix should be homogeneous and the high concentration gives good counting statistics. The measured Fe:Cr ratio was 0.137 ± 0.005, therefore, if the Cr is homogeneously distributed, I estimate the random error of the APT composition measurement to be better than 4%.

Having shown that the error in the composition measurement by atom probe is smaller than the measured variation in the cluster compositions, it must be assumed that the cluster composition varies between individual clusters. Sakasegawa et al. [99] observed a decreasing Y:Ti ratio for particles with decreasing size, but contrary to this Lecoat et al. [25] did not observe a change in Y:Ti ratio with cluster size, though the two alloys in these studies are sufficiently different that differing oxide phases might be expected. However, I have found a weak dependence of both the oxygen content and the Y:Ti ratio as a function of size of the clusters as measured by atom probe.

Figure 5.4.4 suggests that the oxygen content can vary as a function of cluster size and this is shown quantitatively in figure 5.4.5. The O-fraction of the larger clusters ($radius > 5$ nm) is less varied, but with smaller clusters the oxygen fraction decreases and the variation is greater. Some large clusters were attached to Fe or Cr oxides, skewing the O measurement. FeY-hi has the lowest O-fraction in the smallest clusters and is similar to other alloys such as MA957 and Eurofer with reported O-fractions of 0.44 and 0.42 respectively [66, 155]. The relatively high O-fraction observed in this work could be a product of the relatively short milling time (4 h) or my per-cluster peak deconvolution protocol, which better identifies oxygen-containing species like O_2^+ and Fe_2O^{2+}.

The Y:Ti ratio was also observed to vary according to the cluster size as shown in figure 5.4.6. The larger clusters tend to a Y:Ti ratio of 1 for both alloys and the smaller clusters have a higher Y:Ti ratio. This is contrary to behaviour observed by Sakasegawa [99], who observed a reducing Y:Ti ratio with particle size < 7 nm radius in MA957 (Fe–14Cr–0.3Mo–1.0Ti–0.25Y_2O_3 wt% with trace Al). Even after separating out the effect of size on the cluster composition, a variety of cluster compositions are still observed. Figure 5.4.6 also shows some differences between FeTiY and FeCrTiY. Clusters with a ra-

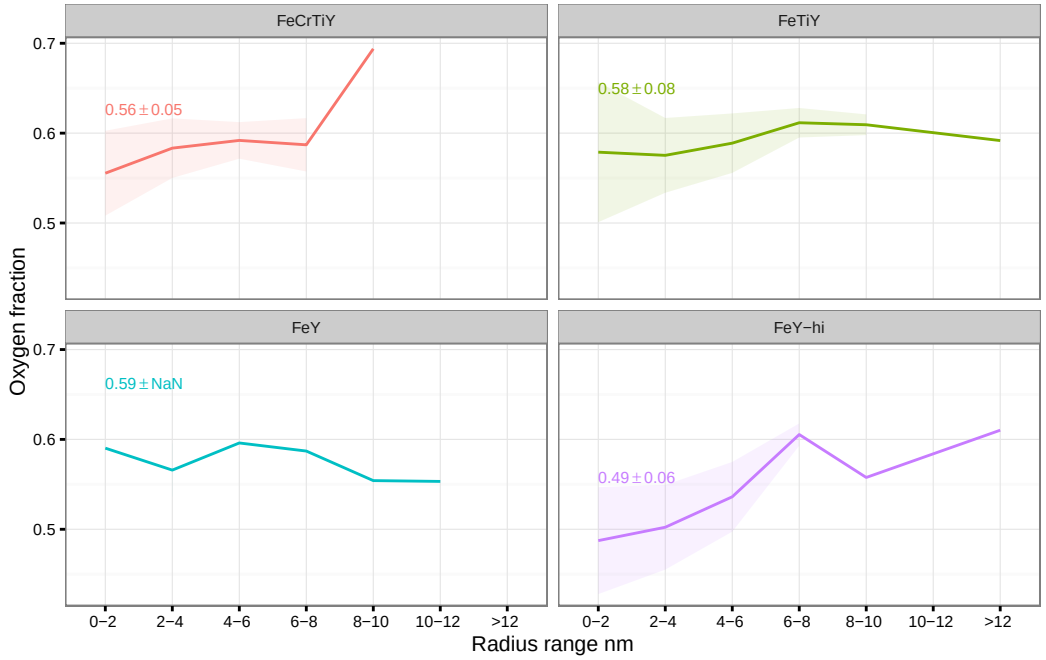

Figure 5.4.5 – Oxygen fraction, not including Fe or Cr ions, of clusters in the 4 different as-received alloys grouped by cluster radius. One standard deviation is indicated by the shaded ribbon for size groups of more than one cluster. The O-fraction of the smallest group is shown in text on the left of each panel.

dius < 4 nm in FeTiY had a higher Y:Ti ratio than the clusters in FeCrTiY. However, the Y:Ti ratio of the largest clusters (radius > 4 nm) was 0.99±0.50 with Cr and 1.10±0.40 without. Therefore, Cr may have some influence on the cluster chemistry; this is investigated further in the next section.

Some authors have observed a variation in cluster chemistry in general [155] and as a function of size [99], but I have also observed that the composition of the clusters varied with their spatial location as revealed by APT and EFTEM in figure 5.4.7. The semi-quantitative analysis of the low-loss EFTEM data shows a large variation in measured Y:Ti ratio, especially for the smaller particles, but overall shows the same behaviour as figure 5.4.6. Both images in figure 5.4.7 show that the oxide composition is not totally random but is correlated to the spatial position.

All of the individual cluster compositions can be visualized using a ternary plot of their Y:Ti:O contents. Figure 5.4.8 shows the individual cluster compositions separated into three

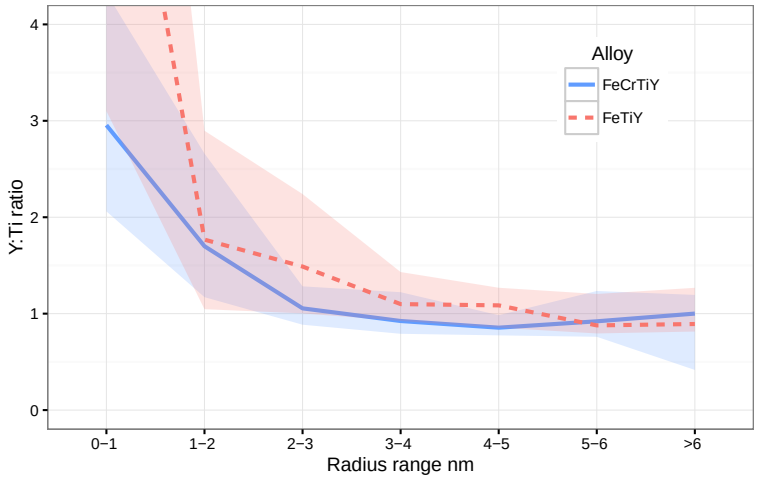

Figure 5.4.6 – Median Y:Ti ratios of clusters in FeTiY and FeCrTiY alloys grouped by cluster radius. The shaded area indicates the upper and lower quartiles for each size range.

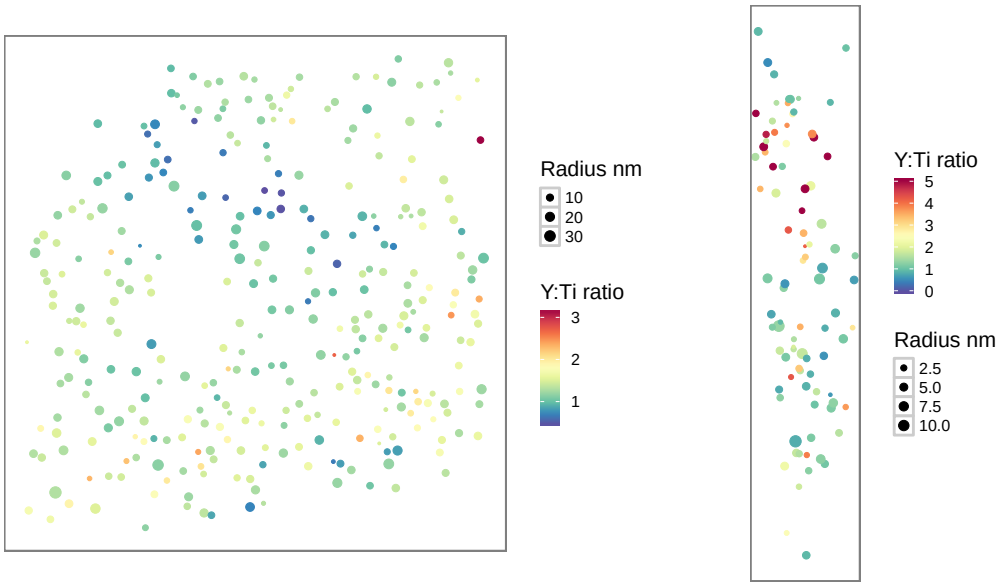

(a) Semi-quantitative analysis of the spatial variation of composition by EFTEM. Image 630 nm wide.

(b) Quantitative analysis of the spatial variation of composition by APT. Dataset is 60 nm wide.

Figure 5.4.7 – Comparison of the spatial variation of Y-Ti-oxide composition in FeTiY as measured by (a) EFTEM and (b) APT. The EFTEM data is only semi-quantitative because the energy-loss cross-section of $Y_{N2,3}$ is not known. Both images show that the Y:Ti ratio varies between particles and with spatial location. The circles in each image are scaled proportionally to the radius of the features.

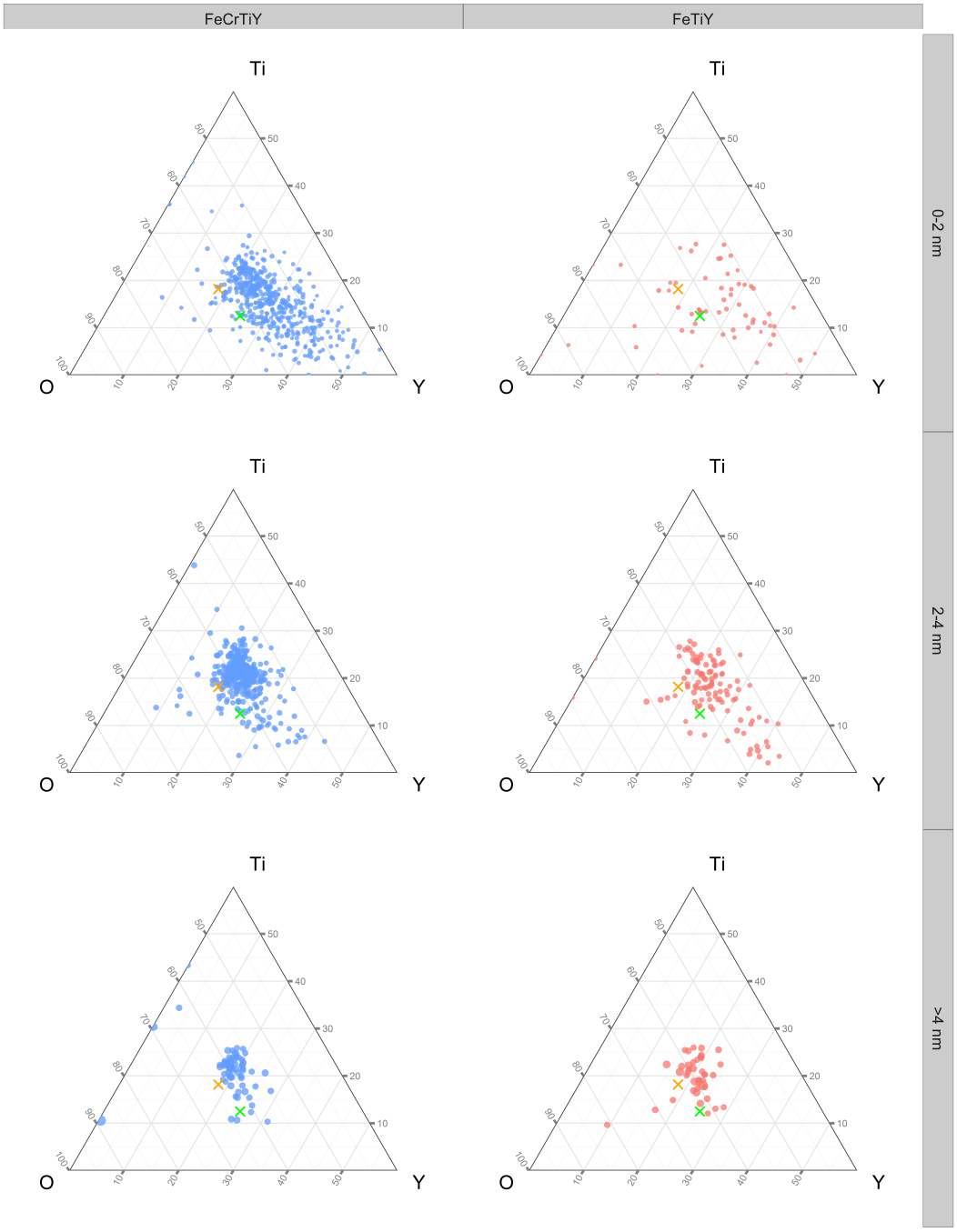

Figure 5.4.8 – Gibbs triangle showing individual cluster Y:Ti:O ratios (red and blue points) as measured by APT. The results are split by cluster radius, with the smallest clusters (<2 nm) at the top and the largest ones (>4 nm) in the bottom panel. The orange and green crosses mark the positions of stoichiometric $Y_2Ti_2O_7$ and Y_2TiO_5 respectively.

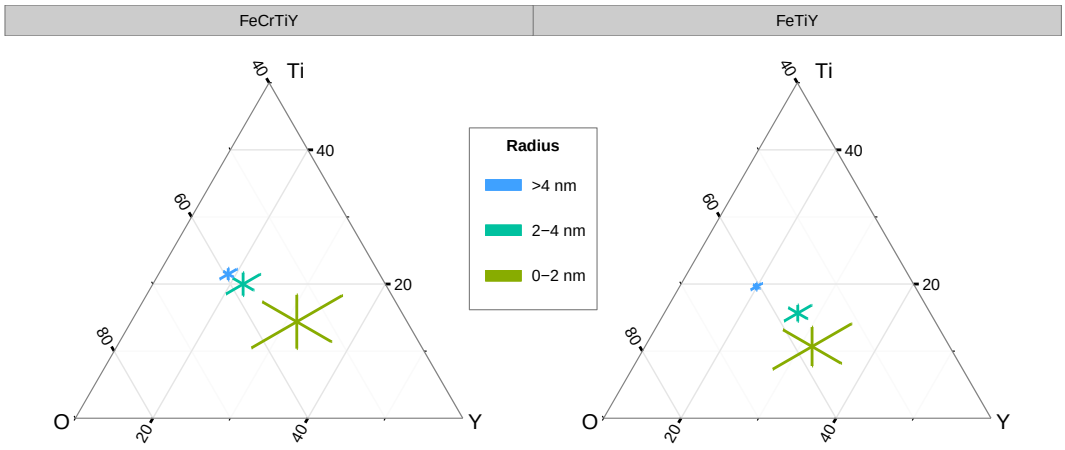

Figure 5.4.9 – Ternary diagram error analysis with estimated counting error for each component (Y,Ti and O) given by $\pm\sqrt{counts}$. The counts of elements are grouped by cluster radius. The centre of the error bar shows the median cluster composition grouped by cluster radius. The smallest radius group has the greatest error. Median number of atoms per cluster in FeTiY: 127, 1039 and 6493 atoms for the 3 size ranges and in FeCrTiY: 89, 680 and 2752 atoms.

size ranges for clarity. Some 2 nm radius clusters have a low metal:oxygen ratio, even as low as 1:1 after removing the ions associated with the matrix. For the >2 nm radii clusters in both FeTiY and FeCrTiY, the variation of Y:Ti ratios is greater than the statistical counting error. The estimated counting error is shown schematically for comparison in figure 5.4.9 for comparison. Figure 5.4.9 also shows the median cluster compositions and demonstrates the systematic variation of cluster composition with size.

In FeCrTiY, there are more clusters with a composition similar to that of $Y_2Ti_2O_7$ and in FeTiY, there is a spread of compositions between $Y_2Ti_2O_7$ and Y_2TiO_5. FeTiY has some larger clusters with high Y-contents, but both FeTiY and FeCrTiY have small clusters with high Y-contents. The spread in cluster compositions is summarised in figure 5.4.10 using Y:(Ti+O) ratio histograms.

The microstructural measurements of cluster chemistry can be compared to the crystal structure observed in the bulk using X-ray diffraction. Glancing incidence XRD was performed to measure the crystal structure for the as-received samples. Figure 5.4.11 compares the as-received samples of FeTiY and FeCrTiY as well as annealed samples of FeTiY. All samples show a peak matching (222)-$Y_2Ti_2O_7$, though the peak in the heat-treated samples

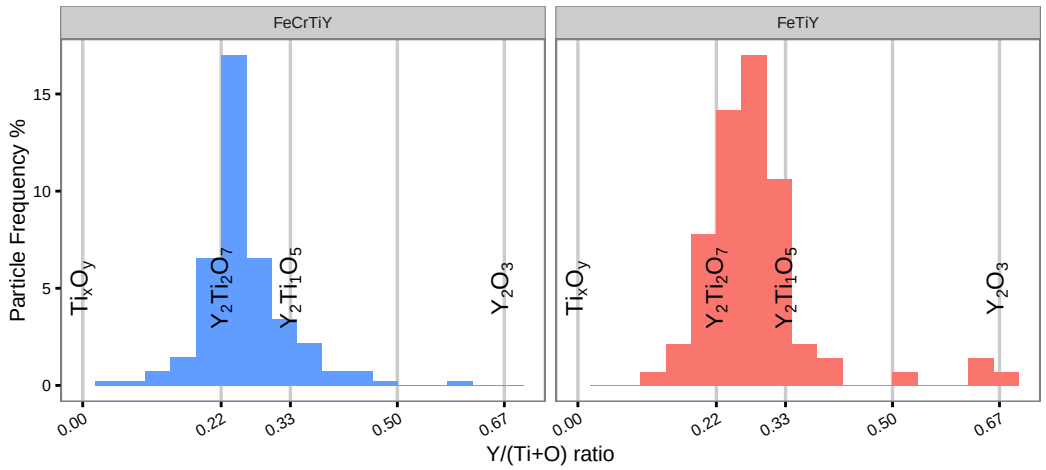

Figure 5.4.10 – Y:(Ti+O) ratio histograms of clusters in FeCrTiY and FeTiY. Only clusters with a radius > 3 nm are shown. The Y:(Ti+O) ratios of the stable bulk oxides are marked for comparison.

is slightly relaxed (smaller d-spacing). The as-received sample of FeTiY also shows a weak broad peak matching the reflections from (230) and (201)-Y_2TiO_5. In both cases, the large peak width is due to strain or small crystallite size rather than instrumental broadening. Despite the difficulty in observing these low volume-fraction and nano-crystalline phases, this XRD data confirms the presence of a $Y_2Ti_2O_7$ crystal structure in both materials. The possible observation of Y_2TiO_5 in FeTiY agrees with the APT data presented in figure 5.4.10 that the cluster compositions of larger clusters in this alloy can contain more yttrium.

5.4.3 Local Cluster Chemistry

Having investigated the individual cluster chemistry, I now consider the interfacial chemistry of the clusters. This is analysis was made using composition line profiles parallel to the analysis direction. The reasoning behind this approach is explained in section 4.5.1 on page 99.

Figure 5.4.12 shows the average composition line profiles for all of the as-received alloys. The Y, Ti and O profiles all define the clusters, with no obvious interfacial enhancement. Any asymmetry in the line profile is an artefact of the atom probe experiment because the orientation of the clusters in the material is random. The O profile is slightly asymmet-

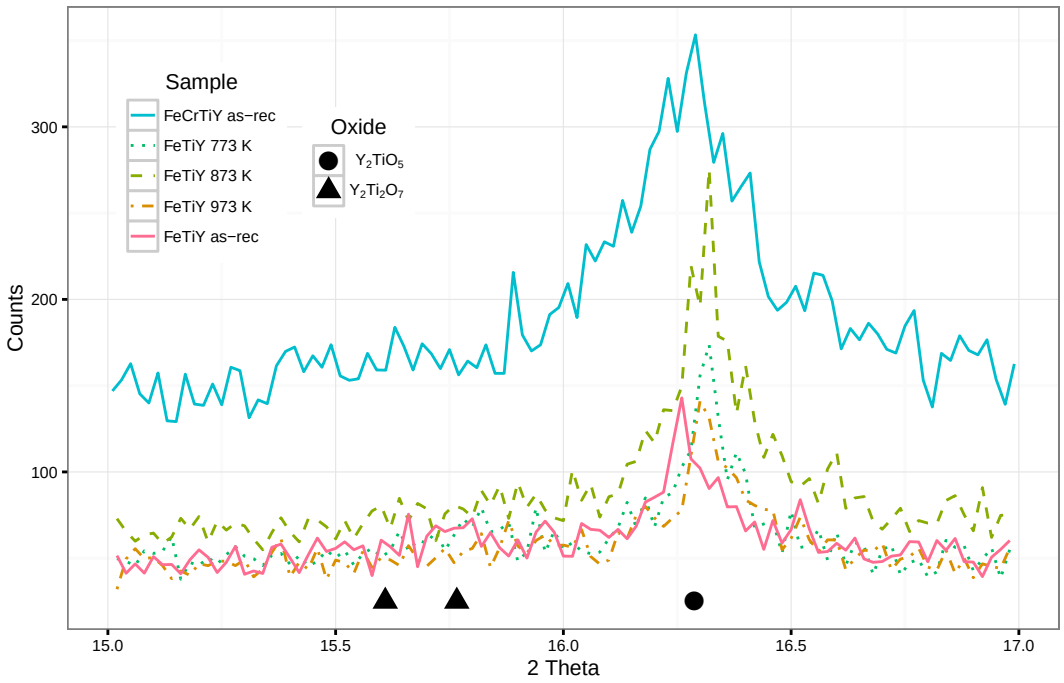

Figure 5.4.11 – X-ray diffractogram of the $Y_2Ti_2O_7$ peak in detail from the as-received FeTiY and FeCrTiY alloys. Additionally, the diffractograms of FeTiY after heat treatments at 723, 823 and 923 K for approximately 14 h are also shown as dashed lines. No obvious peaks for Y_2TiO_5 are visible, but there is a small shoulder at the appropriate 2θ value in FeTiY. The differences in intensity are due to the differing surface areas of the different samples.

rical towards the left (evaporating later), possibly due to retention of oxygen-containing species on the tip. The Cr profile is also slightly skewed, with a higher concentration at the bottom of the clusters than the top.

In FeCrTiY, the Cr-level is about 12 at% in the bulk, but is enhanced at the cluster surface and in the centre. This is consistent with the clusters having a Cr-rich shell which is partially projected into the cluster centre by trajectory aberrations during the atom probe experiment. The Cr-shell is asymmetrical, with a seemingly higher concentration after the cluster than before; this can be explained by looking at the ionic composition.

Table 5.4.2 shows the total ionic cluster compositions excluding Fe and Cr. The majority components are Y, YO, O and FeO in FeY and FeY-hi, with the addition of TiO in FeTiY and CrO in FeCrTiY. Only <20 % of the ionic composition oxygen is detected as elemental oxygen; the remainder is detected as part of a molecular ion with a metal element. Some clusters do contain Fe or Cr oxides, such as the cluster shown in figure 4.4.4 on page 98,

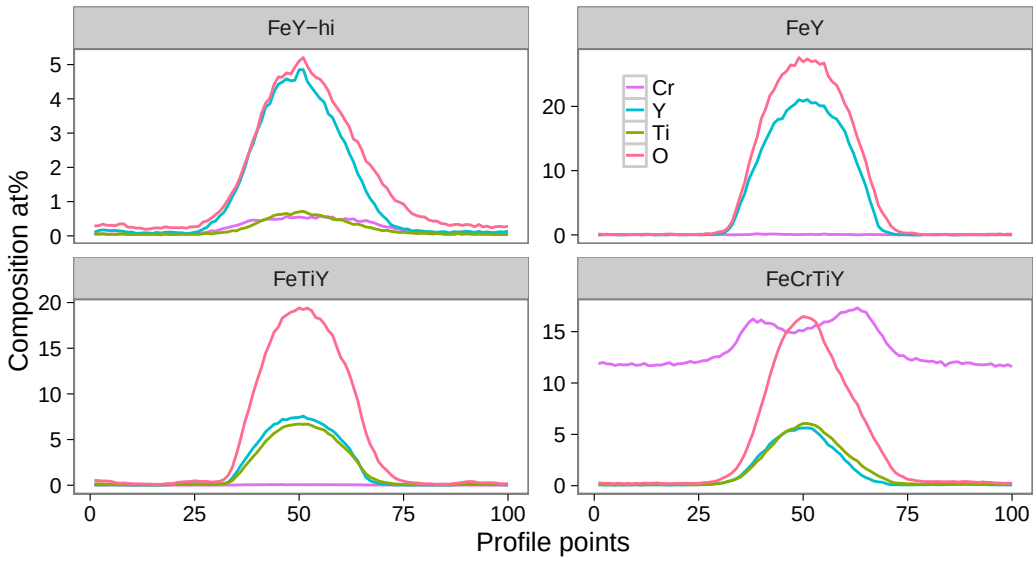

Figure 5.4.12 – Averaged composition line profiles parallel to the analysis direction in FeY, FeY-hi, FeTiY and FeCrTiY. Clusters averaged: FeCrTiY 1058, FeTiY 211, FeY 37 and FeY-hi 1046. Only a few anomalous clusters have been excluded from the analysis. All the ions have been decomposed into elements and Fe has been omitted from the plot for clarity. 20 "profile points" = E_z.

but these are omitted from the average line profiles. Separating out FeO and CrO ions in the composition line profiles highlights some interesting features.

Figure 5.4.13 shows four key pieces of data. Note that this data has no matrix correction and Fe has been included in the composition measurement, therefore the solute (Y, Ti and O) content scales with the average cluster size, c.f. figure 4.5.4 on page 103. The fact that the chemistry varies as a function of cluster size is evident in the relative heights of the Y, Ti and O composition profiles. The Cr ions in FeCrTiY clearly have a shell-like profile for all the cluster size ranges. Though Cr-rich shells have been reported by APT and TEM previously (section 2.3.2 on page 16), the averaged composition line profiles show the size dependence of these features. Finally, the CrO ions in FeCrTiY take a profile similar to the FeO ions in FeTiY, as emphasized in figure 5.4.14 which shows the CrO and FeO profiles in FeCrTiY. Because of the asymmetry of the CrO and FeO ionic profiles in figure 5.4.14, these are considered artefacts of the APT experiment.

Rather than trying to measure the Cr-shell thickness from the averaged line profiles, the Cr behaviour can be inferred from the matrix-corrected cluster composition as a function

Ion	FeCrTiY	FeTiY	FeY	FeY-hi
CrO	13.8	-	9.9	1.4
CrO_2	2.9	-	10.6	-
Fe_2O	2.6	3.7	4.2	4.9
FeO	12.6	13.0	16.7	12.6
O	4.3	7.3	9.8	9.8
O_2	3.3	10.9	9.3	3.0
Ti	-	1.3	-	-
TiO	23.3	25.6	-	7.0
TiO_2	2.7	4.5	-	-
Y	13.1	17.6	15.6	30.1
YO	9.7	13.0	17.4	21.4

Table 5.4.2 – Ionic cluster composition (total) in at % calculated from ionic composition line profile data. A "-" indicates a measured composition of less than 1 at% and ions with <1% composition were omitted from the table. Fe and Cr ions were excluded from the the composition calculation.

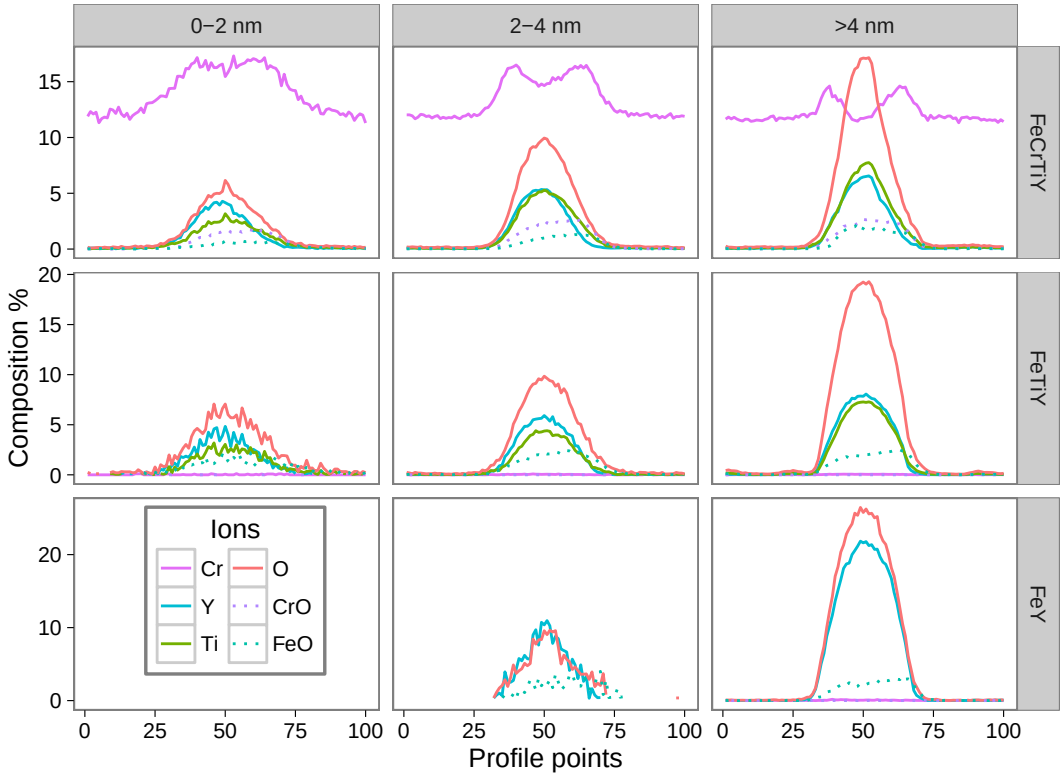

Figure 5.4.13 – Averaged composition line profiles, grouped by cluster radius, parallel to the analysis direction in FeY, FeTiY and FeCrTiY. FeO and CrO ions are shown separately to the other decomposed elements, Cr, Y, Ti and O. 20 "profile points" = E_z.

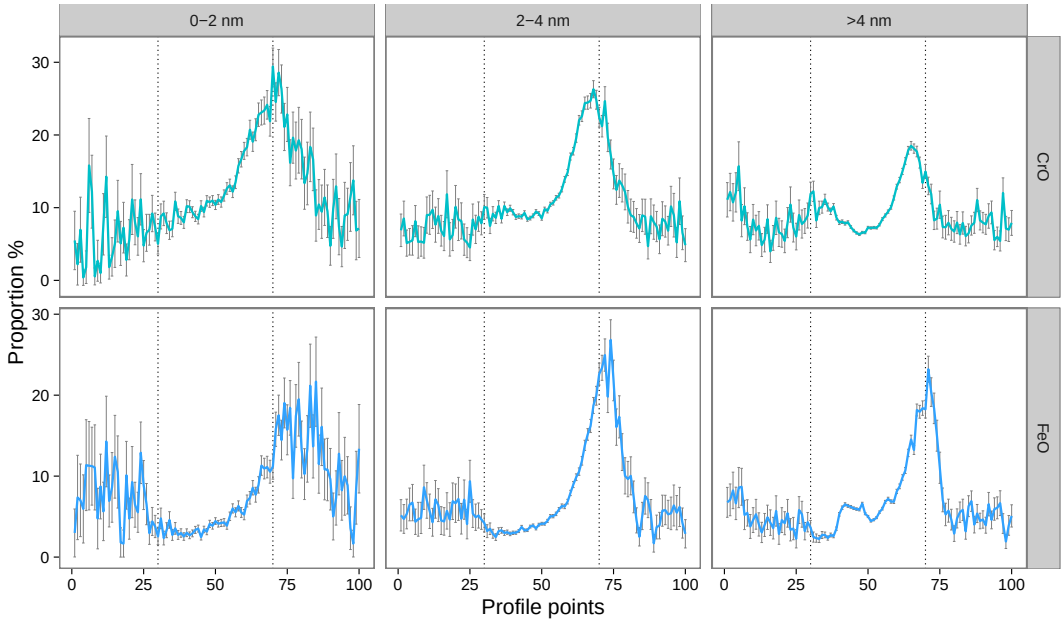

Figure 5.4.14 – Averaged ionic line profile for clusters in FeCrTiY *excluding Fe and Cr* in the composition calculation. Vertical error bars are representative of the counting error; calculated using $\pm\sqrt{N}$, where N is the number of counts of that ion at each profile point. The dashed vertical lines at 30 and 70 profile points mark the cluster extent.

of size, which is shown in figure 5.4.15. Both FeCrTiY and FeY-hi alloys are considered and it is assumed all of the Cr from the shell is included in the clusters. FeY-hi shows some increase in Cr content with decreasing cluster radius, and FeCrTiY has a Cr content proportional to the reciprocal cluster radius. Figure 5.4.16 shows the averaged matrix-corrected Cr composition line profiles for different cluster sizes. With increasing cluster size, the Cr-shell appears broader but also at a lower concentration.

Next we turn to the nominally Cr-free alloys, and investigate the ionic composition of the cluster interface. By excluding Fe from the composition line profile calculation the fraction of each ion can be given for each profile point. The Cr impurities in FeTiY and FeY-hi were investigated in this way in figure 5.4.17. FeTiY contains only a very small amount of Cr, <0.01 at%, but all the Cr that is detected is at the cluster interface. FeY-hi contains 0.05 at% Cr and this is segregated to the clusters, but the proportion profile in figure 5.4.17 shows that this Cr is proportionally greater at the interface (compared to the other solute ions) and is detected primarily as Cr, not CrO ions. Figure 5.4.15 does not show a

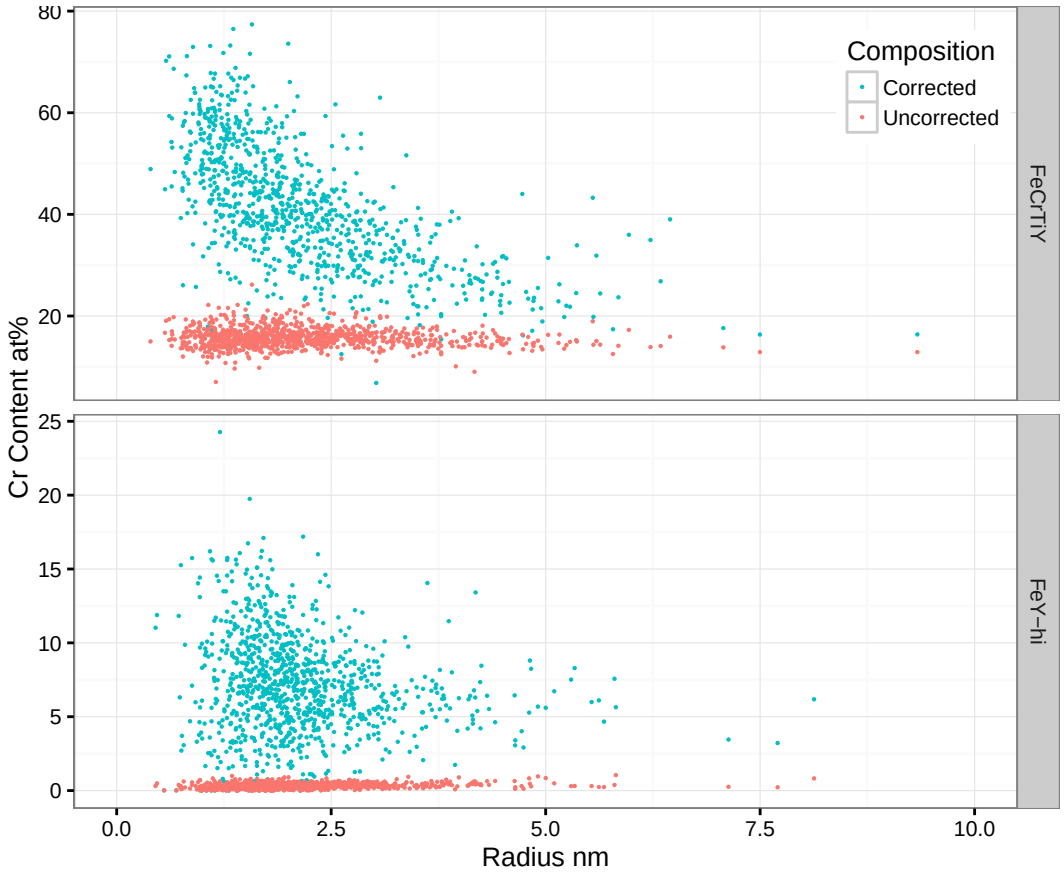

Figure 5.4.15 – Cr content of clusters in FeCrTiY and FeY-hi. "Corrected" refers to a matrix correction of removing Fe with 12 at% Cr.

definitive trend for the content of Cr against size in FeY-hi and the Cr-content is much lower than the FeCrTiY alloy, but the Cr-content of the smaller clusters seems higher than in the larger clusters, which agrees qualitatively with the composition shown in 5.4.17 (compare the Cr-content in the 0–2 nm panel with the >4 nm radius panel). Therefore, though the Cr concentration of the bulk is vastly different between FeCrTiY and FeY-hi, the behaviour of Cr in both alloys seems similar.

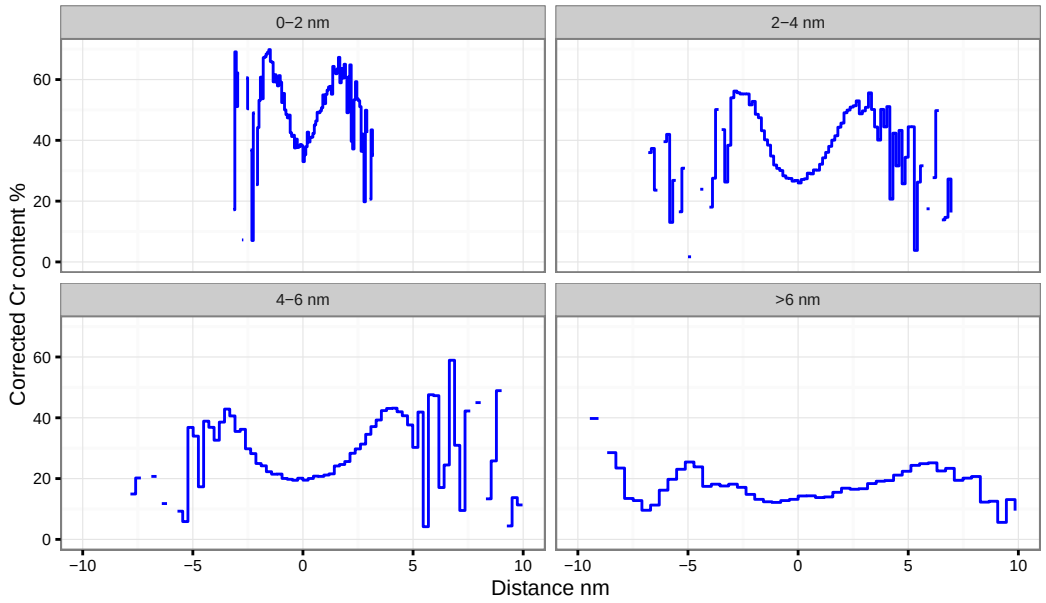

Figure 5.4.16 – The matrix-corrected Cr composition line profiles scaled by the mean cluster radius in FeCrTiY. Line profiles are first scaled to each cluster radius, then averaged together, and finally the averaged line profiles are scaled by the average cluster radii to give an x-axis in nm. $Cr_m = 0.135$.

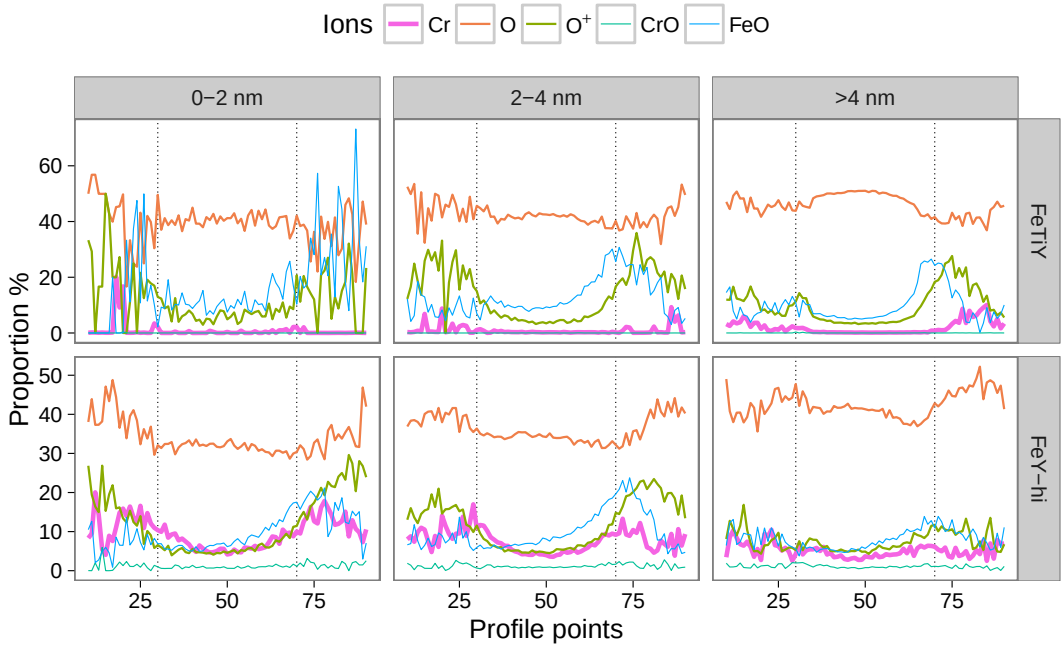

Figure 5.4.17 – Averaged ionic proportion line profiles from FeTiY and FeY-hi excluding Fe in the composition calculation. Outside the clusters there are very few non-Fe counts, hence the increased variance of these points. The dashed vertical lines at 30 and 70 profile points mark the cluster extent.

5.5 Inhomogeneity

5.5.1 Introduction

The powder processing of oxide dispersion strengthened steels often produces an inhomogeneous spatial distribution of oxide particles within the steel as noted in section 2.3.5. The inhomogeneous nature of ODS alloys may affect the materials' properties, and the method used to measure it was explained in section 4.6.

Chemical inhomogeneity was evident in the FeY alloy, which contained Cr-oxide contamination (figure 5.3.1 on page 118), and in the Y:Ti ratio of clusters in FeTiY and FeCrTiY as measured by APT and EFTEM. Spatial inhomogeneity of the particle density and particle size is also apparent and can been seen in EFTEM images like the one shown in figure 5.5.1. Heterogeneity probably arises due to the difficulty of achieving chemical homogeneity during mechanical alloying [295] and this section outlines the observations and measurement of the inhomogeneity of the alloys in their as-received state.

5.5.2 Spatial Variation

Figure 5.5.2 shows the number density of clusters measured in different APT experiments. The results are from electropolished needles with no spatial correlation between the sam-

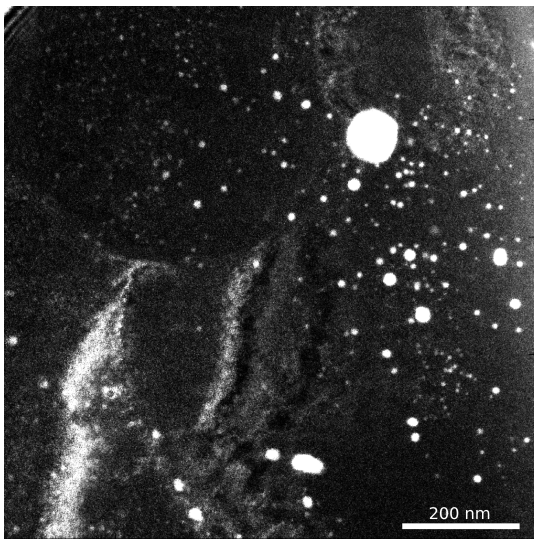

Figure 5.5.1 – Image from EFTEM analysis of FeCrTiY showing the signal from Ti and Y. A varied spatial distribution of particles and particle sizes are present. The particles show as bright on a dark background. The thickness varies from 70 nm in the bottom left corner to 30 nm in the top right corner.

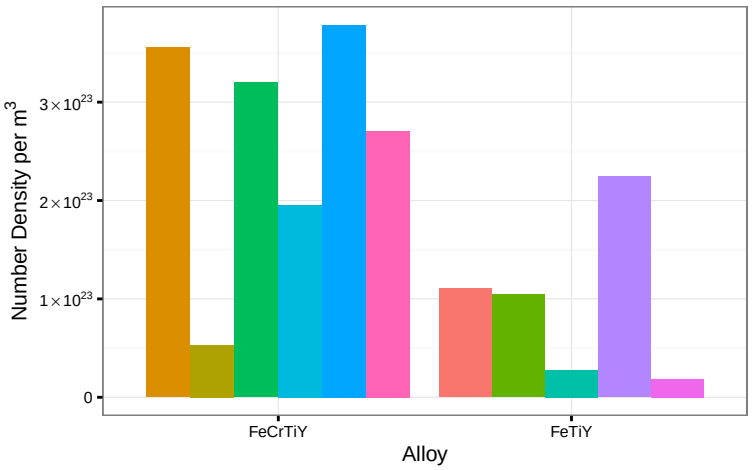

Figure 5.5.2 – The number density of clusters measured by APT. The different coloured bars show the results from different experiments. There is a large variation in the measured number density, numerically reported in table 5.3.1 on page 120.

ples. In experiments prepared by the FIB liftout method, samples are separated by a few micrometers, and so some pairs of experiments yielded very similar particle number densities: 1.06 and 1.09, 3.07 and 2.71, 1.01 and 1.07 (all $\times 10^{23}$ m^{-3}). From these data then, it is possible that the particle number density is homogeneous on a scale of ~4 um. This is greater than the scale that APT can investigate, but looking in detail at the spatial distribution, rather than the average, can give some insight to the spatial inhomogeneity.

5.5.3 Measuring H

Section 4.6 on page 109 describes how spatial inhomogeneity may be quantitatively measured using the normalised H parameter. H is normalised against a random distribution of points so that distributions of different numbers of points can be compared.

Figure 5.5.3 shows how the H of the cluster centres varies with the scale used to measure it. A random distribution of points has $H = 0$ and this is the case for FeY and some experiments in FeCrTiY and FeTiY. A negative H indicates a stronger than random arrangement, which is expected at smaller length scales because physically the cluster centres cannot overlap, whereas random points are not necessarily evenly distributed in space. $H > 0$ indicates some degree of inhomogeneity, and in figure 5.5.3 this occurs at short length scales and this is the tendency of larger length scales as well. $H \gg 0$ at small scales for dense clusters of points, and at larger distances H increases because of larger scale patches of

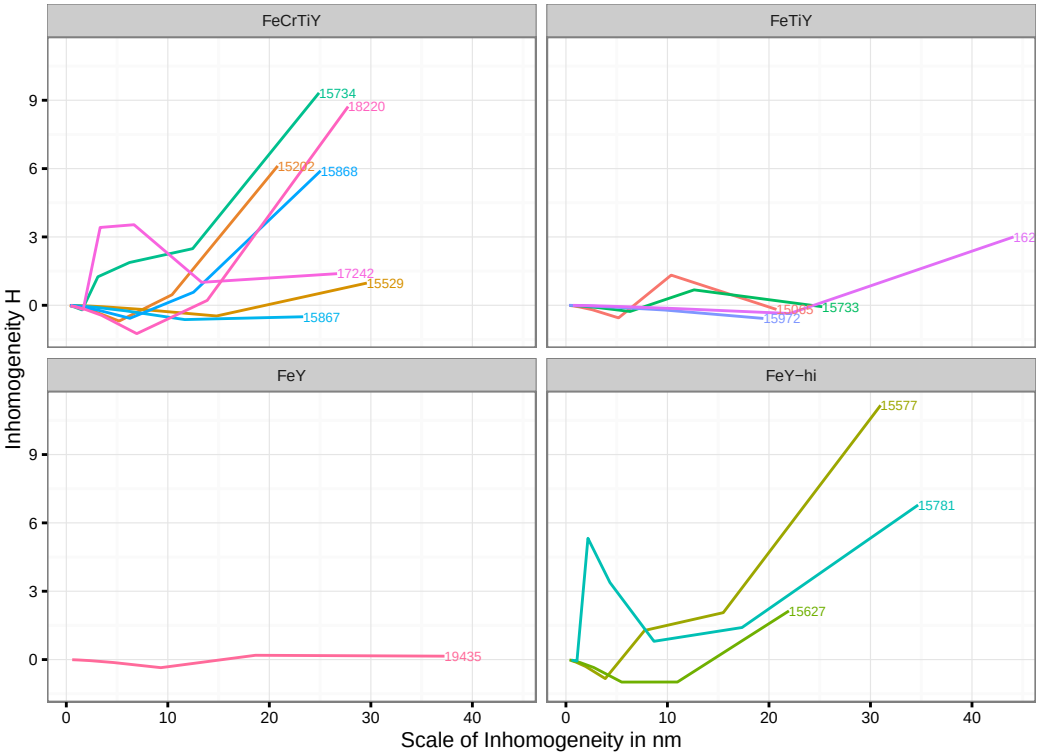

Figure 5.5.3 – Measurement of spatial inhomogeneity of cluster centres in the as-received alloys. The different coloured lines show different atom probe experiments.

high and low point densities. The samples are not consistently inhomogeneous and there is considerable variance between different experiments from the same alloy.

5.6 Discussion

5.6.1 FeY

The simplest extruded model alloy Fe-Y_2O_3 contains much larger clusters than those identified in other alloys without added titanium reported in the literature, such as ODS-Eurofer97, which contains clusters with a r_g of 0.8 ± 0.07 nm, or 2.2 nm corrected radius compared to the mean radius measured in FeY of 6.6 nm. The short mechanical alloying time of 4 h may not have fully mixed the components, resulting in larger clusters, or the contamination introduced by the longer milling time in other alloys may have helped limit the cluster growth. Eurofer97 contains many more elements, such as V, Ta and Cr which are active in

the cluster nucleation and growth mechanisms [155].

5.6.2 Processing Route

Examining the difference between the extruded FeY and HIPed FeY-hi alloys gives some insight to the influence of the processing route on the cluster character. FeY was extruded at 1323 K and FeY-hi was HIPed at a higher temperature of 1423 K (2 h at 195 MPa). The primary difference between these two alloys is the processing route, but it is expected that the difference in milling time, rather than consolidation method, accounts for the difference in behaviour. The FeY-hi sample was milled for 20h compared to the 4h milling time of the FeY sample. The prolonged milling time of FeY-hi is responsible for the higher level of contamination because the milling balls were made from steel containing both titanium and chromium. The contamination may also explain the observed reduction in particle size, as titanium is well known to have this effect [52, 55]. Unfortunately, without further systematic study, it is not possible to quantify the separate contributions of the milling time and the chemistry to the final particle size, but this serves to highlight the importance of processing parameters and the necessity of controlling them.

It is not the primary aim of this work to study the particle formation, but the particle formation and evolution has some bearing on the irradiation behaviour. Hsiung et al. [296] reported that irregular-shaped yttria was produced by the mechanical alloying, but in FeY the particles had a spherical and smooth morphology. Additionally, figure 5.3.1 on page 118 shows Y-oxides attached to Cr-oxides, which suggests that some form of heterogeneous nucleation has occurred, either Cr oxides on Y_2O_3 or the other way around. Therefore, I conclude that the yttria particles are not inert in the ferritic matrix but that during the consolidation there is considerable diffusion and rearrangement, causing the change in morphology and possibly nucleating on existing Cr-oxides. The larger oxide particles, of either initial Y_2O_3 powder or Cr-oxide contaminants, may not be fully broken up by the short duration of mechanical alloying (4 h).

5.6.3 Influence of Ti

The addition of Ti increased the hardness from 1.8 to 2.5 GPa, which is explained by the reduced average cluster radius, 6.6 ± 3.6 nm to 3.0 ± 1.7 nm, and the tenfold increase in cluster number density to 1.3×10^{22} m^{-3}. The strengthening caused by the particles is proportional to the number density and diameter, $\sqrt{Nd}$ [297]. The $\sqrt{Nd}$ values for FeY and FeTiY are 1.2×10^{7} m^{-1} and 2.4×10^{7} m^{-1}, suggesting that the hardening caused by the particles in FeTiY is twice that of the particles in FeY. The plot of $\sqrt{Nd}$ versus hardness (including FeY, FeTiY and FeCrTiY) has a slope of 5.9×10^{-8} GPa.m and an intercept of 0.9–1.3 GPa, consistent with the hardness of pure iron (1.4 GPa) [298]. The refining influence of Ti is consistent with other observations in literature that the addition of Ti produces much finer Y-Ti-O particles [52, 55] and improves the high temperature properties [56], but there is still controversy over exactly why Ti has this effect.

Ribis et al. [114] observed a distinct difference in the athermal behaviours of Y-Ti and Y_2O_3 oxides at high temperatures (>1300 K). Conversely, Williams et al. [128] observed classical coarsening behaviour of both Y-Ti oxides and Y_2O_3 oxides with similar growth rates at 1473 K, even though they had different initial average sizes. Evidence in favour of a strong influence of titanium on the coarsening behaviour is provided by Ratti et al. [299], who milled a base Fe–18Cr–1W powder with 0.3 wt% yttria and an optional 0.8 wt% titanium. After annealing both powders at 1123 K for 1 h, each contained ~1.5 nm particles (as measured by SANS), with the Ti-containing powder having a sharper size distribution. Following annealing at 1373 K for 1 h, the Ti-free powder contained 12 nm particles compared to 2 nm particles in the 0.8 wt% Ti powder. Dramatic coarsening was observed after annealing at 1573 K, with only the 0.8 wt% Ti powder containing sub-20 nm particles. Modelling work focusing on the particle formation has not found a conclusive answer to the role of Ti [156, 157, 300], but shows that both Y and Ti are important in forming a high density of small clusters. Therefore, the role of Ti may be both to enhance the nucleation of clusters and to reduce their rate of growth at elevated temperatures.

As reported in [301], $Y_2Ti_2O_7$ and Y_2TiO_5 structures were observed with different fre-

quencies in FeTiY and FeCrTiY. However, structural analysis of HRTEM images showed a more frequent occurrence of Y_2TiO_5 over $Y_2Ti_2O_7$. In my work, APT identified clusters predominantly chemically similar to $Y_2Ti_2O_7$ and the GIXRD results showed a reflexion consistent with this; however, a significant variation in Y:Ti ratio was observed by APT and EFTEM. The observed variation was partly due to a systematic variation with size but was generally larger than the statistical error. From the results shown in figures 5.4.8 and 5.4.10, I conclude that a range of nano-particles exists with the $Y_2Ti_2O_7$ pyrochlore structure but with a range of compositions: $Y_xTi_yO_{7-\delta}$ (x+y = 4). This might explain some of the observations of clusters with unidentified structures [112] and it is consistent with the observation of defects in the oxide particle structure [144].

5.6.4 Influence of Cr

Besides varying the Cr content between 9 and 14 wt% to give martensitic or ferritic microstructures and the associated alpha-gamma phase transformation [39], there has been little research into the influence of Cr on the oxide particles in ODS steel. The comparison of the FeTiY and FeCrTiY alloys allows some insight to the effect of Cr. My FeCrTiY alloy contains clusters smaller than that of the FeTiY alloy, 2.1 ± 1.2 nm compared to 3.0 ± 1.7 nm with a threefold increase in number density to 3×10^{23} m^{-3}. The hardness was also increased, from 2.5 GPa to 3.2 GPa, presumably due to both the change in particle distribution and additional hardening from the Cr in solution in the Fe. The high number density of small clusters is comparable to results for similar alloys, presented in table 5.6.1. Therefore, the short milling time in an attritor mill and extrusion process used here can produce a fine distribution of clusters similar to alloys produced by long milling times (40 h) in ball mills and hot-isostatic pressing (9Cr-ODS [135] and 12YWT [132]).

The consolidation temperature of the Cr-containing alloy was 1423 K, while for the FeTiY alloy a lower temperature of 1323 K was used. Therefore, the Cr-containing alloy should have a larger average particle size than the FeTiY alloy based solely on the consolidation temperature [70]. Previous work on ODS alloys containing 9 and 18 wt% Cr

Alloy	r_G nm	$N_d \times 10^{23}$ m^{-3}	Ref.
9Cr-ODS	3.4 ± 1.8	9.8	[135]
14YWT	1.0 ± 0.2	4	[66]
12YWT	2.0 ± 0.8	14	[132]
MA957	1.2 ± 0.4	20	[60]

Table 5.6.1 – Guiner radius r_G and particle number density N_d in Cr-ODS alloys measured by APT from the literature. All alloys contain 0.2–0.9 Ti and 0.2–0.3 Y by wt%.

consolidated at the same temperature also show a reduced particle size in the higher Cr content alloy (2.5 nm compared to 4.5 nm modal particle size) [231].

Without the addition of Cr, and in 9Cr ODS alloys, it is expected that the alloy would transform to austenite during the high-temperature extrusion and consolidation processes described above [302], although some residual ferrite may be retained [303]. Kim et al. [304] observed an increased growth rate of ODS oxide particles, which coincided with the transformation from α to γ iron [304]. This could be explained both by the loss of coherency of the particles with the matrix and by the enhanced diffusion of the solute along gamma grain boundaries [305]. Table 5.6.1 shows that the 9Cr-ODS alloy contained larger particles with a lower number density than the higher Cr-content alloys. Therefore, the Cr addition may indirectly affect the particle growth rate by suppressing the α to γ phase transformation of the matrix.

The influence of Cr on the matrix and the Cr-shell around the Y-Ti rich clusters may also contribute to the minor changes in cluster chemistry that were observed between FeCrTiY and FeTiY. The surrounding matrix and the Cr-shell may alter the strain on the growing clusters, which, in turn, could influence the crystal structure and chemistry of the resulting clusters [306]. The difference in extrusion temperature could also explain why more cluster compositions closer to the thermodynamically stable $Y_2Ti_2O_7$ stoichiometry were found in the Cr-containing alloy.

Cr-shell

In all the alloys, Cr was detected at the periphery of the oxide clusters. Composite clusters containing separate regions of Y-oxide and Cr-oxide were especially noticeable in FeY (figure 5.3.1). The small size of the particles limited the measurement of the Cr-shell thickness using EFTEM, and the reduced resolution of the atom probe in the vicinity of the oxide clusters limited quantification of the shell thickness. Nonetheless, FeY-hi showed some increase in apparent Cr content with decreasing cluster radius, and in FeCrTiY, the corrected Cr cluster content was proportional to the reciprocal cluster radius (figure 5.4.15). This behaviour suggests a constant Cr-shell thickness independent of cluster radius. If the shell has a fixed thickness and the cluster radius is small, then the whole cluster will have a high Cr-content, but a large cluster with the same Cr shell thickness will have proportionally much less Cr. Perhaps the most interesting finding is the identification of a Cr-rich shell in clusters with a radius smaller than 2 nm, and the detection of Cr at the cluster interface in alloys with a very low Cr-content (figure 5.4.17).

There may be some influence of the cluster selection method on the exact measurement of excess Cr at the clusters because the selection was optimised for sensitivity, not to detect a Cr-shell. Figure 5.4.16 showed the matrix-corrected shell profile with a decreasing Cr-content with increasing cluster radius but also a broadening of the width of the Cr-enrichment. The segregation is assumed to be a few monolayers thick [307] and therefore the broadness of the shell occurs because of the reduced resolution of the atom probe in the vicinity of the oxide clusters. A fixed shell thickness would be consistent with saturated monolayer Cr segregation to the cluster surface.

5.6.5 Are Fe and Cr oxide components?

The evidence from APT is that Cr segregates to the surface of the clusters whenever it is present. However, it is not convincing from APT results alone that no Cr or Fe exists within the clusters because of the trajectory aberrations that overlap Fe and Cr ions from the matrix into the cluster core. Standard TEM experiments cannot wholly exclude the presence

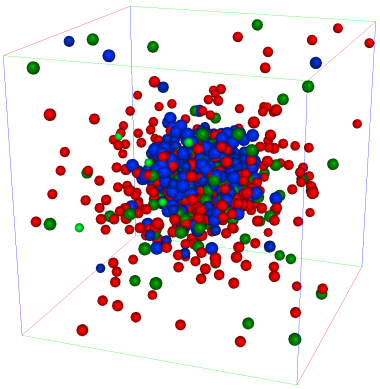

Figure 5.6.1 – Oxygen ions (red) are observed to be spread laterally from the Y-Ti containing cluster (blue and green). The volume is 15x15x15 nm^3

of Fe or Cr in the particles because the measurement is projected through an Fe-Cr matrix, but chemical extraction of the particles has shown that there are no mixed Fe-Cr-Y oxides [106, 308]. The segregation of Cr to the surface of the nanoparticles, rather than its presence within them, is consistent with the results of theoretical calculations that indicate a repulsive interaction between Cr and Y/Ti [156]. Cr segregation is expected from long-range elastic strains caused by the misfit of the oxide particles in the matrix and the difference in thermal expansion coefficients [307].

Based on the evidence above, it seems unlikely that there is either oxidised Fe or Cr in the particles. The molecular FeO and CrO ionic species detected by APT are likely formed by oxygen atoms originating from the particles combining with Fe or Cr from the matrix and evaporating as molecular species. Similarly, partially-oxidised Cr-rich shells have been reported in similar alloys [109]. The concentration of O^+ ions in figure 5.4.17 show some increase at the edges of the cluster but it is not clear if these are part of a oxygen-rich shell, as O ions are often observed spread (laterally) from the cluster, c.f. figure 5.6.1. The evidence from figure 5.4.13 on page 134 suggests that the Cr-shell is metallic and not oxidised, contrary to the observations in smaller clusters that the Cr is oxidised and part of the cluster [153].

5.6.6 Spatial Variation

A variation in the chemistry of the oxide particles has been observed as a function of spatial location. This presumably results from incomplete mechanical alloying, but without examining the powder during the milling process it is not possible to be sure of this. The variation in bulk alloy chemistry does not seem to influence the size or number density of the particle distribution, and only slightly changes the particle chemistry. The spatial inhomogeneity could lead to a change in materials' properties due to dislocations traveling more easily through volumes containing fewer particles [171].

As measured in 3D by APT, the cluster centres are not homogeneously or evenly distributed in my alloys and the level of inhomogeneity varies between different samples of the same alloy. This indicates the scale of the spatial variation is greater than the scale probed by APT. This agrees with the measurement of particle number density by APT (figure 5.5.2), which show a large variation between cluster number densities measured from different locations.

5.7 Summary and Conclusions

The four alloys given in section 3.1 on page 44 have been characterised by TEM, APT, XRD and nanoindentation. It was found that:

- the compositions were as expected, with the exception of a low level of Cr contamination in all nominally Cr-free alloys and significant contamination of Cr and Ti in the FeY-hi alloy, presumably from the milling media;

- the dependence on sample volume was shown to be important in estimating the bulk composition using APT;

- the hardness of the alloys increases with the addition of Ti, from 1.8 to 2.5 GPa, and further increases when Cr is also added, from 2.5 to 3.2 GPa;

- the FeY and FeY-hi alloys contained very different particle distributions and this was explained by the difference in milling times, 4 compared to 20 h;
- the addition of Ti transformed the bcc-Y_2O_3 to the $Y_xTi_yO_{7-\delta}$ pyrochlore, with TEM and APT showing some variation in the exact composition of the phase formed; the O-fraction was ~60 at% and decreased slightly with decreasing cluster radius;
- the addition of Cr did not significantly alter the oxide chemistry, but did cause a decrease in the Y:Ti ratio (which was also shown to vary as a function of cluster size);
- a Cr-rich shell was formed around all the clusters in FeCrTiY and evidence was presented in favour of a constant shell thickness with cluster size; and
- a variation in cluster number density was observed in APT and quantitative measurements of the inhomogeneity of the cluster distributions were made.

The results of ion-irradiation experiments in the following chapter can now be compared to this baseline characterisation to elucidate the influence of irradiation on the oxide particle dispersion.

Chapter 6

Ion Irradiation Experiments

6.1 Introduction

The baseline of the as-received alloys was established in the previous chapter. In this chapter, the influence of ion-irradiation at temperatures between 773 and 973 K to a peak damage dose of 150 dpa is investigated. These temperatures were chosen so that these results would be comparable with others in the literature [23, 135, 309] and to cover the maximum temperature range that these alloys would encounter in service [310]. Additionally, the FeCrTiY and FeTiY alloys were irradiated using Fe^{+} ions to 100 dpa at cryogenic temperatures where almost all diffusion is frozen out to investigate the irradiation damage in the absence of thermal effects. Historically, irradiation at cryogenic temperatures has been used to investigate irradiation damage [311], but only a few groups have applied it to ODS alloys [24, 190, 221].

Following irradiation at selected temperatures (see the tables in section 3.2 on page 45), the microstructure was characterised using the same techniques given in chapter 5: TEM, APT, GIXRD and nanoindentation. This chapter focuses first on the effect of single high-temperature ion-irradiation of FeY before looking at the effect of irradiation of FeTiY and FeCrTiY at 773–973 K. The behaviour of FeTiY and FeCrTiY show some contrasting features, which are compared in section 6.2.4 on page 171. Lastly, the cryogenic irradiation

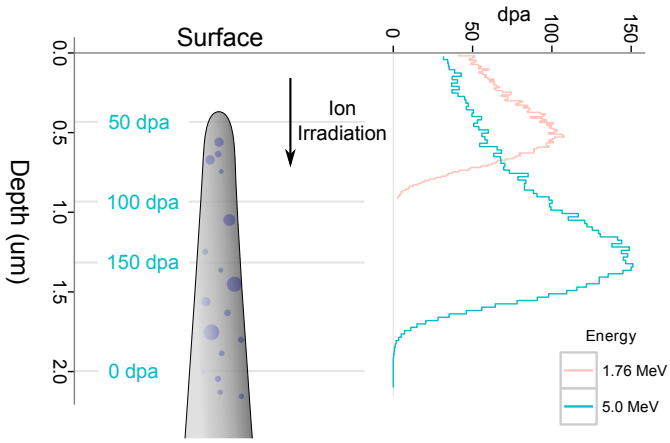

Figure 6.2.1 – Schematic showing the depth-damage dependence of APT samples taken perpendicular to the irradiated surface. Both Fe ion energies are shown, 1.76 MeV and 5 MeV. Damage in dpa predicted by SRIM–see section 3.2 for details.

results are presented, followed by a discussion of the influence of ion-irradiation temperature on the stability of the oxide particles in these model ODS alloys.

6.2 High-Temperature Irradiation

6.2.1 FeY

FeY was only irradiated at one temperature, 773 K, to a peak damage of 150 dpa (as predicted by SRIM). The APT samples taken from FeY had a depth range which translates to a damage range of 43–117 dpa. A schematic showing the depth-damage dependence of APT samples, taken perpendicular to the irradiated surface, is shown in figure 6.2.1.

The oxide particle dispersion after irradiation was examined by EFTEM and APT. Figure 6.2.2 shows typical EFTEM data from a cross-section of the irradiated and unirradiated FeY sample. The unirradiated sample is taken from below the implanted region. The particle number density and average particle size are very similar between the irradiated and unirradiated samples. However, distinct composite Cr-oxide and Y-oxide particles were not observed in the irradiated samples. Atom maps from the irradiated FeY sample are shown in figure 6.2.3. Large clusters, similar to those in the as-received FeY alloy (figure 5.2.2b), can been seen, but there is also a high number density of very small Y-rich clusters. These clusters were observed to align along 1D features, probably pre-existing dislocations (figure 6.2.3a) and at grain boundaries (figure 6.2.3b and 6.2.4a). Figure 6.2.4a shows an atom

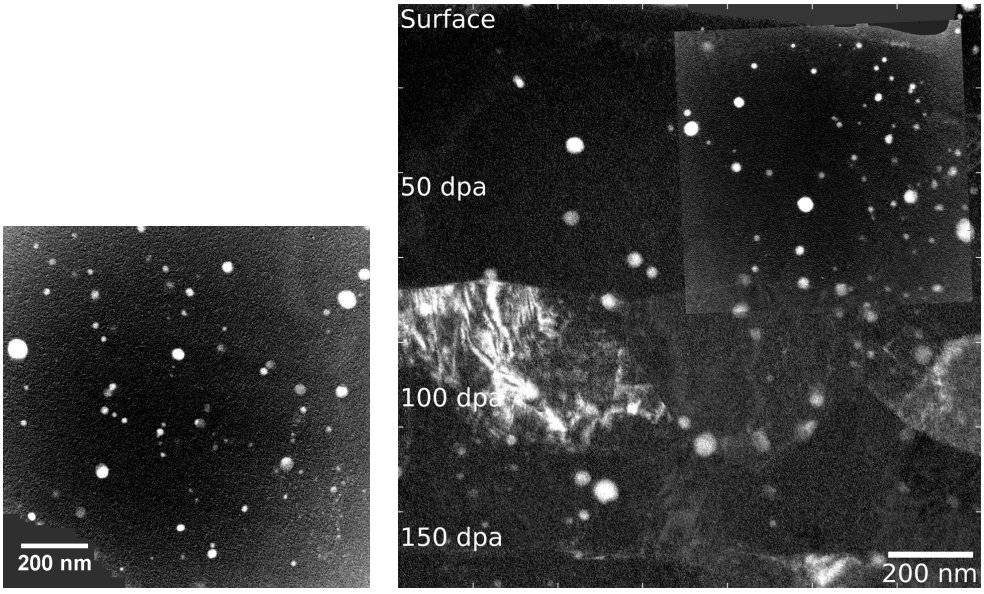

(a) 773 K 0 dpa **(b)** Irrad. 773 K 150 dpa

Figure 6.2.2 – (a) EFTEM image (Y-N2,3 edge) from FeY away from the irradiated surface; no damage but experienced the same 773 K 14 h heat treatment (2–3 h of heating, 14 h of irradiation, and then cooling ~0.5 h). (b) Irradiated FeY cross-sectioned perpendicular to the surface. The peak damage, predicted by SRIM, is at the far right of the image ~150 dpa. Both images have a similar Fourier-log thickness of 1.2

map of a mixed Cr-Y oxide with a composition of $Fe_{59}O_{31}Cr_{8.4}Y_{1.3}$ at% and a high density of very small Y-rich clusters in the plane of a GB. A similar oxide was identified in another sample of the same irradiated material containing $Fe_{59}O_{29}Cr_{9.9}Y_{1.6}$ at%. The extent of the mixing of Cr and Y is compared between the irradiated and as-received samples in figure 6.2.4b. The as-received sample shows very little mixing except at the interface, presumably due to trajectory aberrations; however, the irradiated sample shows considerable mixing of Y with Cr.

The modal cluster radius measured in all 6 experiments was greatly reduced, from 7.12 nm in as-received FeY to 1.05 nm after irradiation (773K). This was accompanied by a dramatic increase in cluster number density from 7.8 ± 4.2 to $47.1\pm28.0 \times 10^{21}$ m^{-3}.

The composition of the GBs observed by APT in as-received and irradiated FeY are summarised in table 6.2.1. The as-received sample showed very little Y on the measured boundary; however, a relatively high O concentration was detected in experiment 15576.

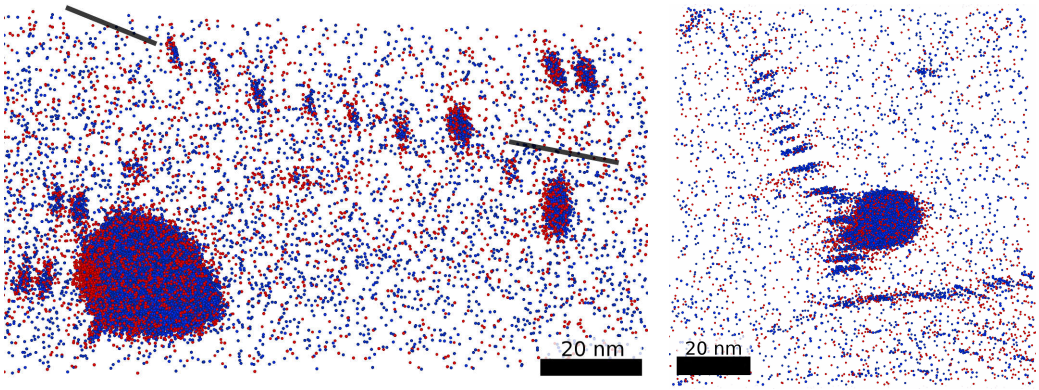

(a) Large Y_2O_3 cluster and smaller Y-rich clusters on a linear feature. Analysis direction right to left. ID: 19793.

(b) Two perpendicular grain boundaries viewed along the line of intersection. Analysis direction top to bottom. ID: 19698

Figure 6.2.3 – Large and small Y-rich clusters in irradiated (773 K ~100 dpa) FeY. Colour key: Y is blue and O is red.

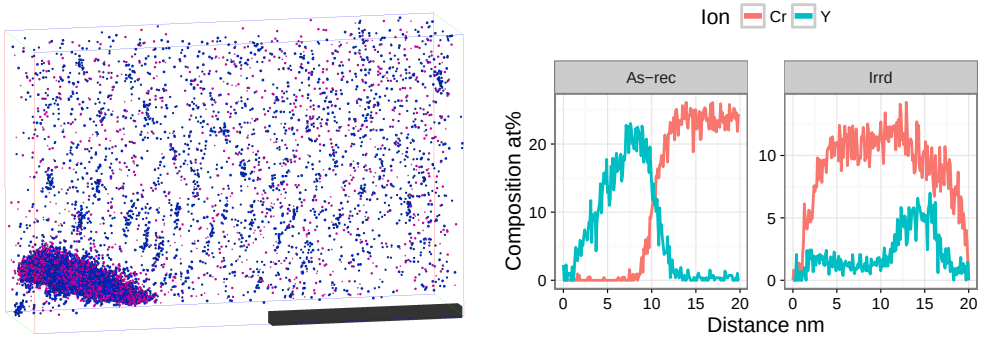

(a) **(b)**

Figure 6.2.4 – (a) Small Y-rich clusters on a grain boundary in irradiated (773 K ~100 dpa) FeY with a mixed Y-Cr oxide $Fe_{59}O_{31}Cr_{8.4}Y_{1.3}$ at%. Viewed perpendicular to the grain boundary. Analysis direction right to left. Colour key: Y is blue and Cr is magenta. ID: 19698. 50 nm scale bar. (b) Y-concentration in a composite cluster in as-received FeY and a mixed Y-Cr oxide cluster in irradiated FeY.

Exp. ID	Alloy	Irrd. T /K	dpa	C	N	Y	O	Cr
15576	FeY	-	0	1.46	0.07	0.06	0.29	0.00
19698	FeY	773	89	0.57	0.00	0.10	0.18	-0.01
19698	FeY	773	94	0.66	-0.01	0.12	0.24	0.04
19698	FeY	773	98	1.21	0.02	0.20	0.48	0.04
19698	FeY	773	101	1.00	0.00	-0.02	0.04	0.04
19698	FeY	773	108	0.32	0.01	0.07	-0.01	-0.04

Table 6.2.1 – Grain boundary segregation in FeY in excess atoms/nm^2.

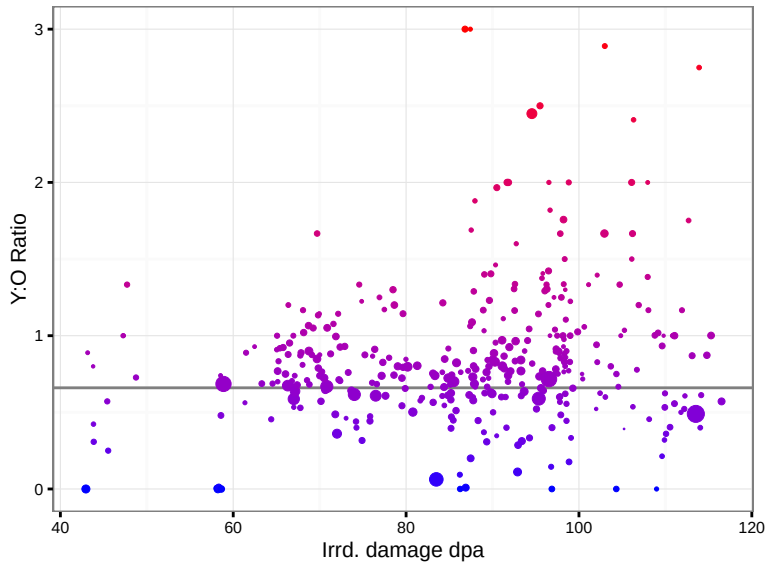

Figure 6.2.5 – Cluster compositions in FeY irradiated at 773 K. Y:O ratio from 6 APT experiments as a function of irradiation damage in dpa. The cluster radius is shown qualitatively by point size.

After irradiation, a reduction in the C and N content of the boundaries was measured and Y with O were consistently observed at the boundaries. As shown in figure 6.2.3, the Y and O were observed in very fine clusters on the boundary plane.

The cluster radius and compositions as a function of irradiation damage are shown in figure 6.2.5. There is no clear trend of radius to damage level, but the clusters with the highest Y:O ratios are in the region of highest damage. Figure 6.2.6 shows that the larger clusters maintained the Y_2O_3 composition of the as-received material but that the smaller clusters have a much larger spread in Y:O ratio and a higher mean Y:O ratio of 0.93 ± 0.55. This is similar to the metal:oxygen ratio of the clusters observed in the FeY-hi alloy; for comparison the metal:oxygen histograms for irradiated FeY and as-received FeY-hi are shown in figure 6.2.7.

Though the composition of the small irradiated clusters in FeY is similar to that of the clusters in as-received FeY-hi, the ionic density is markedly different and mean ionic-density cluster line profiles are shown in figures 6.2.8a and 6.2.8b. In FeY-hi, the Fe ionic density is 30% above the matrix value, but in the irradiated FeY sample, the Fe ionic density is barely perturbed until the cluster radius is greater than 4 nm. Therefore, although the small Y-rich clusters in both samples have similar compositions, their evaporation behaviour is different, possibly indicating a change in cluster nature caused by the irradiation. This

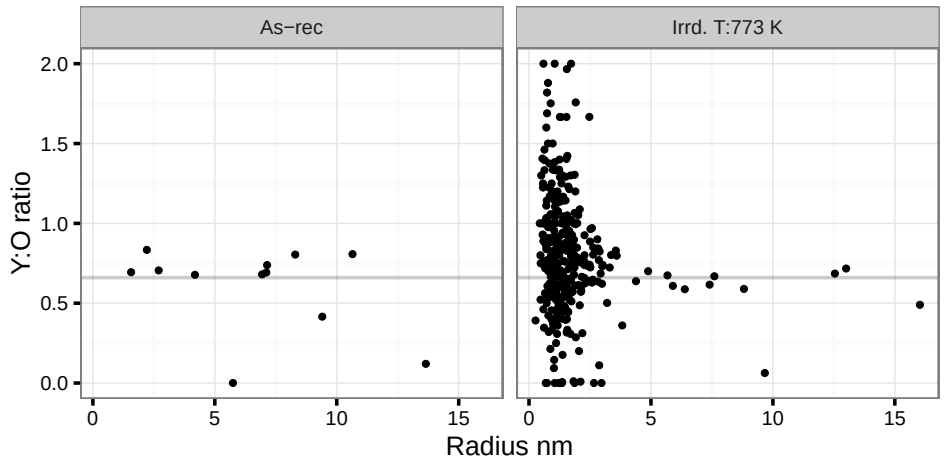

Figure 6.2.6 – Y:O ratio for clusters in FeY before and after irradiation (773 K, 33–57 dpa). Some clusters with Y:O $\simeq$ 0 are Fe-oxides. The horizontal grey line marks the Y:O of Y_2O_3.

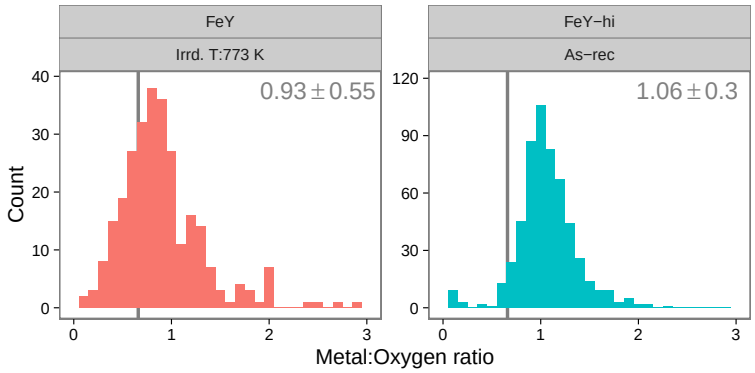

Figure 6.2.7 – Metal:Oxygen ratio of clusters in irradiated FeY and as-received FeY-hi. The numbers in top right of each panel show the mean and standard deviation for both plots. The vertical lines show the M:O of Y_2O_3= 0.67.

change in behaviour may be due to a change in crystal structure.

The crystalline structure of the irradiated layer was investigated by GIXRD and the resulting diffractograms from the as-received, unirradiated and irradiated FeY samples are shown in figure 6.2.9. The (222)-Y_2O_3 peak at 15.6° showed reduced intensity following the irradiation and increased intensity in the unirradiated sample. The increased intensity of the annealed sample indicates some increase in oxide volume fraction and the reduction of intensity in the irradiated sample indicates a reduction in volume or amorphisation of the oxide phase. No new peaks appeared after irradiation, indicating that the newly-formed Y-rich clusters do not diffract.

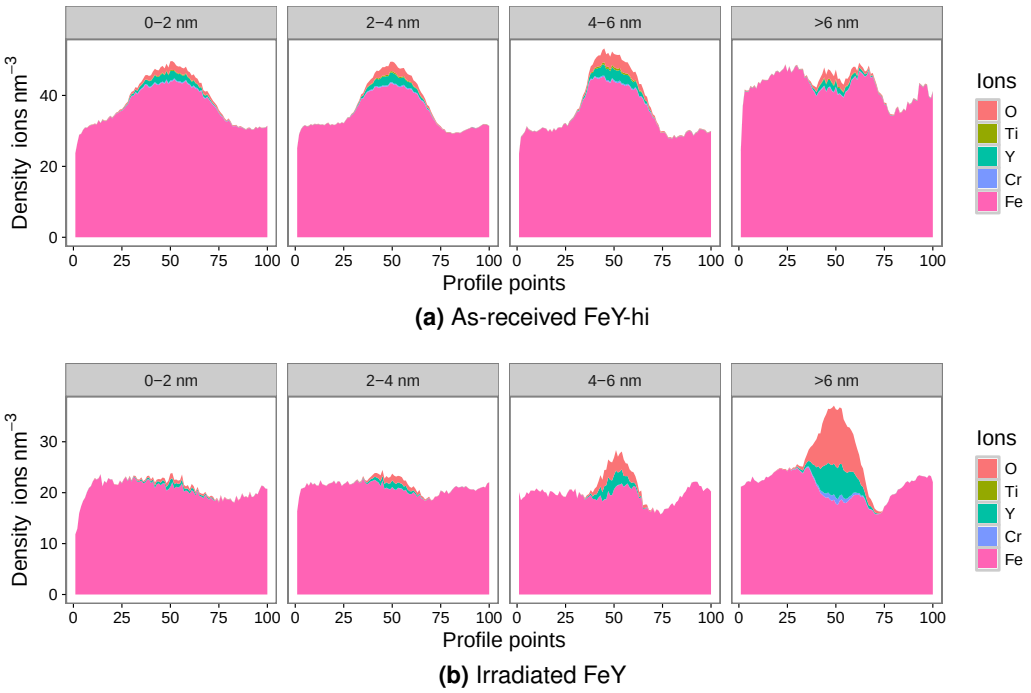

(a) As-received FeY-hi

(b) Irradiated FeY

Figure 6.2.8 – Mean ionic-density line profiles through clusters in (a) the as-received FeY-hi alloy and (b) the irradiated (150 dpa, 773 K) FeY alloy. The clusters are grouped by size (shown at the top of each figure). Profile points from 30–70 represent the total extent of the cluster, $2.E_z$.

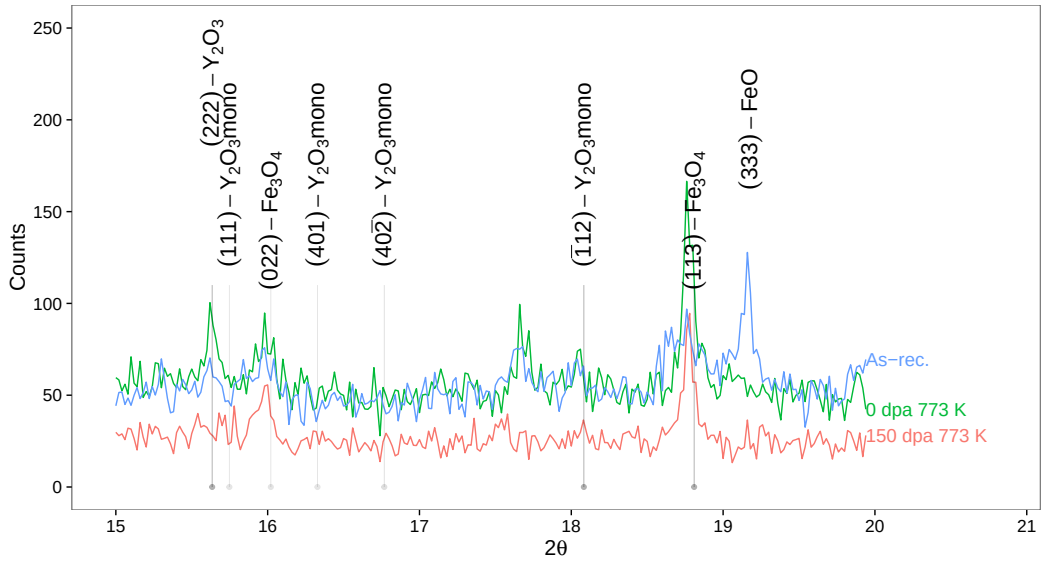

Figure 6.2.9 – As-received FeY, unirradiated (773 K for 14 h, 0 dpa) and irradiated (773 K 150 dpa) examined by GIXRD.

6.2.2 FeTiY

FeTiY was irradiated at three different high temperatures to a peak damage of 150 dpa at 1.2 um from the surface (as predicted by SRIM). The hardness of the irradiated and unirradiated (part of the irradiated sample that was masked during the irradiation) material was investigated using nanoindentation, and the results are shown in figure 6.2.10.

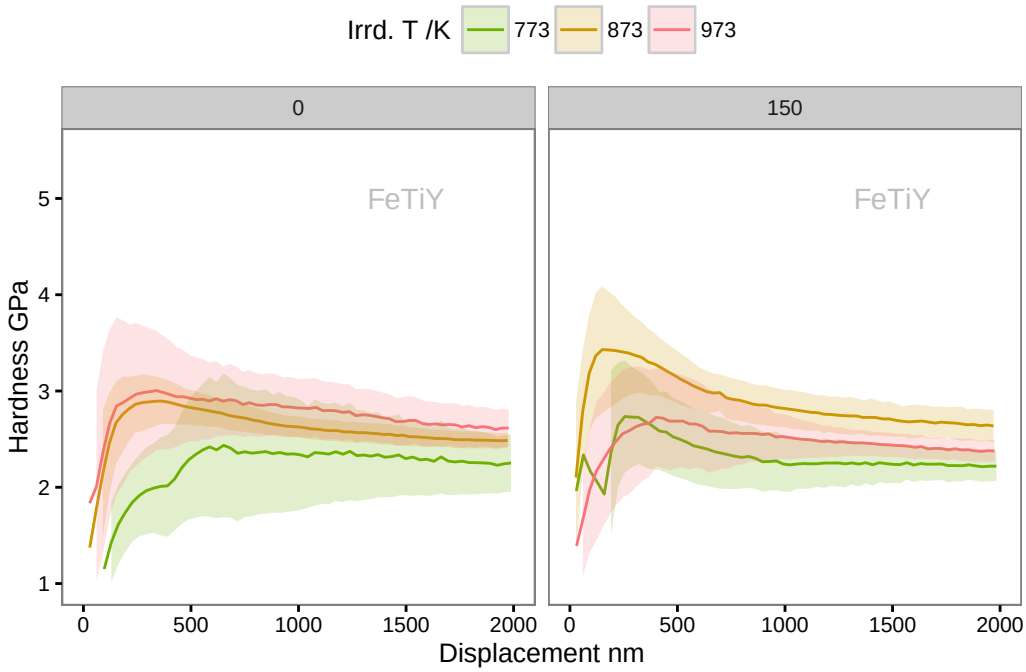

Figure 6.2.10 – Hardness as a function of nanoindentation depth of irradiated and unirradiated FeTiY. The transparent ribbon shows the scatter of indentation results. Approximately 10 indents per sample condition.

The sample surface before irradiation was not ideal due to the mechanical polishing damage, and after irradiation a surface oxide had formed on the samples. Both of these factors make assessment of the nanoindentation difficult as it is very sensitive to the surface finish. However, figure 6.2.10 does show that FeTiY irradiated at 873 K is 0.5 GPa harder at a depth of 200 nm, roughly the overlap of the plastic zone and the peak irradiation-damage layer. FeTiY irradiated at 773 K may also show some hardening compared to the unirradiated 773 K sample.

The crystallinity of the irradiated FeTiY samples was investigated using glancing inci-

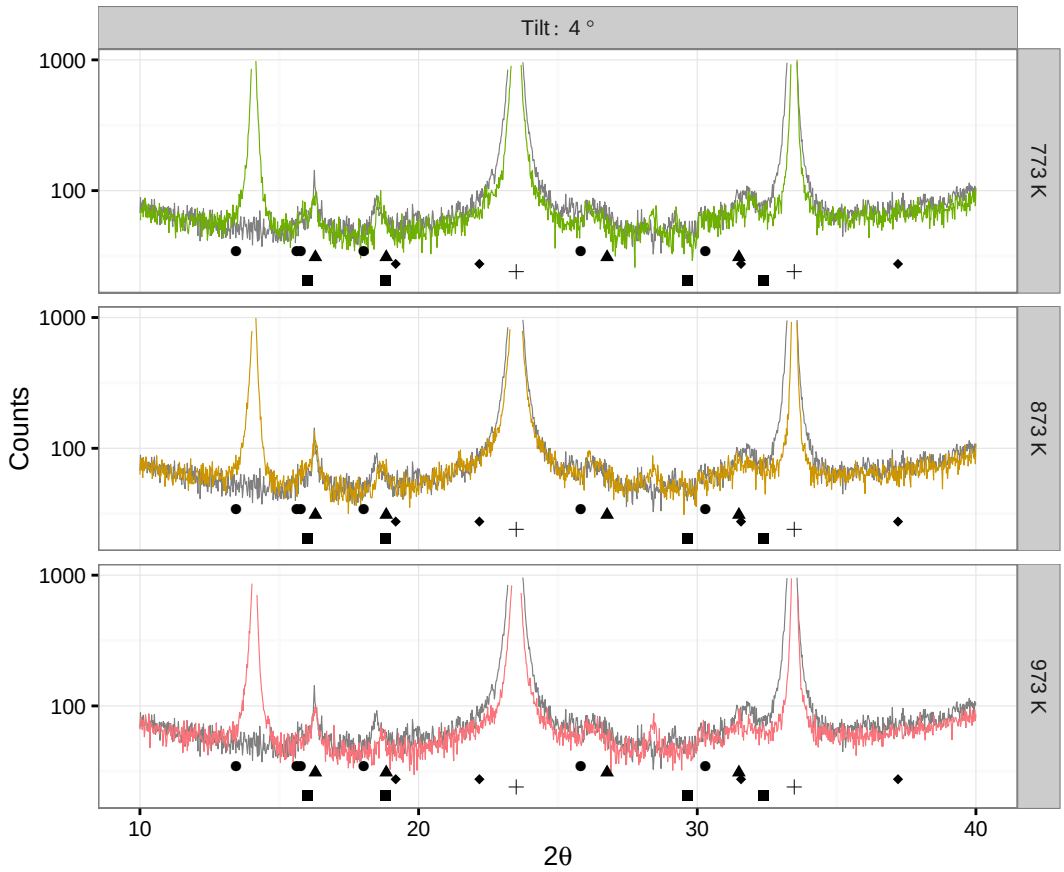

Figure 6.2.11 – GIXRD 10–40° 2θ diffractograms of FeTiY irradiated to a peak damage of 150 dpa. The irradiation temperature is shown on the right hand side. The incident angle is 4° giving a probing depth of 1600 nm, within the 1900 nm deep irradiated layer. The as-received sample is shown in grey. Key: $Y_2Ti_2O_7$ ▲, Y_2TiO_5 ●, FeO ◆, Fe_3O_4 ■, α-Fe +.

dence XRD and the resulting diffractograms are shown in figure 6.2.11. The intense peak at 14° 2θ could not be confidently identified, but is probably due to a surface $Fe(OH)_x$ phase (the peak was stronger in the 2° diffractogram than the 4° incident angle diffractogram, indicating it is a surface feature). There are no other large differences between the irradiated and as-received samples, but the peak at 16° 2θ is shown in detail in figure 6.2.12.

Figure 6.2.12 shows the irradiated and unirradiated (control) diffractograms from FeTiY with an incident angle of 4° focused on the $Y_2Ti_2O_7$-(222) peak at 16.3° 2θ. With the exception of the $T_{irrd} = 873$ K sample, the intensity and widths of peaks in the control samples were very similar to the as-received sample. In the as-received sample and the sample heated to 773 K, small broad peaks, possibly from Y_2TiO_5, were present at 15.6–

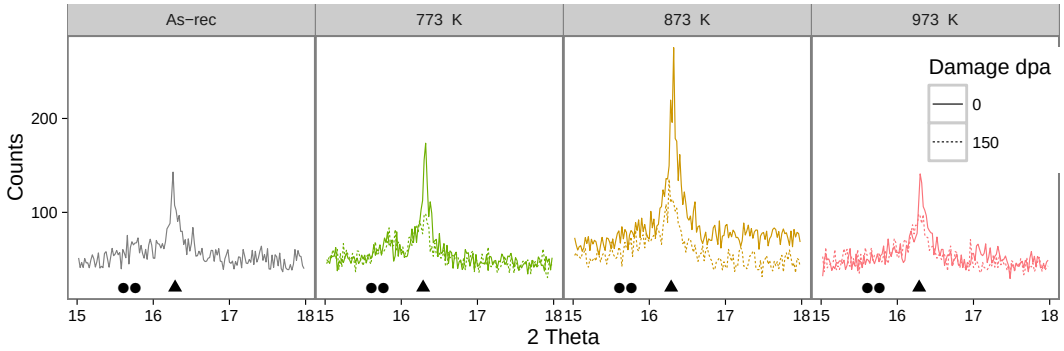

Figure 6.2.12 – Diffractograms of the $Y_2Ti_2O_7$-(222) peak at 16.3 2θ in irradiated and unirradiated FeTiY. The T_{irrd} is shown at the top of each panel. The incident angle is 4° giving a $1/e$ attenuation depth of 1.6 um; therefore 30% of the signal comes from the unirradiated substrate (from >1.9 um deep).

15.7° 2θ, but not in the samples with T_{irrd}>800 K. The sample heated at 873 K (but not irradiated) showed a noticeable increase in intensity compared to both the other unirradiated samples and the as-received sample; however, this sample had a surface area approximately twice that of the other samples. The irradiation had an approximate duration of 14 hours, and even at 973 K, the particles should be stable in the control sample. The thermal stability reported in similar alloys suggests that no effect should be observable until above 1200 K [59, 126, 128, 299, 312].

To quantify the changes the peaks in figure 6.2.12 were fitted using the routine described in section §A.4 (the full fitting results are also given in section §A.4). The peak width, given by the full-width half maximum (FWHM), is shown as a function of irradiation temperature in figure 6.2.13. The instrumental contribution to peak broadening is negligible, ~0.003° FWHM at $2\theta \leqslant 30°$ [234]; therefore the observed peak width comes from a combination of size-strain effects [313]. All of the irradiated FeTiY samples show much broader peaks, with $T_{irrd} = 773$ K having the broadest peak. The background-corrected integrated counts under the (222) peak are given in figure 6.2.14 and the irradiated samples showed systematically fewer peak counts than their respective control samples.

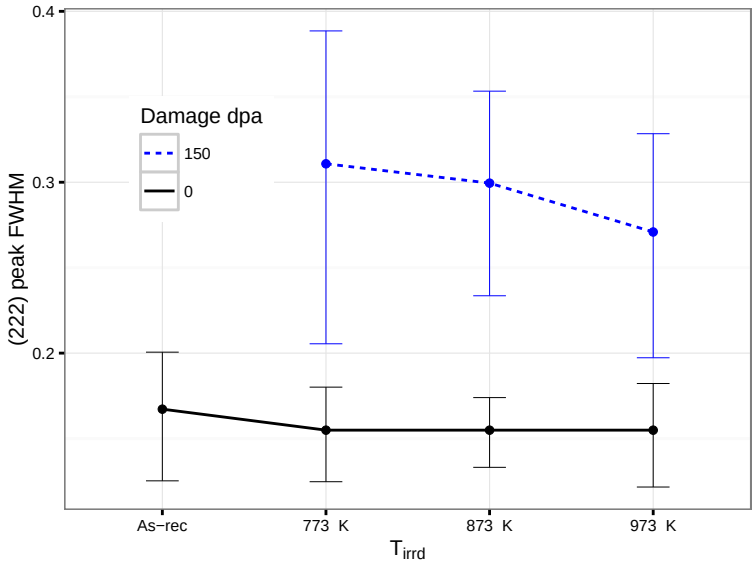

Figure 6.2.13 – The full-width at half maximum of the $Y_2Ti_2O_7$-(222) peak at 16.3 2θ in irradiated and unirradiated FeTiY. Error bars show 95% confidence intervals.

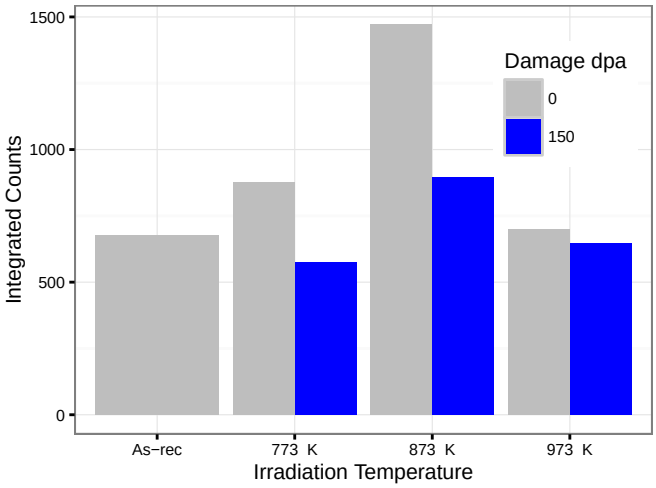

Figure 6.2.14 – The total integrated counts under the $Y_2Ti_2O_7$-(222) peak at 16.3° 2θ in irradiated and unirradiated FeTiY.

The irradiated FeTiY samples were investigated using EFTEM and APT. Ideally, samples would be taken from a specific depth range to give the same level of damage in each; however, this is very difficult and the length of the APT experiment is also variable. Therefore, a range of damage doses were observed; these are given in table 6.2.2. Figure 6.2.15 shows the cluster size (radius r_z) and the approximate cluster number density in irradiated FeTiY measured by APT. After irradiation at 773 K, the cluster distribution was very similar to the as-received state. At 973 K, there was a slight reduction in number density and

Irrd. T /K	Modal radius nm	$N_d \times 10^{23}$ m^{-3}	Damage range dpa
-	2.12	1.0±0.8	0
773	2.01	1.2±0.8	61–102
873	1.28	0.9±1.0	33–150
973	2.65	0.7±0.5	37–65

Table 6.2.2 – Summary of the modal cluster radius, number density and estimated damage range in dpa for FeTiY.

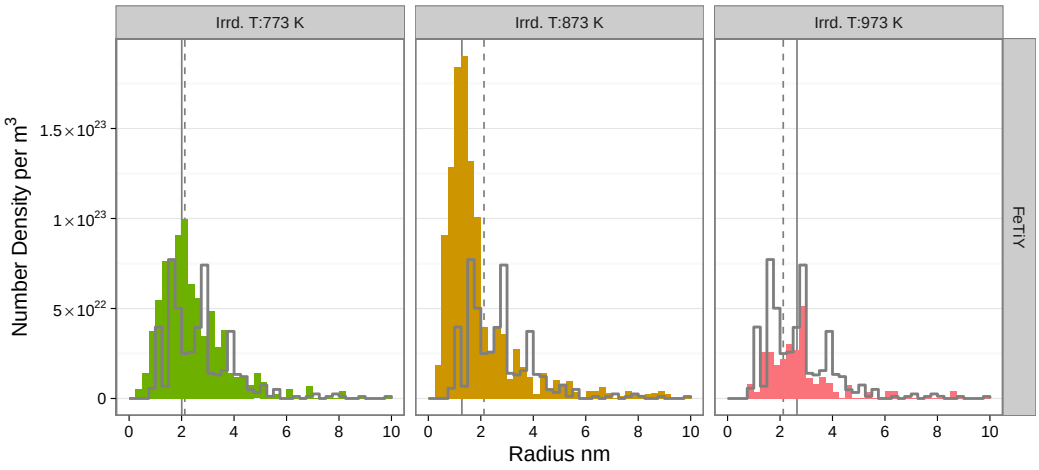

Figure 6.2.15 – Cluster size distribution, scaled by analysis volume to give cluster number density, of clusters in FeTiY irradiated to ~60 dpa at 773, 873 and 973 K. The dashed line shows the histogram of as-received cluster radii. The vertical lines indicate the modal cluster radius for the as-received alloy (dashed line) and the irradiated samples (solid vertical line).

a small increase in cluster size. At 873 K, a high density of 1.2 nm clusters were formed, which increased the number density and reduced the modal radius to 1.28 nm; this is similar to the behaviour of FeY at 773 K noted above.

The odd behaviour of the FeTiY alloy after irradiation at 873 K is also evident in the Y:Ti:O cluster composition data shown in figure 6.2.16. The ternary diagram shows that for T_{irrd} = 773 and 873 K samples, a number of relatively Y-rich clusters were detected, unlike the clusters in FeTiY irradiated at 973 K, which had a higher average Ti-fraction. Only one APT experiment on the T_{irrd} =773 K sample contained many Y-rich clusters, while the clusters in other experiments had a Y:Ti similar to the as-received material. Figure 6.2.16 also shows the effect of the thermal treatment experienced during the ion-irradiation at 773 K on the cluster composition. After the thermal treatment with no irradiation, the average

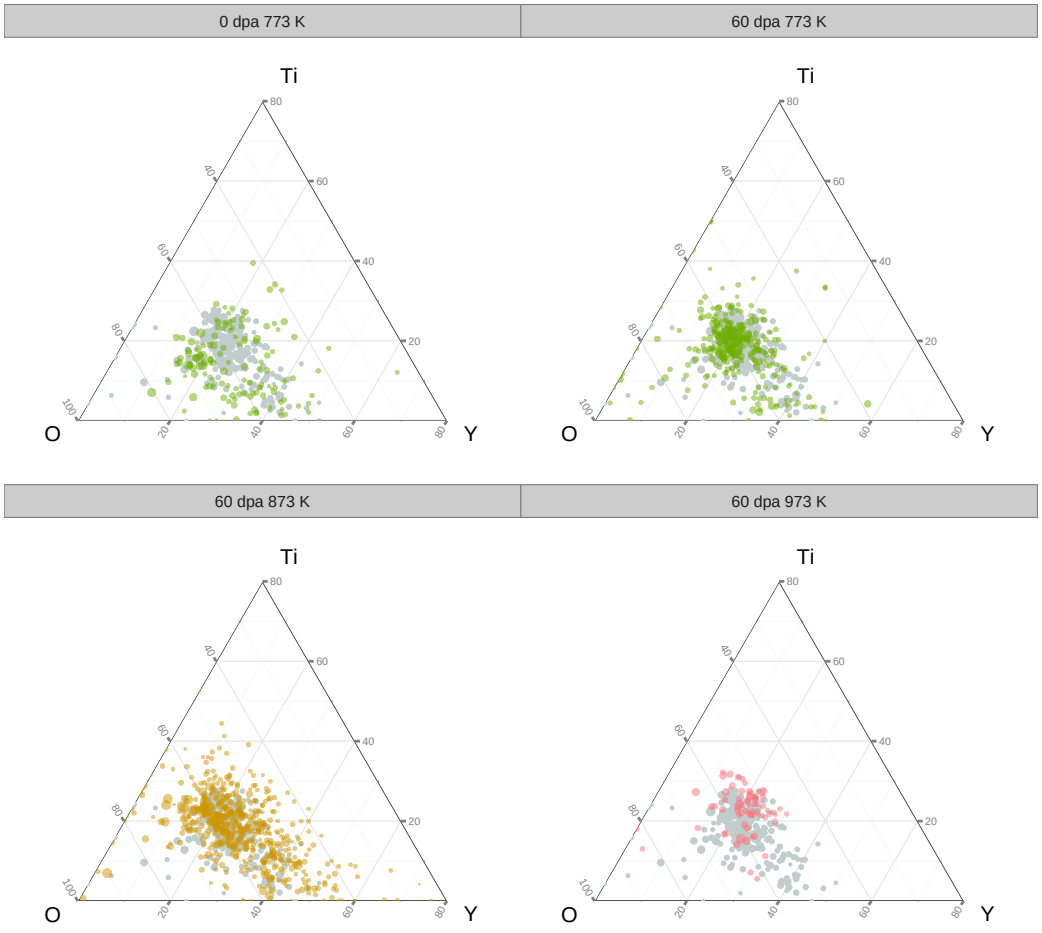

Figure 6.2.16 – Y:Ti:O ternary diagrams showing the change in individual cluster compositions in FeTiY after irradiation to ~60 dpa at 773, 873 or 973 K. The strip at the top of each panel gives the irradiation condition. One panel (top left) shows the cluster composition in the unirradiated material. The points from the as-received clusters (from figure 5.4.8) are shown in grey.

O-content was increased and a wide spread of Y:Ti ratios was observed.

The chemical changes of the overall cluster population is summarised in figure 6.2.17, using a cumulative density plot of the Y:Ti ratio of the clusters. All irradiated FeTiY samples showed an increase in the number of low Y:Ti ratio (Ti-rich) clusters, and the median Y:Ti values of the 773 and 973 K clusters were reduced compared to the as-received sample. The width of the distribution of Y:Ti ratios was reduced for T_{irrd} = 973 K, had a similar breadth for 773 K and was greatly increased for 873 K, in agreement with the observations from the ternary plot (figure 6.2.16). The unirradiated sample heat-treated at 773 K did not show any Ti-rich clusters but had a median Y:Ti of 1.5 and showed broadest distribution of Y:Ti

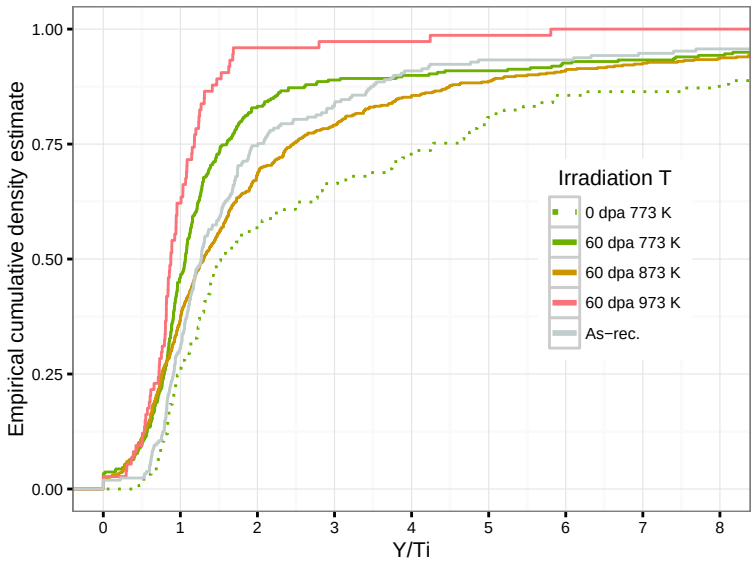

Figure 6.2.17 – Distribution of cluster Y/Ti values in FeTiY after irradiation as shown by an empirical cumulative distribution function (CDF). The empirical CDF is a non-parametric estimator of the distribution of a random variable, resulting in a step function that increases by $1/n$ at each data point. The median is given by the x position at $y = 0.5$.

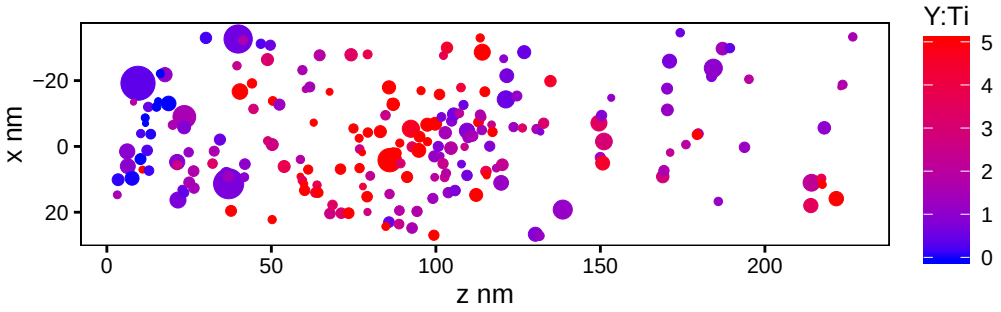

Figure 6.2.18 – Spatial location of clusters in an irradiated sample of FeTiY (~40 dpa, 873 K). The colour scale indicates the Y:Ti ratio and the size of the points is proportional to the cluster radius.

ratios, with 25% of the clusters having Y:Ti > 5.

As for the spatial location of the clusters, figure 6.2.18 shows that the Y-rich clusters in irradiated FeTiY are grouped together, but they do not lie preferentially on grain boundaries like the Y-rich clusters in irradiated FeY. As shown in table 6.2.3, there is generally less solute on the grain boundaries observed in FeTiY as compared to FeY.

Exp. ID	Alloy	Irrd. T /K	dpa	C	N	Y	Ti	O	Cr
15576	FeY	-	0	1.46	0.07	0.06	-	0.29	0.00
19698	FeY	773	98	1.21	0.02	0.20	-	0.48	0.04
17053	FeTiY	873	41	2.10	0.00	0.53	0.42	1.41	0.00
17985	FeTiY	873	120	0.79	0.20	0.08	0.05	0.25	-0.01
19704	FeTiY	873	61	1.46	0.02	-0.01	-0.18	-0.33	-0.08
20013	FeTiY	873	62	1.94	0.06	-0.10	0.04	-0.05	0.00

Table 6.2.3 – Grain boundary segregation in FeTiY in excess atoms/nm^2.

6.2.3 FeCrTiY

Similarly to the FeTiY material, FeCrTiY was irradiated at three different high temperatures to a peak damage of 150 dpa. The hardness of the irradiated and unirradiated samples was investigated using nanoindentation and the results are shown in figure 6.2.19.

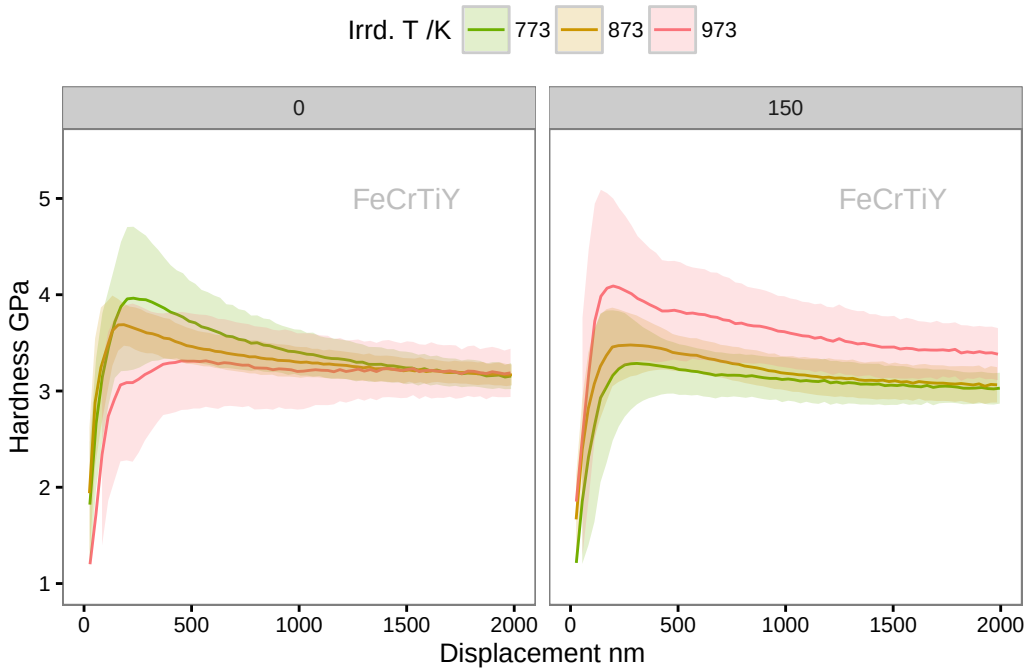

Figure 6.2.19 – Hardness as a function of nanoindentation depth of irradiated and unirradiated FeCrTiY. The transparent ribbon shows the variation in averaged indents. Approximately 10 indents per sample condition.

Again, due to the poor surface finish of the samples before irradiation, a large variation in hardness was measured and no significant hardening was observed in the FeCrTiY sam-

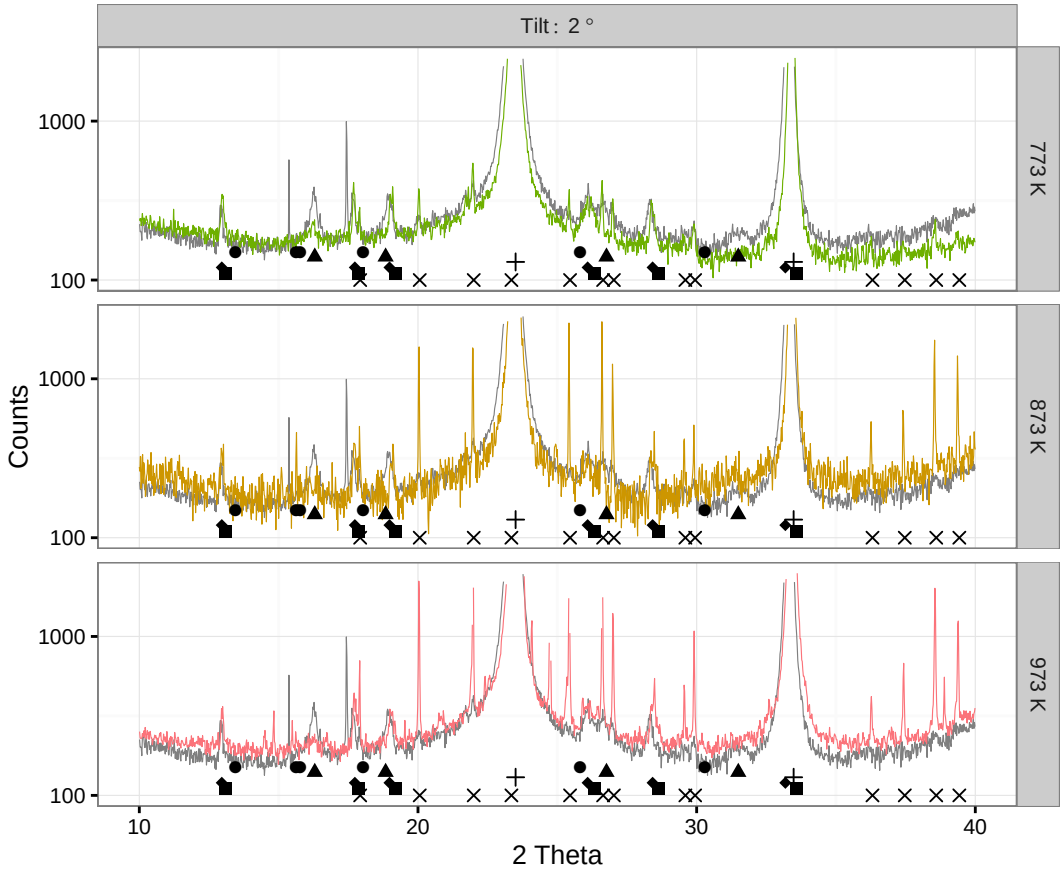

Figure 6.2.20 – GIXRD diffractograms of FeCrTiY irradiated to a peak damage of 150 dpa. The incident angle is 2°, giving a probing depth of 800 nm, well within the 1900 nm deep irradiated layer. The as-received sample is shown in grey. Key: $Y_2Ti_2O_7$ ▲, Y_2TiO_5 ●, $Cr_3Fe_5O_7$ ◆, Cr_2O_3 ■, $Cr_{23}C_6$ x, α-Fe +.

ples irradiated at 773 and 873 K. Figure 6.2.19 shows that the sample irradiated at 973 K was moderately harder (by 0.5 GPa), but this measurement was complicated by the surface oxidation that occurred at high temperature.

To study the changes in bulk crystal structure, GIXRD investigations were performed on the FeCrTiY samples irradiated at high temperature and the diffractograms are shown in overview in figure 6.2.20. The most noticeable change is the increased intensity of peaks from $M_{23}C_6$ carbides, which are just detectable in the as-received sample. The carbide intensity increased with increasing T_{irrd}, and were more intense with a 2° incidence angle (probing depth well within the irradiated layer) than at 4° (probing beyond the irradiated layer), suggesting that the carbide growth is enhanced by the ion-irradiation. The unirradi-

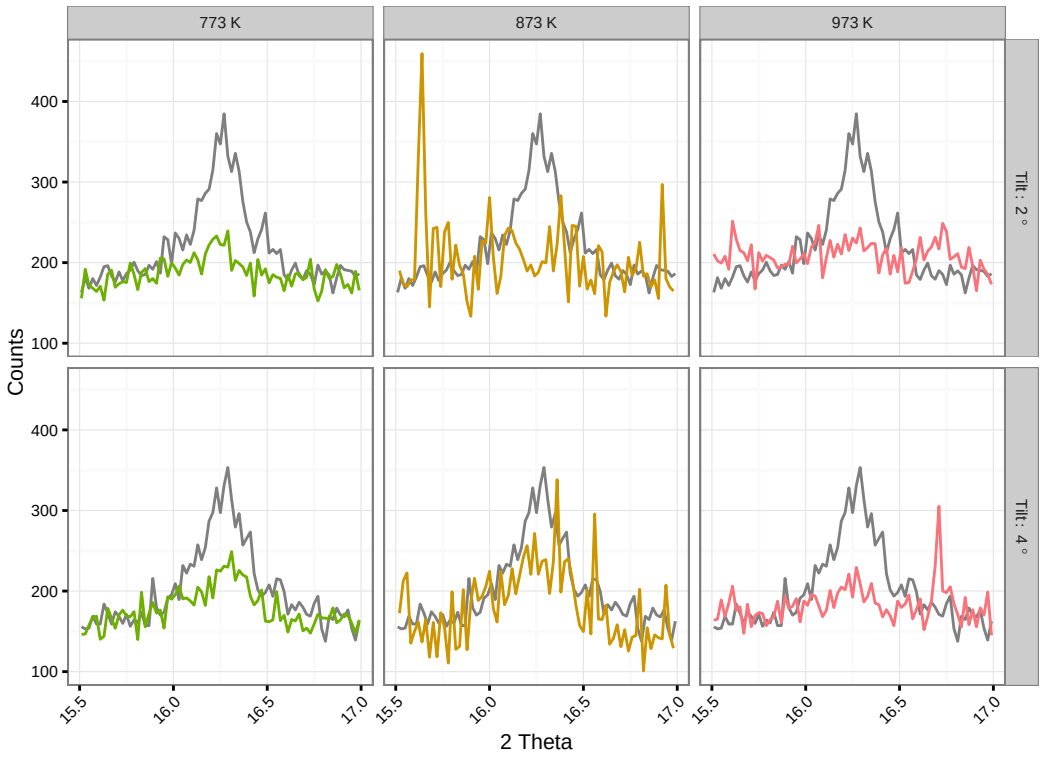

Figure 6.2.21 – The $Y_2Ti_2O_7$-(222) peak at 16.3 2θ in irradiated FeCrTiY (150 dpa). The different irradiation temperatures are shown at the top of the figure. The as-received sample is shown in grey. The $1/e$ attenuation depths at incident angles of 2° and 4° are 800 and 1600 nm respectively. The peak damage is at 1200 nm and the total range of damage is to 1900 nm (predicted by SRIM).

ated control sample (873 K) did not show carbide peaks any stronger than those in the as-received sample. Therefore, the carbide coarsening in this alloy is significantly enhanced by the ion-irradiation. Another feature visible in figure 6.2.20 is that the $Y_2Ti_2O_7$-(222) peak at 16.3° 2θ has a reduced intensity in the irradiated samples compared to the as-received sample—as shown in more detail in figure 6.2.21.

The intensity of the $Y_2Ti_2O_7$ peak is reduced by the ion-irradiation but its position and width are not significantly altered in FeCrTiY. The sample with $T_{irrd} = 973$ K had an increased background either side of the peak due to $M_{23}C_6$ and Fe_3O_4 peaks near by. With an incident angle of 2° ($1/e$ attenuation depth of 800 nm), the majority of the signal is from the irradiated layer (~1900 nm deep) and all samples irradiated at high temperature show some intensity in the $Y_2Ti_2O_7$-(222) peak. With an incident angle of 4°, some of the

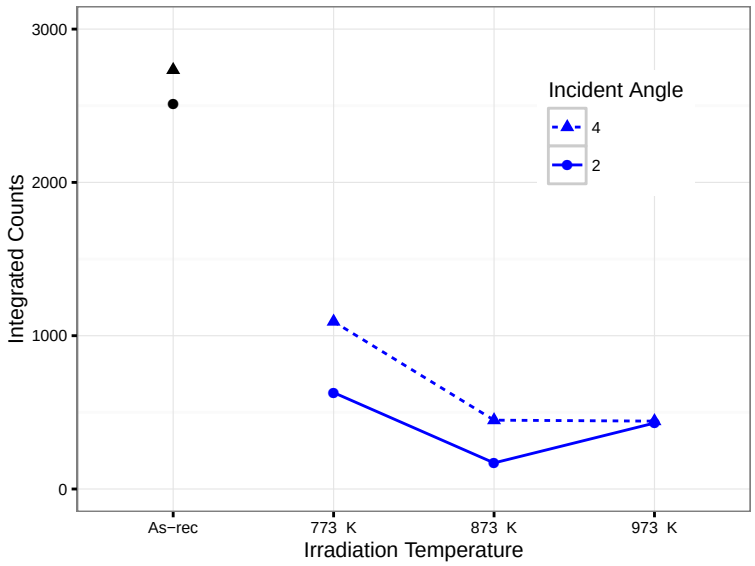

Figure 6.2.22 – The total integrated counts under the $Y_2Ti_2O_7$-(222) peak at 16.3° 2θ in irradiated and unirradiated FeCrTiY. Two incident angles are shown with $1/e$ attenuation depths of 800 and 1610 nm for 2 and 4° respectively, giving 10% and 30% substrate signal for each.

undamaged layer is probed and the area of the $Y_2Ti_2O_7$ peak is increased. The background-subtracted (222) peak area is given in summary in figure 6.2.22. The peak widths of the 2° incident angle diffractograms were slightly broader and the peak fitting was less confident; otherwise the peak widths (FWHM) of the irradiated samples were similar to that measured in the as-received sample FWHM, about ~0.3° 2θ.

These changes suggest that the particle distribution is modified by the ion-irradiation at high temperature, but does not indicate precisely what modification has taken place. The observed peak width does not indicate a change in particle size or strain, so the loss of peak intensity may result from reduction of particle volume, partial dissolution or amorphisation of the particles by the irradiation. To study the changes to the particles at the microstructural level, these FeCrTiY samples were investigated using EFTEM and APT. The summary data and estimated damage range of the APT samples is shown in table 6.2.4.

First, to address any change in cluster size and number density, figure 6.2.23 shows the cluster size (radius r_z) and the approximate cluster number density in irradiated FeCrTiY. After irradiation at all high temperatures, the cluster distribution was very similar to that measured in the as-received state. The difference in cluster number density suggests that

Irrd. T /K	Modal radius nm	$N_d \times 10^{23}$ m^{-3}	Damage range dpa
-	1.36	2.6±1.2	0
773	1.28	1.9±2.3	33–75
873	1.4	1.7±1.0	36–150
973	1.42	3.3±1.9	33–80

Table 6.2.4 – Summary of the modal cluster radius, number density and estimated damage range in dpa for APT analysis of FeCrTiY.

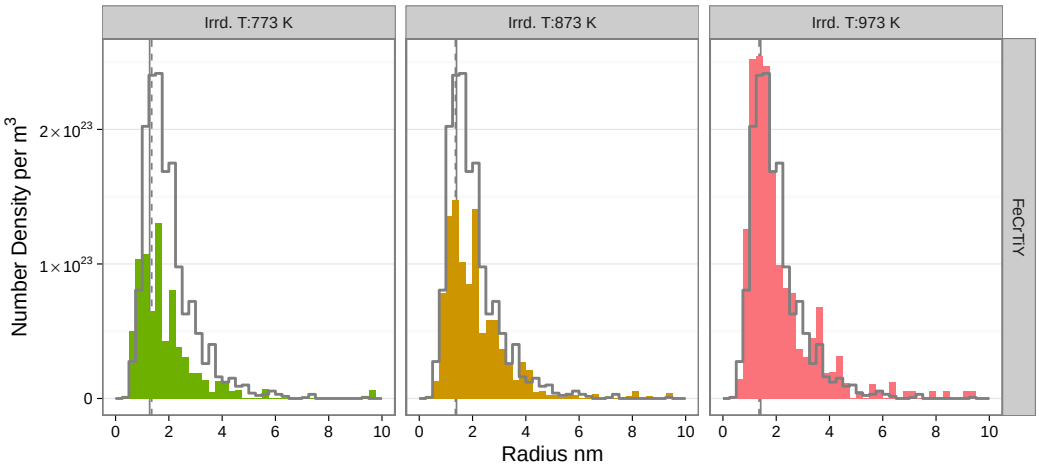

Figure 6.2.23 – Cluster size distributions for FeCrTiY after irradiation to ~60 dpa at high temperature, scaled by volume to give particle number density. The grey line shows the as-received result. Vertical lines mark the modal cluster radius for the as-received alloy (dashed) and irradiated samples (solid) but the two lines overlap in most cases. Measured by APT.

irradiation at lower temperatures causes a reduction in cluster number density, but this could be due to the inhomogeneity of the as-received alloy and the limited sample volume analysed. The modal cluster sizes were also very similar to the alloy in the as-received state; however, the cluster composition was changed.

The individual cluster chemistry is given in figure 6.2.24, which shows the Y:Ti:O ratio of clusters in FeCrTiY irradiated at high temperature. After irradiation, the Y-rich clusters were lost and the median O-content was decreased. These changes also occurred in the unirradiated control sample heated to 973 K, also shown in figure 6.2.24, but without the spread of Y-content observed in the irradiated samples. The change of Y:Ti ratio is summarised for all treatments of FeCrTiY using an estimated CDF in figure 6.2.25. The median Y:Ti ratio is reduced and the width of the distribution of Y:Ti ratios is also reduced (steeper curve in the

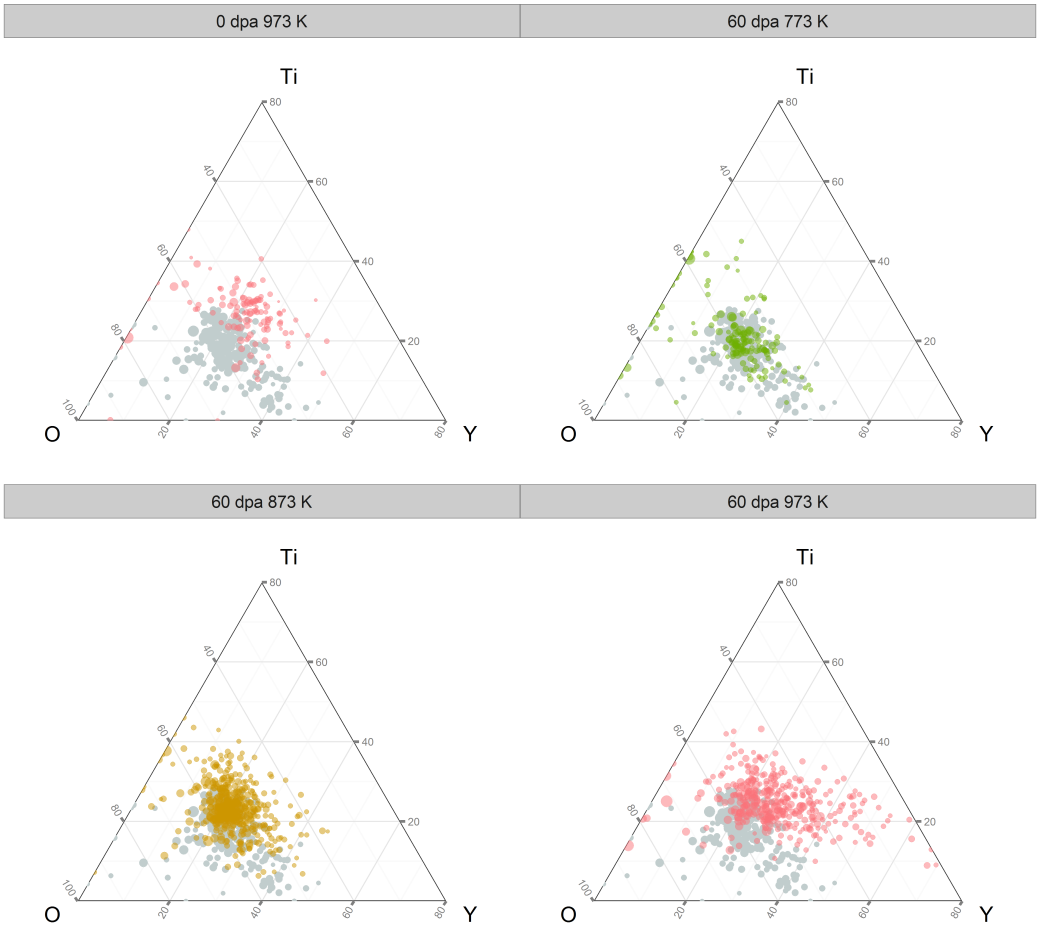

Figure 6.2.24 – Y:Ti:O ternary diagrams showing the change in individual cluster compositions in FeCrTiY after irradiation at 773, 873 or 973 K to ~60 dpa. The top-left panel shows cluster compositions in FeCrTiY after heating during the irradiation experiment but without damage (973 K for 14 h). The points from the as-received clusters (from figure 5.4.8) are shown in grey.

ECDF) for all of the high-temperature irradiations. As well as changes in cluster chemistry, the composition at microstructural interfaces could also be studied by APT.

The segregation behaviour of both grain boundaries (GBs) and the clusters was investigated using composition line profiles. The measurement of GBs was not systematic or targeted and they rarely occurred in the APT analysis. The observed GB segregation behaviour, relative to the bulk composition, is given in table 6.2.5. Carbon, while observed at GBs in FeY and FeTiY materials, was not segregated to the GBs in FeCrTiY despite all alloys having a similar global C composition (0.09 at% in FeCrTiY and 0.14 at% in FeY). The Cr segregation at the GBs was decreased after irradiation compared to the as-received

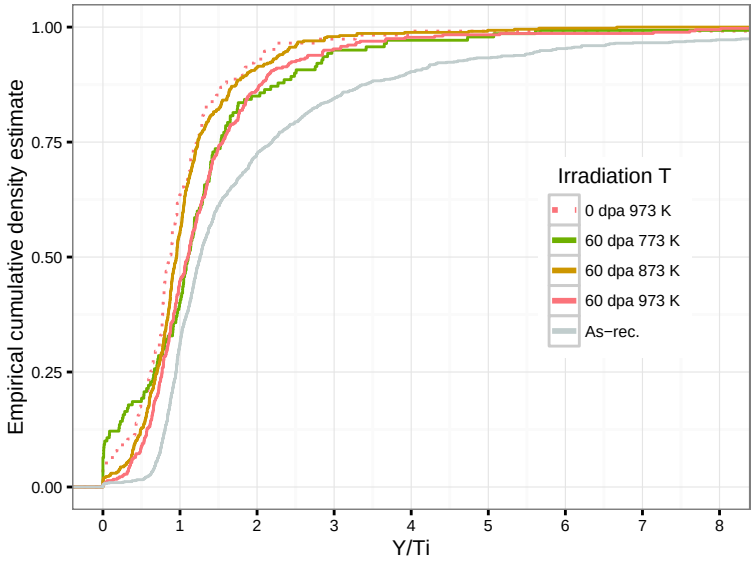

Figure 6.2.25 – Distribution of cluster Y/Ti values in irradiated FeCrTiY

Exp. ID	Alloy	Irrd. T /K	dpa	C	N	Y	Ti	O	Cr
15576	FeY	-	0	2.37	0.18	0.56	0.00	1.10	0.00
15867	FeCrTiY	-	0	0.01	0.11	0.02	0.01	0.00	4.32
16469	FeCrTiY	973	79	0.04	-0.37	-0.06	-0.01	0.06	4.13
17178	FeCrTiY	873	38	-0.11	0.14	0.44	0.30	0.68	1.30
17178	FeCrTiY	873	39	-0.02	0.00	0.02	-0.01	-0.03	0.38

Table 6.2.5 – Grain boundary segregation in FeCrTiY in atoms/nm^2 relative to the bulk composition.

FeCrTiY alloy. A composition line profile taken across a GB in irradiated FeCrTiY showed a W-shaped Cr-composition profile, as shown in figure 6.2.26.

Line profiles of individual clusters contained too few counts to visualise and so to improve the measurement of the composition average, composition line profiles were made (c.f. section §4.5.1). This method was used to investigate if the Cr-shell identified in figure 5.4.12 on page 133 had changed after irradiation. Figure 6.2.27 shows the line profiles of all clusters in irradiated FeCrTiY grouped by cluster radius. For the samples irradiated at 773 and 873 K, the levels of Cr-enrichment at the clusters were very similar to the as-received sample, but at $T_{irrd} = 973$ K the Cr-shell became less distinct and had a lower concentration.

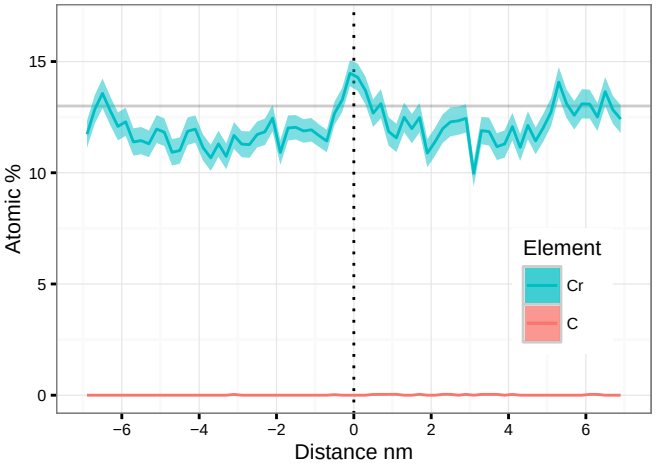

Figure 6.2.26 – Composition line profile of the segregation behaviour of Cr and C in irradiated FeCrTiY ($T_{irrd} = 973$K, 80 dpa), showing a W-shaped Cr profile. The grain boundary position is marked by vertical dashed line. The bulk Cr content is ~13 at% and is marked by a horizontal line. The filled ribbon indicates the approximate error of the measurement. Line profile dimensions: 13 nm radius cylinder 14 nm long. Experiment ID:16469.

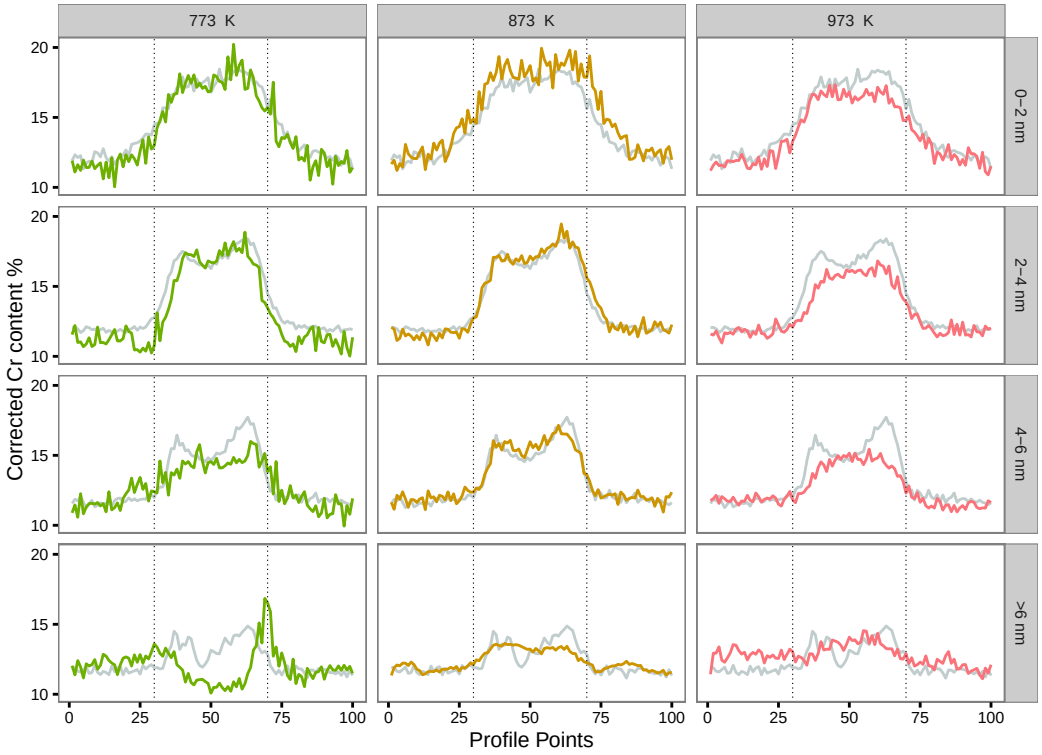

Figure 6.2.27 – Average Cr-composition line profiles from clusters in irradiated FeCrTiY grouped by cluster radius. The columns show different T_{irrd} and the rows show different cluster radius groups. The grey lines shows the Cr-line profiles for the as-received samples. Profile points from 30–70 represent the total extent of the cluster, $2.E_z$.

6.2.4 Comparison

As with the as-received alloys, it is constructive to compare the response of the different alloys to irradiation to elucidate the influence of Ti and Cr on the clusters' radiation tolerance. The change in cluster radius, as measured by APT, is given for all three alloys in figure 6.2.28. After irradiation below 873 K, the cluster radius of all three alloys is reduced compared to the as-received samples, although this reduction is very small for the FeTiY and FeCrTiY alloys. As noted above, the FeY alloy contains two distributions of clusters, one larger population which is consistent with the as-received material, and another of much smaller YO clusters (figure 6.2.3). The chemical changes in FeTiY and FeCrTiY are less marked, but the changes to the Y:Ti:O ratio are compared in figure 6.2.29.

Figure 6.2.29 shows that, for both FeTiY and FeCrTiY, the observed trend is a reduction in O-content with increasing T_{irrd}. As the cluster sizes are similar after irradiation, I do not think that this is due to the effect shown in figure 5.4.5 on page 127. Apparently anomalous results for FeTiY at 873 K and FeCrTiY at 973 K are manifested as a very large spread in measured Y:Ti ratio. For FeTiY, the composition change was accompanied by the formation of small Y-rich clusters. The inconsistency of the FeTiY result prompted me to arrange with my Indian collaborators to repeat the ion-irradiation experiment at 873 K (FeTiY, 150 dpa peak damage), but the clusters detected in this repeat sample also showed the same behaviour. The nanoindentation also showed an anomalous result for this FeTiY sample, with a hardness greater than the other samples irradiated at high temperature. Therefore, I conclude that, for this FeTiY material, the effect at 873 K is real and that APT may give some insight into the explanation for the surprising nanoindentation result.

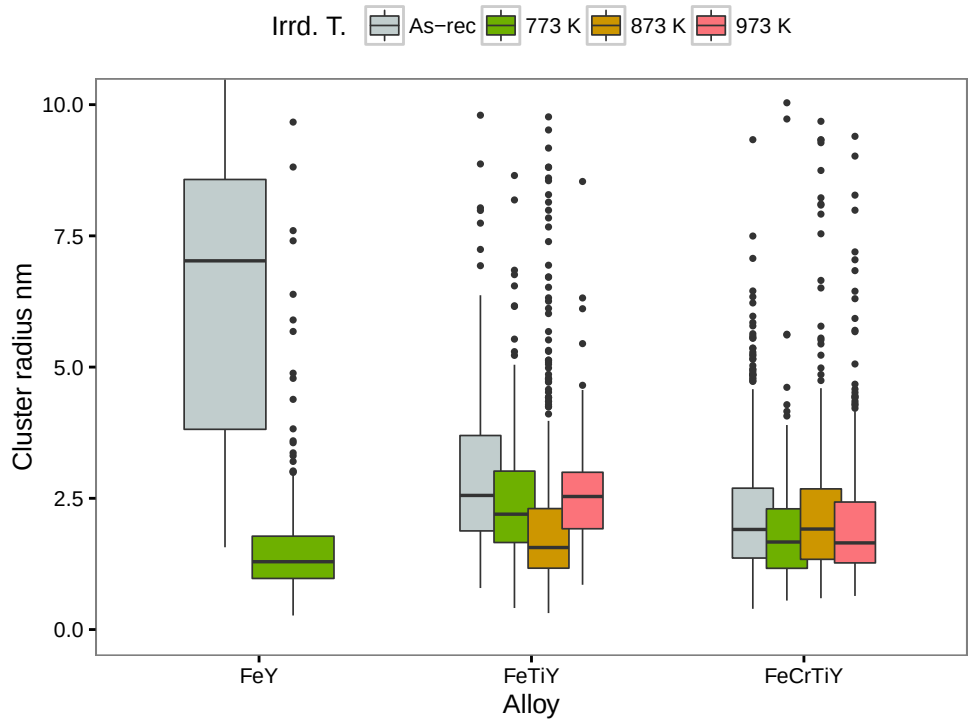

Figure 6.2.28 – Comparison of the cluster sizes measured by APT (radius r_Z) for FeY, FeTiY and FeCrTiY irradiated at different temperatures using box-plots. For the irradiated samples, only clusters coming from a region with an estimated damage > 10 dpa are included. Outliers, which lie outside $1.5\times$ the interquartile range, are rendered as points.

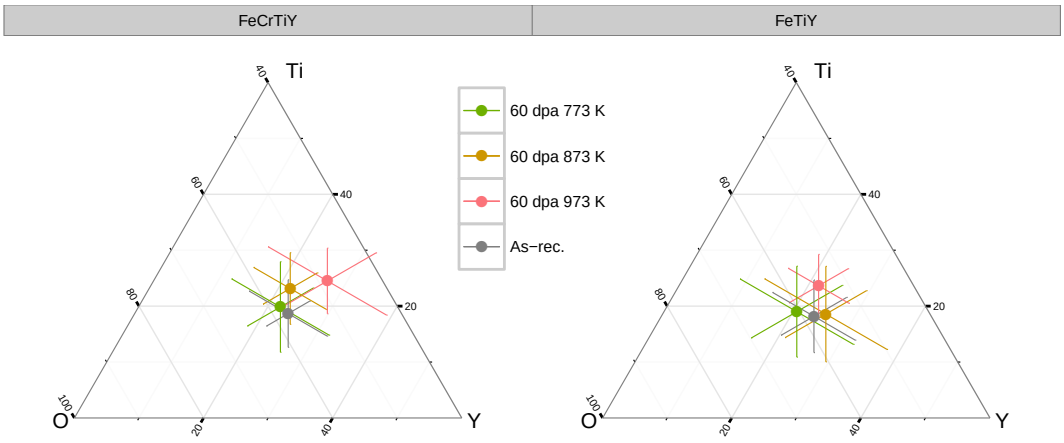

Figure 6.2.29 – Comparison of the median and standard deviation of cluster compositions for FeCrTiY and FeTiY irradiated at high temperature. All samples irradiated to >35 dpa, and approximately 60 dpa on average.

6.3 Low-Temperature Irradiation

6.3.1 Introduction

In addition to ion irradiation carried out at elevated temperatures, it was also possible to perform ion irradiation at cryogenic temperatures at IGCAR, Kalpakkam. These experiments follow the work of others [24, 25, 190, 221] who have used irradiation at low temperatures to minimise thermal diffusion and isolate the effect of the displacement-mixing component of irradiation damage on the microstructure. Due to the variability between ion implants, the samples were irradiated between 110 and 150 K, however, I consider these to be identical because at 150 K thermal diffusion of the solute is very slow.

The hardness of the irradiated layer was investigated by nanoindentation and the resulting hardness as a function depth plots for FeCrTiY and FeTiY are shown in figures 6.3.1 and 6.3.2. All the samples from both materials irradiated at < 150 K (50 or 100 dpa) showed an increased hardness within the first 500 nm from the sample surface. SRIM predicts the peak damage at a depth of 525 nm with a total damage range of 900 nm, meaning that the peak nanoindentation hardness should occur ~130 nm from the surface. For all four samples, the peak hardness was to a similar level of 4 GPa and occurred between 150–200 nm deep. In FeTiY, the peak hardening caused by an ion dose of 50 dpa was the same as in the sample irradiated to 100 dpa, 4.0 and 4.1 GPa respectively. However, in FeCrTiY the peak hardening was higher for the 100 dpa sample (4.7 GPa) than the 50 dpa sample (4.3 GPa).

6.3.2 Crystal Structure

These same samples irradiated at cryogenic temperatures were investigated using EFTEM in cross-section, and an example eigen image highlighting the Y and Ti edges is shown in figure 6.3.3. This micrograph shows only larger particles below the depth of predicted damage a very different dispersion than the as-received material. From other observations, some large (> 50 nm) particles remained but overall the number density of particles has been greatly reduced and the average size is increased.

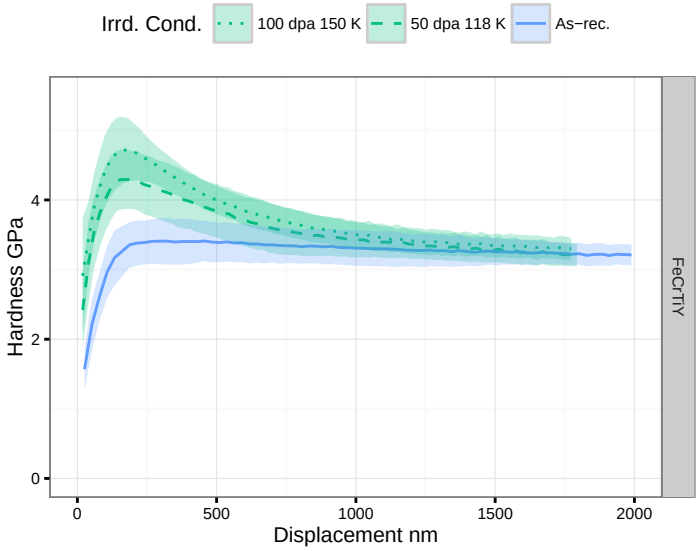

Figure 6.3.1 – Nanoindentation hardness as a function of displacement into the sample of FeCrTiY irradiated at cryogenic temperature. The pale ribbon shows the variation between different indentation results. The reference curve is data from the as-received FeCrTiY sample.

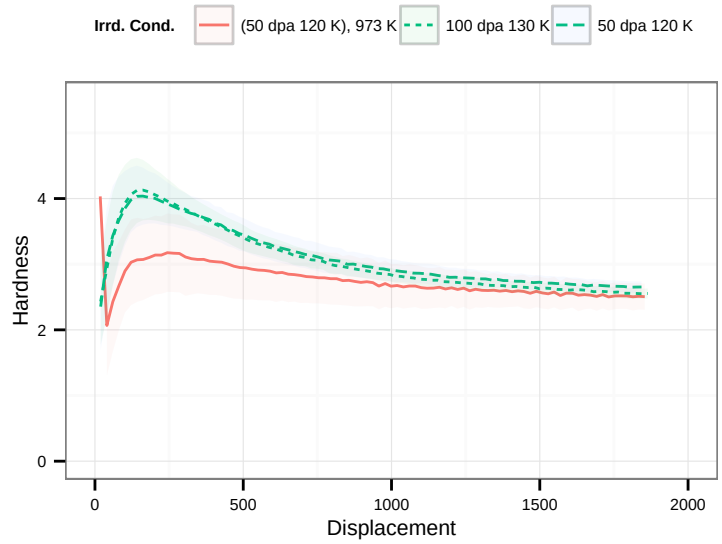

Figure 6.3.2 – Nanoindentation hardness as a function of displacement into the sample of FeTiY irradiated at cryogenic temperature. The pale ribbon shows the variation between different indentation results. The curve shown for reference is from a sample irradiated at low temperature and then annealed for ~10 hours at 973 K.

Looking in detail at one of the larger particles in the same sample, two chemically distinct regions were identified using low-loss EFTEM imaging (figure 6.3.4a). The crystallography of the large particle was observed using HRTEM. The surrounding matrix showed a closely spaced set of planes associated with the α-ferrite; the left half of the particle contained a second larger set of planes; and the Y-rich region on the right showed an amorphous ring in the FFT. It is possible that the amorphisation was caused by the bulk ion irradiation, but it is also possible that the sample preparation by focused ion beam milling may have

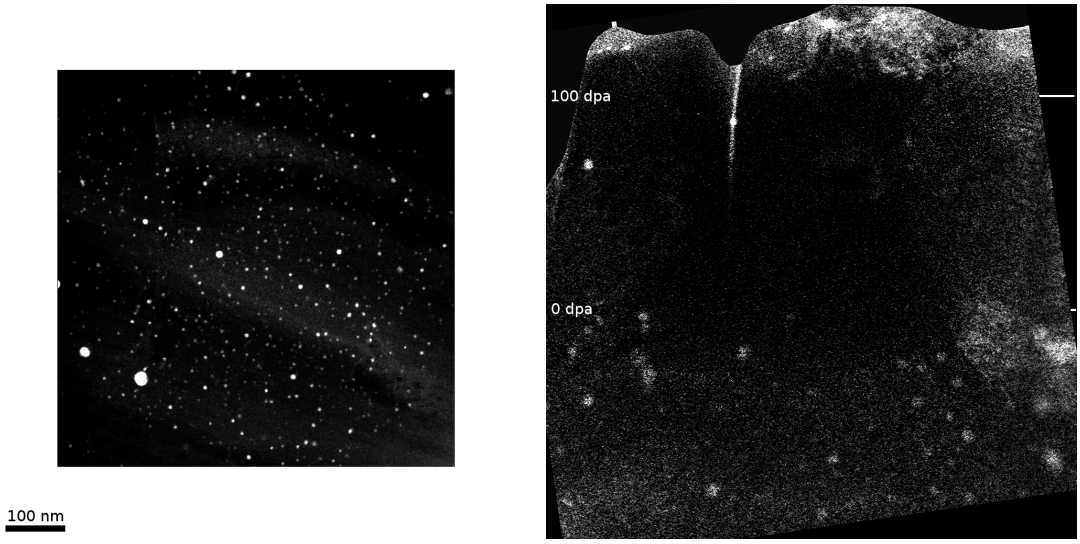

(a) FeCrTiY **(b)** T_{irrd} 150 K, 100 dpa

Figure 6.3.3 – EFTEM of the Y and Ti edges in FeCrTiY (a) as-received and (b) irradiated to 100 dpa (peak damage) at 150 K. The light contrast at the top of image (b) is due to diffraction contrast. Fourier-log thickness: approximately: (a) 0.4 (b) 1.4

caused the damage to the crystal structure. To avoid the artefacts created by site-specific preparation, glancing incidence X-Ray diffraction was performed to examine the crystallography of the irradiated surface layer.

Figure 6.3.5 shows the $Y_2Ti_2O_7$-(222) peak before and after irradiation to 100 dpa with T_{irrd}< 150 K in FeCrTiY. At very low incidence angles, the intensity of the diffracted signal is low because the probed volume is very small (a depth <100 nm over an area of a few square mm), but at incidence angles >1°, the intensity of the (222) peak from the as-received sample increases to over 2000 counts. However, in the irradiated sample, the (222) peak is not detectable at an incidence angle of 1°, and at 4° the (222) peak has half the counts of the corresponding as-received sample, as shown in summary in figure 6.3.6. The fitted peak width was not significantly different between the two samples, with a FWHM of 0.2-0.35° 2θ. These results indicate that the $Y_2Ti_2O_7$ particle volume fraction in the damaged region has been reduced by the low-temperature irradiation without significant change to the size of the scattering domains, which would have been evident by a change in peak width.

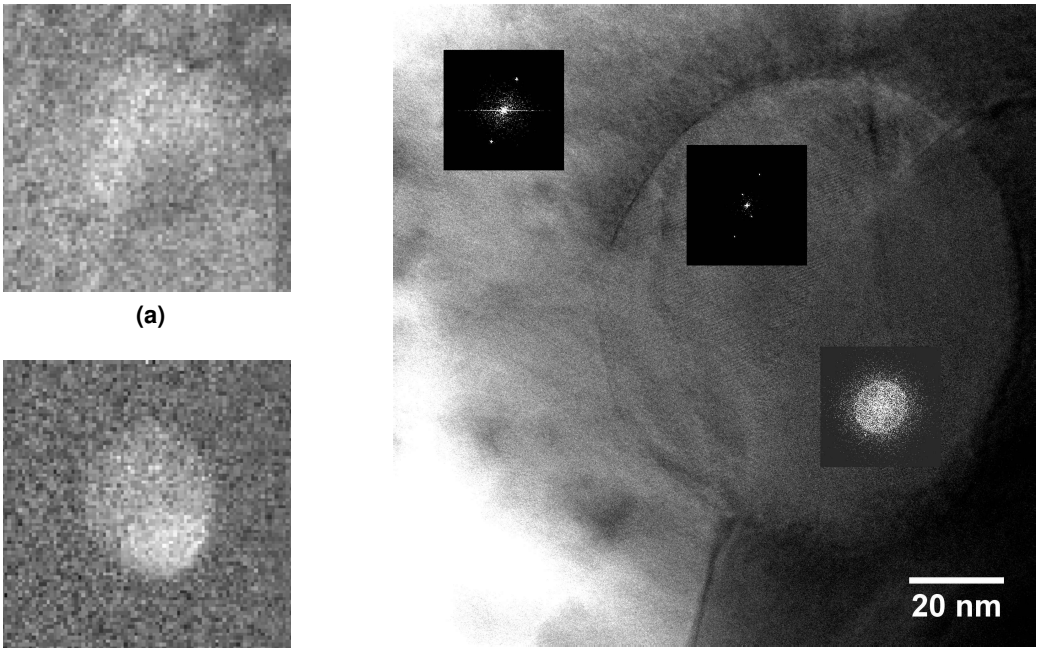

Figure 6.3.4 – (a) EFTEM eigen image corresponding to the Cr edge. (b) EFTEM eigen image corresponding to the Y edge. (c) HRTEM image of a Cr-Y composite oxide particle with the power spectra for the matrix, Cr(Ti)-oxide and Y-oxide areas inset. Approximate lattice spacings from FFT: 0.24 nm matrix, 0.67 nm upper particle and 0.31–0.33 nm for the amorphous ring.

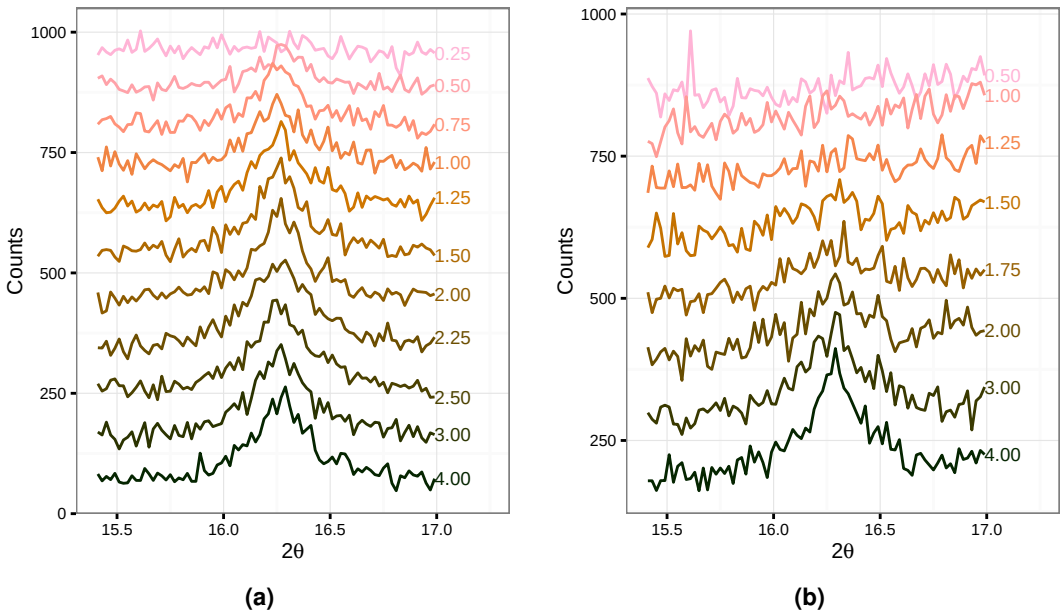

Figure 6.3.5 – Diffractograms at different incidence angles from (a) as-received FeCrTiY (b) FeCrTiY irradiated to 100 dpa at <150 K focused on the peak at $16.3^{\circ}\,2\theta$. The numbers on the right indicate the glancing incidence angle. The actual counts have been scaled so that the peaks do not overlap.

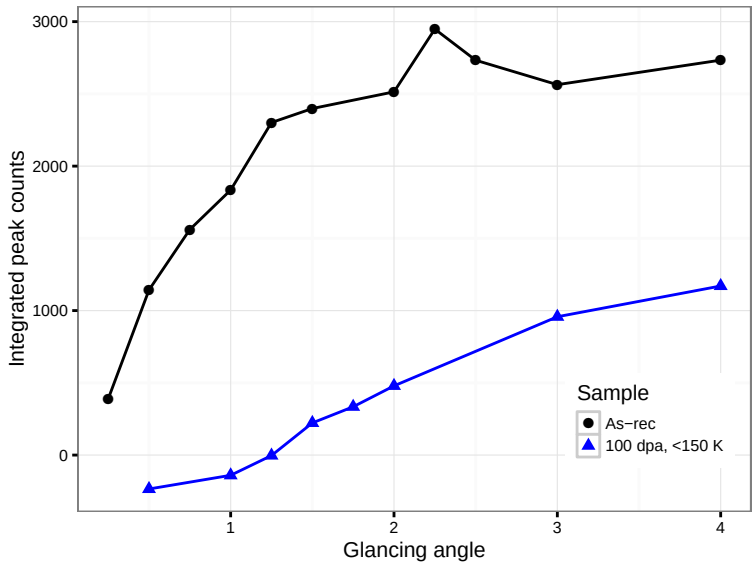

Figure 6.3.6 – Background-subtracted and integrated counts from the $Y_2Ti_2O_7$-(222) peak as a function of GIXRD incident angle (taken from the 2θ scans in figure 6.3.5).

6.3.3 Chemistry

The nanoindentation showed a great increase in hardness following the irradiation at cryogenic temperatures, and both GIXRD and TEM indicate that the crystal structure and volume fraction of the original particles has been altered. APT analysis of samples taken perpendicular to the sample surface was used to investigate the chemical changes of the clusters caused by the irradiation. One such APT experiment is shown in figure 6.3.7, which captures the predicted peak-damage depth (~530 nm) in the analysed volume. Figure 6.3.7 shows two relatively large ($r_z > 10$ nm) clusters made up of Y-, Ti- and O-containing ions. These clusters are much more diffuse than the Y-Ti-O clusters in the as-received material, and also have a lower number density, $< 10^{21}$ m^{-3}. As well as changes to the size and number density, the ionic composition was changed; notably, a high concentration of Ti^{2+} ions were detected around the clusters (~0.15 at% cluster composition), which can be seen circled in figure 6.3.7e. Only a very small concentration of Ti^{++} ions were detected in the as-received sample (<0.05 at% cluster composition), so this indicates that a significant difference has been induced by the irradiation at cryogenic temperature. Other chemical changes were detected, as shown in the atom map from the irradiated FeTiY alloy in fig-

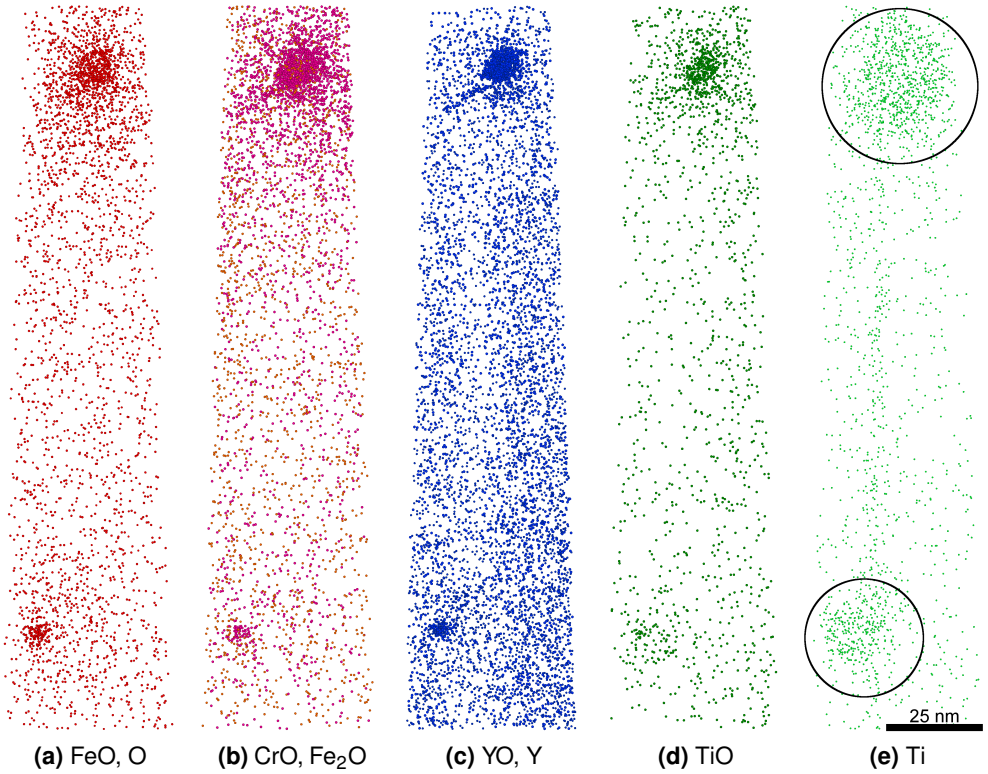

Figure 6.3.7 – Atom map of FeCrTiY irradiated to 100 dpa at 150 K. The sample is taken perpendicular to the surface at a depth equal to the peak-damage depth predicted by SRIM. ID 18225.

ure 6.3.8, indicating that some clusters had greatly differing Y:Ti ratios. The mean solute content of the matrix (after removing the ions identified as being clustered) was increased in the irradiated samples than in the as-received samples, as shown in figure 6.3.9.

The cluster chemistry changes after irradiation seen in figure 6.3.8, can be summarised by the change in Y:Ti:O ratio and total Fe fraction ($^{Fe}/_{total}$ cluster ions). The Y:Ti:O ratio of the individual clusters irradiated to a dose >70 dpa with a T_{irrd}< 150 K are shown in figure 6.3.10. In both FeCrTiY and FeTiY, the spread of Y:Ti ratios increased, and in FeTiY, many more Y_xO_x-type clusters (with very little Ti) were detected. In FeCrTiY, the average O-ternary fraction of the clusters was decreased from 0.57±0.04 in the as-received sample to 0.52±0.09 after irradiation at low temperature.

The Fe-content of the irradiated clusters is also different to the as-received material. Figure 6.3.11 shows the Fe-fraction of the clusters as a function of reduced cluster radius.

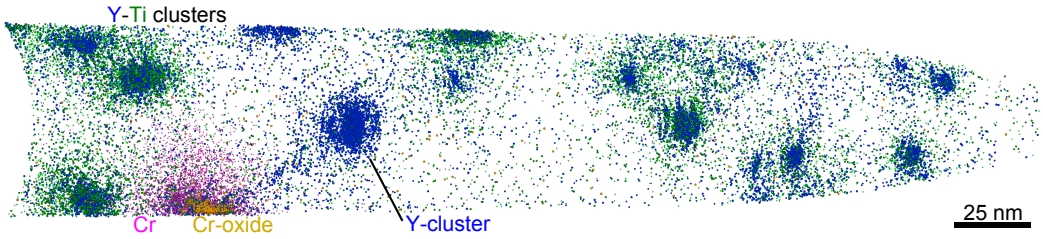

Figure 6.3.8 – Atom map from FeTiY irradiated to 100 dpa. The main features are labelled, the mixed Y-Ti-oxide clusters, a yttrium-rich cluster, a Cr-oxide and Cr ions. Fe ions are omitted for clarity. Map thickness (into the page): 10 nm. Colour key: Cr (pink), CrO (orange), Y (blue), YO (blue), Ti (green) and TiO (dark green). ID: 18970

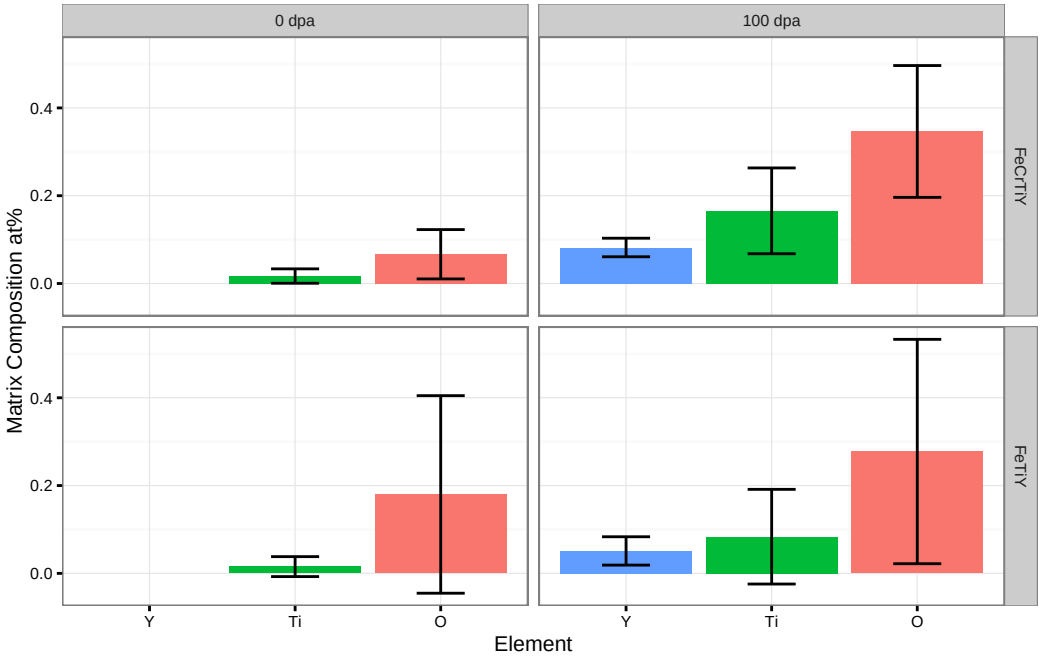

Figure 6.3.9 – Solute content of the matrix after removing ions considered to be clustered in as-received and irradiated FeTiy and FeCrTiY. The results on the right are from samples irradiated to a maximum of 100 dpa at < 150 K. The error bars show standard deviation of compositions measured between different experiments (at least 5 experiments for each panel).

Even relatively large clusters in the T_{irrd}(150 K) sample had an apparent Fe-content greater than 90%. The Cr-content of the clusters in FeCrTiY was also modified by the irradiation at cryogenic temperature. The Cr composition of the clusters in FeCrTiY was decreased from 15.0±0.9 at% to 12.0±0.9 at%, the same as the bulk Cr concentration—indicating that the Cr-enrichment has been lost after irradiation.

The local chemistry of the clusters was investigated using composition line profiles.

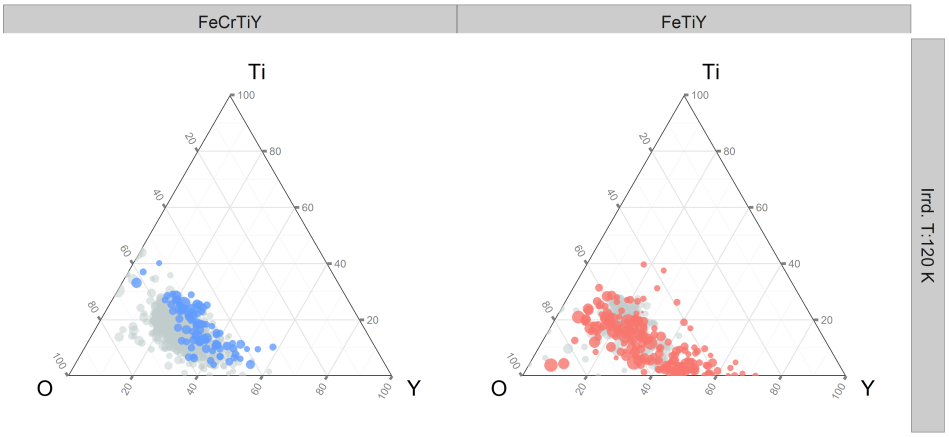

Figure 6.3.10 – Gibbs triangle showing individual cluster Y:Ti:O ratios as measured by APT after irradiation to more than 70 dpa at $T_{irrd} < 150$ K. The Y:Ti:O points from the as-received samples are shown in grey.

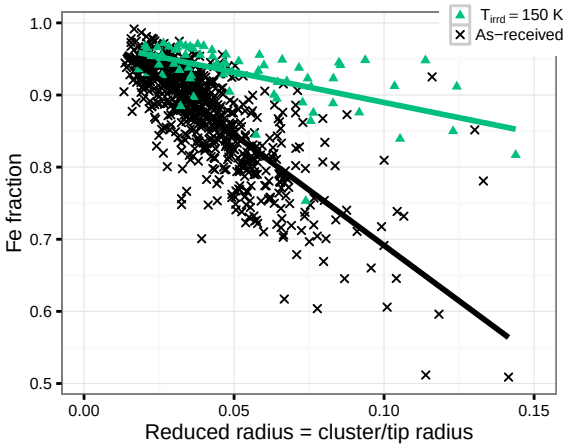

Figure 6.3.11 – Fe-fraction of clusters in FeCrTiY as a function of size, expressed in reduced radius, as-received and after irradiation at T_{irrd} < 150 K.

Two typical line profiles from individual clusters are shown in 6.3.12, one from the as-received FeTiY material and another from a sample that has experienced an ion dose of ~75 dpa at T_{irrd} < 150 K. Both clusters have a similar Y:Ti:O ratio, but the as-received cluster shows much sharper interfaces with the matrix. The irradiated cluster shows relatively high concentrations of solute above and below the cluster, characteristic of their diffuse nature after irradiation. Both line profiles have the same length relative to the measured cluster size, but in the irradiated sample, the solute extends the full length of the line profile. This is partly due to the ambiguity of the cluster definition in this sample, but also an indication of their more diffuse nature.

To get a better picture of the general behaviour of the local cluster chemistry, averaged

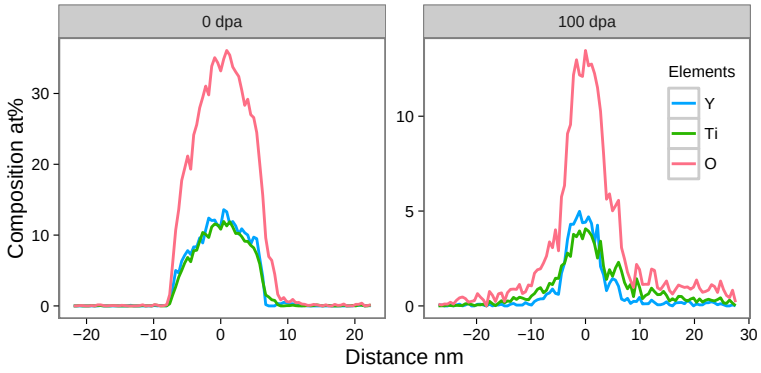

Figure 6.3.12 – Two composition line profiles taken parallel to the analysis direction from as-received FeTiY (left) and FeTiY irradiated to 100 dpa (right). From the estimated depth of the cluster from the surface (left), the predicted damage is 75 dpa. Fe is omitted for clarity, but is included in the composition calculation.

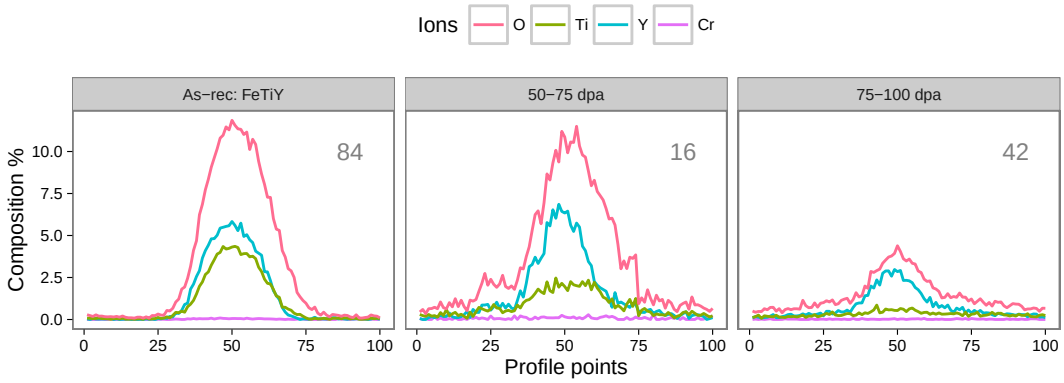

Figure 6.3.13 – Composition line profiles through clusters in FeTiY irradiated at $T_{irrd} < 150$ K, max damage 100 dpa. Only clusters with a radius between 2–4 nm are included. The as-received condition is shown for comparison. Fe is omitted for clarity. The grey numbers show the number of clusters contributing to the average line profiles.

line profiles were compiled from irradiated FeTiY and FeCrTiY samples. Figure 6.3.13 shows average line profiles for clusters in FeTiY. Clusters in the irradiated material had a much wider solute distribution and lower solute content than the as-received clusters, and these effects were increased at higher doses. Similar behaviour was observed in FeCrTiY (figure 6.3.14), and the Cr-shell was not observed in any clusters irradiated to more than 25 dpa. In the smaller clusters, there was no change in Cr-content through the cluster profile, but in the larger clusters, Cr depletion was observed at the cluster core.

As well as a change in the Cr behaviour of the samples irradiated at low temperatures, the Fe density through the clusters was also modified. In general, in the irradiated samples, the ionic density of the clusters was much lower than in the as-received clusters and the

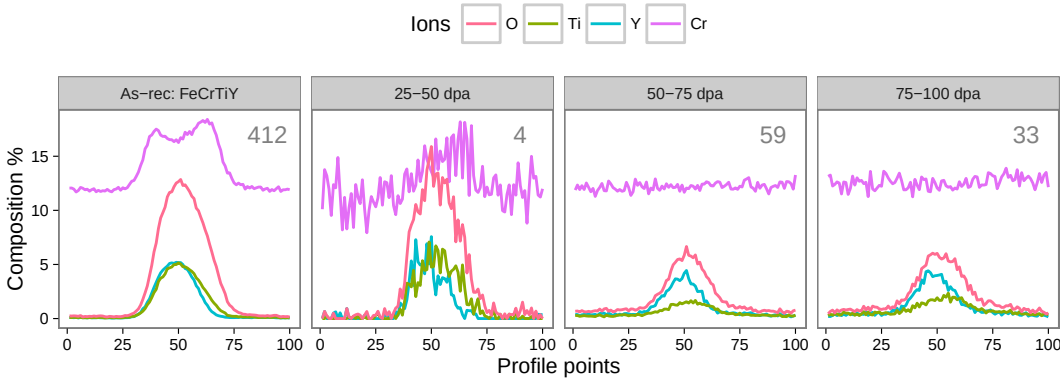

Figure 6.3.14 – Composition line profiles through clusters in FeTiY irradiated at cryogenic temperature ($T_{irrd} < 150$ K, max damage 100 dpa). Only clusters with a radius between 2–4 nm are included. The as-received condition is shown for comparison. Fe is omitted for clarity. The grey numbers show the number of clusters contributing to the average line profiles.

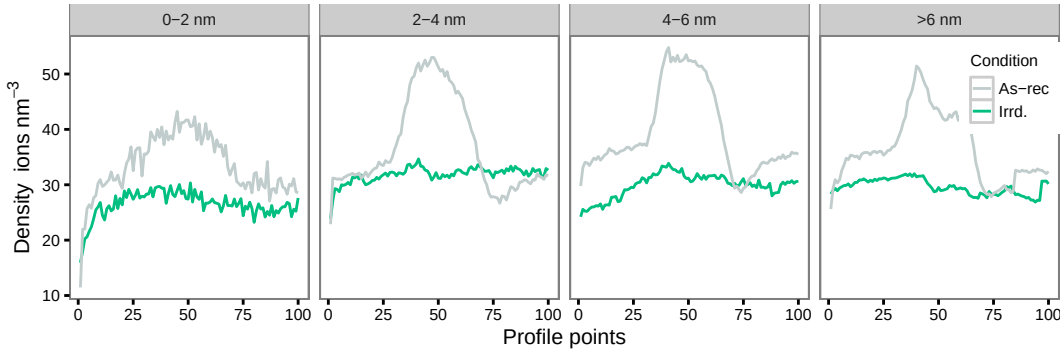

Figure 6.3.15 – Approximate Fe ionic density measured from averaged cluster line profiles, both as-received FeTiY and FeTiY irradiated with T_{irrd} < 150 K are shown. The cluster top and bottom are at profile points 30 and 70 respectively.

ionic density was much less perturbed by the presence of the irradiated clusters. There was a consistent increase in Fe-density in the top half of the clusters, from one radius away from the cluster centre until the cluster centre, but the origin of this effect is unknown.

6.4 Subsequent Treatments

Following the ion irradiation of FeTiY and FeCrTiY at cryogenic temperatures, the same samples were subject to another irradiation treatment at 973 K. Part of the sample surface was masked so that two regions were made; one subject to both irradiation at low temperature and then high temperature (B01010 and C01010 from the Cr-free and Fe14Cr alloys

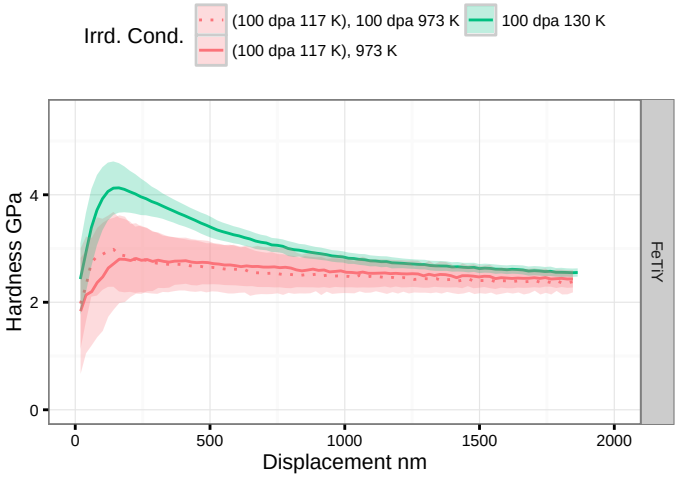

Figure 6.4.1 – Nanoindentation hardness as a function of displacement into the sample of FeCrTiY irradiated at cryogenic temperature. The pale ribbon shows the variation between different indentation results. The reference curve is data from the as-received FeCrTiY sample.

respectively), and the other subject to irradiation at low temperature followed by a thermal treatment only (B010H and C010H). The irradiation details are given in tables 3.2.2 and 3.2.3 on page 46. These treatments are instructive as they allow the separation of the influence of irradiation and thermal annealing on starting samples that are already heavily damaged. The hardness was measured by nanoindentation, the crystal structure of the damaged region was assessed by GIXRD, cross-sectional EFTEM analysis was made and APT was performed on selected sample conditions.

The "bulk" properties of the irradiated layer were assessed by nanoindentation and GIXRD. First, the nanoindentation shows that the hardening caused by the irradiation at $T_{irrd} < 150$ was recovered after the thermal treatment in FeTiY (figure 6.4.1) and mostly recovered in FeCrTiY (figure 6.4.2). The nanoindentation results also show very little difference between irradiation and annealing at 973 K in both FeTiY and FeCrTiY. Second, the GIXRD scans of FeCrTiY (at 1° incidence angle, probing within the damaged layer) showed, for both the irradiated and annealed samples, only peaks from the α-Fe and none from oxide or carbide phases.

The nanoindentation results suggest that whatever hardening was caused by the particle dissolution following cryogenic irradiation has been recovered by the annealing or subsequent irradiation at high temperature. However, GIXRD does not show any evidence of the re-formation of the $Y_2Ti_2O_7$ phase after either irradiation at 973 K or annealing for

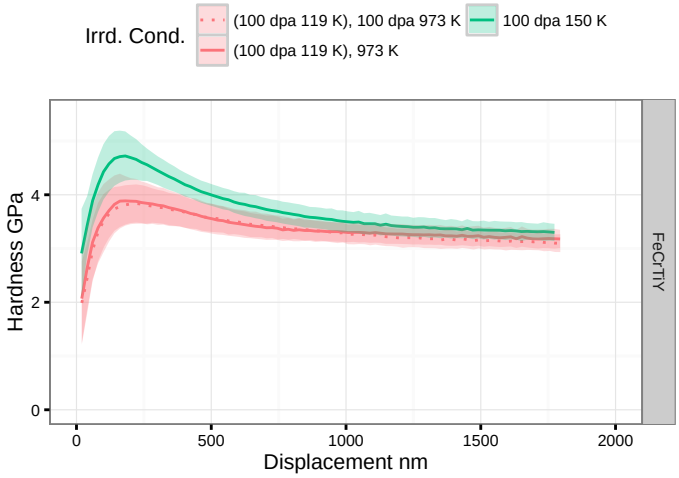

Figure 6.4.2 – Nanoindentation hardness as a function of displacement into the sample of FeTiY irradiated at cryogenic temperature. The pale ribbon shows the variation between different indentation results. The curve shown for reference is from a sample irradiated at low temperature and then annealed for ~10 hours at 973 K.

10 h. APT was performed to investigate the behaviour of the solute following the above treatments, and example atom maps from irradiated and annealed samples are shown in figure 6.4.3.

After irradiation and annealing, the clusters detected had a very different morphology to the clusters in the samples irradiated at cryogenic temperature. The average cluster compositions were similar to the as-received clusters, and in FeCrTiY, the Cr-content of the clusters had recovered to 15.3 ± 1.4 at% and 14.9 ± 2.2 at% in the annealed and irradiated samples respectively. The changes in cluster size are summarised in figures 6.4.4 for FeTiY and 6.4.5 for FeCrTiY.

The cluster distributions in figure 6.4.4 look very similar, with the same number density and sizes, for both the irradiated and annealed FeTiY sample. After both treatments in both alloys, a distribution of very small clusters are formed, with the annealed sample containing slightly smaller clusters, as given in table 6.4.1. In FeCrTiY, the irradiated sample (C01010) has a higher number density of clusters than the annealed sample (C010H), but both have a similar modal cluster size. It is not only the cluster size and number density that are altered by the treatments following irradiation at $T_{irrd} < 150$ K; the chemistry of the clusters is also altered.

Figure 6.4.6 shows the Y:Ti:O ratio of individual clusters from these samples in their starting condition (100 dpa, 120 K) and following irradiation and annealing at 973 K. The

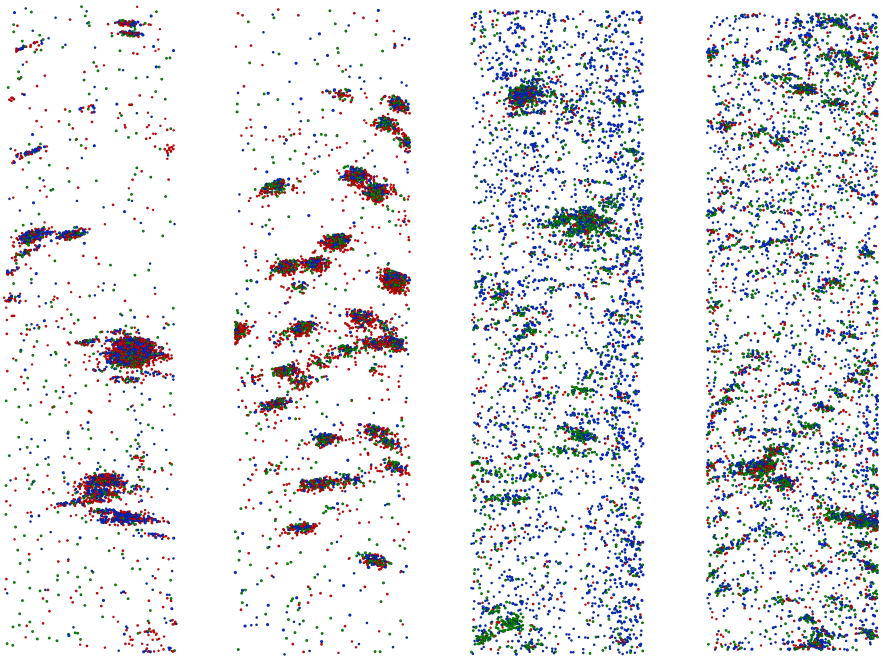

(a) FeTiY, (100 dpa 117 K) 973 K ~10 h

(b) FeTiY, (100 dpa 117 K) 100 dpa, 973 K

(c) FeCrTiY, (100 dpa 118 K) 973 K ~10 h

(d) FeCrTiY, (100 dpa 118 K) 100 dpa 973 K

Figure 6.4.3 – Example atom maps from FeTiY (a,b) and FeCrTiY (c,d) irradiated at cryogenic temperature and then subsequently irradiated (b,d) or annealed (a,c) at 973 K. All volumes are 10x40x150 nm^3. Analysis direction is top to bottom. IDs: 19046, 19161, 18972 and 18890.

Alloy	As-rec.	Irrd.[2] 973K	Irrd.[1] + Annealed	Irrd.[1] + Irrd.[3]
FeTiY	2.12	2.65	1.22	1.52
FeCrTiY	1.36	1.42	0.55	1.04

Table 6.4.1 – Modal cluster radius measured by APT after various irradiation and heat treatments. Irrd.[1]100 peak dpa damage, T_{irrd} < 150 K. Irrd.[2]150 peak dpa damage, T_{irrd} = 973 K. Irrd.[3]100 peak dpa damage, T_{irrd} = 973 K. The annealing of Irrd.[1] was at 973 K for ~10 h.

starting condition had a large spread of Y:Ti:O values, with a median Y:Ti ~2. After annealing, FeCrTiY formed many Ti-O clusters, but on average, the clusters had a reduced O-content compared to the as-received clusters. FeTiY lost some of the Y-rich clusters that were observed in the cryogenic sample, but both annealed samples retained a large variation in cluster composition.

In both irradiated samples, more Ti-rich clusters were formed, and the median Y:Ti ratio was < 1. The clusters formed following irradiation at 973 K are similar to those observed

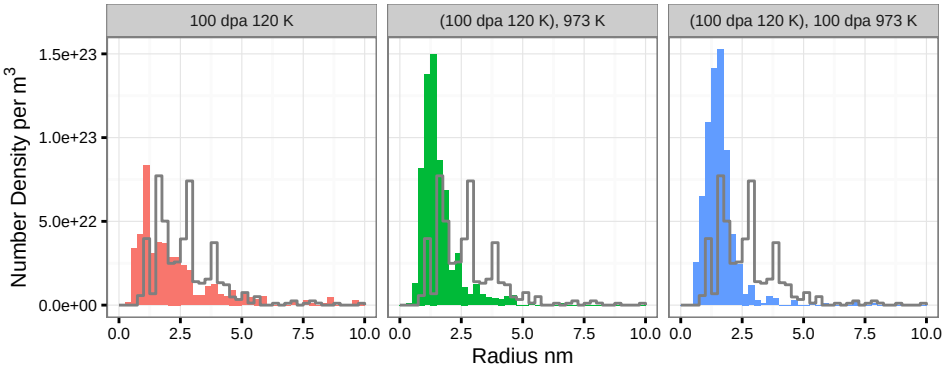

Figure 6.4.4 – Cluster size distribution, scaled by number density, for clusters in FeTiY irradiated to 100 dpa at 130 K, followed by irradiation and annealing at 973 K. The grey line shows the number density of clusters in the as-received sample.

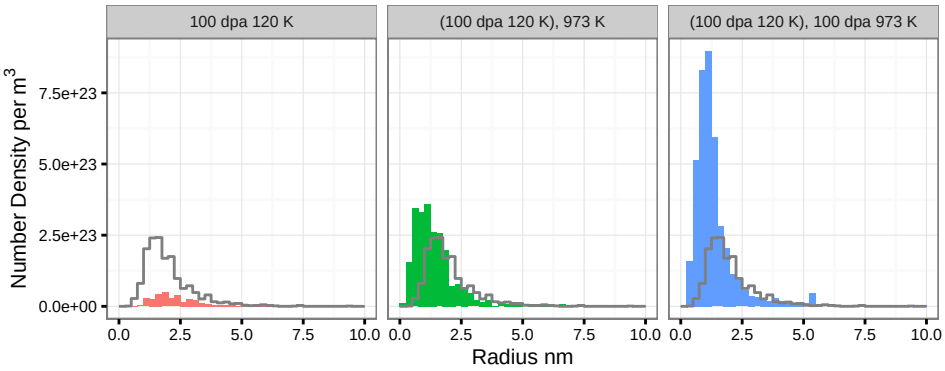

Figure 6.4.5 – Cluster size distribution, scaled by number density, for clusters in FeCrTiY irradiated to 100 dpa at 130 K, followed by irradiation and annealing at 973 K. The grey dashed line shows the number density of clusters in the as-received sample.

in section 6.2 for both materials after high-temperature irradiation. Although the cluster chemistry may be similar to that observed after a single irradiation at 973 K, the morphology of the clusters in the sequentially irradiated samples are quite different. As noted above, the clusters formed by these treatments were smaller and formed preferentially on grain boundaries. The GB excess measurements are summarised in table 6.4.2, which shows 0.20–2.5 excess solute atoms/nm^2 on the GBs. The Cr segregation shows a wide range from depleted to excess values, -2–12 atoms/nm^2. These FeCrTiY samples also contained a non-negligible content of N concentrated at the GBs.

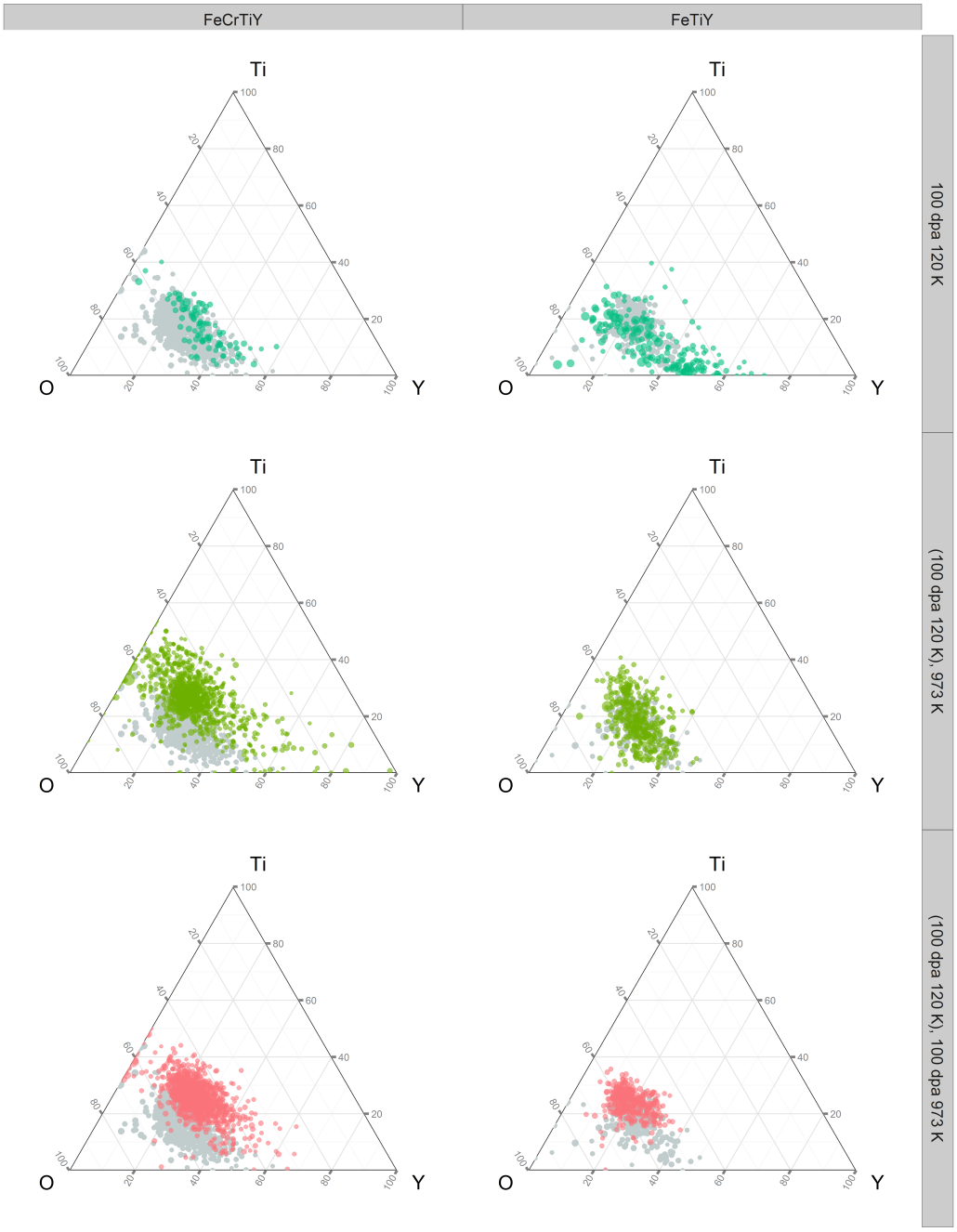

Figure 6.4.6 – Gibbs triangle showing individual cluster Y:Ti:O ratios of clusters in FeTiY and FeCrTiY irradiated to 100 dpa at 130 K, followed by irradiation and annealing at 973 K. The grey points show clusters in the as-received samples.

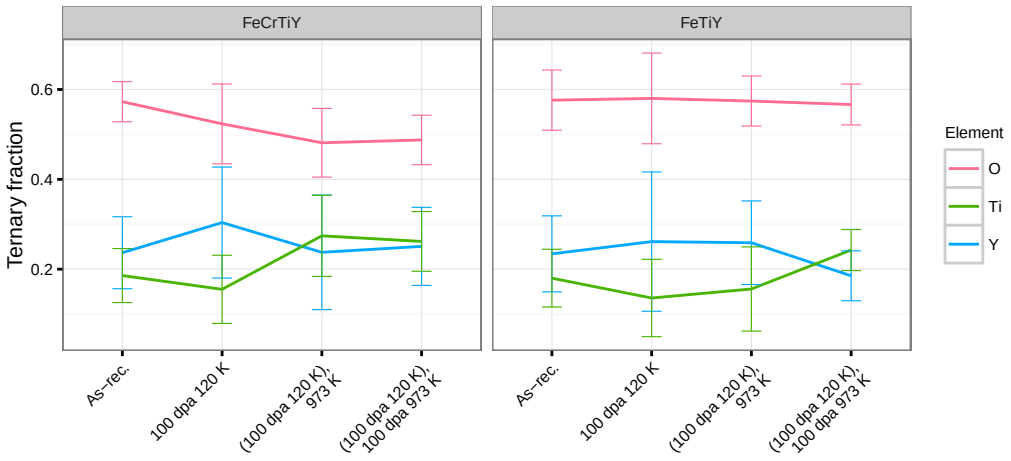

Figure 6.4.7 – Median Y, Ti, O ratios of clusters in FeTiY and FeCrTiY irradiated to 100 dpa at < 150 K, followed by irradiation and annealing at 973 K. Error bars show the standard deviation measured for each component.

Exp. ID	Irradiation Condition	dpa	C	N	Y	Ti	O	Cr
18890	(100 dpa, 120 K), 100 dpa 973 K	94	0.00	0.00	0.07	0.12	0.37	2.42
18890	(100 dpa, 120 K), 100 dpa 973 K	100	0.00	0.14	0.06	0.31	0.45	-2.04
18890	(100 dpa, 120 K), 100 dpa 973 K	89	0.03	0.35	0.34	0.69	1.43	-2.38
18972	(100 dpa, 120 K), 973 K	64	0.03	0.12	0.18	0.02	0.17	1.32
18516	(100 dpa, 120 K), 973 K	63	0.00	0.21	0.10	0.16	0.39	5.65
18516	(100 dpa, 120 K), 973 K	66	0.01	0.10	0.05	0.13	0.18	0.52
18516	(100 dpa, 120 K), 973 K	81	0.04	0.30	0.12	0.19	0.58	0.67
18622	(100 dpa, 120 K), 973 K	59	0.05	0.00	0.14	0.09	0.17	2.34
18622	(100 dpa, 120 K), 973 K	64	0.00	0.00	0.00	0.02	0.04	0.60
18785	(100 dpa, 120 K), 973 K	63	0.02	0.17	0.00	0.12	0.08	2.36
18785	(100 dpa, 120 K), 973 K	64	0.00	0.02	0.14	0.20	0.31	12.79
18785	(100 dpa, 120 K), 973 K	83	0.00	0.47	0.45	0.56	1.36	5.89

Table 6.4.2 – Grain boundary segregation in FeCrTiY irradiated (100 dpa, 973 K) and then irradiated again or annealed, as given in the Irradiation Condition column. All values in excess atoms/nm^2 relative to the bulk composition.

6.5 Discussion

The main aim of the work reported in this chapter is to investigate the behaviour of the oxide particles in ODS steels subject to irradiation, and so to predict how such alloys will behave in service in a fission or fusion reactor environment. My experimental work is ex-situ and the results presented above should be understood in light of the results presented in Chapter 5. As established in Chapter 2, there have been a number of experiments using

different high-energy particles to cause the irradiation damage and I have used heavy self-ions for this purpose. In section 2.4.3, the current understanding of particle irradiation behaviour and its relation to ODS materials were explained. A number of questions were raised, including:

- What is the critical stability temperature of the oxide particles?
- How does it relate to irradiation conditions other than temperature?
- What are the kinetics involved in irradiation-enhanced precipitation and growth?
- Is a universal T^* appropriate, or does it depend on the alloy chemistry and particle character?

First, the general observations about the different alloys irradiated at $T_{irrd} > 700$ K are noted before discussing the evidence for displacement mixing in the samples irradiated at $T_{irrd} < 150$ K. Finally, the different results are brought together in light of the current understanding of the underlying mechanisms of irradiation damage and put into context with other reported results.

6.5.1 FeY

After irradiation at 773 K, the FeY sample contained a bi-modal distribution of clusters: larger clusters of a similar size and composition to those in the as-received material, and smaller clusters with different evaporation behaviour, which formed preferentially on dislocations and grain boundaries.

Looking first at the larger clusters, these were not removed or dissolved by the irradiation and they have the same Y:O ratio as bulk Y_2O_3 and the clusters analysed in the as-received sample, 0.67 (figure 6.2.6). However, the GIXRD analysis indicates a loss of the (222)-Y_2O_3 peak after irradiation at 773 K (figure 6.2.9) and analysis of the evaporation behaviour shows that the irradiated clusters are very different (figure 6.2.8b). Therefore, I conclude that the larger particles are amorphised by the irradiation, though they retain the

same composition. Two Cr-Y-composite oxide particles were detected in the irradiated samples. Unlike in the as-received samples, these oxides also showed some degree of mixing (figure 6.2.4b). While the formation of $YCrO_3$ is possible [314], it seems likely that these oxide phases are inter-mixed by the irradiation, and the time at 773 K is not sufficient for thermal diffusion to unmix the components (the Y_2O_3-Cr_2O_3 equilibrium phase diagram indicates negligible solubility [315]).

The smaller clusters have a metal:oxygen ratio very different to those of as-received clusters and more similar to the M:O of the small clusters observed in FeY-hi. Thus, the irradiated clusters may be oxygen deficient or a loss of oxygen may be apparent due to some APT artefact. Williams et al. [128] also observed clusters with a M:O close to 1 and 0.67, with the 0.67 clusters being larger in size and showing a different evaporation behaviour. When studying bulk Y_2O_3, Williams et al. observed a loss of Y ions, not O, during the experiment due to detector pile-up [121]. No evidence of ion dissociation that could cause the loss of neutral molecules was found [121]. Although the small clusters found after the irradiation have a composition similar to those found in FeY-hi, the ionic density through the clusters is very different (figure 6.2.8b). The ionic density of the small irradiated clusters is much lower than in the as-received material and more similar to the the ionic density of the clusters in the samples irradiated at cryogenic temperatures (figure 6.3.15). Therefore, these small clusters that form during the irradiation are very different to the small clusters observed in the as-received samples, even though they have similar sizes and compositions. Furthermore, the relatively low ionic density of the irradiated clusters reduces the chance that ions are lost due to pile-up at the detector. Therefore, unless another mechanism comes into play only with very small clusters, I judge that no significant loss of ions is occurring.

Another difference between the irradiated clusters and the FeY-hi clusters is their location: the irradiated clusters form preferentially on fast diffusion paths, GBs and dislocations (figure 6.2.3). The most Y-rich clusters were formed in the regions of highest damage (figure 6.2.5), suggesting either clustering of Y by irradiation-induced mechanisms or the preferential loss of O from the clusters. Therefore, this evidence together with that presented above

demonstrates the modification of the original Y_2O_3 oxide clusters and the formation of a new population of different Y-O clusters by irradiation at 773 K.

6.5.2 FeTiY

The GIXRD analysis showed a broader and less intense $Y_2Ti_2O_7$-(222) peak in all the FeTiY samples subject to irradiation at high temperature compared to the unirradiated samples (figure 6.2.13). This indicates both a reduction in volume fraction (reduced intensity) and decrease in scattering domain size or increased strain distribution (increased peak width), but the APT results do not suggest the same reduction in oxide volume fraction or cluster size (figure 6.2.15). This discrepancy may result from the difference in techniques: GIXRD is biased towards the detection of larger crystalline particles and APT toward chemical features. Therefore, the clusters observed by APT may not be the same features observed by GIXRD, meaning that the larger particles may be disrupted preferentially by the irradiation but the smaller clusters are more stable. The evidence from the irradiation of FeY suggests the larger particles are amorphous, which would mean that they do not contribute to the diffracted intensity. The stability of the smaller clusters is consistent with the theory of inverse-Ostwald ripening [226], where the combination of displacement damage and thermal diffusion leads to an eventual steady state with a specific stable particle size [225].

Conversely, the slight growth of the clusters measured by APT and reduction in number density when irradiated at 973 K could be evidence of radiation-induced Ostwald ripening of initially smaller clusters [25]. The increased vacancy concentration caused by the irradiation causes an increase in diffusion rates, leading to accelerated thermal growth. The trend of the GIXRD peak widths in figure 6.2.13 suggests that larger particles are being formed at the higher irradiation temperatures, but the particles resulting from the irradiation are still smaller than those in the as-received and unirradiated samples.

The odd results from the samples irradiated at T_{irrd} 873 K (both nanoindentation and APT) suggest that at this temperature there is some different behaviour. The Y-rich clusters

observed in this sample are spatially correlated (figure 6.2.18) and therefore, with the small sample volume of APT, an analysis may contain Y-rich clusters or may not depending on the exact spatial location. Indeed, some APT experiments contained Y-rich clusters and others did not. These features could be caused by chemical inhomogeneity in the starting material (c.f. figure 5.4.7 on page 128) or may result from the irradiation treatment. The Y-rich clusters in 873 K FeTiY had similar compositions to the small clusters observed in irradiated FeY; however, the clusters in FeTiY formed homogeneously, rather than preferentially on GBs and dislocations. By contrast in FeTiY, Y-, Ti- or O-depletion was observed at the GBs compared to the as-received sample. Comparing FeY and FeTiY, either the addition of titanium or the original particle distribution makes a considerable difference to the interaction of solute with the GBs. As shown in Chapter 5, the addition of Ti to the FeY alloy composition drastically reduces the cluster size, and so I would expect that Ti has the same refining influence during irradiation. The exact influence of Ti, whether it promotes nucleation or simply stabilises clusters, is uncertain, but the effect is the same. The other key difference is the initial cluster distribution in the two alloys: FeY contains much larger clusters and therefore has a much smaller area to act as sinks for point defects. In the absence of strong sinks, the defects may primarily be annihilated at GBs and this could promote the formation of the small clusters there.

6.5.3 FeCrTiY

In FeCrTiY after irradiation, GIXRD analysis of the $Y_2Ti_2O_7$-(222) peak showed reduced intensity, similar to FeTiY, but had the same FWHM as the as-received material (figure 6.2.22). The cluster size distribution measured by APT also showed only slight changes (within the range of variation of the inhomogeneity of the sample) after irradiation (figure 6.2.23). The GIXRD data did show, however, that carbides were formed by the irradiation, with increasing volume fraction at higher T_{irrd} (figure 6.2.20). These carbides, though occasionally observed by TEM, have a low enough number density to evade analysis by APT. APT of the oxide clusters did show a difference between the irradiated and as-received sam-

ples; the Y:Ti of all the irradiated and unirradiated samples was reduced relative to that of the starting material (figure 6.2.25). Unlike in FeTiY, no Y-rich clusters were formed by the irradiation, and the O-fraction of the clusters was slightly reduced. Lescoat et al. [25] similarly reported a reduction of the Y:Ti ratio of the smaller clusters after irradiation to 150 dpa at 773 K. The T_{irrd} 973 K sample showed different Cr segregation behaviour; the Cr-shell around the clusters was deteriorated compared to the as-received sample but still evident (figure 6.2.27) and Cr was depleted around GBs.

Looking at the nanohardness results, only the 973 K sample showed a noticeable increase after irradiation. Above 700 K it is expected that the hardening from loop damage would be annealed out [316, 317]. Though this sample contained the largest clusters of the FeCrTiY samples irradiated at high temperature (1.42 nm modal radius), it also had the highest number density of clusters. Additionally, GIXRD showed the carbide formation was greatest at 973 K; therefore both the oxide cluster distribution and the carbide particles may explain the increased nanoindentation hardness of this sample compared to the other FeCrTiY samples.

6.5.4 Displacement Mixing

To isolate the effect of irradiation damage in the absence of thermal diffusion, irradiation experiments were performed with $T_{irrd} < 150$ K to limit thermal diffusion. After this irradiation, a significant hardening was measured in both FeTiY and FeCrTiY, with FeTiY showing saturation of the hardness after 50 dpa and FeCrTiY showing further hardening at 100 dpa peak damage dose. The similarity of the hardness of the two different alloys leads me to conclude that the hardening comes from the same mechanism in both alloys, irrespective of Cr content. Point defects and dislocation loops may be formed by irradiation at < 150 K, which would cause significant hardening [318].

Looking at the oxide particles, the evidence from HRTEM and GIXRD results shows that larger particles remain intact but are not crystalline (figure 6.3.4). The loss of the smaller particles and reduction in number density seen from the cross-sectional EFTEM

(figure 6.3.3) indicates that particles may have been dissolved by the irradiation. This is in agreement with previous reports, with the critical temperature for amorphisation of $Y_2Ti_2O_7$ reported as 780 K (1 MeV Kr ions, 0.4 dpa critical dose) [319] and < 750 K for Cr-oxide [320].

This was investigated further by APT experiments that showed large and diffuse clusters of solute ions, confirming that the clusters have been disrupted by the irradiation (figure 6.3.7). The presence of metallic Ti^{++} ions, the increased solute content in the matrix (figure 6.3.9) and the difference in detected ionic density through the clusters are further evidence that the clusters have been at least partially dissolved by the irradiation. Therefore, the large increase in nanohardness may result from solid solution strengthening from the Y, Ti and O atoms displaced into the matrix and defects in the matrix caused by irradiation damage.

Though this dissolution behaviour is similar to that observed by others [24, 25, 190, 221], it contradicts the results shown by [24, 25] who noted a complete loss of clustering after irradiation at cryogenic temperatures. The clusters investigated by Parish et al. [190, 221] were larger and not fully dissolved by irradiation at 170 K and 160 dpa. The shape of the concentration profile shown in figure 6.3.12 is qualitatively similar to the Ti line scans shown in [190, 221], although the APT data is at a much smaller scale and better resolution than the STEM EDS line scans. Comparing my APT data with APT data reported elsewhere [24, 25], there is a discrepancy in that my clusters were not fully dissolved despite similar irradiation conditions. This may be due to a number of factors:

1. Larger initial radii of the particles in the as-received material preventing full dissolution [221].

2. Annealing caused by electronic stopping of the incident ions could help reform clusters or increase the solute mobility [221].

3. Other researchers may not have looked at a large enough volume to encounter these larger solute clusters. In both [24] and [25] the volume of examined material is not estimated.

4. Immiscible systems may not mix on irradiation [194], that is, there may be enough energy after the displacement cascade to allow some thermodynamic processes to occur, which is in agreement with the extreme stability of Y_2O_3 particles in α-Fe reported in [220].

On reflection, it is most likely that a combination of the above effects are present. A larger initial particle size seems like the most likely explanation as to the difference between my results and those reported in [24, 25], who started with particle radii of 1.7 and 3.0 nm respectively. My FeTiY and FeCrTiY alloys contained a low number density of larger particles, >5 nm radius and 10^{21} m^{-3}, which could then form the diffuse clusters after irradiation (c.f. figure 6.3.8). If the irradiation at $T_{irrd} < 150$ K causes pure mixing of the components, then it is expected that this would lead to a smaller variation in cluster compositions. However, the cluster compositions showed a wider range of compositions from Y-O to Ti-O, indicating some influence of thermodynamics during the displacement cascade.

6.5.4.1 Mixing Model

Looking at the amount of displacement mixing predicted from a purely physical model, relative to the amount of mixing measured experimentally, gives insight into the actual displacement-mixing mechanism. For example, Monnet et al. [18] used a ballistic model to account for the displacement damage caused to MgO by electron-irradiation, and concluded that the ballistic mechanism could not be solely responsible for the rate of shrinkage of the particles. Displacement mixing [191, 321] can be approximated to a diffusion process with the following diffusion coefficient, using the displacement rate Γ and the mean squared displacement $\langle x^2 \rangle$:

$$D_m = \frac{1}{6} \Gamma \langle x^2 \rangle$$

The analytical solution for the concentration $C(x)$ around a dissolving sphere of initial radius r_0 is given by [322]:

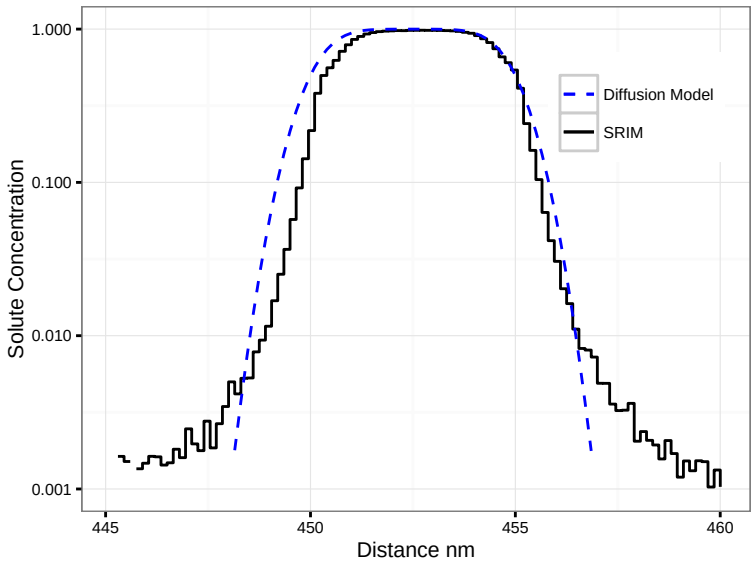

Figure 6.5.1 – SRIM predicted solute (Y+Ti+O) concentration from a 5 nm thick layer of $Y_2Ti_2O_7$ embedded in Fe at a depth of 450 nm (solid black curve). 10,000 simulated incident ions (Fe^+ 1.8 MeV), displacement energies: Fe 40 eV and 57 eV for Y, Ti and O, multiplied by a dose of 9×10^{16} ions/cm^2 to give a peak damage of 100 dpa. Density of $Y_2Ti_2O_7$ set to 5 gcm^{-3}. The dashed line is the fitted diffusion model with $C_0 = 1$ and $\sqrt{D_m t} = 0.49$ nm^{-1}, giving D_m =4.5–7.5 $\times 10^{-20}$ cm^{2}s^{-1}.

$$\frac{C(x)}{C_0} = \frac{1}{2}\left[\text{erf}\left(\frac{r_0 - x}{2\sqrt{Dt}}\right) + \text{erf}\left(\frac{r_0 + x}{2\sqrt{Dt}}\right)\right] \tag{6.5.1}$$

where C_0 is the initial concentration in the sphere, t is time and D is the diffusion coefficient in m^{2}s^{-1}. If D is replaced with D_m and t with the displacement damage dose rate Γ, then this can be used to estimate D_m from a concentration profile of a dissolved particle. Figure 6.5.1 shows the SRIM-predicted concentration profile of a 5 nm Y-Ti oxide particle after irradiation to 100 dpa, overlaid with the diffusion model given in equation 6.5.1 with D_m =4.5–7.5 $\times 10^{-20}$ cm^{2}s^{-1}. This is an underestimation of D_m because SRIM does not account for the accumulation of displaced atoms, as noted by [221], and because SRIM is a purely ballistic simulation, there is no chemical influence on the mixing.

The alternative method for estimating D_m using SRIM is to measure $\langle x^2 \rangle$ directly from the recoil distribution [226]. Lescoat et al. [25] use this method and come to a D_m of 6.7×10^{-19}–1.3×10^{-18} cm^{2}s^{-1}, assuming the displacement rate T is equal to the damage rate in dpa [25]. Once D_m is calculated, it can be used in the same way as by Frost and Russel [321];

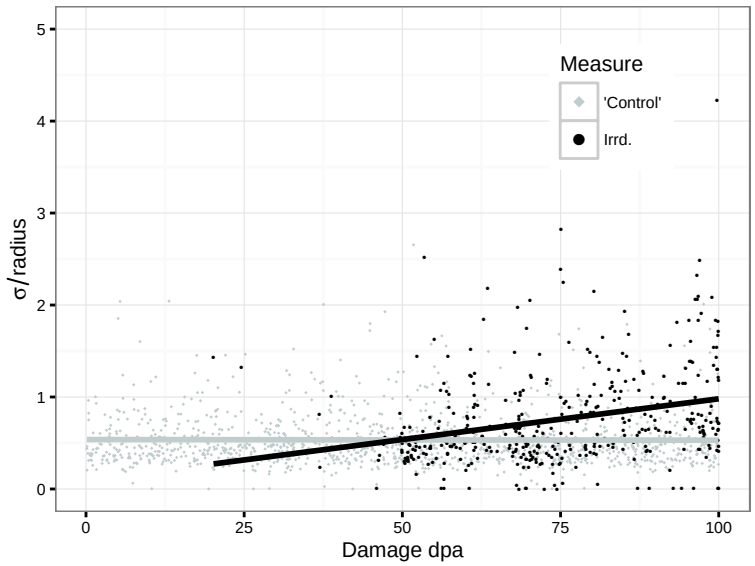

Figure 6.5.2 – Fitted Gaussian width (σ) of (Y+Ti+O) composition line profiles in irradiated FeTiY and FeCrTiY (T_{irrd} < 150 K). The fitted width is divided by an approximate radius estimated from the number of counts in the line profile. The "control" points are the profile widths (σ/radius) of the as-received materials with random dpa values.

thus the shape of the concentration profile should agree with equation 6.5.1. However, the profile predicted by SRIM does not fit this model well, especially as SRIM predicts a higher concentration further from the particle than the diffusive model, but the shape of the SRIM profile does match the experimentally measured composition line profiles given in figures 6.3.12 and 6.3.13, which have a wide spread of solute either side of the cluster.

Despite the limitations of the diffusion model, it allows an approximate measure of the dissolution of the clusters as a function of damage. This is only possible by making an assumption about the initial size of the cluster. Here I have estimated the initial cluster radius from the number of counts (of Y, Ti and O) in the measured line profile. Figure 6.5.2 shows the fitted width of the composition line profile normalised by an estimate of the initial radius. The linear line of best fit from figure 6.5.2 indicates, with a p-value < 0.1%, that the composition profile width is proportional to the damage in dpa, but without knowledge of the exact starting size of the clusters before irradiation, it is not possible to estimate $\sqrt{D_m\Gamma}$.

Having looked at the effects of irradiation in the absence of thermal diffusion, using the data from the samples annealed and irradiated at high temperature, the influence of

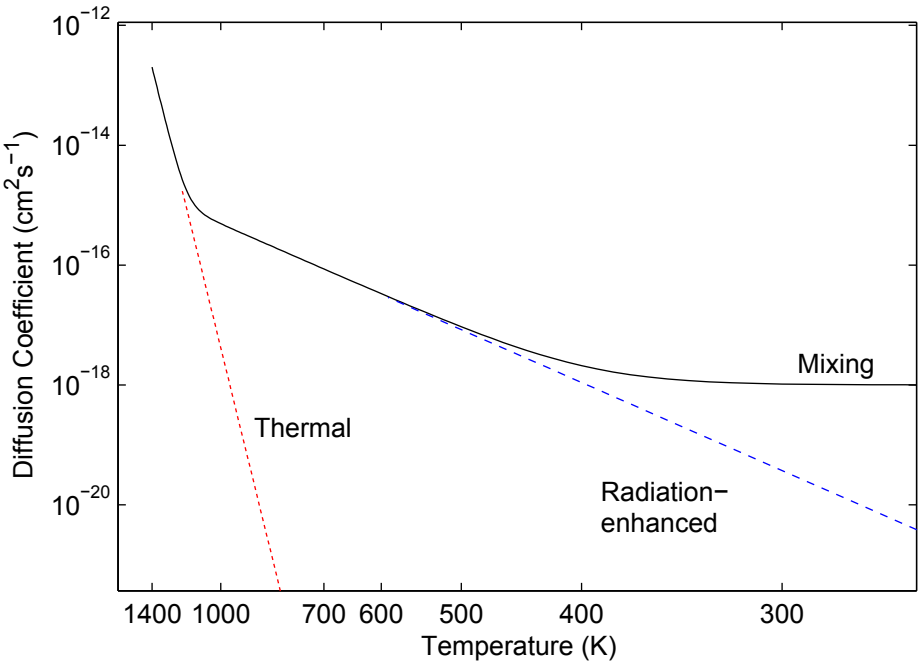

Figure 6.5.3 – The steady-state diffusion coefficient of Y during irradiation, at a displacement rate of 6.4×10^{-3} dpa/s, as a function of temperature. The contributions from displacement mixing, radiation-enhanced diffusion and thermal diffusion are indicated. The values are representative of bulk diffusion of Y in Fe with a sink strength of 4.3×10^{11} cm^{-2}, as per [25].

temperature on the irradiation processes can be investigated.

6.5.5 High-Temperature Irradiation

Lescoat et al. [25] demonstrated the application of established descriptions of irradiation-enhanced diffusion [323] and the estimate of displacement mixing (presented above) to determine the stability of the oxide particles as a function of temperature. They argued that the growth of the particles is controlled by the diffusion of Y in Fe, as this is the slowest diffusing species. The diffusion coefficient of Y as a function of temperature under irradiation (using their parameters and values) is shown in figure 6.5.3.

Figure 6.5.3 has 3 regimes:

1. T > 1000 K: diffusion of Y is dominated by thermal diffusion, D_{th}
2. 400 < T < 1000 K: diffusion is thermal but enhanced by an excess of vacancies created by irradiation, D_{irr}

3. T < 400 K: the diffusion coefficient is defined by displacement mixing (equation 6.5.1), D_m

Lescoat et al. explained the coarsening of the particles at T_{irrd} 773 K by irradiation-enhanced Ostwald ripening due to the enhanced diffusion coefficient, and they explained the loss of particles at T_{irrd} 170 K by D_m being greater than D_{irr}. In another similar experiment by Allen et al. [23], shrinkage of the particles at 773 K was observed. However, in my experiments with T_{irrd} = 773 K, coarsening was not observed, despite the similarity of the irradiation conditions. One important difference between the experiments is the alloy composition because Lescoat's material contained roughly twice the content of Y_2O_3: Fe-18Cr-1W-0.3Ti-0.6Y_2O_3 and Allen's starting material contained much larger particles.

Lescoat considered the particles as either growing or shrinking based on the value of $D_{irr}(T)$ relative to D_m. However, early models of particle stability under irradiation suggest that during irradiation it is possible to reach steady-state conditions [321]. That is, after some initial time, the particle radii will tend to some constant value, rather than continuous growth or dissolution. Some of the limitations of the early models, such as the assumption of fixed displacement distance or the restriction that solute can only be moved from particles to the matrix, have been relaxed by more complex phase-field [225] or molecular dynamics models [226]. It is not in the scope of this work to carry out detailed computer modelling; however, the important implication of the later modelling work indicates that though D_m is analogous to a diffusion process, it does not take place at the atomic length scale. This difference in length scales leads to mesoscopic patterning of the microstructure [324], including the steady-state behaviour described by [321].

Another assumption made by Lescoat et al. was that the growth of the Y-Ti oxides was controlled solely by the diffusion of Y. This is the case with my experimental results on the irradiation of FeY; new Y-rich clusters were formed in diffusion short-cuts. However, they noted the reduction in the Y:Ti ratio of the smaller clusters after irradiation at 773 K, similar to my own findings, and this chemical alteration indicates that Ti has an important role in the cluster growth. In both irradiated FeTiY and FeCrTiY, generally fewer Y-rich clusters were

observed compared to the as-received material. This may be due to the preferential dissolution of these clusters or the gain of Ti by these clusters. Given the much greater diffusion rates of O and Ti in Fe compared to Y (even when enhanced by irradiation), it seems plausible that the redistribution of Ti is responsible for the chemical alteration of the clusters after irradiation at high temperature. For instance, in neutron irradiated MA957, Ti segregation to the grain boundaries was observed [325]. The thermal and radiation-enhanced diffusion coefficients of Y and Ti are shown in in figure 6.5.4. Because the irradiation experiments had some time of annealing after the irradiation (as the samples cooled), the resulting microstructure is a product of both radiation-enhanced and thermal diffusion. The clusters in T_{irrd} 973 K FeTiY show a much smaller variation in composition than in the as-received material, indicating homogenization of the cluster compositions—consistent with the Ti redistribution theory. The samples irradiated at 150 K and then subsequently irradiated also showed a trend to reduced Y:Ti ratio (figure 6.4.7) consistent with this idea. In contrast to this homogenization behaviour, the $T_{irrd} < 150$ K samples show a broader distribution of cluster compositions and the smallest clusters are Y-rich. This behaviour is consistent with chemical unmixing during irradiation, rather than homogenization.

6.5.6 Conclusions

The irradiation behaviour of the oxide clusters in the model ODS alloys studied was a combination of displacement mixing, which is evident at low temperatures, and radiation-enhanced diffusion of both Y and Ti. Although clusters were present in the samples irradiated at high temperature, these may not all be the same clusters which existed before the irradiation, and as the results from FeY showed, new clusters can be nucleated during the irradiation. The presence of Ti and an initial distribution of clusters seems to reduce the solute (Y, Ti and O) segregation to the grain boundaries. However, the samples irradiated at low temperature and then annealed show that if solute is ejected into the matrix then it will segregate to the GBs. As described by numerical models, the cluster population is dynamic with the irradiation conditions and may reach a steady state after prolonged periods

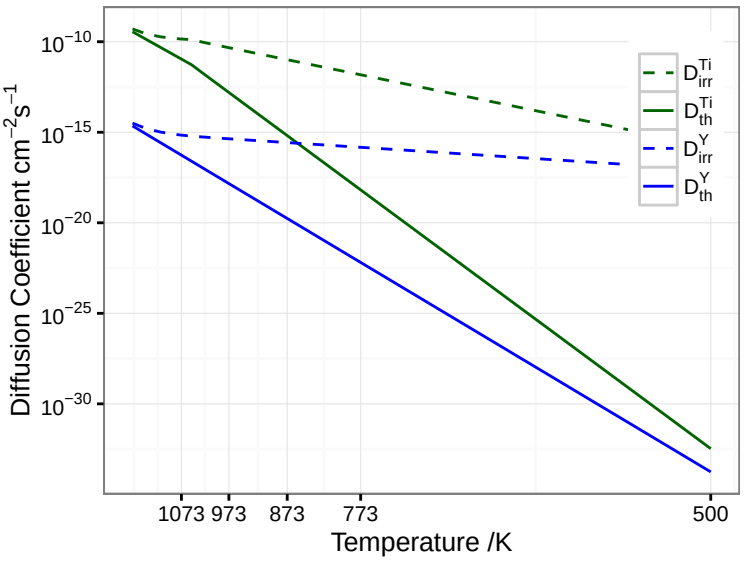

Figure 6.5.4 – Comparison of the estimated diffusion coefficients of Ti (green) and Y (blue) in iron during irradiation. The dashed lines show the irradiation-enhanced diffusion coefficients. Ti diffusion equation from [326]. The values are representative of bulk diffusion in Fe with a sink strength of 3.8×10^{11} cm^{-2}, approximated from the cluster distribution in as-received FeTiY with a displacement rate of 1×10^{-3} dpa/s.

of irradiation with a specific stable cluster radius and number density.

The critical stability temperature (T^*, defined in section 2.4.3) of the oxides can be judged from the APT results. For FeY, the irradiation at 773 K is in the $T \ll T^*$ regime as new clusters are precipitated. For FeTiY, T^* lies between 873 and 973 K because the clusters in the T_{irrd} 973 K sample showed some coarsening. However, $T^*$for the clusters in FeCrTiY must lie above 973 K for the irradiation conditions used in my experiments, as no coarsening was observed at this temperature. Even ignoring the chemical behaviour of the clusters, the cluster size evidence presented shows that T^* depends on the alloy composition. Thus, it is possible that the ODS alloy composition can be tuned to form clusters with an adequate irradiation resistance for the conditions they will experience in service.

6.6 Summary

Three model ODS alloys have been subject to a high dose of self-ion irradiation at a range of different temperatures to investigate the irradiation stability of the oxide particles they con-

tain. In general, the volume fraction of crystalline oxide phase was reduced by irradiation, but clusters of similar radii and number density to the as-received material were observed in all alloys. Evidence from HRTEM indicates that the particles may be amorphised by ion-irradiation, something the APT is insensitive to. However, changes in the ionic density of the clusters detected using my new averaging line profile methodology may be a result of amorphisation.

The cluster stability was observed as a function of temperature, with subtle differences in chemistry and distribution in the samples irradiated at higher temperatures, and more dramatic changes in the samples irradiated below 150 K. The samples irradiated at cryogenic temperatures showed no crystalline oxide reflections in GIXRD data and large increases in hardness, but the APT data showed some clustering of Y, Ti and O was still present. Investigation of the chemistry of these clusters indicated the displacement mixing of the material was not purely a physical process and had some chemical component. Changes in cluster chemistry at high temperature also suggest that redistribution of Ti, rather than only Y, is important for determining the response of the clusters to irradiation.

Critically, it is clear from these results that the distinction of "stable" or "not stable" is insufficient to describe the irradiation response, as it involves many factors including the cluster size, number density, morphology and chemistry. The experimental results presented in this chapter highlight some of limitations of the current understanding of precipitate stability under irradiation, specifically the role of diffusion short-cuts (in irradiated FeY) and that the growth of the clusters may not be limited solely by the Y flux.

Chapter 7

Summary and Conclusions

7.1 Introduction

The safe and reliable operation of fission and fusion power production relies on the structural stability of their construction materials. Oxide dispersion strengthened steels possess high-temperature properties that make them suitable for the fuel cladding material in advanced fission reactors and for the first wall and blanket materials for fusion reactors. It is important to understand the behaviour of these oxide clusters under irradiation, as they provide the high-temperature stability and irradiation resistance of these materials. However, few studies on ODS alloys have been conducted in a systematic manner and to such a level of detail before, while very few studies have compared the irradiation resistance of different alloys under the same irradiation conditions. This chapter gives an overview summary of the work in the preceding chapters, followed by the overall conclusions of the work and suggestions for future research.

7.2 Summary

The empirical findings of this work are given in summary in chapters 5 and 6. A graphical summary of the atom probe results are shown in figure 7.2.1. These findings were made possible through the application of high-resolution characterisation techniques de-

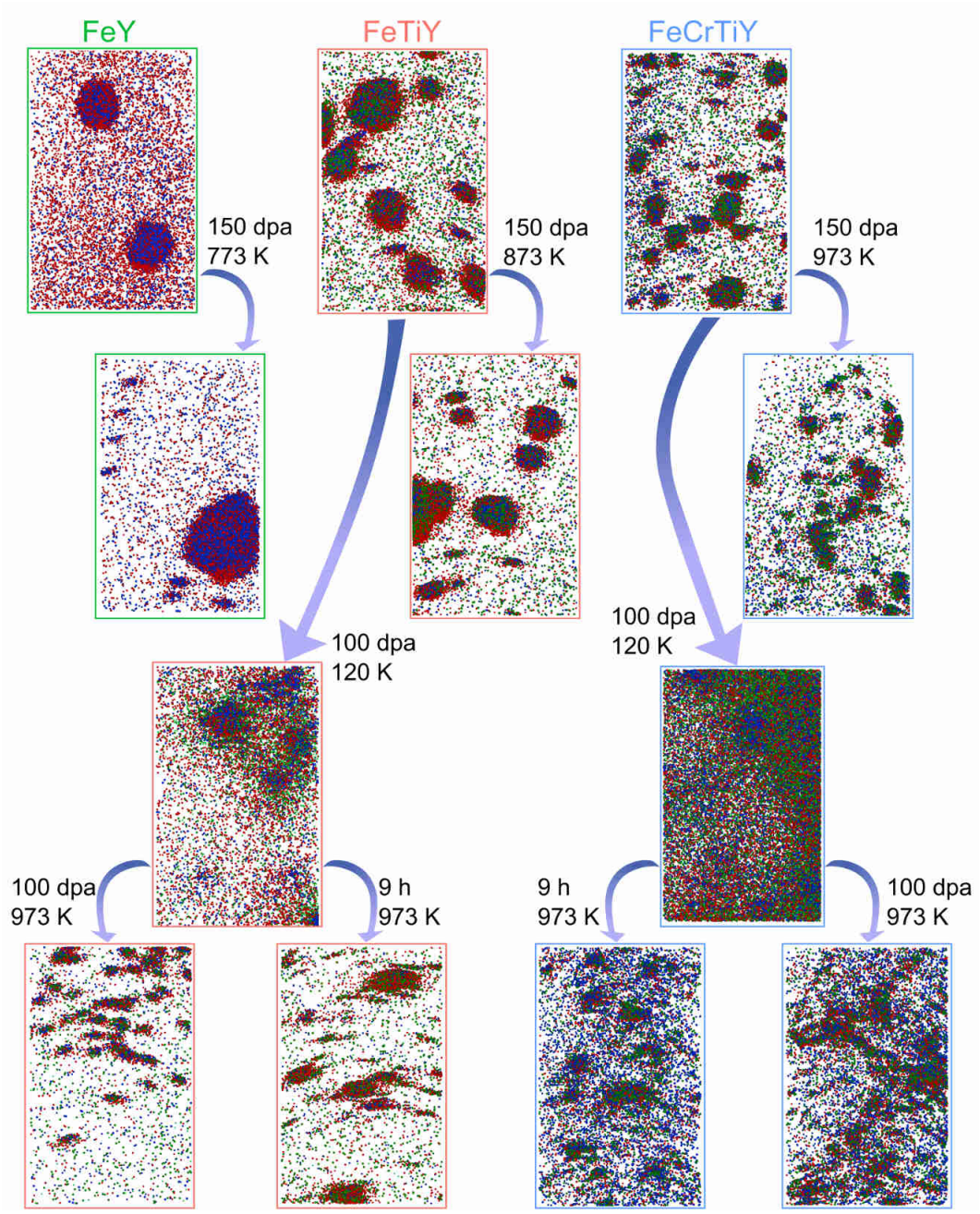

Figure 7.2.1 – Summary image of atom maps from samples subject to different irradiation conditions. The as-received samples are shown at the top, second row shows the samples after irradiation at high temperature, the 3rd row are samples irradiated at 120 K and the bottom row shows the result of subsequent irradiation and thermal treatments.

tailed in chapter 3 and the extended data analysis techniques given in chapter 4. This section summarises how the findings of this work address the research questions posed in the introduction: what is the effect of alloy composition on the particles; what is the irradiation behaviour of the oxide clusters; and how does this behaviour depend on T_{irrd} and alloy composition? I have been the first to apply GIXRD to study irradiation damage of ODS alloys and I have implemented improved atom probe data analysis methods in order to address these questions.

The methods of TEM and APT using FIB to prepare samples, though complex, has become routine for the site-specific study of the shallow damage layers produced by ion irradiation. However, the inhomogeneity of my ODS samples studied (section §5.5) has posed some difficulties for the small-scale characterisation techniques of TEM and APT. Therefore, glancing incidence XRD was applied to study the irradiation response of the oxide phases on a macroscopic scale. This technique is complementary to APT, and revealed changes in both the oxide clusters as a function of irradiation temperature and the radiation-enhanced growth of carbides in the Cr-containing ODS alloy.

The main limitation of using APT to study ODS materials is the differing evaporation behaviour of the metal matrix and the oxide phases. Refinements to the reconstruction protocol and continuous or *in-situ* measurement of the tip shape [327] are necessary to further improve the reconstruction accuracy. The current reconstruction protocol may also be improved by comparison of the reconstructed data with computer models of the APT experiment [258]. However, chapter 4 explains how I used automated, systematic and organised methods to enhance the current analysis of the APT data. I have taken pragmatic approaches to analyse the oxide clusters, using composition line profiles parallel to the APT analysis direction and implementing a matrix correction to measure the composition. My extended methods illuminated changes in the cluster chemistry as a function of irradiation treatment and gave more statistical confidence to the findings. Certain et al. [135] noted that composition line profiles of some clusters in an irradiated ODS sample analysed by APT "were too noisy to detect a subtle increase in Cr concentration." [135]. However, the profile averaging

routine I have developed (section §4.5.1) has demonstrated Cr-rich shells in even sub-2 nm radii clusters in the irradiated samples (figure 6.2.27).

7.3 Conclusions

Evidence from my own results and that summarised in the literature suggest the oxide phases present in ODS alloys are formed during the consolidation and are not simply a dispersion of the original Y_2O_3 oxide. The effect of Ti on the oxide structure is well known and my results are in agreement with those reported elsewhere, that Ti strongly interacts with the oxide clusters and produces a new Y-Ti oxide phase. My work shows that a range of Y:Ti ratios in the oxide clusters are possible and I suggest these may occur due to micrometre-range variations in the chemistry of the mechanically alloyed powders before consolidation. These findings are in agreement with TEM studies of similar alloys, which show that defective or vacancy-rich oxides may form. The effect of Cr on the oxides is less well understood, but my results show conclusively that the presence of Cr reduces the cluster size, enhances number density and induces the formation of Cr-rich shells around the clusters.

The high-temperature irradiation behaviour was observed to be different for each of the three alloy compositions; the Fe–Y_2O_3 alloy nucleated many small Y-rich clusters on grain boundaries and dislocations; the Fe–Ti–Y_2O_3 alloy showed anomalous behaviour at $T_{irrd} \leq 873$ K by forming Y-rich clusters homogeneously and showing cluster coarsening at 973 K; and the clusters Fe–Cr–Ti–Y_2O_3 alloy retained their Cr-rich shells, average radius and number density after irradiation. After irradiation at 973 K, the predominantly Ti-rich clusters were observed, and it is proposed that this is due to the redistribution of Ti during the irradiation by combination of displacement damage and irradiation-enhanced diffusion. However, after irradiation at < 150 K, the smallest clusters were removed but larger diffuse clusters remained. These larger clusters had a large variety of different compositions and this was taken to be evidence of chemically-driven displacement un-mixing rather than a purely physical homogenisation. Annealing or further irradiation of these samples at 973 K

resulted in a high number density of very small clusters that formed on grain boundaries in the Fe–Cr–Ti–Y_2O_3 alloy. The larger clusters formed in the irradiated samples are evidence of irradiation enhancing the diffusion rates and causing accelerated growth of the clusters, rather than causing dissolution of the clusters. Comparison of the FeTiY and FeCrTiY alloys showed that the critical temperature T^* (for the irradiation conditions used) was $T^*_{FeTiY} \ll 973\,\mathrm{K}$ and $T^*_{FeCrTiY} < 973\,\mathrm{K}$ for samples that had been irradiated at low-temperature first.

7.4 Suggestions for Future Work

The conclusions and results presented above highlight the need for further investigation of specific aspects. These are given below:

- Creation of an alloy of Fe, Cr and Y_2O_3 to compare the influence of Cr in the absence of Ti
- A detailed investigation of the dose rate effects, using different displacement damage rates and including a comparison of a diffuse and rastered ion beam
- A control experiment of cryogenic irradiation of an Fe-Cr alloy to measure the extent of the hardening caused in the matrix in the absence of oxide particles
- Some kind of modelling work, similar to [220], to replicate the partial dissolution of the oxide particles at high-dose irradiation at < 150 K
- An experiment to determine how the mechanical properties depend on the microstructural properties of ODS alloys, for example, what is the optimal oxide particle size and volume fraction? This information could be used to optimise ODS alloys
- Good progress has been made on the modelling of point defects and clusters in irradiated metals, however the modelling of chemical segregation and clustering is less well understood. Therefore further investigation should be made into the chemical changes which occur during irradiation, including the development of a unified framework for understanding these effects in any irradiated metal

- The measurement of clustering in this work required an arbitrarily parameterised selection procedure. In the future an objective approach, perhaps the maximisation of information c.f. [328] or such as that used in principal component analysis, should be used to inform the cluster selection.

*****

This study set out to improve our understanding of irradiation damage of oxide particles in oxide dispersion strengthened steel through the use of model alloys. Well controlled and systematically varied alloy compositions provided insight into the refining influence of Ti, but also into the effect of Cr to form shells around the particles and restrict their size. The irradiation stability was shown to depend on the initial particle distribution, particle chemistry and irradiation temperature. Irradiation at cryogenic temperature did not fully dissolve the particles, and the cluster compositions showed evidence for the thermodynamic influence on displacement mixing. These results were only made possible by the application of novel analysis techniques applied to APT data and careful processing of the mass-spectrum data. Changes to the crystalline structure were observed in bulk samples using the new application of GIXRD to study the shallow depth irradiation damage. The irradiation damage at high temperature was explained in the context of existing models, and the discrepancies between their predictions and the experimental results presented highlighted the need for the use of more sophisticated modelling techniques.

Chapter 8

Bibliography

[1] Petroleum, B. *BP Statistical Review*. http://www.bp.com/statisticalreview, 2010.

[2] Pachauri, R.K. *"Climate Change 2007: Synthesis Report. Contribution of Working Groups I, II and III to the Fourth Assessment Report of the Intergovernmental Panel on Climate Change"*, vol. 446. IPCC, 2007.

[3] Abrams, B., et al. *A technology roadmap for generation IV nuclear energy systems*. In *US DOE Nucl. Energy Res. Advis. Comm. Gener. IV Int. Forum*, 1–97. 2002.

[4] Ehrlich, K. *The development of structural materials for fusion reactors*. Philos. Trans. R. Soc. London. Ser. A Math. Phys. Eng. Sci., 357(1752):595, 1999.

[5] Raffray, A.R., et al. *Breeding blanket concepts for fusion and materials requirements*. J. Nucl. Mater., 307-311:21, 2002.

[6] Bloom, E.E., et al. *Materials to deliver the promise of fusion power–progress and challenges*. J. Nucl. Mater., 329:12, 2004.

[7] Mansur, L.K., et al. *Materials needs for fusion, Generation IV fission reactors and spallation neutron sources–similarities and differences*. J. Nucl. Mater., 329:166, 2004.

[8] Murty, K., et al. *Structural materials for Gen-IV nuclear reactors: Challenges and opportunities*. J. Nucl. Mater., 383(1-2):189, 2008.

[9] Vladimirov, P., et al. *Comparison of material irradiation conditions for fusion, spallation, stripping and fission neutron sources*. J. Nucl. Mater., 329:233, 2004.

[10] Bloom, E.E., et al. *Critical questions in materials science and engineering for successful development of fusion power*. J. Nucl. Mater., 367:1, 2007.

[11] Boutard, J.L., et al. *Fissile core and Tritium-Breeding Blanket: structural materials and their requirements*. Comptes Rendus Phys., 9(3):287, 2008.

[12] Cheon, J.S., et al. *Sodium fast reactor evaluation: Core materials*. J. Nucl. Mater., 392(2):324, 2009.

[13] Baluc, N., et al. *On the potentiality of using ferritic/martensitic steels as structural materials for fusion reactors*. Nucl. fusion, 44:56, 2004.

[14] Hoelzer, D.T., et al. *Influence of particle dispersions on the high-temperature strength of ferritic alloys*. J. Nucl. Mater., 367:166, 2007.

[15] Mouawad, B., et al. *Tailoring the microstructure and the mechanical properties of ultrafine grained high strength ferritic steels by powder metallurgy*. J. Nucl. Mater., 465:54, 2015.

[16] Okuda, T. *Control of Oxide Particle Size and Recrystallized Grain Structure in Oxide Dispersion Strengthened Ferritic Steel*. Tetsu-to-Hagane, 83(12):797, 1997.

[17] Ukai, S., et al. *Alloying design of oxide dispersion strengthened ferritic steel for long life FBRs core materials*. J. Nucl. Mater., 204:65, 1993.

[18] Monnet, I., et al. *Microstructural investigation of the stability under irradiation of oxide dispersion strengthened ferritic steels*. J. Nucl. Mater., 335(3):311, 2004.

[19] Yamamoto, T., et al. *The transport and fate of helium in nanostructured ferritic alloys at fusion relevant He/dpa ratios and dpa rates*. J. Nucl. Mater., 367:399, 2007.

[20] Miller, M.K., et al. *Radiation Response of a 12YWT Nanostructured Ferritic Steel*. In *MRS Proc.*, vol. 1215. Cambridge Univ Press, 2009.

[21] Mazey, D. *Fundamental aspects of high-energy ion-beam simulation techniques and their relevance to fusion materials studies*. J. Nucl. Mater., 174(2-3):196, 1990.

[22] Was, G.S., et al. *Emulation of neutron irradiation effects with protons: Validation of principle*. J. Nucl. Mater., 300(2):198, 2002.

[23] Allen, T.R., et al. *Radiation response of a 9 chromium oxide dispersion strengthened steel to heavy ion irradiation*. J. Nucl. Mater., 375(1):26, 2008.

[24] Certain, A.G., et al. *Radiation stability of nanoclusters in nano-structured oxide dispersion strengthened (ODS) steels*. J. Nucl. Mater., 434(1-3):311, 2013.

[25] Lescoat, M.L., et al. *Radiation-induced Ostwald ripening in oxide dispersion strengthened ferritic steels irradiated at high ion dose*. Acta Mater., 78:328, 2014.

[26] Little, E. *Development of Ferritic–Martensitic Steels for Fast Reactor Applications*. Irradiat. Behav. Met. Mater. Fast React. Core Components, 31–37, 1979.

[27] Rosenwasser, S.N., et al. *The application of martensitic stainless steels in long lifetime fusion first wall/blankets*. J. Nucl. Mater., 85:177, 1979.

[28] Klueh, R.L. *Elevated temperature ferritic and martensitic steels and their application to future nuclear reactors*. Int. Mater. Rev., 50(5):287, 2005.

[29] Kimura, A., et al. *Development of Al added high-Cr ODS steels for fuel cladding of next generation nuclear systems*. J. Nucl. Mater., 2011.

[30] Garner, F.A., et al. *Comparison of swelling and irradiation creep behavior of fcc-austenitic and bcc-ferritic/martensitic alloys at high neutron exposure*. J. Nucl. Mater., 276(1):123, 2000.

[31] Baluc, N. *Materials for fusion power reactors*. Plasma Phys. Control. fusion, 48:B165, 2006.

[32] Sublet, J.C., et al. *The neutronic basis for elemental substitution in martensitic steels*. J. Nucl. Mater., 212:695, 1994.

[33] Tanigawa, H., et al. *Status and key issues of reduced activation ferritic/martensitic steels as the structural material for a DEMO blanket*. J. Nucl. Mater., 2011.

[34] Klueh, R.L., et al. *High-chromium ferritic and martensitic steels for nuclear applications*, vol. 3. ASTM International, 2001.

[35] Klueh, R.L., et al. *Ferritic/martensitic steels–overview of recent results*. J. Nucl. Mater., 307:455, 2002.

[36] Odette, G.R., et al. *Recent Developments in Irradiation-Resistant Steels*. Annu. Rev. Mater. Res., 38(1):471, 2008.

[37] Humphreys, F.J. *Dislocations and properties of real materials*. London Inst. Met., 1985.

[38] Nembach, E. *Particle strengthening of metals and alloys*. New York: John Wiley & Sons, 1997.

[39] Ukai, S., et al. *Development of 9Cr-ODS Martensitic Steel Claddings for Fuel Pins by means of Ferrite to Austenite Phase Transformation*. J. Nucl. Sci. Technol., 39(7):778, 2002.

[40] Li, L., et al. *Solubilities of Cerium, Neodymium, and Yttrium in alpha-Iron*. Acta Metall. Sin. Repub. China), 29(3), 1993.

[41] Klueh, R.L., et al. *A potential new ferritic/martensitic steel for fusion applications*. J. Nucl. Mater., 283:697, 2000.

[42] Sigler, D.R. *Aluminum oxide adherence on Fe-Cr-Al alloys modified with group IIIB, IVB, VB, and VIB elements*. Oxid. Met., 32(5):337, 1989.

[43] Benjamin, J.S. *Composite Metal Powder, US Patent 3,591,362*, 1971.

[44] Huet, J., et al. *Dispersion-Strengthened Ferritic Steels For Fast Reactor Fuel Cans*. *Tech. rep.*, CEN/SCK, Mol, Belg., 1970.

[45] Breyer, J.P., et al. *Ferritic Stainless alloys containing titanium and molybdenum as major alloying additions*. *Tech. Rep. 36*, Centre de Recherches Metallurgique, Liege, 1973.

[46] Huet, J.J., et al. *Dispersion-strengthened ferritic steels as fast-reactor structural materials*. Nucl. Technol., v. 24, no. 2, pp. 216-224, 24(2), 1974.

[47] Fischer, J.J. *Dispersion strengthened ferritic alloy for use in liquid-metal fast breeder reactors (LMF-BRS)*, 1978.

[48] Hamilton, M.L., et al. *Fabrication Technological Development of the Oxide Dispersion Strengthened Alloy MA957 I for Fast Reactor Applications*. PNL-13168, 1—-110, 2000.

[49] Ukai, S., et al. *Development of oxide dispersion strengthened ferritic steels for FBR core application,(I).*

Improvement of mechanical properties by recrystallization processing. J. Nucl. Sci. Technol., 34(3):256, 1997.

[50] Ukai, S., et al. *Preliminary tube manufacturing of oxide dispersion strengthened ferritic steels with recrystallized structure*. J. Nucl. Sci. Technol., 36(8):710, 1999.

[51] Ukai, S., et al. *Tube manufacturing and characterization of oxide dispersion strengthened ferritic steels*. J. Nucl. Mater., 283:702, 2000.

[52] Ukai, S., et al. *Perspective of ODS alloys application in nuclear environments*. J. Nucl. Mater., 307-311:749, 2002.

[53] Ukai, S., et al. *Oxide Dispersion Strengthened (ODS) Fuel Pins Fabrication for BOR-60 Irradiation Test*. J. Nucl. Sci. Technol., 42(1):109, 2005.

[54] Ohtsuka, S., et al. *Nano-mesoscopic structural control in 9CrODS ferritic/martensitic steels*. J. Nucl. Mater., 351(1):241, 2006.

[55] Okuda, T., et al. *Development of Oxide Dispersion Strengthened (ODS) Ferritic Alloys With Excellent High Temperature Creep Strength and Neutron Irradiation Resistance*. New Mater. Process. Futur., 1616–1621, 1989.

[56] Kim, I.S., et al. *Effect of Ti and W on the mechanical properties and microstructure of 12% Cr base mechanical-alloyed nano-sized ODS ferritic alloys*. ISIJ Int., 43(10):1640, 2003.

[57] Uchida, Y., et al. *Effect of Minor Alloying Element on Dispersing Nano-Particles in ODS Steel*. In *Mater. Res. Soc. Symp. Proc.*, vol. 981, 107. Cambridge Univ Press, 2007.

[58] Gaganidze, E., et al. *Processing and TMT of Ferritic/martensitic ODS Steels for Fast Reactor Cladding*. ODS Workshop 24–26th Sept, Oxford University, 2012.

[59] Odette, G.R., et al. *Multiple Technique Characterization of a Nanostructured Ferritic Alloy: Heat-to-Heat, Long Term High Temperature Thermal Aging and Friction Stir Welding Effects on Nano-Scale Dispersion Strengthening Features*. Microsc. Microanal., 16(S2):1600, 2010.

[60] Miller, M.K., et al. *Nanometer scale precipitation in ferritic MA/ODS alloy MA957*. J. Nucl. Mater., 329-333(2004):338, 2004.

[61] Hedrich, H.D., et al. *New Materials by Mechanical Alloying Techniques*, 1986.

[62] De Gaudenzi, G.P., et al. *ODS alloys for high temperature heat exchangers, evaluation of hot corrosion resistance of MA 956 and PM 2000*. Mater. Adv. Power Eng. 1994, 1563–1572, 1994.

[63] Kasada, R., et al. *Pre- and post-deformation microstructures of oxide dispersion strengthened ferritic steels*. J. Nucl. Mater., 367-370 A:222, 2007.

[64] Yutani, K., et al. *Evaluation of Helium effects on swelling behavior of oxide dispersion strengthened ferritic steels under ion irradiation*. J. Nucl. Mater., 367-370:423, 2007.

[65] Larson, D.J., et al. *Three-dimensional atom probe observation of nanoscale titanium-oxygen clustering*

in an oxide-dispersion-strengthened Fe-12Cr-3W-0.4Ti+Y2O3 ferritic alloy. Scr. Mater., 44(2001):359, 2001.

[66] Miller, M.K., et al. *Characterization of precipitates in MA/ODS ferritic alloys*. J. Nucl. Mater., 351(1-3):261, 2006.

[67] Lindau, R., et al. *Mechanical and microstructural properties of a hipped RAFM ODS-steel*. J. Nucl. Mater., 307:769, 2002.

[68] Lindau, R., et al. *Present development status of EUROFER and ODS-EUROFER for application in blanket concepts*. Fusion Eng. Des., 75-79:989, 2005.

[69] Sakasegawa, H., et al. *Precipitation behavior of oxide particles in mechanically alloyed powder of oxide-dispersion-strengthened steel*. J. Alloys Compd., 452(1):2, 2008.

[70] Alinger, M.J., et al. *On the role of alloy composition and processing parameters in nanocluster formation and dispersion strengthening in nanostuctured ferritic alloys*. Acta Mater., 57(2):392, 2009.

[71] Hin, C., et al. *Formation of Y2 O3 nanoclusters in nanostructured ferritic alloys during isothermal and anisothermal heat treatment: A kinetic Monte Carlo study*. Phys. Rev. B - Condens. Matter Mater. Phys., 80, 2009.

[72] Barnard, L., et al. *An ab initio study of Ti–Y–O nanocluster energetics in nanostructured ferritic alloys*. Acta Mater., 60(3):935, 2012.

[73] Miller, M.K., et al. *Vacancies as a constitutive element for the design of nanocluster-strengthened ferritic steels*. Front. Mater. Sci. China, 3(1):9, 2009.

[74] Suryanarayana, C. *Mechanical alloying and milling*. Prog. Mater. Sci., 46(1-2):1, 2001.

[75] Benjamin, J.S. *Dispersion strengthened superalloys by mechanical alloying*. Metall. Mater. Trans. B, 1(10):2943, 1970.

[76] Capdevila, C., et al. *Manufacturing and microstructural evolution of mechanuically alloyed oxide dispersion strengthened superalloys*. Adv. Eng. Mater., 3(9):647, 2001.

[77] Walker, J.C., et al. *Fabrication of Fe–Cr–Al Oxide Dispersion Strengthened PM2000 Alloy Using Selective Laser Melting*. Adv. Eng. Mater., 11(7):541, 2009.

[78] Liu, Y., et al. *Formation of oxides particles in ferritic steel by using gas-atomized powder*. J. Nucl. Mater., 396(1):86, 2010.

[79] Rieken, J.R., et al. *Reactive gas atomization processing for Fe-based ODS alloys*. J. Nucl. Mater., 2011.

[80] Munir, Z.A., et al. *The effect of electric field and pressure on the synthesis and consolidation of materials: a review of the spark plasma sintering method*. J. Mater. Sci., 41(3):763, 2006.

[81] Okuda, T., et al. *Processing condition of oxide dispersion strengthened ferritic steel by mechanical alloying*. Solid State Powder Process., 195–202, 1989.

[82] Yamashita, S., et al. *Effect of mechanical alloying parameters on irradiation damage in oxide dispersion strengthened ferritic steels*. J. Nucl. Mater., 283-287:647, 2000.

[83] Roldan, M., et al. *Comparative study of helium effects on EU-ODS EUROFER and EUROFER97 by nanoindentation and TEM*. J. Nucl. Mater., 460:226, 2015.

[84] Lasalmonie, A., et al. *Influence of grain size on the mechanical behaviour of some high strength materials*. J. Mater. Sci., 21(6):1837, 1986.

[85] Sakasegawa, H., et al. *Microstructural evolution during creep of 9Cr-ODS steels*. Fusion Eng. Des., 81(8):1013, 2006.

[86] Han, W., et al. *Hardness and Micro-Texture in Friction Stir Welds of a Nanostructured Oxide Dispersion Strengthened Ferritic Steel*. Mater. Trans., 53(2):390, 2012.

[87] Alinger, M.J. *On the formation and stability of nanometer scale precipitates in ferritic alloys during processing and high temperature service*. Ph.D. thesis, Ph.D., University of California, Santa Barbara, 2004.

[88] Mathon, M., et al. *Small angle neutron scattering study of irradiated martensitic steels: relation between microstructural evolution and hardening*. ASTM Spec. Tech. Publ., 1475:120, 2006.

[89] Alinger, M.J., et al. *The development and stability of Y–Ti–O nanoclusters in mechanically alloyed Fe–Cr based ferritic alloys*. J. Nucl. Mater., 329-333:382, 2004.

[90] Krsak, V., et al. *Application of positron annihilation spectroscopy on the ion implantation damaged Fe–Cr alloys*. Appl. Surf. Sci., 255(1):153, 2008.

[91] Ortega, Y., et al. *Positron annihilation characteristics of ODS and non-ODS EUROFER isochronally annealed*. J. Nucl. Mater., 376(2):222, 2008.

[92] Gault, B., et al. *Spatial resolution in atom probe tomography*. Microsc. Microanal., 16(01):99, 2010.

[93] Cho, H.S., et al. *Effects of neutron irradiation on the tensile properties of high-Cr oxide dispersion strengthened ferritic steels*. J. Nucl. Mater., 367:239, 2007.

[94] Kinoshita, H., et al. *Microstructural change on electron irradiated oxide dispersion strengthened ferritic steels*. J. Nucl. Mater., 191:874, 1992.

[95] Saito, J., et al. *Void formation and microstructural development in oxide dispersion strengthened ferritic steels during electron-irradiation*. J. Nucl. Mater., 258-263:1264, 1998.

[96] Lescoat, M.L., et al. *In situ TEM study of the stability of nano-oxides in ODS steels under ion-irradiation*. J. Nucl. Mater., 428(1-3):176, 2012.

[97] Okuda, T., et al. *Dispersion behaviour of oxide particles in mechanically alloyed ODS steel*. J. Mater. Sci. Lett., 14(22):1600, 1995.

[98] Kim, I.S., et al. *Defect and void evolution in oxide dispersion strengthened ferritic steels under 3.2 MeV Fe+ ion irradiation with simultaneous helium injection*. J. Nucl. Mater., 280(2000):264, 2000.

[99] Sakasegawa, H., et al. *Correlation between chemical composition and size of very small oxide particles in the MA957 ODS ferritic alloy*. J. Nucl. Mater., 384(2):115, 2009.

[100] Eiselt, C.C., et al. *Characterization of microstructural and mechanical properties of a reduced activation ferritic oxide dispersion strengthened steel*. J. Nucl. Mater., 416(1):30, 2011.

[101] Kim, S.W., et al. *Kinetic Approach for Growth and Coalescence of Nano-Size Oxide Particles in 9Cr-ODS Steel Using High-Energy Synchrotron Radiation X-rays in SPring-8*. Mater. Trans., 50(4):917, 2009.

[102] Cunningham, N.J., et al. *Characterization of the composition and structure of Y–Ti–O rich precipitates in nanostructured ferritic alloy MA957 by transmission electron microscopy and atom probe tomography*. *Tech. rep.*, Semi-annual Progress Report 2009, 2009.

[103] Ohnuma, M., et al. *A new method for the quantitative analysis of the scale and composition of nanosized oxide in 9Cr-ODS steel*. Acta Mater., 57(18):5571, 2009.

[104] Klimiankou, M., et al. *TEM characterization of structure and composition of nanosized ODS particles in reduced activation ferritic–martensitic steels*. J. Nucl. Mater., 329:347, 2004.

[105] Yamashita, S., et al. *Nano-oxide particle stability of 9–12Cr grain morphology modified ODS steels under neutron irradiation*. J. Nucl. Mater., 329:377, 2004.

[106] Wu, Y., et al. *Transmission electron microscopy characterization of the nanofeatures in nanostructured ferritic alloy MA957*. Acta Mater., 60:3456, 2012.

[107] Zhang, P., et al. *Energetics of Cubic and Monoclinic Yttrium Oxide Polymorphs: Phase Transitions, Surface Enthalpies, and Stability at the Nanoscale*. J. Phys. Chem. C, 112(4):932, 2008.

[108] Brandes, M.C., et al. *Morphology, structure, and chemistry of nanoclusters in a mechanically alloyed nanostructured ferritic steel*. J. Mater. Sci., 1–11, 2012.

[109] Castro, V.D., et al. *Stability of nanoscale secondary phases in an oxide dispersion strengthened Fe-12Cr alloy*. Acta Mater., 59(10):3927, 2011.

[110] Bhattacharyya, D., et al. *On the structure and chemistry of complex oxide nanofeatures in nanostructured ferritic alloy U14YWT*. Phil. Mag., 92(16):2089, 2012.

[111] Odette, G.R., et al. *Irradiation-tolerant nanostructured ferritic alloys: Transforming helium from a liability to an asset*. J. Miner. Met. Mater. Soc., 62(9):84, 2010.

[112] Yamashita, S., et al. *Formation of nanoscale complex oxide particles in mechanically alloyed ferritic steel*. Philos. Mag. Lett., 84(8):525, 2004.

[113] Klimiankou, M., et al. *Energy-filtered TEM imaging and EELS study of ODS particles and argon-filled cavities in ferritic-martensitic steels*. Micron, 36(1):1, 2005.

[114] Ribis, J., et al. *Interfacial strained structure and orientation relationships of the nanosized oxide particles deduced from elasticity-driven morphology in oxide dispersion strengthened materials*. Acta Mater., 60(1):238, 2012.

[115] Haider, M., et al. *Electron microscopy image enhanced.* Nature, 392:768, 1998.

[116] Krivanek, O.L., et al. *Towards sub-0.5 Å electron beams*. Ultramicroscopy, 96(3):229, 2003.

[117] Marquis, E.A. *Core/shell structures of oxygen-rich nanofeatures in oxide-dispersion strengthened Fe-Cr alloys*. Appl. Phys. Lett., 93(18):181904, 2008.

[118] Sakasegawa, H., et al. *Stability of non-stoichiometric clusters in the MA957 ODS ferrtic alloy*. J. Nucl. Mater., 417:229, 2011.

[119] Ciston, J., et al. *The Structure of Nanoscale Precipitates and Precipitate Interfaces in an Oxide Dispersion Strengthened Steel*. Microsc. Microanal., 18(S2):760, 2012.

[120] Wells, P., et al. *Recent progress on understanding and quantifying atom probe tomography artifacts for high evaporation rate nm-scale phases in Fe based alloys*. *Tech. rep.*, University of California Santa Barbara, 2012.

[121] Williams, C.A., et al. *Quantifying the composition of yttrium and oxygen rich nanoparticles in oxide dispersion strengthened steels*. Ultramicroscopy, 125:10, 2013.

[122] Müller, M., et al. *Some aspects of the field evaporation behaviour of GaSb*. Ultramicroscopy, 111(6):487, 2011.

[123] Nomura, S., et al. *Effect of Alloying Elements on High-Temperature Strength of Oxide. Dispersion Strengthened 12 Cr Ferritic/Martensitic Steels*. Solid State Powder Process., 203–211, 1989.

[124] Ukai, S., et al. *Characterization of High Temperature Creep Properties in Recrystallized 12Cr-ODS Ferritic Steel Claddings*. J. Nucl. Sci. Technol., 39(8):872, 2002.

[125] Yamashita, S., et al. *Phase stability of oxide dispersion-strengthened ferritic steels in neutron irradiation*. J. Nucl. Mater., 307-311:283, 2002.

[126] Zhong, S.Y., et al. *Study of the thermal stability of nanoparticle distributions in an oxide dispersion strengthened (ODS) ferritic alloys*. J. Nucl. Mater., 2012.

[127] Sun, Q.X., et al. *Microstructure and mechanical properties of oxide dispersion strengthened ferritic steel prepared by a novel route*. J. Nucl. Mater., 424(1):279, 2012.

[128] Williams, C.A., et al. *The effect of Ti on the coarsening behavior of oxygen-rich nanoparticles in oxide-dispersion-strengthened steels after annealing at 1200Â°C*. Scr. Mater., 67:108, 2012.

[129] Lee, J.H. *Development of oxide dispersion strengthened ferritic steels with and without aluminum*. Front. Energy, 6(1):29, 2012.

[130] Dawson, K., et al. *Characterisation of nanosized oxides in ODM401 oxide dispersion strengthened steel*. J. Nucl. Mater., 444:252, 2014.

[131] Lu, C., et al. *Microstructure of a 14Cr-ODS ferritic steel before and after helium ion implantation*. J. Nucl. Mater., 455(1):366, 2014.

[132] Miller, M.K., et al. *Atom probe tomography of nanoscale particles in ODS ferritic alloys*. Mater. Sci. Eng. A, 353(2003):140, 2003.

[133] Ohtsuka, S., et al. *Improvement of 9Cr-ODS martensitic steel properties by controlling excess oxygen and titanium contents*. J. Nucl. Mater., 329:372, 2004.

[134] Miller, M.K., et al. *Stability of ferritic MA ODS alloys at high temperatures*. Intermetallics, 13(3):387, 2005.

[135] Certain, A.G., et al. *Response of nanoclusters in a 9Cr ODS steel to 1dpa, 525C proton irradiation*. J. Nucl. Mater., 407(1):2, 2010.

[136] Saroja, S., et al. *Development and characterization of advanced 9Cr ferritic/martensitic steels for fission and fusion reactors*. J. Nucl. Mater., 409(2):131, 2011.

[137] Hirata, A., et al. *Atomic structure of nanoclusters in oxide-dispersion-strengthened steels*. Nat. Mater., 10(12):922, 2011.

[138] Brocq, M., et al. *Nanoscale characterization and formation mechanism of nanoclusters in an ODS steel elaborated by reactive-inspired ball-milling and annealing*. J. Nucl. Mater., 409(2):80, 2011.

[139] Hirata, A., et al. *Characterization of oxide nanoprecipitates in an oxide dispersion strengthened 14YWT steel using aberration-corrected STEM*. Acta Mater., 60(16):5686, 2012.

[140] Williams, C.A., et al. *The formation and evolution of oxide particles in oxide-dispersion-strengthened ferritic steels during processing*. Acta Mater., 61(6):2219, 2013.

[141] He, J., et al. *Stability of nanoclusters in 14YWT oxide dispersion strengthened steel under heavy ion-irradiation by atom probe tomography*. J. Nucl. Mater., 455(1–3):41, 2014.

[142] Kim, J.H., et al. *Effects of processing condition on the microstructural and tensile properties of 14Cr-based oxide dispersion strengthened alloys*. J. Nucl. Mater., 449(1):300, 2014.

[143] Boutard, J.L., et al. *Oxide dispersion strengthened ferritic steels: a basic research joint program in France*. J. Nucl. Mater., 455(1):605, 2014.

[144] Badjeck, V., et al. *New insights into the chemical structure of Y2Ti2O7-d nanoparticles in oxide dispersion-strengthened steels designed for sodium fast reactors by electron energy-loss spectroscopy*. J. Nucl. Mater., 456:292, 2015.

[145] Bentley, J., et al. *Characterization of Irradiated Nanostructured Ferritic Steels*. Microsc. Microanal., 13(S02):1072, 2007.

[146] Williams, D.B., et al. *The Transmission Electron Microscope*. Transm. Electron Microsc., 3–22, 2009.

[147] Reyes-Gasga, J., et al. *On the interpretation of the forbidden spots observed in the electron diffraction patterns of flat Au triangular nanoparticles*. Ultramicroscopy, 108(9):929, 2008.

[148] W. Lefebvre F. Cuvilly, C.V. *Atomic reconstruction and single atom detection in an APT specimen by Cs-probe corrected stem*. In *Int. F. Evaporation Symp. 2012, Alabama*, 169. 2012.

[149] Bouchet, D., et al. *Yttrium segregation and intergranular defects in alumina*. Philos. Mag., 86(10):1401, 2006.

[150] Tafto, J., et al. *Crystal site location of dopants in semiconductors using a 100-keV electron probe*. J. Appl. Phys., 54:5014, 1983.

[151] Klimenkov, M., et al. *New insights into the structure of ODS particles in the ODS-Eurofer alloy*. J. Nucl. Mater., 386-388:553, 2009.

[152] Verbeeck, J., et al. *Model based quantification of EELS spectra*. Ultramicroscopy, 101(2–4):207, 2004.

[153] Lozano-Perez, S., et al. *Achieving sub-nanometre particle mapping with energy-filtered TEM*. Ultramicroscopy, 109(10):1217, 2009.

[154] Trebbia, P., et al. *EELS elemental mapping with unconventional methods I. Theoretical basis: Image analysis with multivariate statistics and entropy concepts*. Ultramicroscopy, 34(3):165, 1990.

[155] Williams, C.A., et al. *Nanoscale characterisation of ODS-Eurofer 97 steel: An atom-probe tomography study*. J. Nucl. Mater., 400(1):37, 2010.

[156] Murali, D., et al. *The role of minor alloying elements on the stability and dispersion of yttria nanoclusters in nanostructured ferritic alloys: An ab initio study*. J. Nucl. Mater., 403(1-3):113, 2010.

[157] Alinger, M.J., et al. *Lattice Monte Carlo simulations of nanocluster formation in nanostructured ferritic alloys*. J. Nucl. Mater., 367-370 A(SPEC. ISS.):153, 2007.

[158] Derby, B., et al. *Neutron reflection studies of titanium segregation to metal–ceramic interfaces*. Phys. B Condens. Matter, 248(1):304, 1998.

[159] Capdevila, C., et al. *Role of Y-Al Oxides During Extended Recovery Process of a Ferritic ODS Alloy*. JOM, 67(10):2208, 2015.

[160] Marquis, E.A., et al. *Chromatic aberrations in the field evaporation behavior of small precipitates*. Microsc. Microanal., 14(6):561, 2008.

[161] Pareige, P., et al. *Ion irradiation induced solute clustering in steel: A 3D nanoanalysis with the tomographic atom-probe*. Nucl. Instruments Methods Phys. Res. Sect. B Beam Interact. with Mater. Atoms, 178(1):233, 2001.

[162] Etienne, A., et al. *Atomic scale investigation of radiation-induced segregation in austenitic stainless steels*. J. Nucl. Mater., 406(2):244, 2010.

[163] Williams, C.A., et al. *Effects of heavy-ion irradiation on solute segregation to dislocations in oxide-dispersion-strengthened Eurofer 97 steel*. J. Nucl. Mater., 412:100, 2011.

[164] Marquis, E.A., et al. *Applications of atom-probe tomography to the characterisation of solute behaviours*. Mater. Sci. Eng. R Reports, 69(4):37, 2010.

[165] Castro, V.D., et al. *Microstructural characterization of Y2O3 ODS-Fe-Cr model alloys*. J. Nucl. Mater., 386-388(C):449, 2009.

[166] Etienne, A., et al. *Effects of friction stir welding and post-weld annealing on nanostructured ferritic alloy*. Mater. Sci. Technol., 27(4):724, 2011.

[167] Schilcher, U., et al. *Measuring Inhomogeneity in Spatial Distributions*. VTC Spring 2008 - IEEE Veh. Technol. Conf., 2690–2694, 2008.

[168] Garncarek, Z., et al. *Effective conductivity in association with model structure and spatial inhomogeneity of polymer/carbon black composites*. J. Phys. D. Appl. Phys., 29(5):1360, 1996.

[169] Czainski, A., et al. *Quantitative characterization of inhomogeneity in thin metallic films using Garncarek's method*. J. Phys. D. Appl. Phys., 27:616, 1999.

[170] Torquato, S. *Unified methodology to quantify the morphology and properties of inhomogeneous media*. Phys. A Stat. Mech. its Appl., 207(1–3):79, 1994.

[171] Queyreau, S., et al. *Orowan strengthening and forest hardening superposition examined by dislocation dynamics simulations*. Acta Mater., 58(17):5586, 2010.

[172] Pyrz, R., et al. *Topological disorder of microstructure and its relation to the stress field*. Int. J. Solids Struct., 35(19):2413, 1998.

[173] Segurado, J., et al. *Computational micromechanics of composites: The effect of particle spatial distribution*. Mech. Mater., 38(8–10):873, 2006.

[174] Kinchin, G.H., et al. *The Displacement of Atoms in Solids by Radiation*. Reports Prog. Phys., 18:1, 1955.

[175] Bohr, N. *The penetration of atomic particles through matter*. Munksgaard, 1948.

[176] Brinkman, J.a. *On the nature of radiation damage in metals*. J. Appl. Phys., 25(8):961, 1954.

[177] Silcox, J., et al. *Dislocation loops in neutron-irradiated copper*. Philos. Mag., 4(48):1356, 1959.

[178] Jenkins, M.L., et al. *Characterization of radiation damage by transmission electron microscopy*. Taylor & Francis, 2001.

[179] Averback, R.S., et al. *Ion-irradiation studies of the damage function of copper and silver*. Phys. Rev. B, 18(8):4156, 1978.

[180] De La Rubia, T.D., et al. *Role of thermal spikes in energetic displacement cascades*. Phys. Rev. Lett., 59(17):1930, 1987.

[181] Norgett, M.J., et al. *A proposed method of calculating displacement dose rates*. Nucl. Eng. Des., 33(1):50, 1975.

[182] Ougouag, A.M., et al. *Defect Production Efficiency in Neutron-Irradiated Iron*. In *Eff. Radiat. Mater. 15th Int. Symp.*, 1125, 420. ASTM International, 1992.

[183] Robinson, M.T. *Basic physics of radiation damage production*. J. Nucl. Mater., 216:1, 1994.

[184] Stoller, R., et al. *On the use of SRIM for computing radiation damage exposure*. Nucl. Instruments Methods Phys. Res. Sect. B Beam Interact. with Mater. Atoms, 310:75, 2013.

[185] Domain, C., et al. *Simulation of radiation damage in Fe alloys: an object kinetic Monte Carlo approach*. J. Nucl. Mater., 335(1):121, 2004.

[186] Ziegler, J.F., et al. *Stopping and range of ions in matter*. SRIM Co., 2008.

[187] Samaras, M., et al. *Modelling of advanced structural materials for GEN IV reactors*. J. Nucl. Mater., 371(1-3):28, 2007.

[188] Webb, R. *SUSPRE—Ion Ranges in Solids Computer Program*, 1987.

[189] Wang, G., et al. *Computationally efficient ion implantation damage model: modified Kinchin-Pease model*. In *Soc. Photo-Optical Instrum. Eng. Conf. Ser.*, vol. 3212, 324–333. 1997.

[190] Parish, C.M., et al. *Direct observation of ion-irradiation-induced chemical mixing*. J. Nucl. Mater., 418(1):106, 2011.

[191] Martin, G. *Phase stability under irradiation: Ballistic effects*. Phys. Rev. B, 30(3):1424, 1984.

[192] Siegel, S. *Effect of neutron bombardment on order in the alloy Cu3Au*. Phys. Rev., 75:1823, 1949.

[193] Jenkins, M.L., et al. *Transmission electron microscopy studies of displacement cascades in Cu3Au*. Philos. Mag., 34(6):1155, 1976.

[194] Wang, Z.L., et al. *Laser and ion-beam mixing of Cu-Au-Cu and Cu-W-Cu thin films*. Nucl. Instruments Methods Phys. Res., 209–210(1):115, 1983.

[195] Cheng, Y.T. *Thermodynamic and fractal geometric aspects of ion-solid interactions*. Mater. Sci. reports, 5(2):45, 1990.

[196] D'Heurle, F., et al. *Correlation between chemistry and the amount of mixing in bilayers submitted to ion bombardment*. J. Appl. Phys., 57(4):1426, 1985.

[197] Zhang, L., et al. *Radiation-induced mixing between metals of low solid solubility*. Acta Mater., 76:135, 2014.

[198] Russell, K.C. *Phase stability under irradiation*. Prog. Mater. Sci., 28(3-4):229, 1984.

[199] Alamo, A., et al. *Assessment of ODS-14% Cr ferritic alloy for high temperature applications*. J. Nucl. Mater., 329:333, 2004.

[200] McClintock, D.A., et al. *Mechanical properties of irradiated ODS-EUROFER and nanocluster strengthened 14YWT*. J. Nucl. Mater., 392(2):353, 2009.

[201] Oh, S., et al. *Irradiation hardening and embrittlement in high-Cr oxide dispersion strengthened steels*. J. Nucl. Mater., 386:503, 2009.

[202] Asano, K., et al. *Microstructural evolution of an oxide dispersion strengthened steel under charged particle irradiation*. J. Nucl. Mater., 155:928, 1988.

[203] Shiraishi, H., et al. *Helium effects in iron-and nickel-base developmental alloys*. J. Nucl. Mater., 155:1049, 1988.

[204] Kusanagi, H., et al. *Influence of tensile stress on cavity growth in nickel under helium irradiation*. Fusion Eng. Des., 9:123, 1989.

[205] Chen, C.L., et al. *Dual-beam irradiation of friction stir spot welding of nanostructured ferritic oxide dispersion strengthened alloy*. J. Alloys Compd., 2011.

[206] Little, E. *Influence of thermomechanical treatment on irradiation microstructures in an ODS ferritic steel*. ASTM Spec. Tech. Publ., (1270):739, 1996.

[207] Akasaka, N., et al. *Microstructural changes of neutron irradiated ODS ferritic and martensitic steels*. J. Nucl. Mater., 329:1053, 2004.

[208] Dubuisson, P., et al. *Behavior of an Oxide Dispersion Strengthened Ferritic Steel Irradiated in Phenix*. Eff. Radiat. Mater. 18th Int. Symp., ASTM STP 1:882, 1999.

[209] Yamashita, S., et al. *Microstructural development of a heavily neutron-irradiated ODS ferritic steel (MA957) at elevated temperature*. J. Nucl. Mater., 367:202, 2007.

[210] Yamashita, S., et al. *Irradiation behavior evaluation of oxide dispersion strengthened ferritic steel cladding tubes irradiated in JOYO*. J. Nucl. Mater., 442(1–3):417, 2013.

[211] Allen, T.R., et al. *The stability of 9Cr-ODS oxide particles under heavy-ion irradiation*. Nucl. Sci. Eng., 151(3):305, 2005.

[212] Kishimoto, H., et al. *Heavy-ion irradiation effects on the morphology of complex oxide particles in oxide dispersion strengthened ferritic steels*. J. Nucl. Mater., 367:179, 2007.

[213] Miller, M.K., et al. *Atom Probe Tomography as a Tool for Characterizing Irradiated Materials*. Microsc. Microanal., 16(S2):1602, 2010.

[214] Miller, M.K., et al. *Effect of neutron irradiation on nanoclusters in MA957 ferritic alloys*. J. Nucl. Mater., 418(1):307, 2011.

[215] Rogozhkin, S.V., et al. *Atom probe characterization of nano-scaled features in irradiated ODS Eurofer steel*. J. Nucl. Mater., 409(2):94, 2011.

[216] Rogozhkin, S.V., et al. *Atom probe tomography of nanoscaled features of oxide-dispersion-strengthened ODS Eurofer steel in the initial state and after neutron irradiation*. Phys. Met. Metallogr., 113(1):98, 2012.

[217] Pareige, P., et al. *Stability of nanometer-sized oxide clusters in mechanically-alloyed steel under ion-induced displacement cascade damage conditions*. J. Nucl. Mater., 360(2):136, 2007.

[218] Schaublin, R., et al. *Microstructural development under irradiation in European ODS ferritic/martensitic steels*. J. Nucl. Mater., 351(1-3):247, 2006.

[219] Brodrick, J., et al. *Mechanism for radiation damage resistance in yttrium oxide dispersion strengthened steels*. J. Nucl. Mater., 445(1–3):291, 2014.

[220] Lazauskas, T., et al. *Simulating radiation damage in a bcc Fe system with embedded yttria nanoparticles*. J. Nucl. Mater., 437(1–3):317, 2013.

[221] Parish, C.M., et al. *Response of nanostructured ferritic alloys to high-dose heavy ion irradiation*. J. Nucl. Mater., 445(1–3):251, 2014.

[222] Kimura, A. *Current Status of Reduced-Activation Ferritic/Martensitic Steels R&D for Fusion Energy*. Mater. Trans., 46(3):394, 2005.

[223] Schulson, E. *The ordering and disordering of solid solutions under irradiation*. J. Nucl. Mater., 83(2):239, 1979.

[224] Swenson, M., et al. *Correlation Between the Microstructure and Mechanical Properties of Irradiated Fe-9Cr ODS*. In *2014 Annu. Meet. - Trans. Am. Nucl. Soc. Embed. Top. Meet. Nucl. Fuels Struct. Mater. Next Gener. Nucl. React.*, 421—-424. American Nuclear Society, Illinois., 2014.

[225] Bellon, P., et al. *Preface to viewpoint set on: materials under driving forces*. Scr. Mater., 49(10):921, 2003.

[226] Heinig, K.H., et al. *Interfaces under ion irradiation: Growth and taming of nanostructures*. Appl. Phys. A Mater. Sci. Process., 77(1):17, 2003.

[227] Ribis, J., et al. *Comparison of the neutron and ion irradiation response of nano-oxides in oxide dispersion strengthened materials*. J. Mater. Res., 30(14):2210, 2015.

[228] Xie, Y. *Dynamic Documents with R and knitr*. Chapman and Hall/CRC, Boca Raton, Florida, 2nd ed., 2015.

[229] Nagini, M., et al. *Influence of the duration of high energy ball milling on the microstructure and mechanical properties of a 9Cr oxide dispersion strengthened ferritic–martensitic steel*. Mater. Sci. Eng. A, 620:490, 2015.

[230] Vijay, R., et al. *Structure and Properties of Nano-Scale Oxide-Dispersed Iron*. Metall. Mater. Trans. A, 45(2):777, 2013.

[231] Sundararajan, G., et al. *Development of 9Cr ferritic-martensitic and 18Cr ferritic oxide dispersion strengthened steels*. Curr. Sci., 105(8):1100, 2013.

[232] Miller, M.K., et al. *Atom probe field ion microscopy*. Oxford Science Publications, Oxford, 1996.

[233] Miller, M.K., et al. *Fabrication and characterization of APT specimens from high dose heavy ion irradiated materials*. Ultramicroscopy, 111:672, 2011.

[234] Thompson, S.P., et al. *Beamline I11 at Diamond: a new instrument for high resolution powder diffraction.* Rev. Sci. Instrum., 80(7):075107, 2009.

[235] London, A.J., et al. *Glancing angle XRD analysis of particle stability under self-ion irradiation in oxide dispersion strengthened alloys*. Scr. Mater., 2015.

[236] Henke, B., et al. *X-Ray Interactions: Photoabsorption, Scattering, Transmission, and Reflection at E = 50-30,000 eV, Z = 1-92*. At. Data Nucl. Data Tables, 54:181, 1993.

[237] Pharr, G.M., et al. *Measurement of thin film mechanical properties using nanoindentation*. Mrs Bull., 17(07):28, 1992.

[238] Armstrong, D.E.J., et al. *Hardening of self ion implanted tungsten and tungsten 5-wt% rhenium*. J. Nucl. Mater., 432(1–3):428, 2013.

[239] Oliver, W., et al. *An improved technique for determining hardness and elastic modulus using load and displacement-sensing indentation systems*. J. Mater. Res., 7(6):1564, 1992.

[240] Aitkaliyeva, A., et al. *Comparison of preparation techniques for nuclear materials for transmission electron microscopy (TEM)*. J. Nucl. Mater., 459:241, 2015.

[241] Schaffer, B., et al. *Automated spatial drift correction for EFTEM image series*. Ultramicroscopy, 102(1):27, 2004.

[242] Hyvarinen, A., et al. *Independent component analysis: algorithms and applications*. Neural Networks, 13(4–5):411, 2000.

[243] de la Pena, F., et al. *Mapping titanium and tin oxide phases using EELS: An application of independent component analysis*. Ultramicroscopy, 111(2):169, 2011.

[244] Jolliffe, I. *Principal component analysis*. Wiley Online Library, 2002.

[245] Miller, M.K. *Atom probe tomography*. Plenum Pub Corp, 2000.

[246] Gault, B., et al. *Atom Probe Microscopy*, vol. 160. Springer, 2012.

[247] Larson, D.J., et al. *Local Electrode Atom Probe Tomography: A User's Guide*. Springer-Verlag New York, 2013.

[248] Tsong, T.T. *Field penetration and band bending for semiconductor of simple geometries in high electric fields*. Surf. Sci., 85(1):1, 1979.

[249] Haydock, R., et al. *Post-Ionization of Field-Evaporated Ions*. Phys. Rev. Lett., 44(23):1520, 1980.

[250] Gault, B., et al. *Impact of directional walk on atom probe microanalysis*. Ultramicroscopy, 113(0):182, 2012.

[251] Keller, H., et al. *A position sensitive microchannelplate detector using a delay line readout anode*. Nucl. Instruments Methods Phys. Res. Sect. A Accel. Spectrometers, Detect. Assoc. Equip., 258(2):221, 1987.

[252] Da Costa, G., et al. *Design of a delay-line position-sensitive detector with improved performance*. Rev. Sci. Instrum., 76(1):, 2005.

[253] R Core Team. *R: A Language and Environment for Statistical Computing*. R Foundation for Statistical Computing, Vienna, Austria, 2015.

[254] Wickham, H. *ggplot2: elegant graphics for data analysis*. Springer Science & Business Media, 2009.

[255] Geiser, B., et al. *Wide-Field-of-View Atom Probe Reconstruction*, 2009.

[256] Boll, T., et al. *Investigation of the site occupation of atoms in pure and doped TiAl/Ti3 Al intermetallic*. Ultramicroscopy, 107(9):796, 2007.

[257] Vurpillot, F., et al. *Trajectories of field emitted ions in 3D atom-probe*, 1999.

[258] Oberdorfer, C., et al. *A full-scale simulation approach for atom probe tomography*. Ultramicroscopy, 128:55, 2013.

[259] Oberdorfer, C., et al. *On the field evaporation behavior of dielectric materials in three-dimensional atom probe: a numeric simulation.* Microsc. Microanal., 17(1):15, 2011.

[260] Haley, D., et al. *Guided mass spectrum labelling in atom probe tomography*. Ultramicroscopy, 159, Part 2(""):338, 2015.

[261] Hellman, O.C., et al. *Efficient sampling for three-dimensional atom probe microscopy data*. Ultramicroscopy, 95(0):199, 2003.

[262] Hellman, O.C., et al. *Analysis of three-dimensional atom-probe data by the proximity histogram.* Microsc. Microanal., 6(05):437, 2000.

[263] Hyde, J.M., et al. *Microstructural processes in irradiated materials*. In *MRS 2000 Fall Meet. Symp. Boston, MA*, 27–29. 2001.

[264] Lefebvre, W., et al. *3DAP measurements of Al content in different types of precipitates in aluminium alloys*. Surf. Interface Anal., 39(2-3):206, 2007.

[265] Stephenson, L.T., et al. *Nearest neighbour diagnostic statistics on the accuracy of APT solute cluster characterisation.* Philos. Mag., 93(8):975, 2013.

[266] Stephenson, L.T., et al. *Theory of solute clustering in materials for atom probe*, 2011.

[267] Hyde, J.M., et al. *A sensitivity analysis of the maximum separation method for the characterisation of solute clusters*. Ultramicroscopy, 111:440, 2011.

[268] Williams, C.A., et al. *Defining clusters in APT reconstructions of ODS steels*. Ultramicroscopy, 132:271, 2013.

[269] Stephenson, L.T., et al. *New techniques for the analysis of fine-scaled clustering phenomena within atom probe tomography (APT) data*. Microsc. Microanal., 13(6):448, 2007.

[270] Styman, P.D., et al. *Quantitative methods for the APT analysis of thermally aged RPV steels*. Ultramicroscopy, 132:258, 2013.

[271] Kolli, R.P., et al. *Comparison of compositional and morphological atom-probe tomography analyses for a multicomponent Fe-Cu steel.* Microsc. Microanal., 13:272, 2007.

[272] Hudson, D., et al. *Optimisation of mass ranging for atom probe microanalysis and application to the corrosion processes in Zr alloys*. Ultramicro., 111(6):480, 2011.

[273] Naish, P.J., et al. *Exponentially modified Gaussian functions–a good model for chromatographic peaks in isocratic HPLC?* Chromatographia, 26(1):285, 1988.

[274] Vella, A., et al. *Field evaporation mechanism of bulk oxides under ultra fast laser illumination*. J. Appl. Phys., 110(4), 2011.

[275] Bachhav, M., et al. *Investigation of wustite (Fe1-xO) by femtosecond laser assisted atom probe tomography*. Ultramicro., 111(6):584, 2011.

[276] Lardé, R., et al. *Investigation at the atomic scale of the Co spatial distribution in Zn(Co)O magnetic semiconductor oxide*. In *J. Appl. Phys.*, vol. 105. 2009.

[277] Ngamo, M., et al. *Characterization of Arsenic segregation at Si/SiO2 interface by 3D atom probe tomography*. Thin Solid Films, 518(9):2402, 2010.

[278] Larson, D.J., et al. *Analysis of Bulk Dielectrics with Atom Probe Tomography*. Microsc. Microanal., 14(SupplementS2):1254, 2008.

[279] Hudson, D., et al. *Zirconium oxidation on the atomic scale*. Ultramicroscopy, 109(5):667, 2009.

[280] Lozano-Perez, S., et al. *Atom-probe tomography characterization of the oxidation of stainless steel*. Scr. Mater., 62(11):855, 2010.

[281] Bachhav, M., et al. *Investigation of O-18 enriched hematite (alpha-Fe2O3) by laser assisted atom probe tomography*. Int. J. Mass Spectrom., 335:57, 2013.

[282] Marquis, E.A., et al. *Probing the improbable: Imaging C atoms in alumina*. Mater. Today, 13(10):34, 2010.

[283] Devaraj, A., et al. *Role of photoexcitation and field ionization in the measurement of accurate oxide stoichiometry by laser-assisted atom probe tomography*. J. Phys. Chem. Lett., 4:993, 2013.

[284] Saxey, D.W. *Correlated ion analysis and the interpretation of atom probe mass spectra*. Ultramicroscopy, 111(6):473, 2011.

[285] De Geuser, F., et al. *Correlated field evaporation as seen by atom probe tomography*. Surf. Sci., 601(2):536, 2007.

[286] Kalokhtina, O. *Study Of The Formation Of Nano-particles In ODS And NDS Steels By Atom Probe Tomography*. Ph.D. thesis, Universite de Rouen, 2012.

[287] Müller, E.W., et al. *The Atom-Probe Field Ion Microscope*. Rev. Sci. Instrum., 39(1):83, 1968.

[288] Arslan, I., et al. *Towards better 3-D reconstructions by combining electron tomography and atom-probe tomography*. Ultramicroscopy, 108:1579, 2008.

[289] Williams, D.B., et al. *Transmission electron microscopy: a textbook for materials science*. New York: Plenum Press, 1996.

[290] Larson, D.J., et al. *On the use of simulated field-evaporated specimen apex shapes in atom probe tomography data reconstruction*. Microsc. Microanal., 18(5):953, 2012.

[291] Garncarek, Z. *Constructions of the Measures of Distribution Features for Finite Point Sets with Examples of Applications in Natural and Technical Sciences (Opole*. ZN WSP Opole, Stud. I Monogr. NR, 203:1, 1993.

[292] Barber, C.B., et al. *The quickhull algorithm for convex hulls*, 1996.

[293] Suzuki, S., et al. *Site competition between sulfur and carbon at grain boundaries and their effects on the grain boundary cohesion in iron*. Metall. Trans. A, 18(13):1109, 1987.

[294] Bechade, J.L., et al. *Application of synchrotron radiation to analyze the precipitation in {ODS} materials before irradiation in Fe–9%Cr single grain of powder and consolidated Fe–18%Cr*. J. Nucl. Mater., 428(1–3):183, 2012.

[295] Hilger, I., et al. *The structural changes of Y2O3 in ferritic ODS alloys during milling*. J. Nucl. Mater., 447(1-3):242, 2014.

[296] Hsiung, L.L., et al. *Formation mechanism and the role of nanoparticles in Fe-Cr ODS steels developed for radiation tolerance*. Phys. Rev. B - Condens. Matter Mater. Phys., 82(18):184103, 2010.

[297] Martin, J.W. *Micromechanisms in particle-hardened alloys*. Cambridge, Cambridge University Press., 1980.

[298] Hardie, C.D., et al. *Nanoindentation of model Fe-Cr alloys with self-ion irradiation*. J. Nucl. Mater., 433(1-3):174, 2013.

[299] Ratti, M., et al. *Influence of titanium on nano-cluster (Y, Ti, O) stability in ODS ferritic materials*. J. Nucl. Mater., 386-388:540, 2009.

[300] Posselt, M., et al. *Energetics, structure and composition of nanoclusters in oxide dispersion strengthened Fe–Cr alloys*. Model. Simul. Mater. Sci. Eng., 22(8):85003, 2014.

[301] London, A.J., et al. *Effect of Ti and Cr on dispersion, structure and composition of oxide nano-particles in model ODS alloys*. Acta Mater., 97:223, 2015.

[302] Yoshitake, T., et al. *Ring-tensile properties of irradiated oxide dispersion strengthened ferritic/martensitic steel claddings*. J. Nucl. Mater., 329–333,(0):342, 2004.

[303] Yamamoto, M., et al. *Formation of residual ferrite in 9Cr-ODS ferritic steels*. Mater. Sci. Eng. A, 527(16–17):4418, 2010.

[304] Kim, S., et al. *Formation of nano-size oxide particles and delta-ferrite at elevated temperature in 9Cr-ODS steel*. J. Nucl. Mater., 417(1–3):209, 2011.

[305] Yazawa, Y., et al. *Effect of matrix recrystallization on morphology, crystallography and coarsening behavior of vanadium carbide in austenite*. Acta Mater., 52(12):3727, 2004.

[306] Chang, W., et al. *Electron microscopy studies of phase transformations in nanostructured Yttriumoxide*. Nanostructured Mater., 2(1):29, 1993.

[307] Krajnikov, A., et al. *Chromium interaction with TiO2 dispersoids in oxide dispersion strengthened ferritic steel*. Mater. Sci. . . . , 15(December):1425, 1999.

[308] Unifantowicz, P., et al. *Statistical analysis of oxides particles in ODS ferritic steel using advanced electron microscopy*. J. Nucl. Mater., 422(1-3):131, 2012.

[309] Kishimoto, H., et al. *Helium cavity formation research on oxide dispersed strengthening (ODS) ferritic steels utilizing dual-ion irradiation facility*. Fusion Eng. Des., 81(8-14):1045, 2006.

[310] Zinkle, S.J., et al. *Operating temperature windows for fusion reactor structural materials*. Fusion Eng. Des., 51-52(2000):55, 2000.

[311] Takaki, S., et al. *The resistivity recovery of high purity and carbon doped iron following low temperature electron irradiation*. Radiat. Eff., 79(1-4):87, 1983.

[312] Miller, M.K., et al. *Stability of ferritic MA ODS alloys at high temperatures*. Intermetallics, 13(3-4):387, 2005.

[313] Williamson, G.K., et al. *X-ray line broadening from filed aluminium and wolfram*. Acta Metall., 1(1):22, 1953.

[314] Przybylski, K., et al. *Observation of coherent perovskite particles in growing chromia films*. J. Am. Ceram. Soc., 69(11):C, 1986.

[315] Levin, E.M., et al. *Phase diagrams for ceramists, 1975 supplement*. 1975.

[316] Seidel, G.P. *Neutron radiation hardening of polycrystalline iron*. Radiat. Eff., 1(3):177, 1969.

[317] Little, E. *Neutron-irradiation hardening in irons and ferritic steels*. Int. Met. Rev., 21(1):25, 1976.

[318] Robertson, I., et al. *Formation of dislocation loops in iron by self-ion irradiations at 40K*. Scr. Metall., 18(4):317, 1984.

[319] Lian, J., et al. *Radiation-induced amorphization of rare-earth titanate pyrochlores*. Phys. Rev. B, 68(13):134107, 2003.

[320] Matzke, H. *Ion-bombardment-induced structural changes in Fe2O3 , Cr2O3 and U3O8*. Radiat. Eff., 28(3-4):249, 1976.

[321] Frost, H., et al. *Particle stability with recoil resolution*. Acta Metall., 30(5):953, 1982.

[322] Crank, J. *The mathematics of diffusion*. Oxford university press, 1979.

[323] Wiedersich, H. *Kinetic processes during ion bombardment*. Nucl. Instruments Methods Phys. Res. Sect. B Beam Interact. with Mater. Atoms, 7:1, 1985.

[324] Bellon, P. *Precipitate and Microstructural Stability in Alloys Subjected to Sustained Irradiation*. In *Mater. Sci. with Ion Beams*, 29–52. Springer, 2010.

[325] Bailey, N.A., et al. *Atom probe tomography analysis of high dose MA957 at selected irradiation temperatures*. J. Nucl. Mater., 459:225, 2015.

[326] Klugkist, P., et al. *Tracer diffusion of titanium in α-iron*. Phys. status solidi, 148(2):413, 1995.

[327] Kirchhofer, R., et al. *Development of In-situ STEM and APT*. In *Atom Probe Tomogr. Microsc.* 2014.

[328] Ceguerra, A.V., et al. *A three-dimensional Markov field approach for the analysis of atomic clustering in atom probe data*. Philos. Mag., 90(12):1657, 2010.

Appendix A

Appendices

A.1 SRIM Calculation

Stopping Range In Matter (SRIM) calculations were performed using the "simple" Kichin-Pease mode with 40 eV displacement energy and 0 eV lattice binding energy as per the guidelines given in [184]; 10,000 ions were simulated in the SRIM 2013 version with the 2008 stopping power version. Details of the calculation and operation can be found in [186]. An image of the TRIM calculation window is shown in figure A.1.1. The damage in dpa was calculated from the VACANCY.txt output; by summing the vacancies due to ions and recoils, multiplying by the ion dose (ions cm^{-2}) and dividing by the number of atoms in a 1 cm^2 area by 1 Å thick layer, 8.48×10^{14} for Fe. This calculation is performed by the R function SRIM2dpa.R:

```
SRIM2dpa <- function(fileName, dose = 1.5E17, atoms = 8.48E14) {
# reads the VACANCY.txt file produced by SRIM
# atoms = number of atoms in a 1 angstrom thick layer of area A
# dose = number of ions per area A (eg per 1 cm^2)
# returns a data frame, names: depth, ions, recoils, total, dpa
# library(data.table)
# library("dplyr")
# read file using fread
vac <- fread(fileName, header=TRUE, nrows=100, skip="----------
    ----------")
# rename and select columns
setnames(vac,c("depth","b1","ions","b2","recoils")) %>% select(depth,ions
    ,recoils) %>% mutate(total=ions+recoils, dpa=total*dose/atoms)
}
```

A.2 Principal Component Analysis Example

Principal component analysis (PCA) was performed on EFTEM data using the singular value decomposition method described in [153, 242, 243] and implemented in HyperSpy [243]; for more information regarding PCA, see [244].

Supposing a line-spectrum D that can be described by a linear model:

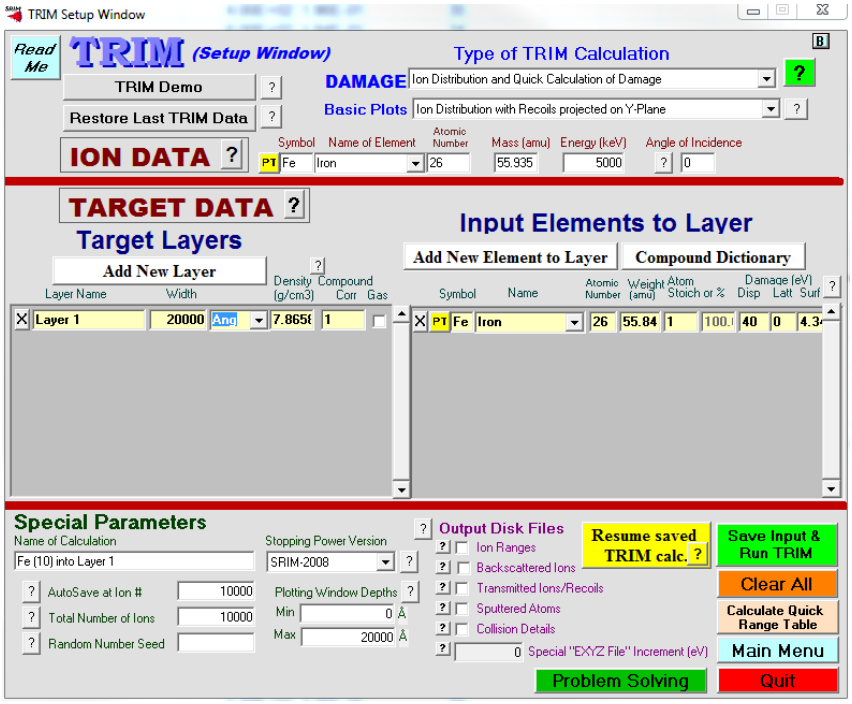

Figure A.1.1 – Screen shot of the TRIM calculation window.

$$D = [d_{i,j}]_{m\times n} = [p_{i,j}]_{m\times l} \times [s_{i,j}]_{l\times n} \tag{A.2.1}$$

where m is the number of pixels in the line scan, n the number of channels in the spectrum and l the number of components, e.g. spectra of individual compounds. Normally, what we actually measure is a noisy version of D, D':

$$D = [d_{i,j}]_{m\times n} = [p_{i,j}]_{m\times l} \times [s_{i,j}]_{l\times n} + Noise \tag{A.2.2}$$

D' could be factorized as follows:

$$D^{'} = [\bar{p}_{i,j}]_{m\times k} \times [\bar{s}_{i,j}]_{k\times n} \text{ where } k \leq \min(m,n). \tag{A.2.3}$$

Extra constraints are needed to fully determine the matrix factorization; therefore orthogonality is imposed. This decomposition is called Principal Component Analysis and is performed using singular value decomposition (SVD). The components k are sorted in order of decreasing "explained variance" (eigen values), which are multiplied by the corresponding eigen vectors to retrieve the original data. The assumption, stated in equation A.2.2, is that the combination of components and noise is linear and that there are k principal components (which are selected based on their explained variance):

$$D^{'} = [\bar{p}_{i,j}]_{m\times k} \times [\bar{s}_{i,j}]_{k\times n} + [\bar{p}_{i,j}]_{m\times k-l} \times [\bar{s}_{i,j}]_{k-l\times n} \tag{A.2.4}$$

Therefore the de-noised data is retrieved as:

$$D'' \approx [\bar{p}_{i,j}]_{m\times k} \times [\bar{s}_{i,j}]_{k\times n} \tag{A.2.5}$$

with the noise components equal to:

$$Noise \approx [\bar{p}_{i,j}]_{m\times k-l} \times [\bar{s}_{i,j}]_{k-l\times n} \tag{A.2.6}$$

For EFTEM data, either the eigen vectors $\bar{p}$ themselves or the reconstructed data D'' are used for further analysis.

A.3 File Formats

A.3.1 .POS file

Used to store the x, y, z and m/z ratios of reconstructed ion species from an APT experiment. Read in MATLAB using *readpos.m*:

```
[x,y,z,m,nb]=readpos(fileName)
```

A.3.2 .EPOS file

Used to store the pos file information with additional information from the experiment. This includes, the raw time-of-flight value, the voltage pulse amplitude, the standing voltage amplitude, the detector coordinates (X_D and Y_D), the number of pulses since the last detected ion and the hit multiplicity. Read in MATLAB using *readepos.m*:

```
[x,y,z,m,tof,vdc,vp,xd,yd,dP,nm,nb]=readepos(fileName)
```

A.3.3 .RRNG file

Specifies ranges of m/z values which correspond to specific ionic species. My function rangeReader.m can read the format specified below into the MATLAB work-space.

```
[element_num, range_num, elements, ranges] = rangeReader (rrrgFile)
```

```
[Ions]
Number=9
Ion1=Fe
Ion2=C
Ion3=N
...
Ion9=W
[Ranges]
Number=59
Range1=27.9475 27.9913 Vol:0.01177 Fe:1 Color:FF00FF
Range2=55.8950 55.9738 Vol:0.01177 Fe:1 Color:FF00FF
```

5.9633	6.0735	0.00878	660033	0	0	0	0	1	0
11.948	12.1039	0.00878	660033	0	0	0	0	1	0
15.9349	16.1149	0.02883	FF0000	0	0	0	1	0	0
23.9265	24.147	0.01757	660033	0	0	0	0	2	0
24.9132	25.1382	0.01201	FF33CC	0	1	0	0	0	0
25.9102	26.1396	0.01201	FF33CC	0	1	0	0	0	0
26.3932	26.6247	0.01201	FF33CC	0	1	0	0	0	0
26.9029	27.1367	0.01177	FF00FF	1	0	0	0	0	0
27.8881	28.1261	0.01177	FF00FF	1	0	0	0	0	0
28.3877	28.6278	0.01177	FF00FF	1	0	0	0	0	0
28.8859	29.1281	0.01177	FF00FF	1	0	0	0	0	0
29.5536	29.7986	0.03301	0000FF	0	0	1	0	0	0
31.8974	32.1519	0.05766	FF0000	0	0	0	2	0	0
32.8846	33.143	0.03449	0000FF	0	1	0	0	0	1
33.882	34.1442	0.04083	FF6600	0	1	0	1	0	0
34.3783	34.6425	0.04083	FF6600	0	1	0	1	0	0
34.8786	35.1447	0.06184	0000FF	0	0	1	1	0	0
35.8877	36.1576	0.0406	FF0000	1	0	0	1	0	0
39.8726	40.1571	0.02934	00FFFF	1	0	0	0	2	0

Table A.3.1 – Example ranges cell array. Columns are (left to right): range start, range end, volume (nm^3), hexadecimal colour and element columns. The elements here are `elements={'Fe';'Cr';'Y';'O';'C';'N'}`. Therefore, range 4 contains C_2 and the last range FeO_2.

```
...
Range24=69.9125 69.9738 Vol:0.04060 Fe:1 O:1 Color:FF0000
Range59=23.9750 24.0363 Vol:0.01757 C:2 Color:660066
```

RRNG files can be written using *rangeWriter.m*. and the range definition as a cell array with columns: range start, range end (both in m/z), the ionic volume, range colour (in hexadecimal) and one column for each element with the number of each element in each ion given. An example ranges cell array is given below.

```
[newFile] = rangeWriter( ranges, elements, rangeFile )
```

A.4 Lorentzian Peak Fitting

Peaks in GIX diffractograms were fit using a Lorentzian peak:

$$f(x) = \frac{\alpha}{(x-\beta)^2+\gamma} + c + m.x \tag{A.4.1}$$

Where α is the amplitude of the the peak, β is the peak position, γ is the peak width ($2\times\sqrt{\gamma} = FWHM$), and where c and m describe a linear background. The fitting is performed in MATLAB using the following:

T_{irrd} /K	Damage dpa	Amp	FWHM /° 2θ	Integrated counts	Centre /2θ
-	-	2.92	0.26	2514	16.26
773	150	0.63	0.23	629	16.22
873*	150	0.63	0.53	170	16.16
973	150	1.15	0.43	430	16.24

(a) 2°, 800 nm attenuation length.

T_{irrd} /K	Damage dpa	Amp	FWHM /° 2θ	Integrated counts	Centre /2θ
-	-	4.55	0.32	2734	16.27
773	150	1.43	0.29	1092	16.28
873	150	0.84	0.35	449	16.28
973	150	0.50	0.23	443	16.25

(b) 4°, 1600 nm attenuation length.

Table A.4.1 – The result of fitting a Lorentzian peak, with a background subtraction, to the $Y_2Ti_2O_7$-(222) peak at 16.3 2θ in the GIX diffractograms from irradiated FeCrTiY. * This sample had a very low intensity diffractogram overall but the experiment could not be repeated, therefore the fitting should not be considered reliable.

T_{irrd} /K	Damage dpa	Amp	FWHM /° 2θ	Integrated counts	Centre /2θ
-	-	0.47	0.17	675	16.27
773	150	0.96	0.31	576	16.26
773	-	0.57	0.15	876	16.31
873	150	1.38	0.30	895	16.28
873	-	0.90	0.15	1470	16.31
973	150	0.85	0.27	648	16.28
973	-	0.44	0.15	701	16.32

Table A.4.2 – The result of fitting a Lorentzian peak, with a background subtraction, to the $Y_2Ti_2O_7$-(222) peak at 16.3 2θ in the GIX diffractograms from irradiated FeTiY. Incident angle 4°; 1600 nm attenuation length.

```
function F = lfun3L(p,x)
F = p(1)./((x-p(2)).^2+p(3)) + p(4) + p(5).*x;
end
[params, resnorm, residual] = lsqcurvefit(@lfun3L,p0,x,y,lb,ub);
```

The result of using the above routine on the FeCrTiY samples irradiated at high temperature is shown in table A.4.1.

A.5 MATLAB Programs

List of the most important MATLAB scripts I have written, some to be used in-conjunction with *posgen* (D Haley*). The source code for these functions and others are available digi-

*http://apttools.sourceforge.net

tally as supplementary materials.

massDecomp.m Calculate the peak deconvoluted and background corrected composition for a specific POS file, range file and definition of overlapping peaks.

GB_seg.m Calculate the composition of a grain boundary from a 1D line profile (exported from IVAS in the CSV file format).

multipleHits3.m Process an EPOS file to produce the data presented in section §4.3.

clusterDetails.m Reads many CSV cluster statistics files produced using IVAS and was used to produce table A.6.1.

clusterAspect.m Returns the details (composition, size, location etc.) from an IVAS CSV cluster statistics file. Related: *clusterExtent.m*.

clusterCompAndProfileDecompIonic.m Using cluster POS, range and statistics files, produce a per-cluster peak-overlap deconvoluted composition and composition line profile. Important functions: *clusterDecompTablesIonic.m* and *clusterProfileEleNP.m* which perform the computation. See *zprofileCacheSummary.m* for how to extract the results from the "zprofileCache" results file.

rangeCheck.m Using a POS file, remove ranges which contain no mass peaks.

rangeSynthetic.m Produce an estimate range file from a list of possible ions.

rangeCorrector.m Automatic range width identification. Fits a function to the mass peaks in a m/z spectrum and returns a range file with specific FWf(x)M.

peakDecompFail.m Least squares estimation of the ionic composition of overlapping mass peaks.

dataBase.m Reads the data stored in *data.mat* and returns experimental details, file locations and meta-analysis of atom probe experiments.

rangeReader.m/rangeWriter.m Read and write RRNG format range files.

posgenOptionGen.m Produces an XML file to be used in-conjunction with *posgen*. See *posgenWrapper.m* for a practical example.

dmax_variation.m Runs *posgen* with many different cluster selection parameters and returns the variation of composition, size, number and solute fraction as a function of D_{max}.

clusterSizeDistMultiDmax_whole.m Run *posgen* with many times using the same cluster selection parameters and returns the number of random clusters identified.

A.6 Cluster selection parameters

Cluster selection parameters for APT data were chosen according to the details given in section 3.7.8 on page 73 and the specific parameters used are given in table A.6.1.

Table A.6.1 – Cluster selection parameters used in "usable" experimental data sets. ID prefix = "R14_". D_{max}, L and E_r are in nm. Sample codes with "u" suffix are unirradiated (heat treated only).

ID	Alloy	Sample Code	D_{max}	L	E_r	N_{min}	Core ions	No.
15065	FeTiY	FeTiY	0.8	0.8	0	12	Fe2O, O, TiO, Y, YO	99
15202	FeCrTiY	FeCrTiY	1	1	0	15	O, TiO, Y, YO	86
15529	FeCrTiY	FeCrTiY	1.2	1.2	0	20	O, TiO, Y, YO	76
15576	FeY	FeY	1.2	1.2	0	20	O, O2, Y, YO, YO2	6
15577	FeY-hi	FeY-hi	1.2	1.2	0	20	Y, YO	715
15627	FeY-hi	FeY-hi	2	2	0	12	Y, YO	217
15645	FeY	FeY	1.3	1.3	0	30	Y, YO, YO2	4
15733	FeTiY	FeTiY	0.9	0.9	0	12	O, TiO, Y, YO	86
15734	FeCrTiY	FeCrTiY	0.85	0.85	0	10	O, TiO, Y, YO	372
15781	FeY-hi	FeY-hi	0.8	0.8	0	12	Y, YO	114
15783	FeTiY	FeTiY	1	1	0	12	Y, YO	11
15867	FeCrTiY	FeCrTiY	1.2	1.2	0	20	TiO, Y, YO	63
15868	FeCrTiY	FeCrTiY	0.8	0.8	0	20	TiO, Y, YO	86
15972	FeTiY	FeTiY	0.86	0.8	0	6	Y, YO	8
15975	FeY	FeY	1	1	0	29	Y, YO	2
16245	FeTiY	FeTiY	1.4	1.4	0	12	O, Y, YO	7
16416	FeCrTiY	C2	0.8	0.8	0	25	O2, Y, YO	16
16421	FeCrTiY	C2	0.8	0.8	0	15	TiO, Y, YO	102
16469	FeCrTiY	C2	1	1	0	20	TiO, Y, YO	62
16559	FeCrTiY	C1	1	1	0	17	YO	17
16725	FeCrTiY	C2	1	1	0	15	TiO, YO	58
16731	FeCrTiY	C2	0.9	0.9	0	20	Y, YO	22
16915	FeCrTiY	C1	0.7	0.7	0	15	O, TiO, Y, YO	83
16917	FeCrTiY	C1	0.9	0.9	0	15	O, TiO, Y, YO	19
16919	FeCrTiY	C2	1	1	0	10	CrO, TiO, YO	115
16933	FeCrTiY	C1	0.8	0.6	0	15	CrO, O, TiO, Y, YO	21
16977	FeTiY	B2	1.4	0.5	0	15	O, O2, TiO, Y, YO	8
17014	FeTiY	B1	0.7	0.7	0	15	O, TiO, Y, YO	23
17031	FeTiY	B1	1.2	1.2	0	15	O, TiO, Y, YO	1
17053	FeTiY	B3	0.95	0.95	0	15	O, TiO, Y, YO	100
17125	FeTiY	B3	1	1	0	12	TiO, Y, YO	52
17156	FeCrTiY	C3	0.8	0.8	0	10	Y, YO	56
17167	FeTiY	B2	0.9	0.9	0	20	O, TiO, Y, YO	18
17169	FeTiY	B2	0.8	0.8	0	15	O, TiO, Y, YO	38
17178	FeCrTiY	C3	1.05	1.05	0	10	TiO, Y, YO	38
17183	FeCrTiY	C3	0.7	0.7	0	10	CrO, TiO, YO	94
17226	FeTiY	B2	0.8	0.8	0	20	TiO, Y, YO	10
17242	FeCrTiY	C2u	0.7	0.7	0	11	O, TiO, Y, YO	116
17343	FeTiY	B3	0.9	0.9	0	10	O, TiO, Y, YO	207
17344	FeTiY	B3	0.8	0.8	0	8	O, TiO, Y, YO	69
17757	FeTiY	B1u	0.7	0.7	0	12	TiO, Y, YO	18

Table A.6.1 – Cluster selection parameters used in "usable" experimental data sets. ID prefix = "R14_". D_{max}, L and E_r are in nm. Sample codes with "u" suffix are unirradiated (heat treated only).

ID	Alloy	Sample Code	D_{max}	L	E_r	N_{min}	Core ions	No.
17758	FeTiY	B1u	0.9	0.9	0	20	O, TiO, Y, YO	4
17868	FeTiY	B1u	0.7	0.7	0	25	O, TiO, Y, YO	23
17870	FeTiY	B1u	0.9	0.9	0	10	O, TiO, Y, YO	38
17886	FeTiY	B1u	0.8	0.8	0	21	O, TiO, Y, YO	44
17890	FeTiY	B1u	1	1	0	10	FeO, YO	1
17985	FeTiY	B3	1.1	1.1	0	8	O2, Y, YO	4
17989	FeTiY	B3	1.3	1.3	0	8	O2, Y, YO	15
17996	FeTiY	B3	0.8	0.8	0	12	O, TiO, Y, YO	22
18002	FeTiY	B3	0.9	0.9	0	15	O, TiO, Y, YO	6
18053	FeTiY	B3	0.85	0.85	0	12	O, TiO, Y, YO	22
18090	FeTiY	B3	1.3	1.3	0	12	Y, YO	8
18097	FeTiY	B3	1	1	0	15	TiO, Y, YO	25
18138	FeCrTiY	C3	1.1	1.1	0	12	TiO, Y	160
18141	FeCrTiY	C3	0.95	0.95	0	12	TiO, Y, YO	53
18146	FeCrTiY	C3	1	1	0	12	Y, YO	34
18220	FeCrTiY	FeCrTiY	0.9	0.9	0	15	CrO, TiO, Y, YO	259
18225	FeCrTiY	C010	1.2	1.2	0	14	TiO, Y, YO	47
18357	FeCrTiY	C010	1.1	1.1	0	20	Y, YO	15
18420	FeCrTiY	C010	1.5	1.5	0	16	Y	5
18422	FeCrTiY	C010	1.1	1.1	0	24	TiO, Y, YO	81
18452	FeCrTiY	C0510	0.9	0.9	0	10	TiO, YO	64
18516	FeCrTiY	C010H	0.9	0.9	0	6	TiO, Y, YO	371
18622	FeCrTiY	C010H	1.2	1.2	0	12	TiO, Y, YO	79
18628	FeCrTiY	C0510	1.1	1.1	0	12	TiO, Y, YO	122
18633	FeCrTiY	C010	1	1	0	20	Y, YO	59
18784	FeCrTiY	C010H	0.8	0.8	0	15	Y, YO	20
18785	FeCrTiY	C010H	0.8	0.8	0	15	Y, YO	90
18799	FeCrTiY	C01010	1.1	1.1	0	12	TiO, Y, YO	91
18800	FeCrTiY	C01010	0.9	0.9	0	6	TiO, YO	32
18818	FeCrTiY	C010H	1	1	0	12	TiO, Y, YO	121
18890	FeCrTiY	C01010	1	1	0	12	TiO, Y, YO	582
18927	FeCrTiY	C01010	0.8	0.8	0	8	TiO, Y, YO	363
18953	FeCrTiY	C01010	1	1	0	10	O2, Y, YO	312
18959	FeTiY	B010	1.3	1.3	0	12	YO	12
18965	FeTiY	B010	1	1	0	15	Ti, TiO, Y, YO	44
18969	FeTiY	B010	1.3	1.3	0	15	Y, YO	20
18970	FeTiY	B010	1.5	1.49	0	15	TiO, Y, YO	59
18972	FeCrTiY	C010H	0.6	0.6	0	6	CrO, FeO, TiO, Y, YO	517
18973	FeCrTiY	C010H	1.2	1.2	0	8	TiO, Y, YO	108
18974	FeCrTiY	C01010	0.85	0.85	0	8	TiO, Y, YO	20
19009	FeCrTiY	C01010	1	1	0	12	TiO, Y, YO	92

Table A.6.1 – Cluster selection parameters used in "usable" experimental data sets. ID prefix = "R14_". D_{max}, L and E_r are in nm. Sample codes with "u" suffix are unirradiated (heat treated only).

ID	Alloy	Sample Code	D_{max}	L	E_r	N_{min}	Core ions	No.
19016	FeCrTiY	C01010	1.2	1.2	0	12	TiO, Y, YO	246
19046	FeTiY	B010H	1.4	1.4	0	12	Y, YO	126
19080	FeTiY	B010	0.8	0.8	0	10	TiO, Y, YO	104
19081	FeTiY	B010	1	1	0	10	Y, YO	18
19105	FeTiY	B010	1.4	1.4	0	15	TiO, Y, YO	5
19128	FeTiY	B010H	1.2	1.2	0	12	TiO, Y, YO	284
19129	FeTiY	B010H	1.4	1.4	0	10	TiO, Y, YO	109
19161	FeTiY	B01010	1	1	0	10	TiO, Y, YO	203
19169	FeTiY	B01010	1	1	0	10	TiO, Y, YO	153
19272	FeY	A1	1.6	1.6	0	12	Y, YO	35
19435	FeY	FeY	1.6	1.6	0	15	Y, YO	25
19616	FeY	A1	1.4	1.4	0	8	O, O2, Y, YO	55
19644	FeY	A1	1.5	1.5	0	6	Y, YO	55
19663	FeY	A1	1.05	1.05	0	4	Fe2O, FeO, YO	14
19698	FeY	A1	1.4	1.4	0	6	FeO, Y, YO	161
19704	FeTiY	B3b	1.4	1.4	0	12	TiO, Y, YO	20
19793	FeY	A1	1	1	0	8	Y, YO	35
19834	FeTiY	B1	1.4	1.4	0	12	O2, Y, YO	45
19835	FeTiY	B1	1.4	1.4	0	6	O2, TiO, Y, YO	24
19855	FeTiY	B1	1.5	1.5	0	6	TiO, TiO2, Y, YO	58
19858	FeTiY	B1	1.2	1.2	0	6	TiO, TiO2, Y, YO	46
19948	FeTiY	B05	1.2	1.2	0	12	TiO, Y, YO	5
19950	FeCrTiY	C0510	1	1	0	12	TiO, Y, YO	78
20013	FeTiY	B3b	1.2	1.2	0	8	TiO, Y, YO	20
20021	FeTiY	B1	1.4	1.4	0	12	FeO, O, TiO, Y, YO	108
20066	FeTiY	B3b	1.2	1.2	0	12	TiO, Y, YO	6

A.7 knitr information

This document has been compiled using Knitr [228] for LaTeX, as a Rnw file, meaning that, where possible, graphs and their accompanying source code are included in the source of this document itself. The source files are available on request and in the Oxford Research Archive `https://ora.ox.ac.uk/`. The session information is attached to allow the direct reproduction of this document from its source .Rnw and data files.

```
devtools::session_info()
```

```
## Session info -----------------------
```

```
##   setting  value
##   version  R version 3.3.1 (2016-06-21)
##   system   x86_64, mingw32
##   ui       RTerm
##   language (EN)
##   collate  English_United States.1252
##   tz       Europe/London
##   date     2016-08-31
```

```
## Packages --------------------------
```

```
##   package       * version    date       source
##   assertthat      0.1        2013-12-06 CRAN (R 3.3.1)
##   chron           2.3-47     2015-06-24 CRAN (R 3.3.1)
##   colorspace      1.2-6      2015-03-11 CRAN (R 3.3.1)
##   data.table    * 1.9.6      2015-09-19 CRAN (R 3.3.1)
##   DBI             0.4-1      2016-05-08 CRAN (R 3.3.1)
##   devtools        1.12.0     2016-06-24 CRAN (R 3.3.1)
##   digest          0.6.9      2016-01-08 CRAN (R 3.3.1)
##   directlabels  * 2015.12.16 2015-12-18 CRAN (R 3.3.1)
##   dplyr         * 0.5.0      2016-06-24 CRAN (R 3.3.1)
##   evaluate        0.9        2016-04-29 CRAN (R 3.3.1)
##   formatR         1.4        2016-05-09 CRAN (R 3.3.1)
##   ggplot2       * 2.1.0      2016-03-01 CRAN (R 3.3.1)
##   ggtern        * 1.0.6.0    2015-08-03 CRAN (R 3.1.3)
##   gtable          0.2.0      2016-02-26 CRAN (R 3.3.1)
##   knitr         * 1.14       2016-08-13 CRAN (R 3.3.1)
##   lattice         0.20-33    2015-07-14 CRAN (R 3.3.1)
##   magrittr        1.5        2014-11-22 CRAN (R 3.3.1)
##   MASS            7.3-45     2016-04-21 CRAN (R 3.3.1)
##   memoise         1.0.0      2016-01-29 CRAN (R 3.3.1)
##   munsell         0.4.3      2016-02-13 CRAN (R 3.3.1)
##   plyr            1.8.4      2016-06-08 CRAN (R 3.3.1)
##   png           * 0.1-7      2013-12-03 CRAN (R 3.3.0)
##   polyclip        1.3-2      2015-05-27 CRAN (R 3.1.3)
##   proto           0.3-10     2012-12-22 CRAN (R 3.1.2)
##   quadprog        1.5-5      2013-04-17 CRAN (R 3.3.0)
##   R6              2.1.2      2016-01-26 CRAN (R 3.3.1)
##   RColorBrewer  * 1.1-2      2014-12-07 CRAN (R 3.3.0)
##   Rcpp            0.12.5     2016-05-14 CRAN (R 3.3.1)
##   reshape2      * 1.4.1      2014-12-06 CRAN (R 3.3.1)
##   scales          0.4.0      2016-02-26 CRAN (R 3.3.1)
##   sp              1.1-1      2015-06-05 CRAN (R 3.1.3)
##   stringi         1.1.1      2016-05-27 CRAN (R 3.3.0)
##   stringr         1.0.0      2015-04-30 CRAN (R 3.3.1)
##   tibble          1.0        2016-03-23 CRAN (R 3.3.0)
##   withr           1.0.2      2016-06-20 CRAN (R 3.3.1)
```